Effect of Transverse Convex Surface Curvature on Turbulent Fluid Flow and Heat Transfer

by

Man-Woong Kim

A thesis submitted to the school of Graduate Studies
and Research in partial fulfilment of
the requirements for the degree of

Doctor of Philosophy
in
Mechanical Engineering

The Ottawa-Carleton Institute for
Mechanical and Aeronautical Engineering

Department of Mechanical Engineering
University of Ottawa
Ottawa, Ontario
Canada

ISBN 0-612-16415-2

ABSTRACT

The effect of transverse convex surface curvature on turbulent boundary layer flow and heat transfer over circular cylinders, and on fully developed turbulent flow and heat transfer in concentric annular ducts with smooth surfaces are studied both analytically and experimentally.

The analytical results are obtained through a turbulence model based on the variable von Kármán's constants, κ_i, proposed for the first time in the present study. A computer program is developed for calculation of the desired momentum and thermal characteristics. A numerical calculation using the standard k-ε turbulence model, with a modified procedure is also carried out. It is assumed that the thermodynamic fluid properties are independent of temperature.

An experimental study is conducted to study the effect of the transverse convex surface curvature of the core tubes both on fully developed turbulent flows and heat transfer in concentric annular ducts. Air is used as the working fluid. Three annuli having different radii of the inner cores, $R_i = 3.98$ mm, 8.57 mm, and 16.7 mm, with a fixed radius ratio of $\alpha = 0.3$, are used over a range of the Reynolds number between about 20,000 and 60,000. The inner cores are heated electrically to provide constant heat fluxes throughout the test sections and are instrumented for the temperature and power measurements. The outer tubes are insulated to minimize the leakage of heat. In the case of the experimental study for turbulent boundary layer flows and heat transfer on circular cylinders, the experimental data of Willmarth et al. [31] and Kim and Lee [45, 46] are recompiled for the present study.

It is seen that both the friction coefficient and heat transfer increase with decreasing value of the inner core radius of concentric annuli and the radius of circular cylinders, R_i

It is concluded that, while the effect of transverse concave curvature on fluid flow and heat transfer is negligible, that of transverse convex curvature is rather significant.

ACKNOWLEDGEMENT

The author wishes to express his sincere appreciation for the opportunity to have worked under the supervision and guidance of Professor Yung Lee, whose help and patient with countless love and knowledge of the field of turbulent fluid flow and heat transfer were paramount in bringing this study to be fruition.

The author expresses his sincere thanks to Professors W. Hallet and R. Milane for their kind advice and interest, and also to Mr. M. Makasare, technical staffs, and secretaries, Department of Mechanical Engineering, University of Ottawa, for their valuable help.

Sincere thanks also go to Mrs. J. H. Lee, Mrs. S. Amyot, and Reverend Dr. T.J. Moon for their love and encouragement. I am also indebted to colleagues and friends, Dr. H.J. Kim, Mr. B.S. Kim and Dr. Choi for their various advice.

Thanks also go to Dr. S.H. Lee, Dr. Y.K. Yim, and Dr. S-H Lee of KINS and Dr. S.Y. Kim of KAERI for their encouragement and supports.

Finally, the author specially appreciates to the Load, his parents, and family: the author's wife, Myung-Hee, and his two daughters, Min-Sun and Bo-Kyung, whose continuous support and patient with endless love made it possible to persevere during the years of work.

TABLE OF CONTENTS

LIST OF TABLES

LIST OF FIGURES

NOMENCLATURE

A	surface area of the hot junction [m^2] or van Driest's damping constant
A^+	dimensionless van Driest's damping parameter
b	outside thickness of pitot tube
c	constant
c_1, c_2, c_μ	coefficients in turbulent transport equations
c_p	specific heat at constant pressure [kJ/kg·°C]
C_f	skin friction coefficient, circular cylinder, ($2\tau_w/\rho \cdot u_\infty^2$)
D	distance between the walls, concentric annulus, ($R_o - R_i$) [m]
D^+	modified distance parameter, concentric annulus, ($D \cdot u_o^*/\nu$)
De	equivalent diameter of annulus, $2(R_o - R_i)$, [m]
E	electrical voltage [v]
f_j	friction factor, concentric annulus, ($2\tau_j/\rho \cdot \bar{u}_j^2$)
F	force, function
F_g	radiation geometry factor
F_ϵ	surface emissivity for hot junction
G	mass flow rate of the fluid [kg/m^2]
h	convective heat transfer coefficient [W/m^2 °C]
I	integral function or amperage [Amp]

k	thermal conductivity [W/m°C] or turbulent kinetic energy
k_t	eddy conductivity [W/m°C]
l	Prandtl's mixing length [m]
l^+	dimensionless Prandtl mixing length parameter, circular cylinder, $(l \cdot u^* / \nu)$
L	length [m]
n	constant
Nu	Nusselt number; circular cylinder $(= h \cdot x / k)$, concentric annulus $(= h \cdot De / k)$
P	pressure [N/m^2]
Pr	Prandtl number, $(c_p \cdot \mu / k)$
Pr_t	turbulent Prandtl number, $(\varepsilon_M / \varepsilon_H)$
q	heat flux per unit area [W/m^2]
q'	heat generation per unit volume [J/m^3]
q^+	dimensionless heat flux parameter
r	radial coordinate measured from cylinder axis [m]
R_i	radius of circular cylinder [m]
R_i^+	dimensionless cylinder radius, $(R_i \cdot u^* / \nu)$
R_j	radius of concentric annuli [m]
R_j^+	dimensionless radius parameter, concentric annulus, $(R_j \cdot u_o^* / \nu)$
Re	Reynolds number
S	source term
t	time [sec]

T	temperature [°C]
T^+	dimensionless temperature parameter, $((T_w - T)\cdot\rho\cdot c_p\cdot u_j{}^*/q_i)$
u	velocity in x-direction [m/s]
u^+	dimensionless velocity parameter, (u/u_j^*)
u_j^*	friction velocity, $(\tau_j/\rho)^{0.5}$ [m/s]
υ	velocity in y-direction [m/s]
w	velocity in z-direction [m/s]
x, y, z	cartensian coordinates [m]
y	distance from the wall [m]
y^+	dimensionless distance parameter, $(y\cdot u_j{}^*/\nu)$
Y^+	modified distance parameter

<u>Greek Symbols</u>:

α	radius ratio of annulus, (R_i/R_o) or thermal diffusivity [m^2/s]
Γ	general diffusion coefficient
Δ	enthalpy defect area [m^2] or displacement of pitot tube [m]
δ	boundary layer thickness [m] or deflection of rod [m]
δy	y-direction distance between two adjacent grid points
ϵ	surface emissivity
ε	eddy diffusivity [m^2/s], emissivity, or dissipation rate of turbulent kinetic energy

ζ	normalized distance, concentric annlus, (y^+/D^+), or coordinate for circumferential direction of fluid flow
η	coordinate for normal direction of fluid flow
θ	momentum defect area [m^2] or azimuthal coordinate
κ	von Karman's constant, 0.4
ξ	coordinate for streamwise direction of fluid flow
μ	dynamic viscosity [kg/m·s]
μ_t	eddy viscosity [kg/m·s]
ν	kinematic viscosity [m^2/s]
ϕ	generalized dependent variable
ϕ_1, ϕ_2	function
ρ	density [kg/m^3]
σ_k, σ_ε	coefficients in turbulent transport equations
τ	shear stress [kg/m·s^2]

Superscripts:

$^+$	quantity non-dimesionalized by means of ν, τ_w, and ρ
$'$	fluctuating component
$-$	mean
$*$	normalized by the wall value, e.g., q^* (= $q/q_{w,j}$), τ^* (= $\tau/\tau_{w,j}$)

Subscripts:

b	bulk
H	thermal
i	inner
i, j, k	inner or cartesian coordinate direction
j	designate number (i or o)
k	turbulent kinetic energy
m	corresponding to the maximum velocity point
M	momentum
l	laminar
o	outer
p	flat plate or value at a node adjacent to the wall
p.p	parallel planes
R_j	radius of circular cylinder or concentric annulus
s	at sublayer boundary
t	turbulent
w	wall
x	local
∞	free stream

Fixed Dimensionless Quantity:

A^+	dimensionless van Driest's damping parameter, 26
y^+_{is}	26, sublayer thickness for inner region, concentric annulus
y^+_{os}	26, sublayer thickness for outer region, concentric annulus

CHAPTER 1
INTRODUCTION

1.0 General Overview

Fluid flow has been studied extensively because of its importance in engineering. Ducts with circular cross-sections are the most convenient geometry from an engineering point of view, but annular cross-sections are also important because of their use in a variety of heat transfer systems, such as nuclear reactors and heat exchangers. In nuclear reactors, fuel elements of cylindrical form are in cylindrical coolant channels. Design considerations for such reactors, therefore, require data concerning turbulent fluid flow and heat transfer in annular ducts. However, much of the data currently available for annular ducts does not consider the effect of the transverse surface curvatures (concave and convex surface curvatures) on fluid flow and heat transfer phenomena. As a result, information concerning friction coefficients and heat transfer rates [including critical heat flux (CHF)] in such systems could be incomplete and thus inadequate for practical purposes.

Investigated in this study are; (i) turbulent boundary layer flows and heat transfer over circular cylinders and (ii) turbulent fluid flows and heat transfer in annular ducts. In the latter case, the boundary layer is developed to be fully developed. Since velocity profiles for fully developed turbulent flows in annular ducts are asymmetric, two separate boundary layers, one on the inside wall and one on the outside wall, exist. Fully developed turbulent annular duct flow is more complicated than turbulent pipe flow, which is the simplest case of axisymmetric flow. In axisymmetric flow, velocity distributions, flow friction, and heat transfer are well documented. The documentation for those factors in annular duct flows, however, is incomplete and must be updated to include the effect of the transverse surface curvature.

There are presently three techniques used to treat turbulent flows: (1) boundary layer theory, (2) numerical solution and (3) experimentation.

The boundary layer concept, first introduced in 1904 by Prandtl [1][1], divides the flow over a body into two regions: (i) an inviscid region, governed by the Euler equations of motion, and (ii) a viscous region near the body, governed by the boundary layer equation. For laminar flow, the existence of a well-defined relationship between shear stress and velocity gradients gives rise to a set of partial differential equations that are mathematically soluble. The problem of turbulent flow, on the other hand, is phenomenological as well as mathematical, and, thus, exact solutions of the boundary layer are not yet available. The usual boundary layer equations for turbulent flow contain a term involving the time mean of the product of fluctuating velocities, Reynolds shear stresses, and a term involving the time mean of the product of fluctuating velocity. In order to proceed, this solution must be simplified by some empiricism, which lead to a variety of turbulence models with questionable accuracy in predicting boundary layer parameters.

Numerical analysis of turbulent flows is still in the development stage. Many computer solutions for fluid flows have been published, and computer speeds and graphical presentation are improving rapidly, but, to date, most of these solutions are laminar. Although there is a rapid growth in computer analysis of turbulent fluid flows, accurate numerical models of turbulence are still

[1] The number(s) in square bracket indicate(s) the reference section of this thesis.

numerically complicated and must be simplified with empirical constants in order to be manageable. Experimentation is, thus, the most common method of studying turbulent flows, because it alone can give an adequate description of the turbulent flow phenomena.

In recent years, direct numerical simulations (DNS) of turbulent fluid flows in a circular channel have been introduced for the prediction of fluid flow fields. The fluid flow can be calculated directly by solving the three-dimensional, time-dependent Navier-Stokes equations, and no approximation for the Reynolds closure is required. These simulations have become an important research tool in studying the basic physics of turbulence in channels. For a computing simulation of turbulence, the computational resources, however, required vary as the cube of the Reynolds number. It is estimated that successful simulation for higher Reynolds numbers will not be accomplished for a long time.

1.1 Transverse Curvature of Wall Surface

In many practical situations, significant transverse curvature effects may occur with streamwise pressure gradients. For fluid flow over two-dimensional curved surfaces, as in annular ducts, two transverse surface curvatures must be considered as shown in Figs. 1.1 and 1.2.

In Fig. 1.1, the flow outside of the maximum velocity, u_m, is subject to transverse <u>concave</u> surface effects, whereas the flow inside of the maximum velocity is subject to transverse <u>convex</u> surface effects. An example of the latter type of flow is the boundary layer flow along a cylindrical body. In this case, if the body is sufficiently long and slender, the boundary layer will grow to a thickness that is comparable with the radius of body. A knowledge of the effect of the transverse convex surface curvature on boundary layer characteristics is, therefore, important in estimating the surface resistance of objects on which the boundary layer thickness is comparable to its transverse radius of curvature [2].

In annular ducts, the turbulence models for the prediction of flow fields and the standard universal velocity are inadequate to predict the inner velocity distributions of annular duct flows. While a fixed value of von Kármán constant, κ_o between 0.36 and 0.41 is usually taken for the outer region of annular ducts, it has been found that the value of the constant for the inner region, κ_i, must be calculated from other appropriate boundary conditions [3-6]. The latter implies that transverse concave surface curvatures have little effect on the radial development of turbulent flow , whereas the effects of the transverse convex surface curvatures are significant. Thus, the behaviour of the Reynolds stresses for concave surfaces (outer wall) and convex surfaces (inner wall) in annular ducts will differ in a way that must be accounted for when modelling turbulent flow over these surfaces. In Fig. 1.2, the terms $(-\overline{u'v'})_{concave}$ and $(-\overline{u'v'})_{convex}$ at $y_1 = y_2$ will, therefore, be different because of differing rates of turbulence production caused by the two types of surface curvature.

The accepted convention in fluid flow and heat transfer is to make all influencing parameters dimensionless via dimensional analysis. For fully developed turbulent fluid flow and heat transfer in smooth annular ducts, the following dimensionless quantities are considered sufficient to define the governing relations (see Appendix A):

$$\begin{aligned} f &= f(Re\,,\,\alpha) \\ Nu &= Nu\,(Re\,,\,Pr\,,\,\alpha) \end{aligned} \tag{1.1}$$

That is, heat transfer is considered to be a function of radius ratio α ($= R_i / R_o$), Prandtl number, Pr, and Reynolds number, Re.

Such dimensionless analysis, however, fails to account for the effect of the transverse surface curvature. Since transverse convex surface curvature may affect flow phenomena such as friction and heat transfer, the degree of the transverse convex surface curvature must somehow be integrated into the description of the governing relations, in addition to the other influencing dimensionless parameters. Including the effect of the transverse convex surface curvature in concentric annuli by introducing new dimensionless quantities such as Re_{R_i} $(= R_i \cdot \bar{u}/\nu)$ or R_i^* $(= R_i \cdot u^*/\nu)$ may seem appropriate, but a close examination of the nature of Re_{R_i} and R_i^* reveals that an infinite number of combinations of R_i and $\bar{u}$ can be found that result in the same value of Re_{R_i} for a given fluid (see Appendix B). This implies that the parameter Re_{R_i} $(or\ R_i^*)$ itself cannot characterize the degree of the transverse convex surface curvature in a given annular duct. The absolute radius of the inner core, R_i, should, therefore, be used to reflect degrees of curvature.

1.2 Scope of Study

The objective of this research is to validate the proposed hypothesis on transverse convex curvature for turbulent flow over convex surfaces, and to introduce the proposed variable von Kármán constant that can successfully describe the effect of the transverse convex surface curvature on turbulent fluid flow and heat transfer.

In the present work, two studies are carried out. The first considers the effect of the transverse convex surface curvature on the turbulent boundary layer flow over heated longitudinal circular cylinders, while the second considers fully developed turbulent fluid flow and heat transfer in internally heated annular ducts. Analytical and experimental analyses are carried out on both configurations.

For the experimental analysis, three specially designed annular ducts (see Table 4.6) were constructed to conduct the required measurements of heat transfer rates and friction factors. All the ducts had uniformly heated cores, insulated outer walls and a fixed radius ratios (about 0.3). The experiments were conducted over a Reynolds number range of 10,000 to 60,000, using air as the working fluid.

For the analytical analysis, the integral momentum and energy equations were combined with modified versions of previously accepted turbulence models to predict friction factors and heat transfer rates in the experimental duct geometries. The modified mixing length model of Hornby et al. [7] was used for the analysis of turbulent boundary layer flows on the heated circular cylinders, whereas the turbulence models of van Driest [8] and Reichardt [9] were used for fully developed turbulent fluid flow and heat transfer in annular ducts. All the turbulence models were adapted to reflect the variable von Kármán constants, κ_i, which was first introduced in the present thesis required for the transverse convex surface curvatures. For a comparison, the k-ε two equation turbulence model was tested for the turbulent flow in annular ducts.

The work is subdivided into several components. First, a survey of relevant works in the literature is carried out, outlining past theoretical analyses and experimental measurements of: (i) turbulent boundary layer flows and heat transfer and (ii) fully developed turbulent flows and heat transfer on the geometries in question.

This is followed by a mathematical development of analytical analyses, showing the integration of the momentum and energy equations with the adapted turbulence models based on variable von Kármán constants, κ_i. The governing equations of the systems are presented. Their numerical solution is then described, demonstrating the approximation of the governing equations. A grid generation scheme for the geometry used is also presented, along with the predicted flow fields in the calculation of the k-ε turbulence model.

A description of the experimental apparatus, instrumentations, and results is also included, summarizing the findings for velocity profiles, friction fatore, temperature profiles, and heat transfer coefficients for various radii, R_i, of the inner cores, i.e., <u>transverse convex surface curvature</u>, at various Reynolds numbers in test sections of the apparatus.

Finally, the analytical and experimental results are compared to evaluate the effects of the transverse convex surface curvatures, the performance of mathematical models, and conclusions regarding the validity of the proposed variable von Kármán constants, κ_i, are outlined.

CHAPTER 2
LITERATURE SURVEY

2.0 General Overview

Studies of turbulent fluid flows in smooth ducts have long been the subject of research and most of the earlier investigations were concerned with circular cross-sections. Annular ducts have also been dealt with in many studies because they are the simplest non-circular flow channel, widely used in practice.

A fair number of experimental and analytical analyses of the turbulent boundary layer on cylindrical bodies have been carried out. The analytical analyses are based on the application of turbulent transport coefficients which apply to the turbulent flows in round pipes and on flat plates.

In recent years, however, a better approach for the prediction of fluid flow fields has been introduced with the appearance of direct numerical simulations (DNS) of turbulent fluid flows in a circular channel [10-15]. In these simulations, the fluid flow is calculated directly by solving the three-dimensional, time-dependent Navier-Stokes equations without any approximation for the Reynolds closure. The simulation databases, which contain three-dimensional velocity and pressure fields, have provided information to complement experimental data in the study of the physics of turbulent flows.

Time has also been devoted to the study of turbulent fluid flow and heat transfer in smooth annular ducts but little has been done to explore a way of representing convex curvature effects.

Understanding of the flow characteristics and heat transfers in this kind of duct is important since this shape occurs in a wide variety of heat transfer systems.

2.1 Turbulent Boundary Layer Flow in Circular Channels and over Circular Cylinders

2.1.1 Relevant Experimental Studies

An extensive investigation of turbulent fluid flow in circular channels has been done during the last several decades because of the practical importance of pipes in engineering applications. The results are relevant not only to pipe flow but also to flow in non-circular ducts, and contribute to the extension of fundamental knowledge about turbulent fluid flow in general. The simple geometry of circular channels allowed for many experimental and theoretical investigations of turbulence interactions near the wall.

Among many studies, Deissler [16], in 1950, carried out an experimental measurement and analytical investigation of turbulent fluid flow and heat transfer in smooth tubes. In his report, equations of the velocity and temperature distribution for the fully developed turbulent flow using air as a working fluid in smooth tubes were derived. The Nusselt numbers and friction factors were predicted and agreed with those experimentally determined in tubes for Reynolds numbers above 10,000.

Laufer [17], in 1951, measured the structure of turbulence for the fully developed turbulent flow in round pipes (10 in. diameter) at speeds of 10 and 100 feet per second. He noted that the flow field could be divided into three regions: (i) wall proximity where turbulence production, diffusion and viscous action are all important; (ii) the central region of pipe where energy diffusion plays the predominant role, and (iii) the region between (i) and (ii) where the local change rate of turbulent-energy production dominates the energy received by diffusion action. Laufer found that the rates of turbulent energy production, dissipation, and diffusion had maximum values near the edge of the viscous sublayer.

Barbin and Jones [18], in 1963, reported measurements of mean velocities, turbulence intensities and turbulence (Reynolds) stresses in the inlet region of a smooth pipe at a Reynolds number of 388,000. They obtained the wall shear stress from the measured static pressure gradient. Since the momentum flux was approximately constant in a channel, the static pressure gradient could determine the wall shear stress. From their measurements, they found that the wall shear stress and static pressure gradient were influenced by the flow near the wall.

Clark [19], in 1968, published a study of fully developed turbulent flow in a channel. He measured mean velocities, turbulence intensities and Reynolds stresses using constant-temperature hot-wire anemometry at a range of Reynolds number from 10,000 to 130,000. He constructed the empirical mean velocity expression for the fully developed turbulent flow in a channel. However, his expression is limited to Reynolds numbers between 10^4 and 10^5.

Eckelmann [20], in 1974, reported measurements of turbulence structure for the viscous sublayer and the adjacent wall region in fully developed turbulent channel flow using oil as a working fluid. He found that velocity fluctuations decreased at a higher rate than the mean velocity in the viscous sublayer.

Hussain and Reynolds [21], in 1975, measured mean velocities, turbulence intensities and Reynolds stresses for fully developed turbulent channel flow using air as a working fluid at three Reynolds numbers of 13,800, 23,200 and 32,300. Johansson and Alfredsson [22,23], in 1982 and 1983, also carried out measurements of the velocity components and the turbulence structures in fully developed turbulent channel flows using water as a working fluid for Reynolds numbers of 13,800, 34,600 and 48,900.

The problem of turbulent flow along the outside surface of cylinders is also important in engineering applications, yet has received less attention than internal turbulent pipe flow. Experimental data for this type of flow are, therefore, more scarce. The experimental and analytical studies which exist concern themselves with measuring and predicting the mean velocity profile over circular cylinders with transverse convex surface curvatures.

Landweber [25], in 1949, published a report on the effect of the transverse curvature on friction resistance from experiments. There, he proposed a transverse curvature effect using a one-seventh power law for the velocity distributions and the Blasius empirical expression [26] for shear stress at the wall for turbulent boundary layer flows over circular cylinders. He calculated the skin friction coefficient using the momentum integral equations and noted that, for given values of the momentum thickness Reynolds number, skin friction coefficients on a circular cylinder were higher than those on flat plates.

Eckert [27], in 1957, measured the turbulent boundary layer characteristics on a cylinder in axisymmetric flow. He reported that local skin coefficients were higher than those for the flat plates, while the boundary layer thicknesses for circular cylinders were less than those for the flat plates.

Glauert and Lighthill [28], in 1955, measured the velocity profiles for asymmetric laminar boundary layer flow over circular cylinders. The authors found that the production of turbulence in the boundary layer increased with the rate of momentum exchange, as the velocity profile was fuller (flatter). The skin friction coefficient also increased as the growth of the boundary layer thickness decreased.

Coles [29], in 1956, proposed the "law of the wake" for turbulent boundary layers from his experimental measurement. He proposed that the velocity profile on the outside of a cylinder could be obtained by linear combination of two universal functions for the turbulent boundary layer flow. One function was called the "law of the wall" and the other was called the "law of the wake". For steady two-dimensional mean flow of an incompressible fluid, he established a universal law for values of y^+ ($= y \cdot u^* / \nu$) greater than 50 as

$$\frac{u}{u^*} = \frac{1}{\kappa} \ln\left(\frac{y u^*}{\nu}\right) + c \tag{2.1}$$

where the von Kármán constant, κ, and c were universal constants determined from experiment data. He suggested that the von Kármán constant, κ, lay between 0.39 and 0.41

Yu [30], in 1958, investigated the effect of the transverse surface curvature on turbulent boundary layer characteristics. He measured velocity distributions and shear stresses in the turbulent boundary layer flow on the outside of a slender cylinder (2 inch diameter) with zero pressure gradient at Reynolds numbers of 15,200, 30,740 and 45,060. He constructed a modified "law of the wall" to account for the transverse wall surface curvature. The "modified logarithmic law" based on the radius Reynolds number, Re_{Ri} ($= U \cdot R_i / \nu$), is

$$\frac{U - u}{u^*} = - m \ln \frac{y u^*}{\nu} e^{a/m} + b \tag{2.2}$$

The length scale, L, is

$$L = -\frac{u^*}{\nu} e^{\sigma/k} \tag{2.3}$$

where U is free-stream velocity and u^* is the friction velocity defined in Nomenclature. y is the distance of radial direction and ν is kinematic viscosity. In the length scale, σ, is defined as U / u^*, the constant m is 5.75 and b is empirically determined. He introduced a length scale, L, of the turbulent boundary layer based on the friction velocity. His proposed "law of the wall" of the velocity profile seemed to depend on the radius Reynolds number, Re_{Ri} (= $R_i \cdot u/\nu$). In his results, the effect of transverse surface curvature decreased the turbulent boundary layer thickness and increased the surface shear stress.

Willmarth and Yang [31], in 1970, published experimental measurements of pressure fluctuations near the wall in turbulent boundary layers on flat plates and cylinders. They measured the mean velocity profiles and the wall shear stresses for various diameters (0.02 to 2.0 inches). They reported that there were two effects of the transverse surface curvature that reduced the size of turbulent eddies in the turbulent boundary layer. The first effect was the increased steepness of the velocity profile, i.e., velocity gradient, due to reduction in the size of turbulent eddies. In the turbulent boundary layer, as velocity profiles become fuller (flatter), the turbulent eddies near the wall might be smaller because the mean velocity could be further reached at nearer the wall. The second effect was that the size of large eddies reduced more than small eddies in the transverse direction. Since the mean velocity is higher than that at the sides of plane boundary layer in the transverse direction, this shearing motion acts to reduce the transverse scale of large eddies.

Patel et al. [2,32], in 1965 and 1974, reported experimental measurements in the thick axisymmetric turbulent boundary layers near the tails of revolution bodies. They measured pressure distributions, mean velocity profiles and Reynolds stresses. They found that thick boundary layers were characterized by variations in the static pressure across the body. This static pressure variation was associated with an interaction between the boundary layer and the potential flow outside it, while the observed changes in the turbulence structures were associated with the effect of the transverse surface curvature. Patel et al. compared their results against the experimental results of Yasuhara [33] and justified their conclusions.

Lueptow et al. [34,35], in 1985 and 1987, measured the mean velocity and Reynolds stresses as associated with the turbulent boundary layers that developed on the walls of circular cylinders in axial flow. They noted that Reynolds stresses and turbulence intensities in the mean flow direction were a function of the inverse radial distance from the center of the cylinder. From their results, they proposed a mean velocity derived from the logarithmic law of the wall using the non-dimensional radial coordinate y^+ ($= y \cdot u^* / \nu$) and the ratio of local boundary layer thickness to the radius of the cylinder, δ / R_i, as:

$$u^+ = \frac{1}{m} \ln y^+ + n \tag{2.4}$$

where u^+ is dimensionless velocity defined as u/u^*, and m and n are constants determined from experiment.

Many similarity laws deduced from the experimental measurements have been proposed for the mean velocity profiles in the boundary layers for turbulent fluid flows on cylindrical bodies summarized in Table 2.1. Most of the proposed scaling parameters consist of R_i^+ $(=R_i \cdot u^*/\nu)$, δ/R_i, and Re_{Ri}. The first of these represents a radius scaling based on the friction velocity, u^*, the second one is a curvature ratio based on the boundary layer thickness, δ, and the third one is Reynolds number, Re_{Ri}, based on the free stream velocity, u_∞.

These three proposed similarity laws, however, can not identify adequately the effect of the transverse convex curvature for turbulent boundary layer flows over circular cylinders. For example, the Reynolds number based on the cylinder radius, Re_{Ri}, one of the major similarity laws, would seem to be a good dimensionless choice to characterize the effect of the transverse convex curvature. Unfortunately, the parameter, Re_{Ri}, could consist of an infinite number of combinations between the radius, R_i, and mean velocity, $\bar{u}$, for a given fluid (i.e. a fixed value of kinematic viscosity, ν) [see Appendix B]. The other major similarity law, R_i^+, based on the radius of the cylinder, also presents the same situation as Re_{Ri}. Therefore, the radius based similarity law, R_i, and the radius Reynolds number based similarity law, Re_{Ri}, can not adequately characterize the effect of the transverse convex surface curvature for turbulent boundary layer flows over circular cylinders.

Throughout the review of the relevant experimental literature, it is concluded that there are not any experiments to describe explicitly <u>the effect of the transverse convex surface curvature</u>.

2.1.2 Relevant Theoretical Studies

Sparrow et al. [36], in 1963, conducted a theoretical study of heat transfer and skin friction for turbulent boundary layer flows over circular cylinders. They calculated skin friction coefficients as a function of the local Reynolds number, Re_x for various cylinder sizes. The analysis was based on the concept of turbulent transport coefficients. Eddy viscosity, μ_t, and eddy conductivity, k_t, based on those of Deissler [16] were applied to the turbulent boundary layer flows over circular cylinders. They noted that skin friction and heat transfer coefficients for circular cylinders always exceed those for flat plates at corresponding flow conditions.

Cebeci [37], in 1970, reported the solution of incompressible turbulent boundary layer equations with heat transfer. In his work, the boundary layer equations for laminar and turbulent incompressible flows were solved via an implicit finite difference method. He used the concept of eddy diffusivity for momentum to eliminate the Reynolds shear stress term. In calculation, the turbulent boundary layer was treated as a composite layer characterized by the inner and outer region. In the inner region, an eddy diffusivity expression for momentum based on Prandtl's mixing length theory [26] was used, and in the outer region, a constant eddy diffusivity expression modified by an intermittency factor was used. For the inner region, the eddy diffusivity for momentum is:

$$\varepsilon_{M,i} = (0.4y)^2 [1 - \exp(-y/A)]^2 \left| \frac{\partial u}{\partial y} \right| \tag{2.5}$$

For the outer region, the eddy diffusivity for momentum is:

$$\varepsilon_{M,o} = 0.0168 \left| \int_0^{\infty} (u_o - u) dy \right| \tag{2.6}$$

where u_o is the velocity at the outer edge of the boundary layer and y is the distance from the wall. Constant A is a damping length constant defined as $26\,\nu / \sqrt{\tau_w/\rho}$. However, this model can not adequately predict turbulent boundary layer flows over circular cylinders because it does not predict the effect of the transverse surface curvature.

Rao [38,39], in 1967 and 1972, published an experimental and theoretical study of axisymmetric turbulent boundary layer flows over circular cylinders for radius-based Reynolds numbers, Re_{Ri}, up to 2×10^5. He proposed a curvature dependent "law of the wall" that predicted the curvature effects as:

$$u^+ = R_i^+ \ln(1 + \frac{y^+}{R_i^+}) \tag{2.7}$$

and in the sublayer, Eq. (2.7) can be given as;

$$u^+ = \frac{\bar{u}}{u^*} = R_i^+ \ln(\frac{r}{R_i}) \tag{2.8}$$

where r (= $y+R_i$) is the radial distance from the center of the cylinder and $\bar{u}$ is the mean velocity.

White et al. [40], in 1973, carried out an analysis of the skin friction coefficient for thick axisymmetric turbulent boundary layer flows. In their study, they computed the skin friction coefficient for thick, axisymmetric turbulent boundary layer flows on arbitrary bodies of revolution, using a velocity "law of the wall" . However, these analyses were restricted to the steady state fluid flow of a perfect gas and needed more refined velocity profiles.

Afzal and Narasimha [42,43], in 1976 and 1985, carried out theoretical analyses for axisymmetric turbulent boundary layer flows over circular cylinders at constant pressure. The analyses were conducted at large values of the frictional Reynolds number, R_i^+, based on the radius of the cylinder, R_i, and the boundary layer thickness, δ, using the equations of mean motion. It was found that, when the frictional Reynolds number, R_i^+, became an infinite value, the velocity profiles approached those for flat plates.

Kim and Lee [45-47], in 1990 , 1993 and 1996, also studied the effect of the transverse convex curvature on turbulent flow and heat transfer. They carried out theoretical and experimental studies of turbulent boundary layer flows over circular cylinders. In their theoretical analysis, the modified mixing-length model of Hornby et al. [7] was used to predict the velocity profiles in the wall region. It was noted that both the friction coefficient and Stanton number increased as the cylinder radius decreased, so that the values of these quantities were always greater than those for flows on flat plates. However, they concluded that the analyses were not able to predict quantitatively the effect of transverse convex surface curvature.

With development of fast computers in recent years, three-dimensional, time-dependent computations of turbulent fluid flows are now feasible. Several numerical methods for use in three-dimensional analysis have been reported.

Deardorff [48], in 1970, conducted a numerical study of three-dimensional turbulent channel flow. He calculated a numerical integration of the three-dimensional equations of motion for turbulent flow in time, using a central difference grid scheme to increase computing speed and reduce storage requirements. However, he treated turbulence components as isotropic and his eddy diffusivity expression for momentum was inadequate for turbulent boundary layer flow calculation.

Throughout the literature review, it is concluded that there are not any closure models to predict turbulent boundary layer flow and heat transfer characteristics nor are there any models to describe explicitly the effect of the transverse convex wall surface curvature in published literature.

The flow fluid can be calculated directly by solving the three-dimensional, time-dependent Navier-Stokes equations without any approximation for the Reynolds closure by a direct numerical simulation (DNS) developed recently.

Moin and Kim [13-15, 49], in 1980, 1982 and 1985, solved the incompressible Navier-Stokes equations for turbulent flow using boundary conditions for the decay of the homogenous isotropic turbulence and a fully explicit (time advancing) scheme. The database from that simulation has been used extensively for studying the structure of wall-bounded turbulent flows, but the computational resolution was not good enough to completely resolve turbulence scales of the flow structures near the wall. The qualitative statistical and time-dependent features of the turbulent flow agreed with experimental measurements considered, but the scales of the flow structures in the wall region were generally larger than those observed in experiments. Reliable quantitative information on turbulence structures could, therefore, not be extracted from the computations.

Kim et al. [24] in 1987, calculated a direct numerical simulation for fully developed turbulent channel flow. They numerically solved the unsteady Navier-Stokes equations for a Reynolds number of 3,300 with about 4×10^6 grid points (192 x 129 x 160 in x, y, z). A large number of turbulence statistics were computed and compared with the existing experimental data. The computed turbulence statistics showed good agreement with the experimental data. The computed Reynolds stresses were, however, lower than the measured values, while the computed vorticity fluctuations at the wall were higher.

Neves et al. [11], in 1994, reported the effects of the transverse convex curvature on wall bounded turbulence. They carried out direct numerical simulations of turbulent boundary layer flows over circular cylinders for radii of curvature, δ/R_i of 5 and 11. In their study, it is found that, as the curvature, δ/R_i increased, the skin friction coefficient increased and the shape of the logarithmic velocity profile decreased because of reducing turbulence kinetic energy and intensities. Near the wall, the flow is more anisotropic than that in plane channels because of production and ejection of turbulence kinetic energy due to increasing velocity fluctuations.

In a direct numerical simulation (DNS) of turbulence, the computational resources required for a computing simulation varies as the cube of the Reynolds number. In the literature [10-15], the highest Reynolds number, Re, simulated for the turbulent channel flow is about 3,000 and it is estimated that a successful simulation for higher Reynolds numbers will not be accomplished for a long time.

2.2 Turbulent Fluid Flows and Heat Transfer in Concentric Annular Ducts

The understanding of fluid flow and heat transfer characteristics in a concentric annulus is important as this geometry is encountered extensively in industry (e.g., double-tube heat exchangers, nuclear reactor core, etc.). In fully developed flows, both laminar and turbulent types have been the subjects of analytical and experimental studies. This is because of its simplicity compared with other non-circular cross sections and its wide engineering design applications.

Most information on turbulent structures in annular ducts is based on experimental results concerning turbulent fluid flows, through a pipe or between parallel plates. These flows are special cases of annular flows with symmetrical velocity profiles. Therefore, the position of zero shear stress is coincident with the position of the maximum velocity. In non-circular channels, the position of zero shear stress may not be coincident with the position of maximum velocity because the velocity profiles are asymmetric [53-56]. These asymmetric velocity profiles result from the interaction of different fluid element sizes and the different kinetic energies in two flow regions of turbulence flow field. Turbulent transport phenomena in such flows differ from those of symmetrical flows.

From a review of the available literature [53-67], some major experimental studies on turbulent fluid flow and heat transfer in concentric annuli are summarized in Table 2.2. It is interesting to note in the table that the experimental annulus diameters of outer tubes commonly used by the investigators was about 100 mm (≈ 4 inches), and it seems that this size is not only convenient to handle but very practical from the point of view of investigators.

2.2.1 Relevant Experimental Studies

Mean Velocity Distribution

The basic aspect in the analyses of the friction coefficient and the heat transfer is the velocity distribution of fluid fields in a duct. In a channel flow, there have been historically two basic velocity profile [26] which described the velocity distribution for the turbulent fluid flow in a tube: (i) the "power law" and (ii) the "law of the wall".

The power law was developed by Prandtl [26]. He constructed the velocity profiles in turbulent flow from Blasius' friction coefficient expression for fluid flow in tubes given as:

$$\frac{u}{U} = \left(\frac{y}{\delta}\right)^{\frac{1}{n}} \tag{2.9}$$

where n is taken to be seven. Eq. (2.9) is an excellent fit for low Reynolds numbers in fully developed turbulent flows. However, it was seen to be not valid beyond a Reynolds number of about 10^5 due to the limitation of the Blasius' friction coefficient expression.

The "law of the wall" was developed by the mixing length theory of Prandtl and the similarity hypothesis of von Kármán [26]. This relationship can be given as:

$$\frac{u}{u^*} = \frac{1}{\kappa}\ln y + c \tag{2.10}$$

Rearranging Eq. (2.10) into dimensionless form as:

$$u^{+} = \frac{1}{\kappa} \ln y^{+} + C \tag{2.11}$$

The von Kármán constant, κ, and constant c are determined by experiment.

Knudsen and Katz [50], in 1950, reported velocity profile measurements for turbulent fluid flows using water as a working fluid in an annular duct of radius ratio 0.27 over a Reynolds number range from 10,000 to 70,000. Their results were correlated separately for the inner and outer regions. As a result, these two separate expressions were proposed for the inner and outer regions of a concentric annular duct:

$$u_i^{+} = 4.4 \ln y_i^{+} + 6.2 \qquad \text{for } y_i^{+} \geq 40 \tag{2.12}$$

and

$$u_o^{+} = 6.1 \ln y_o^{+} + 3.0 \qquad \text{for } y_o^{+} \geq 30 \tag{2.13}$$

In comparison with other research, the predictions of Eqs. (2.12) and (2.13) differed by up to 45 per cent from the data of Rothfus et al. [51]. This disagreement was thought to be the result of Kundsen and Katz' negligect of the radius ratio effect.

Rothfus et al. [51], in 1950, reported experimental measurements of the velocity distribution and fluid friction in concentric annuli with smooth surfaces. Velocity profiles for the laminar, transitional, and turbulent fluid flows over a Reynolds number range from 1,250 to 21,600 in concentric annular ducts were measured. They proposed a "modified law of the wall" relation that was valid across the annular cross-section. The radius of the maximum velocity for turbulent fluid flow in a concentric annular duct was noted to be the same as that predicted by Lamb [52] for laminar flow in concentric annuli. Modified equations of velocity distributions in the annuli were used as the distance parameters with the modified wall radial distance, $(R_o^2 - r_m^2)/R_o$ and with the shear stress in the outer region, τ_o. The modified velocity and radial distance parameters are given as:

$$u = \frac{\Delta p g}{4\mu L}\left(\frac{R_o^2 - r_m^2}{R_o} - [(\frac{R_o^2 - r_m^2}{R_o})^2 - R_o^2 + r^2 + 2r_m^2 \ln(\frac{R_o}{r})]^{0.5}\right) \tag{2.14}$$

and

$$Y = \frac{R_o^2 - r_m^2}{R_o} - [(\frac{R_o^2 - r_m^2}{R_o})^2 - R_o^2 + r^2 + 2r_m^2 \ln(\frac{R_o}{r})]^{0.5} \tag{2.15}$$

They constructed a universal velocity profile with modified u^+ versus y^+ coordinates given as:

$$U^+ = \frac{u}{u_o^*}, \qquad Y^+ = \frac{Y u_o^*}{\nu} \tag{2.16}$$

They noted that the results plotted in this way correlated well over the entire fluid field within their experimental limits but the velocity profiles in the buffer layer were uncertain.

Lee and Barrow [53], in 1963, reported experimental measurements of turbulent fluid flows and heat transfer in concentric and eccentric annular ducts for the radius ratios of 0.26, 0.39 and 0.61 over a Reynolds number range between 10,000 and 50,000 using air as the working fluid. They also correlated the velocity profiles from their experiments and proposed the following modified forms:

$$U^{+} = 2.5 \ln Y^{+} + 5.5, \qquad for \;\; Y^{+} \geq 27 \tag{2.17.a}$$

$$U^{+} = \frac{1}{0.0695} \tanh\left(0.0695\, Y^{+}\right), \qquad for \;\; 0 \leq Y^{+} \leq 27 \tag{2.17.b}$$

where U^{+} and Y^{+} are defined by Eq. (2.16). It had been noted that the inner velocity profiles in concentric annuli were different from the universal form in circular pipe flows.

Kays and Leung [55], in 1963, proposed a modified logarithmic velocity profile for the turbulent flow from their experimental results. The velocity profile in the outer region was given as:

$$u_o^{+} = 2.5 \log Y_o^{+} + 5.5 \tag{2.18}$$

where

$$Y_o^{+} = 1.5 \log y_o^{+} (1 + z_o) / (1 + 2z_o^2) \tag{2.19}$$

and

$$z_o = (r - r_m) / (R_o - r_m) \tag{2.20}$$

The velocity profile in the inner region was given as:

$$u_i^{+} = A \log Y_i^{+} + C \tag{2.21}$$

where

$$Y_i^{+} = 1.5 \log y_i^{+} (1 + z_i) / (1 + 2z_i^2) \tag{2.22}$$

and

$$z_i = (r_m - r) / (r_m - R_i) \tag{2.23}$$

The constants A and C were found by matching the outer velocity profile at the radius of maximum velocity, r_m, with the value of the inner region, u_i^*. They noted that from the predictions and measurements of velocity distributions, the deviation of the velocity profiles for the inner region from those for the outer region could be attributable to the effect of the radius ratio, α.

Lawn and Elliott [54], in 1972, reported turbulence measurements for fully developed turbulent flows in concentric annular ducts for three different radius ratios of 0.088, 0.176, and 0.396 over Reynolds numbers up to 35,000. They also correlated the velocity profiles from their experimental results and proposed a modified velocity profile for both the inner and outer regions in a single modified logarithmic relation given as:

$$U^+ = 2.5 \ln(1 + 0.4Y^+) + 7.8[1 - \exp(-\frac{Y^+}{11}) - (\frac{Y^+}{11})\exp(-0.33Y^+)] \quad for \ Y^+ \geq 0 \tag{2.24}$$

and

$$Y^+ = \frac{R_o^{+2} - r_m^{+2}}{R_o^{+2}} - \left[\left(\frac{R_o^{+2} - r_m^{+2}}{R_o^{+2}}\right)^2 - R_o^{+2} + r^{+2} + 2r_m^{+2}\ln(\frac{R_o^+}{r^+})\right]^{0.5} \tag{2.25}$$

There are a number of the correlated expressions of velocity profiles for the turbulent fluid flows in concentric annuli. However, throughout the literature review, the effect of the transverse wall curvature was not recognized at all in all studies in the published literature.

Radius of Maximum Velocity

For turbulent fluid flows in concentric annuli, the point of the maximum velocity is not at the midpoint between the two tubes because the velocity profile is asymmetrical. This asymmetric velocity profile divides the profiles into two regions: (i) the inner region from the maximum velocity to the inner tube wall, and (ii) the outer region extending from the outer tube wall to the point of the maximum velocity, as shown in Fig. 1.1.

Unlike two regions which meet at the center of a pipe or midway between parallel planes, these regions of interest in concentric annular ducts may be quite different from each other in distributions of velocity, shear stress, and turbulence intensity. Therefore, to obtain the velocity profiles for each region, one approach is to know the location of the maximum velocity.

Rothfus et al. [51], in 1950, proposed that the radius of the maximum velocity in turbulent fluid flow as a function of a radius ratio, α, was derived from the velocity distribution and given as:

$$r_m = \left(\frac{R_o^2 - R_i^2}{2 \ln(1/\alpha)} \right)^{0.5} \tag{2.26}$$

They noted that the radius of the maximum velocity for highly turbulent flow might be the same as predicted for laminar flow by the theoretical analysis of Lamb [52].

Kays and Leung [55], in 1963, reported that the radius of the maximum velocity in the fully developed turbulent fluid flow as a function of a radius ratio, α, can be given as:

$$\frac{r_m}{R_o} = \frac{\alpha^{n-1} + 1}{\alpha^n + 1} \tag{2.27}$$

where n was taken as 0.343. They noted that the radius of the maximum velocity in turbulent flow was less than that in laminar flow, which was the same conclusion made by Lee and Barrow [53]. However, Eq. (2.27) did not demonstrate any Reynolds number dependence on r_m.

Brighton and Jones [56], in 1964, reported the measurement of the mean velocity distributions and the location of the maximum velocity for the fully developed turbulent flow in annuli with four different radius ratios of 0.0625, 0.125, 0.375, and 0.562 over a Reynolds number range from 4,000 to 30,000, using air and water as the working fluids. Their results agreed with those of Lee and Barrow [53] is that the location of the maximum velocity in turbulent flow occurred at a smaller radius than in laminar flow. They noted that as the radius ratio, α, was reduced, the velocity distribution could be flatter than that for laminar flow. It was also noted that as α was reduced, the effect of Reynolds number on velocity distribution was less on the inner profile than on the outer profile.

Throughout reviewing the literature with regarding to the radius of the maximum velocity, it is concluded that the effects of the transverse wall curvatures were never included in these correlations in published literature.

Friction Factor

In a concentric annular duct with smooth surfaces, most of the researches for turbulent fluid flow presented the friction coefficient in terms of a hydraulic equivalent diameter, De, and all these experimental results have shown that the friction coefficient was higher than that for circular tube.

Rothfus et al. [51], in 1950, measured an overall friction coefficient from their measurements and proposed two friction coefficients based either on the shear stress at the outer wall, τ_o or on that at the inner wall, τ_i. They proposed the friction coefficient for the outer region, f_o, as:

$$\frac{1}{\sqrt{f_o}} = 4.0 \log \left(Re_o \sqrt{f_o}\right) - 0.4 \tag{2.28}$$

where

$$Re_o = \frac{2(R_o^2 - r_m^2)}{R_o} \frac{\bar{u}\rho}{\mu} \tag{2.29}$$

and friction coefficient for the outer region, f_o, as:

$$f_o = \frac{\tau_o}{\frac{1}{2}\rho\bar{u}^2} = \frac{(R_o^2 - r_m^2)}{R_o} \frac{\Delta p}{\rho\bar{u}^2 L} \tag{2.30}$$

Eq. (2.28) is similar to that proposed by Nikuradse [26] for a round pipe. The Reynolds number is based on a length defined as $(R_o^2 - r_m^2)/2R_o$, where r_m is the radius of the maximum velocity and R_o is the inner radius of the outer tube. They reported that highly turbulent flow should be the same as that in a circular channel with a diameter equal to the equivalent diameter, De. The results of their investigations were correlated from experimental results for a Reynolds number range between 10,000 and 45,000 and radius ratios of 0.34 and 0.56, using water as the working fluid. The results showed that the friction coefficient depended on the radius ratio, α as:

$$u = \frac{\Delta P}{4\mu L}[R_i^2 - r^2 + \frac{R_o^2 - R_i^2}{\ln(1/\alpha)}\ln\frac{r}{R_i}] \tag{2.31}$$

Beck [57], in 1960, reported on friction coefficients correlated from his experimental measurements for concentric annuli with a radius ratio, α, ranging from 0.5 to 0.976, and a range of Reynolds number from 2,300 to 50,000 using water and oil as working fluids. He proposed the following friction coefficient correlated for annuli:

$$f = \frac{0.11}{Re^{0.23}}(\frac{1-\alpha}{1+\alpha})^{0.2}[1.22\exp 1.5(1-\alpha)] \tag{2.32}$$

In this relationship between the friction coefficient and the Reynolds number, once the velocity distribution is determined, the friction coefficient is directly defined.

Reynolds et al. [58], in 1963, proposed the friction coefficient for turbulent fluid flow in a concentric annulus with the radius ratio, α. It was assumed that the velocity profile of Deissler [16] for the tube was valid across the whole cross section of the annular passage. From a force balance on annular fluid elements between R_i and r_m, and between R_o and r_m, they calculated the point of the maximum velocity. The friction coefficient was defined with the shear stress distribution as:

$$f = \frac{2}{\overline{u^+}^2}\frac{(1+\frac{\tau_i\alpha}{\tau_o})}{1+\frac{1}{\alpha}} \tag{2.33}$$

From the above relationship, $\overline{u^{+2}}$ can be calculated from the universal velocity profile for the round channels. They also reported that the predicted friction coefficients were higher than those for a circular tube at the same Reynolds number.

Lee and Barrow [53], in 1963, proposed an average friction coefficient, $\bar{f}$, from the velocity profile measured from their experiments for annular ducts whose radius ratios were 0.26, 0.39 and 0.61 over a Reynolds number range from 10,000 to 50,000 using air as a working fluid. They constructed the average friction coefficient, $\bar{f}$, in terms of radius ratio, α, from the velocity profile as follow:

$$\bar{f} = \frac{\alpha(\alpha - 1)R_o^{+2}}{\alpha^2 R_i^{+2} - r_m^{+2}} f_o \tag{2.34}$$

and

$$f_o = \frac{(R_o^{+2} - r_m^{+2})^2}{2\left(\int_{r_m^+}^{R_o^+} u_o^+ r^+ dr^+\right)^2} \tag{2.35}$$

where the parameters used in Eqs. (2.34) and (2.35) are defined in the Nomenclature. They noted that the average friction coefficient increased as radius ratio, α, increased. Jonsson and Sparrow [6] also concluded that the friction coefficient was dependent on the radius ratio, α, and increased as the radius ratio, α, increased.

As was the same for the cases of the velocity and the radius of the maximum velocity in annuli, throughout the literature review, the effect of the transverse wall curvature was not included in the correlations of the friction coefficient.

Heat Transfer

Mizushina [59], in 1951, conducted experiments for turbulent fluid flow and heat transfer with air for a radius ratio of 0.46, and Reynolds numbers up to 40,000. He constructed an analogy to the annulus, based on the concept of "seventh power law" for both velocity profiles, and assumed the radius of the maximum velocity, r_m, in fully developed turbulent flow. He has taken the heat transfer resistance of the sublayer as that of Prandtl and Taylor, and as Reynolds analogy for the resistance in the fully turbulent layer when heat was transferred from the annulus to both boundaries. He obtained the ratio of the turbulent-core resistance with heat transfer at the inner wall and noted that the calculated thermal resistance of the fully turbulent regions was as twice of heat transfer at both walls.

Lee and Barrow [53], in 1963, further improved Mizushina's method for the region of the near wall. They proposed a heat transfer coefficient in terms of Nu, at the inner boundary of an internally heated concentric annulus that could be calculated the total temperature difference in two regions as:

$$Nu = \frac{Re^{7/8}\,Pr}{5.03\,Pr\,\beta^{-0.125}\,J + (50.6/\gamma)\,(Re\,\beta)^{-0.125}\,[1 - 2.73\,(Re\,\beta)^{-0.125}]} \tag{2.36}$$

and

$$I = \int_0^{27} \frac{dY^+}{Pr\,\sigma\,\gamma\cosh^2(0.0695\,Y^+) - (\sigma\,Pr - 1)}$$

where the following assumption were given for the complexity of the problem,

(*i*) $0 \le Y^+ \le 27, \quad \tau = \tau_{w,i}, \quad q = q_{w,i}, \quad \sigma = constant,$

(*ii*) $Y^+ \ge 27, \quad \sigma = 1$

They also showed that the heat transfer coefficient at the inner wall of a concentric annulus increased as the radius ratio increased.

However, throughout the literature, no study was found which included or recognized the effect of the transverse convex surface curvature on the heat transfer in concentric annuli in published literature.

2.2.2 Relevant Theoretical Studies

Analysis of Turbulent Fluid Flow in Annular Ducts

In the literature, a number of analytical approaches for fully developed turbulent flows and heat transfer in annular ducts have been published. Most of the analytical studies used were based on the eddy diffusivity concept for momentum and heat. They assumed that velocity and eddy diffusivity for the momentum of the two regions at the plane of zero shear are the same.

Levy [60], in 1967, reported an analysis for fully developed turbulent flows in concentric annular ducts. He derived equations based on Reichardt's expression [9] for the momentum eddy diffusivity.

He predicted the location of the zero shear stress and the distributions of the eddy diffusivity, the velocity profile, and the friction coefficient. His predicted results were compared with available experimental data, and reported to be in good agreement each other.

Wilson and Medwell [61], in 1970, carried out analyses for fully developed turbulent flows in concentric annular ducts. They used the eddy diffusivity distribution expression proposed by Levy [60] with a constant universal mixing length for the fully developed turbulent annular flow. However, their predicted results did not agree with the experimental data at low radius ratios, α.

Quarmby [62], in 1969, also derived equations for the velocity distributions based on Deissler's expression [16] for the eddy diffusivity of momentum in the sublayer. The theoretical predictions of the friction coefficients and radius of the maximum velocity as a function of the Reynolds numbers and radius ratios were in reasonably good agreement with their experimental data.

Lee and Park [63], in 1971, reported the velocity distributions for each region in concentric annuli. They derived equations based on Reichardt's expression [9] for the eddy diffusivity of momentum for the sublayers and on Levy's expression [60] in the fully turbulent layers. Their analytical results were compared with their experimental data for the turbulent fluid flow of air in four concentric annular ducts at a Reynold number range from 20,000 to 110,000 and were in good agreement.

<u>Analysis of Turbulent Heat Transfer in Annular Ducts</u>

Bailey [64], in 1950, reported an analysis for the turbulent heat transfer in concentric annular ducts. He computed the heat transfer coefficients for the inner core wall having a constant heat flux for liquid metals. He used the fully developed modified velocity distribution of Prandtl's equation combined with the equation of von Kármán [26] by direct integration of the energy equation. The modification of Prandtl's equation for a fully turbulent layer was necessary because of the different friction coefficients for each wall. However, he assumed that the overall friction coefficient in an annulus was equal to the friction coefficient for smooth tubes at the same Reynolds number. In his analysis, the radii of zero-shear and maximum velocity were assumed to be the same. The flow in each region divided by the radius of maximum velocity was divided into three zones, a laminar sublayer, a buffer layer, and a fully turbulent layer. The ratio of eddy diffusivities for heat and momentum was taken as unity.

Reynolds et al. [58], in 1963, made a general formulation of the annulus problem and had a superposition approach to the solution of the governing equation. Their research considered four "fundamental" solutions from which the solution for any prescribed set of boundary conditions could be determined. In their study, the fundamental solution of "the second kind" considered the fluid flowing with a constant temperature in the annulus with both tube walls kept at the same temperature. The heat fluxes from either the core wall or the outer wall was increased stepwise, while the opposite wall was insulated.

Lee and Park [63], in 1971, carried out a study of the simultaneous developing turbulent flow and heat transfer in concentric annuli based on a modified model for the eddy diffusivity of momentum with a new ratio of eddy diffusivities obtained from experiment. In their studies, solutions were obtained for one surface uniformly heated and the other insulated. The analytical results were compared with experimental results and were in good agreement.

Throughout the literature review, in studies of the turbulent fluid flow and heat transfer in concentric annular ducts, most of the earlier studies only considered the effect of radius ratio, α and

Reynolds number, Re, and for Prandtl number, Pr, (for heat transfer). It is concluded that there are no turbulent closure models to describe the effect of the transverse convex wall surface curvature, at least in the published literature.

2.3 Numerical Analyses of Turbulent Fluid Flow using the k-ε Turbulence Model

Computer methods of solving the differential equations of fluid dynamics are well advanced for three-dimensional, time-dependent flows. As the practical need for computation of turbulent flows progresses, a variety of turbulence models are being developed [72].

Recently, the development of large powerful computers has led to a wider use of higher-order turbulence models to predict turbulent flows. The most popular class includes the two-equation model in which two partial differential equations are used to describe the development of turbulent kinetic energy and the turbulence length scale. One such model is the k-ε turbulence model, where k represents the turbulent kinetic energy, and ε represents the dissipation rate of turbulent kinetic energy.

Jones and Launder [71], in 1972, extended the original k-ε model to the low Reynolds number form that allows calculations right to the wall. Later, they further developed the k-ε model. These models, however, still include extra terms in the transport equations for the improvement of predictions in the wall region.

Launder and Spalding [72], in 1974, set the equations for high Reynolds number flows. For the wall flows, they applied empirical wall function formulas to those equations. Ng and Spalding [73], in 1976, conducted the calculation of the two-dimensional, boundary layer flows on a smooth wall with the k-ε turbulence model. However, when disagreements are found between measurements and predictions used with empirical wall function formulas for the wall flows, it is difficult to judge whether the weakness of the method lies in the basic model equations or in the wall function formulas.

To the best of the author's knowledge, the works of Leschziner and Rodi (1981), Lee et al.

(1988), Fujji et al. (1991), Torii et al. (1991), and Desai and Vafai (1994) are the only reported numerical analyses pertinent to fluid flow in the annular geometry using the k-ε turbulence model.

Leschziner and Rodi [74], in 1981, reported the performance of three discretization schemes for convection and three turbulence-model variations to simulate the recirculation flow in an annular jet and a plane twin-parallel jet in air.

Lee et al. [75], in 1988, published an analysis of periodical fully developed turbulent flow and heat transfer in artificially roughened annuli using the k-ε turbulence model. They reported a new method of obtaining the roughness functions from numerically predicted velocity and temperature profiles.

Fujji et al. [76], in 1991, reported the theoretical and experimental investigations on heat transfer of highly heated turbulent gas flow in an annular duct. They carried out numerical analyses for heated turbulent gas flow using three types of turbulence models: k-kl-$\overline{u'\upsilon'}$, k-ε-$\overline{u'\upsilon'}$, and k-ε model. These calculations were compared with their experimental measurements and it was concluded that k-kl-$\overline{u'\upsilon'}$ model was in better agreement than any other models.

Torii et al. [77], in 1991, published the laminarization phenomena of a strongly heated gas flow in concentric annular tubes. They carried out a numerical analysis by means of a modified k-ε turbulence model.

Desai and Vafai [78], in 1994, reported the simulation of turbulent buoyancy driven flows in an annular duct bounded by concentric and horizontal cylinders with adiabatic end walls. The time-average equations of turbulent fluid motion and heat transfer were calculated using a wall function approach with the standard k-ε model of turbulence. They obtained the effects of Prandtl number, Pr, and radius ratios, α, on the turbulent fluid flow and heat transfer for a Rayleigh number range from

10^6 to 10^9.

A two-equation turbulence model is likely to be more general than any other turbulence models but its ability to represent the turbulent flow characteristics has to be assessed from a limited range of experiments. The assumptions necessary to solve the equations for turbulence energy and dissipation rates can not be tested directly.

One of the weaknesses of this model is that in the ε model, this equation is more complicated than the turbulent kinetic equation and involves several unknown double and triple correlations which give rise to accuracy problems in predicting the behavior of fluctuating velocity near the wall. In these correlations, the effects of the transverse surface curvature were not also included.

From the literature review, it is concluded again that there are not any models to predict turbulent fluid flow and heat transfer characteristics near the wall adequately in the k-ε turbulence model nor are there any models to recognize the effect of the transverse wall curvature in published literature.

CHAPTER 3
ANALYTICAL STUDY

3.1 Basic Equations

3.1.1 General Equation

Consider incompressible viscous fluid flow in a straight uniform cross-section with the x direction along the wall, r the radial direction to the wall and θ the azimuthal direction to the wall, while t is time. The velocities corresponding to these coordinates are u, v, and w, respectively.

The Navier-Stokes equations for steady incompressible viscous fluid flow in cylindrical coordinates can be expressed in the following form [79]:

$$\rho\left(\frac{\partial u}{\partial t} + u\frac{\partial u}{\partial x} + \upsilon\frac{\partial u}{\partial r} + \frac{w}{r}\frac{\partial u}{\partial \theta}\right) = F_x - \frac{\partial p}{\partial x} + \mu\nabla^2 u \tag{3.1.a}$$

$$\rho\left(\frac{\partial \upsilon}{\partial t} + u\frac{\partial \upsilon}{\partial x} + \upsilon\frac{\partial \upsilon}{\partial r} + \frac{w}{r}\frac{\partial \upsilon}{\partial \theta} - \frac{w^2}{r}\right) = F_r - \frac{\partial p}{\partial r} - \mu\left(\frac{\upsilon}{r^2} + \frac{2}{r^2}\frac{\partial w}{\partial \theta}\right) + \mu\nabla^2 \upsilon \tag{3.1.b}$$

$$\rho\left(\frac{\partial w}{\partial t} + u\frac{\partial w}{\partial x} + \upsilon\frac{\partial w}{\partial r} + \frac{w}{r}\frac{\partial w}{\partial \theta} + \frac{\upsilon w}{r}\right) = F_\theta - \frac{1}{r}\frac{\partial p}{\partial r} - \mu\left(\frac{w}{r^2} - \frac{2}{r^2}\frac{\partial \upsilon}{\partial \theta}\right) + \mu\nabla^2 w \tag{3.1.c}$$

If the thermodynamic properties of density, ρ, specific heat, c_p, and thermal conductivity, k, are assumed independent of temperature, the corresponding energy equation has the following form:

$$\rho c_p \frac{DT}{Dt} = k\nabla^2 T + \upsilon\frac{Dp}{Dt} + q' + \mu\left(\frac{\partial u}{\partial r}\right)^2 \tag{3.2}$$

where the Laplacian operator is

$$\nabla^2 = \frac{1}{r}\frac{\partial}{\partial r}(r\frac{\partial}{\partial r}) + \frac{1}{r^2}\frac{\partial^2}{\partial \theta} + \frac{\partial^2}{\partial x^2}$$

The terms, $\frac{DT}{Dt}$ and $\frac{Dp}{Dt}$ are the substantial derivative of temperature,T, and pressure, p. q' is heat generation.

The continuity equation for incompressible steady flow is:

$$\frac{\partial u}{\partial x} + \frac{\partial \upsilon}{\partial r} + \frac{1}{r}\frac{\partial w}{\partial \varphi} + \frac{\upsilon}{r} = 0 \tag{3.3}$$

In turbulent flow, the velocity components are the sums of the time mean component. Then, the Reynolds transformation [79] of the Navier-Stokes equations in cylindrical coordinates for incompressible steady flow in a straight uniform cross section (see Figs. 3.1 and 3.2) in which the body force can be neglected has the following form:

$$\rho(\frac{\partial u}{\partial t} + u\frac{\partial u}{\partial x} + \upsilon\frac{\partial u}{\partial r} + \frac{w}{r}\frac{\partial u}{\partial \theta}) = -\frac{\partial p}{\partial x} + \mu\nabla^2 u \tag{3.4.a}$$

$$-\{\frac{\partial}{\partial x}(\rho\overline{u'^2}) + \frac{1}{r}\frac{\partial}{\partial r}(r\rho\overline{u'\upsilon'}) + \frac{1}{r}\frac{\partial}{\partial \theta}(\rho\overline{u'w'})\}$$

$$\rho(\frac{\partial \upsilon}{\partial t} + u\frac{\partial \upsilon}{\partial x} + \upsilon\frac{\partial \upsilon}{\partial r} + \frac{w}{r}\frac{\partial \upsilon}{\partial \theta} - \frac{w^2}{r}) = -\frac{\partial p}{\partial r} + \mu(\nabla^2\upsilon - \frac{\upsilon}{r^2} - \frac{2}{r^2}\frac{\partial w}{\partial \theta}) \tag{3.4.b}$$

$$-\{\frac{\partial}{\partial x}(\rho\overline{u'\upsilon'}) + \frac{1}{r}\frac{\partial}{\partial r}(\rho\overline{\upsilon'^2}) + \frac{1}{r}\frac{\partial}{\partial \theta}(\rho\overline{\upsilon'w'}) - \frac{(\rho\overline{w'^2})}{r}\}$$

$$\rho(\frac{\partial w}{\partial t} + u\frac{\partial w}{\partial x} + \upsilon\frac{\partial w}{\partial r} + \frac{w}{r}\frac{\partial w}{\partial \varphi} + \frac{\upsilon w}{r}) = -\frac{1}{r}\frac{\partial p}{\partial \theta} + \mu(\nabla^2 w + \frac{2}{r^2}\frac{\partial w}{\partial \theta} - \frac{w}{r^2}) \tag{3.4.c}$$

$$-\{\frac{\partial}{\partial x}(\rho\overline{u'w'}) + \frac{\partial}{\partial r}(\rho\overline{\upsilon'w'}) + \frac{1}{r}\frac{\partial}{\partial \theta}(\rho\overline{w'^2}) - \frac{2(\rho\overline{\upsilon'w'})}{r}\}$$

The corresponding equation for heat transfer in turbulent flow is:

$$\frac{\partial T}{\partial t} + u\frac{\partial T}{\partial x} + \upsilon\frac{\partial T}{\partial r} + \frac{w}{r}\frac{\partial T}{\partial \theta} = \alpha\nabla^2 T - \{\frac{\partial}{\partial x}(\overline{u'T'}) + \frac{1}{r}\frac{\partial}{\partial r}(r\overline{\upsilon'T'}) + \frac{1}{r}\frac{\partial}{\partial \theta}(\overline{w'T'})\} \tag{3.5}$$

The problem under consideration here is that of a steady, incompressible, turbulent flow for straight uniform cross section. Therefore, all of the derivatives with respective to time, t, and the body force can also be neglected.

In turbulent flow through the same cross-section, the shear stresses are nearly constant along the sides, dropping off sharply to zero in the corners of cross-section. This is because of the phenomenon of turbulent secondary flow, in which there are non-zero mean velocities υ and w in the plane of the cross-section. This kind of fluid flow occurs for non-circular cross section geometry [80]. In a circular cross section, if there is no secondary flow, Eq. (3.4.a) is sufficient for determining the axial velocity distribution. In most situations, axial thermal conduction and eddy diffusion are either zero or negligibly small, and terms $\frac{\partial^2 T}{\partial x^2}$ - $\frac{\partial}{\partial x}(\overline{u'T'})$ can be ignored. The boundary layer approximation is applied, so that terms $\frac{\partial^2 u}{\partial x^2}$ and $\frac{\partial \overline{u'^2}}{\partial x}$ are also ignored. The υ and w are zero in axisymmetric and two-dimensional flow.

For axisymmetric and two-dimensional flow such as in a pipe or in a concentric annulus, the appropriate equation of momentum is:

$$u\frac{\partial u}{\partial x} + \upsilon\frac{\partial u}{\partial r} + \frac{1}{\rho}\frac{\partial p}{\partial x} = \frac{\nu}{r}\frac{\partial}{\partial r}(r\frac{\partial u}{\partial r}) - \frac{1}{r}\frac{\partial}{\partial r}(r\overline{u'\upsilon'}) \tag{3.6}$$

The equation of energy is:

$$u\frac{\partial T}{\partial x} + \upsilon\frac{\partial T}{\partial r} = \frac{k}{r}\frac{\partial}{\partial r}(r\frac{\partial T}{\partial r}) - \frac{1}{r}\frac{\partial}{\partial r}(r\overline{\upsilon' T'}) \tag{3.7}$$

To solve Eqs. (3.6) and (3.7) using the concept of eddy diffusivity, ε, the turbulence terms $-\overline{u'\upsilon'}$ and $-\overline{\upsilon' T'}$ are expressed as $\varepsilon_M \frac{\partial u}{\partial r}$ and $\varepsilon_H \frac{\partial T}{\partial r}$ respectively. The eddy diffusivity is not a fluid property because it depends on position and flow conditions. For the momentum equation, Prandtl [1] hypothesized that the behaviour of the apparent shear stress was similar to the laminar stress, and proposed the identity:

$$-\overline{u'\upsilon'} = \varepsilon_M (\frac{\partial u}{\partial r}) \tag{3.8}$$

And for the energy equation is;

$$-\overline{\upsilon' T'} = \varepsilon_H (\frac{\partial T}{\partial r}) \tag{3.9}$$

With Eqs. (3.8) and (3.9), Eqs (3.7) and (3.8) become

$$u\frac{\partial u}{\partial x} + \upsilon\frac{\partial u}{\partial r} + \frac{1}{\rho}\frac{\partial p}{\partial x} = \frac{1}{r}\frac{\partial}{\partial r}[r(\nu+\varepsilon_M)\frac{\partial u}{\partial r}] \tag{3.10}$$

and

$$u\frac{\partial T}{\partial x} + \upsilon\frac{\partial T}{\partial r} = \frac{1}{r}\frac{\partial}{\partial r}[r(\alpha+\varepsilon_H)\frac{\partial T}{\partial r}] \tag{3.11}$$

Corresponding equations for the rectangular coordinates are

$$u\frac{\partial u}{\partial x} + \upsilon\frac{\partial u}{\partial y} + \frac{1}{\rho}\frac{\partial p}{\partial x} = \frac{\partial}{\partial y}[(\nu+\varepsilon_M)\frac{\partial u}{\partial y}] \tag{3.12}$$

and

$$u\frac{\partial T}{\partial x} + \upsilon\frac{\partial T}{\partial y} = \frac{\partial}{\partial y}[(\alpha+\varepsilon_H)\frac{\partial T}{\partial y}] \tag{3.13}$$

3.1.2 Governing Equations: Turbulent Boundary Layer Flow over a Circular Cylinder

In an axisymmetric turbulent boundary layer flow on a circular cylindrical body in a zero pressure gradient, the distribution of the shear stress, τ, and heat flux, q, can be derived from the equations of momentum and energy. The time rate change of momentum in the cylindrical fluid element is:

$$\rho\frac{d}{dt}[\{(u + \frac{\partial u}{\partial x}dx) - u\} + \{(u + \frac{\partial u}{\partial r}dr) - u\}]\ 2\ \pi\ r\ dr\ dx = \rho(u\frac{\partial u}{\partial x} + \upsilon\frac{\partial u}{\partial r})\ 2\ \pi\ r\ dr\ dx \tag{3.14}$$

Employing the momentum theorem, the rate of creation of momentum is equal to the external forces and yields the following:

$$-\frac{\partial p}{\partial x} + \frac{1}{r}\frac{\partial}{\partial r}(\tau \cdot r) = \rho(u\frac{\partial u}{\partial x} + \upsilon\frac{\partial u}{\partial r}) \tag{3.15}$$

Rearranging Eq. (3.15) becomes

$$(u\frac{\partial u}{\partial x} + \upsilon\frac{\partial u}{\partial r}) + \frac{1}{\rho}\frac{\partial p}{\partial x} = \frac{1}{\rho r}\frac{\partial}{\partial r}(r\cdot\tau) \tag{3.16}$$

If there is no pressure gradient, the boundary layer equation for the mean flow from Eq. (3.16) is

$$u\ \frac{\partial u}{\partial x} + \upsilon\ \frac{\partial u}{\partial r} = \frac{1}{\rho r}\ \frac{\partial(r\cdot\tau)}{\partial r} \tag{3.17}$$

Now, a heat balance on a cylindrical fluid element gives:

$$-\ 2\ \pi\ r\ dr\ \rho\ u\ c_p\frac{\partial T}{\partial x}dx\ -\ 2\ \pi\ r\ dr\ \rho\ \upsilon\ dx\ \frac{\partial T}{\partial r}dr = 2\ \pi\ dx\ \{(r + dr)\ (q + \frac{\partial q}{\partial r}dr)\ -\ qr\} \tag{3.18}$$

The equation of energy then becomes

$$u\frac{\partial T}{\partial x} + \upsilon\frac{\partial T}{\partial r} = -\frac{1}{\rho c_p r}\frac{\partial}{\partial r}(q \cdot r) \tag{3.19}$$

and the continuity equation is:

$$\frac{\partial(r \cdot u)}{\partial x} + \frac{\partial(r \cdot \upsilon)}{\partial r} = 0 \tag{3.20}$$

where the shear stress is defined as

$$\tau = \mu\frac{\partial u}{\partial x} - \rho\overline{u'\upsilon'} \tag{3.21}$$

Eqs. (3.17) and (3.19) in combination with Eqs. (3.11) and (3.13) yield

$$\frac{\tau}{\rho} = (\nu + \varepsilon_M)\frac{\partial u}{\partial r} \tag{3.22}$$

and

$$-\frac{q}{c_p \rho} = (\alpha + \varepsilon_H)\frac{\partial T}{\partial r} \tag{3.23}$$

For the momentum equation, the behaviour of the apparent shear stress was proposed by Prandtl [1] as the identity

$$-\overline{u'\upsilon'} = \varepsilon_M\left(\frac{\partial \bar{u}}{\partial r}\right) = l^2\left(\frac{\partial \bar{u}}{\partial r}\right)^2 \tag{3.24}$$

where Prandtl's mixing length is

$$l = \kappa \cdot y$$

and κ is von Kármán constant. The velocity and temperature distributions, u and T, for a given wall heat flux and fluid flow can be determined from Eqs. (3.22) and (3.23) if both the momentum eddy diffusivity, ε_M, and thermal eddy diffusivity, ε_H, are known.

3.1.3 Governing Equations: Fully Developed Turbulent Fluid Flow in a Concentric Annulus

For an axisymmetric turbulent flow in a concentric annular cross section, the distribution of the shear stress, τ, and heat flux, q, can be derived from the equations of momentum and energy in a straight duct of uniform cross-section as shown in Figs. 3.2. The time rate change of momentum in the cylindrical fluid element is:

$$\rho \frac{d}{dt}[\{(u + \frac{\partial u}{\partial x}dx) - u\} + \{(u + \frac{\partial u}{\partial r}dr) - u\}]\ 2\ \pi\ r\ dr\ dx = \rho(u\frac{\partial u}{\partial x} + \upsilon\frac{\partial u}{\partial r})\ 2\ \pi\ r\ dr\ dx \tag{3.25}$$

Employing the momentum theorem, the rate of creation of momentum is equal to the external forces described in the following equation:

$$-\frac{\partial p}{\partial x} + \frac{1}{r}\frac{\partial}{\partial r}(\tau \cdot r) = \rho(u\frac{\partial u}{\partial x} + \upsilon\frac{\partial u}{\partial r}) \tag{3.26}$$

Rearranging Eq. (3.26) can result in

$$(u\frac{\partial u}{\partial x} + \upsilon\frac{\partial u}{\partial r}) + \frac{1}{\rho}\frac{\partial p}{\partial x} = \frac{1}{\rho r}\frac{\partial}{\partial r}(\tau \cdot r) \tag{3.27}$$

Now a heat balance on a cylindrical fluid element becomes:

$$- 2 \pi r \, dr \, \rho \, u \, c_p \frac{\partial T}{\partial x} dx - 2 \pi r \, dr \, \rho \, \upsilon \, dx \frac{\partial T}{\partial r} dr = 2 \pi \, dx \, \{(r + dr)(q + \frac{\partial q}{\partial r} dr) - q \cdot r\} \tag{3.28}$$

Simplifying Eq. (3.28) gives

$$u \frac{\partial T}{\partial x} + \upsilon \frac{\partial T}{\partial r} = - \frac{1}{\rho c_p r} \frac{\partial}{\partial r}(q \cdot r) \tag{3.29}$$

Eqs. (3.27) and (3.29) in combination with Eqs. (3.11) and (3.13) will yield:

$$\frac{\tau}{\rho} = (\nu + \varepsilon_M) \frac{\partial u}{\partial r} \tag{3.30}$$

and

$$- \frac{q}{c_p \rho} = (\alpha + \varepsilon_H) \frac{\partial T}{\partial r} \tag{3.31}$$

The velocity and temperature distributions, u and T, for a given wall heat flux and fluid flow can be determined from Eqs. (3.30) and (3.31) if the momentum eddy diffusivity, ε_M and the thermal eddy conductivity, ε_H are both known.

3.2 Variable von Kármán Constants, κ_i : A New Concept Proposed

Consider a turbulent shear flow which is steady and two-dimensional on average. Let u (x,y) and υ (x,y) be the mean velocity in the direction of increasing rectangular coordinates x and y ,respectively. Experiments with turbulent shear flow have shown that the mean-velocity profile in the region near the surface can be described by a relationship, $\frac{u}{u^*} = f(\frac{yu^*}{\nu})$, called the " law of the wall" For the special case of steady two-dimensional mean flow of an incompressible fluid, the form of the universal law is well established as:

$$\frac{u}{u^*} = \frac{1}{\kappa}\ln(\frac{yu^*}{\nu}) + c \tag{3.32}$$

in which von Kármán constant, κ, and c are constants to be determined experimentally. Eq. (3.32) can also be obtained from Prandtl's mixing length.

The mixing length analogy of Prandtl or von Kármán implies a logarithmic variation of the function $f(y \cdot u^*/\nu)$ in flows near the wall and the shear stress, τ, does not depend on y because of the assumption that τ is constant. However, the velocity distribution u(y) is dependent on the shear stress distribution, τ(y). From the "law of the wall", $u/u^* = f(y \cdot u^*/\nu)$, it follows that

$$\frac{y}{u^*}\frac{\partial u}{\partial y} = \frac{yu^*}{\nu} f'(\frac{yu^*}{\nu}) \tag{3.33}$$

In the logarithmic-overlap layer, the equation requires that

$$\frac{y}{u^*}\frac{\partial u(x,y)}{\partial y} = \frac{yu^*}{\nu}f'\left(\frac{yu^*}{\nu}\right) = \frac{1}{\kappa(x,y)} \tag{3.34}$$

$$\text{or} \qquad \frac{\partial u(x,y)}{\partial y} = \frac{u^*(x)}{y\cdot\kappa(x,y)}$$

When the variable $y\cdot u^*/\nu$ is specific, von Kármán constant κ (x,y) can be fixed. However, this variable, $y\cdot u^*/\nu$, is formally dependent on shear stress, τ(y). Therefore, the von Kármán constant κ (x,y) is also variable. In the study of Yu [30] and Rao [38], it was found that the von Kármán constant, κ, varied with the Reynolds number based on the radius of the circular cylinder, Re_{Ri}. In their study, such variation in the value of the von Kármán constant, κ, has been observed in the turbulent boundary layer. Rao and Keshavan [39] suggested that the value of the von Kármán constant, κ, also has a tendency to reach a value of about 0.4 as Reynolds number becomes large.

In the experimental literature [29,31,45,46] for turbulent boundary layer flow on a cylindrical body, it is reported that the velocity gradient, (∂u/∂y), near the wall surface becomes steeper and the value of the von Kármán constant κ increases as the radius becomes smaller. This implies that the turbulent eddy is strongly affected by the change in the value of the transverse convex wall curvature, i.e, the cylinder radius, R_i.

To characterize the effect of transverse convex surface curvature, it is proposed in the present study for the first time that the von Kármán constant, κ_i, is not a fixed constant as has been assumed, but it would take the following form:

$$\kappa_i = \kappa\cdot F(R_i) \tag{3.35}$$

From experimental data for the velocity profiles for the logarithmic region in the boundary layer flow over a cylindrical body by Willmarth et al. [31], and by Kim and Lee [45], $F(R_i)$ may be approximated in the following form as a hyperbolic tangent function of the radius of a cylindrical body, R_i, as:

$$F(R_i) = 1 + 1.5 \tanh(0.0064/R_i^{0.72}) \tag{3.36}$$

In the curve fitting operation, it has been assumed that the measurements of values of y^+ ($= y \cdot u^* / \nu$) less than about 100 would be unreliable as a result of large fluctuations in velocity, wall interference, poor probe sensitivity at small velocity, probe position error, or uncertainty in the static pressure.

The function $F(R_i)$ together with the experimental results of Willmarth et al. [31] and Kim and Lee [45,46] are shown in Fig. 3.3 and are summarized in Table 3.1.

From the figure, the slope in the logarithmic region of dimensionless velocity profiles implies that a completely different physical mechanism may be involved. For a turbulent fluid flow over a flat plate with dp/dx < 0, the range of the von Kármán constant, κ, is fixed at 0.4 to 0.41. However, Fig. 3.3 shows that the value of κ increases with decreasing value of cylinder radius, R_i, suggesting that for $\delta/R_i \approx O(1)$, the length scale distribution of the turbulent eddies, which is a function of wall shear stress is strongly affected by the change in the value of R_i, i.e., the <u>transverse convex surface curvature</u>.

Our hypothesis, that <u>the von Kármán constant κ is strongly affected by the transverse convex surface curvature</u>, R_i, is verified, and Eqs. (3.35) and (3.36) are the bases of the present analytical studies given in the following.

3.3 Analysis: Turbulent Boundary Layer Flow and Heat Transfer over a Circular Cylinder

3.3.1 Problem Definition and Assumption

The modelling of the equations for the problem here is based on a series of assumptions, and the fluid flow and heat transfer to be analysed are subjected to the following conditions:

(1) The thermodynamic properties (density, viscosity, specific heat etc.) of the fluid are constant. The turbulent Prandtl number Pr_t is assumed to be unity[1];

(2) The turbulent velocity and thermal boundary layers develop along a cylinder whose axis is parallel to the free-stream fluid flow;

(3) The surface of the circular cylindrical body is considered as uniform heat flux.

3.3.2 Velocity Distribution

If the Reynolds stress is related to the mean velocity distribution through the concept of the mixing-length theory, integration of Eq. (3.22) with Eq. (3.24) can yield a dimensionless relationship as;

$$u^+ = \int_0^{y^+} \frac{2\tau^+}{1+\sqrt{1+4l^{+2}\tau^+}}\, dy^+ \tag{3.37}$$

The expression of Eq. (3.37) can be made in dimensionless form as shown in Appendix C.2. To solve for the velocity distribution using Eq. (3.37), information on the mixing length, l, is needed. For

[1] The turbulent Prandtl number is defined as $Pr_t = \varepsilon_M / \varepsilon_H$. The turbulent Prandtl number is difficult to measure accurately and most formulae incorporate constants or functions to make them conform to the limited data and the difficulties of measurements. For air, Pr_t is suggested as unity [82]. A further discussion is given in Section 3.3.4.

the flow near the wall, various composite mixing length and eddy diffusivity formulae have been suggested as empirical correlations of experimental observations [26]. Hornby, Mistry and Barrow [7] proposed a modified mixing length theory, extending the van Driest turbulence model which is based on Stoke's Second Problem, concerned with laminar flow near an oscillating plate.

The van Driest model [26] is for a flat plate and does not recognize the influence of the duct shape. To obtain a new model that recognizes the duct shape, Hornby, Mistry and Barrow [7] obtained the velocity distribution by solving the laminar momentum equation with the whole duct oscillating. Once the fluid velocity was obtained, the damping factor for turbulent flow in ducts of any shape was found, applying van Driest's analogy. The resulting damping factor depends on both wall distance and duct geometry. However, they retained the same constant von Kármán constant, κ, used for turbulent flow in pipes and over a flat plate and the dimensionless radius R_i^+, which was discussed in Section 1.1.

The turbulence model of Hornby, Mistry and Barrow for external turbulent flow over a circular cylinder is given as:

$$l^+ = l_-^+ \left[1 - \frac{Mo\left(\dfrac{\sqrt{2}\, r^+}{A^+}\right)}{Mo\left(\dfrac{\sqrt{2}\, R_i^+}{A^+}\right)} \right] \tag{3.38}$$

where $l_-^+ = K_i \cdot y^+$ and $Mo\,(x) = \sqrt{Ker^2(x) + Kei^2(x)}$. Constant A^+ is the van Driest damping factor (= 26.0) and $Ker(x)$ *and* $Kei(x)$ are Kelvin Functions. Therefore, in Eq. (3.28), the effect of the transverse convex surface curvature was not explicitly nor implicitly accommodated, even though a new dimensionless parameter R_i^+ is employed.

In the present study, to accommodate the effect of the transverse convex surface curvature, it is assumed that Eq. (3.38) is retained but with the von Kármán constant, κ_i, as given in Eqs. (3.35) and (3.36).

To solve Eq. (3.37), information on the shear stress distribution, τ_w, is also needed. For the circular cylinder, the shear stress is proportional to the distance r from the axis. Integration of Eq. (3.37) with respect to y (neglecting the inertia terms) gives us the following shear stress distribution, τ^*, as:

$$\tau^* = \frac{R_i^+}{R_i^+ + y^+} \tag{3.39}$$

where R_i is the radius of the cylindrical body and y is the distance from the surface of the cylindrical body. The boundary condition for the flow velocity in dimensionless form, u^+, is:

$$u^+ = 0 \qquad at \;\; y^+ = 0 \tag{3.40}$$

Therefore, from Eqs. (3.37) through (3.40), the velocity distribution can be calculated for a given radius of cylinder, R_i, at the local Reynolds number.

3.3.3 Skin Friction Coefficient

With the velocity distribution known, the local skin friction coefficient can be determined from the definition of skin friction, $C_{f,x}$ as:

$$C_{f,x} = \frac{2\,\tau_w}{\rho\,u_x^2} = \frac{2}{u_x^{*2}} \tag{3.41}$$

The dimensionless parameter, R_i^+, can also be expressed by:

$$R_i^* = \frac{R_i\,u^*}{\nu} = \frac{Re_{R_i}}{u_\infty^*} \tag{3.42}$$

From the integral momentum equation for the axisymmetric boundary equation, the momentum defect (or momentum thickness) area in an axisymmetric flow for a constant pressure, p, and constant density, ρ, is [79];

$$\frac{d\theta}{dx} = \frac{2\,\pi\,R_i}{\rho\,u_\infty^2}\,\tau_w \tag{3.43}$$

where the momentum defect area, θ, is

$$\theta = 2\,\pi \int_{R_i}^{\delta} \frac{u}{u_\infty}\,(1 - \frac{u}{u_\infty})\,r\,dr \tag{3.44}$$

The length Reynolds number, Re_x may be expressed from the definition as:

$$Re_x = \frac{u_\infty\,x}{\nu} = u_\infty^*\,x^* \tag{3.45}$$

With the aid of Eqs. (3.44) and (3.45), one can obtain Eq. (3.43) in the form:

$$\frac{dRe_x}{dI} = u_\infty^{*2} \tag{3.46}$$

where the integral function becomes:

$$I(u_\infty^*\,,\,R_i^*) = \int_0^{\delta^*} u^*\,(1 - \frac{u^*}{u_\infty^*})\,(1 + \frac{y^*}{R_i^*})\,dy^*$$

Integrating, Eq. (3.46) can become:

$$Re_x = u_\infty^* I(u_\infty^*, R_i^*) - \int_0^{u_\infty^*} 2\, I(u_\infty^{*\prime}, r_\infty^*)\, u_\infty^{*\prime}\, du_\infty^{*\prime} \tag{3.47}$$

where $u_\infty^{*\prime}$ is a dummy variable. The derivation of equations in dimensionless form is given in Appendix C.3.

The desired relationship between C_f and Re_x is obtained by numerical integration of Eq. (3.47) for a preassigned Reynolds number based on the cylinder radius, R_i. Therefore, with Eqs. (3.41), (3.42), (3.47) and the velocity distribution, the skin friction coefficient can be calculated.

3.3.4 Temperature Distribution

The basic energy equation in Eq. (3.19) in dimensionless quantities with the concept of the thermal eddy diffusivity is:

$$q^* = \frac{q}{q_w} = \left(\frac{1}{Pr} + \frac{\varepsilon_H}{\nu} \right) \frac{\partial T^*}{\partial y^*} \tag{3.48}$$

When the convective terms are neglected as mentioned in Section 3.3.2, the following relation is obtained from the energy equation for the radial heat flux distribution within the thermal boundary layer on the cylinder:

$$q^* = \frac{R_i}{r} = \frac{R_i^*}{R_i^* + y^*} = \tau^* \tag{3.49}$$

Therefore, the radial temperature distribution can be obtained from Eq (3.19) as:

$$dT^{+} = \left[\frac{1 + \frac{\varepsilon_M}{\nu}}{\frac{1}{Pr} + \frac{1}{Pr_t}\left(\frac{\varepsilon_M}{\nu}\right)} \right] \frac{du^{+}}{dy^{+}} dy^{+} \tag{3.50}$$

The derivations of equations in dimensionless form are given in Appendix C.2. Knowing the velocity distribution from Eq. (3.37) in terms of R_i, the temperature profile can be obtained by integrating Eq. (3.50). For the turbulent Prandtl number, Pr_t, the expression of Gräber [81] as given below is used:

$$Pr_t = 0.91 + 0.13\, Pr^{0.545} \tag{3.51}$$

where for air as a working fluid ($Pr \approx 0.71$), the turbulent Prandtl number, Pr_t, becomes about unity. From the definition of T^{+}, the boundary condition at the wall is

$$T^{+} = 0 \qquad at \;\; y^{+} = 0 \tag{3.52}$$

Therefore, with Eqs. (3.37) through (3.52), the temperature distribution can be calculated for a given radius of a cylinder, R_i, at a given local Reynolds number.

3.3.5 Nusselt Number

As was the case for the integral momentum equation, the integral energy equation for the axisymmetric boundary equation is expressed in terms of enthalpy defect (or thickness) area. The problem of defining a thickness of the thermal boundary layer is similar to that of the momentum boundary layer, i.e.,

$$\frac{d\Delta}{dx} = \frac{2\pi R_i}{\rho c_p u_\infty (T_w - T_\infty)} q_w \tag{3.53}$$

where the enthalpy defect area, Δ, is defined for constant-property flow of a perfect gas with no chemical reaction as [26]:

$$\Delta = 2\pi \int_{r_i}^{\delta_H} \frac{u}{u_\infty} \frac{(T - T_w)}{(T_w - T_\infty)} r\, dr \tag{3.54}$$

In dimensionless parameters, Eq. (3.51) can be rearranged for the case of uniform heat flux at the wall surface as:

$$\frac{dRe_x}{dI_H} = 1 \tag{3.55}$$

where the integral function is:

$$I_H = \int_0^{\delta_H^+} u^+ u_\infty^+ (T_\infty^+ - T^+)(1 + \frac{y^+}{R_i^+}) dy^+$$

Therefore, integration of Eq. (3.55) yields:

$$Re_x = \int_0^{\delta_H^+} u^+ u_\infty^+ (T_\infty^+ - T^+)(1 + \frac{y^+}{R_i^+}) dy^+ \tag{3.56}$$

Rearranging Eq. (3.56) with the definition of the temperature in dimensionless form becomes:

$$T_\infty^+ = \frac{\dfrac{Re_x}{u_\infty^+} + \displaystyle\int_0^{\delta_H^+} u^+ T^+ (1 + \frac{y^+}{R_i^+}) dy^+}{\displaystyle\int_0^{\delta_H^+} u^+ (1 + \frac{y^+}{R_i^+}) dy^+} \tag{3.57}$$

From the definition, the local Nusselt number, Nu_x, can yield

$$Nu_x = \frac{Pr \cdot Re_x}{T_\infty^* \cdot u_\infty^*} \tag{3.58}$$

The expression of Eq. (3.58) in dimensionless form was made as shown in Appendix C.3. With Eqs. (3.56) through (3.58) for a given radius of cylinder, R_i, one selects a value for a given local Reynolds number, and the Nusselt number can be calculated.

3.3.6 Results

The theoretical velocity profiles calculated from Eqs. (3.37) through (3.40) for turbulent boundary layer flows over circular cylinders for three radii of cylinders, R_i = 6.35 mm, 12.7 mm, and 25.4 mm at a given local Reynolds number based on the same free stream velocity are shown in Fig. 3.4.

In Fig. 3.5, the calculated results of the local skin friction coefficients for turbulent boundary layer flows over circular cylinders for three radii of cylinders, R_i = 6.35 mm, 12.7 mm, and 25.4 mm, for a given local Reynolds number based on the same free stream velocity are plotted and are summarized in Table 3.2. The skin friction coefficients normalized by that for a flat plate for three radii of cylinders, R_i = 6.35 mm, 12.7 mm, and 25.4 mm, at a given local Reynolds number based on a same free stream velocity are given in Fig. 3.6.

The theoretical temperature profiles calculated from Eqs. (3.49) through (3.51) for turbulent boundary layer flows over circular cylinders for three radii of cylinders, R_i = 6.35 mm, 12.7 mm, and 25.4 mm, for a given local Reynolds number are given in Fig. 3.7. The theoretical temperature profiles for two Prandtl numbers of 0.7 and 1.0 with a fixed cylinder radius and Reynolds number are also plotted in Fig. 3.8.

The calculated results of the local Nusselt number for three radii of cylinders, R_i = 6.35 mm, 12.7 mm, and 25.4 mm, with a given local Reynolds number and Prandtl number of Pr = 0.7 are plotted in Fig. 3.9 and are summarized in Table 3.3. The Nusselt numbers normalized by that for a flat plate for three radii of cylinders, R_i = 6.35 mm, 12.7 mm, and 25.4 mm, with a given local Reynolds number and Prandtl number of Pr = 0.7 are given in Fig. 3.10. For various Prandtl numbers, the normalized Nusselt numbers are also plotted in Fig. 3.11 and are summarized in Table 3.4.

3.4 Analysis: Fully Developed Turbulent Fluid Flow and Heat Transfer in a Concentric Annulus

3.4.1 Problem Definition and Assumption

The fluid flow and heat transfer to be analysed are subjected to the following conditions:

(1) The annulus is concentric, inner core is heated with constant heat flux, and outer core is insulated;

(2) The thermodynamic properties (density, viscosity, specific heat etc.) of the fluid are constant;

(3) Velocity and temperature profiles are fully developed and turbulent;

(4) The location of maximum velocity coincides with the position of zero shear stress;

(5) The flow fields can be divided into two regions such as the sublayer and the fully turbulent region.

3.4.2 Velocity Distribution

From the basic equations, Eq. (3.27), the governing turbulent transport equation for momentum can be written in dimensionless parameters as:

$$\left|\frac{\partial u^*}{\partial \zeta}\right| = D^* \left[\frac{(\tau/\tau_o)}{1+(\varepsilon_M/\nu)}\right] \qquad (0 \le \zeta \le 1) \qquad (3.59)$$

To solve Eq. (3.59), information on the eddy diffusivity and the shear stress distribution are needed. Once the eddy diffusivity for momentum, $(\varepsilon_M/\nu)_j$, and the shear stress ratio, τ / τ_o, are known for the entire fluid region, the velocity profiles can be derived. The details of the derivation of Eq. (3.59) are given in Appendix D.2.

The boundary layer equations contain the term involving the time mean of the product of fluctuating velocities, the Reynolds shear stress. Since these terms have not been related to the mean velocity, the solution would be depending on some empiricism, which leads to various approaches and to various methods.

One of the most popular multi-equation models is the k-ε turbulence model [72]. In formulating the k-ε model, the idea is to derive the exact equation for the turbulent transport of dissipation, ϵ, and to find a closure approximation for the exact equation governing its behaviour. This equation involves several double or triple correlations. These correlations are impossible to measure with any degree of accuracy to find a closure approximation. For these reasons, there is an accuracy problem to predict the behaviour of fluctuating velocity near the wall. If the turbulent fluid flow involved is that of the bounded flow, the k-ε model may not be used because the conventional k-ε turbulence model can not be clearly defined for the wall shear stress.

To resolve the closure problem of the turbulence fluctuation terms in this study, the concept of eddy diffusivity for momentum is used. The eddy diffusivity models for momentum used here are originally due to van Driest [8] and Reichardt [9]. <u>Those models were modified for the present flow channel geometry with the variable von Kármán constant, κ_i, proposed in this thesis. It is assumed that von Kármán constant, κ_i, for the inner core having a transverse convex surface curvature, is a function of the radius of an inner core in a concentric annulus, R_i, discussed in Section 3.2</u>.

(A) <u>For the sublayers (inner and outer regions); modified van Driest model</u>

The van Driest hypothesis [26] is to provide an eddy diffusivity in the sublayer that becomes zero at y = 0. It has the virtue that it allows a continuous calculation through the sublayer and into the fully turbulent region. With this, the Prandtl mixing length [26] can be used all the way to the wall. For simulating the sublayer, a damping function is needed in the mixing length equation, given as:

$$l = \kappa \cdot y \left(1 - \frac{1}{e^{y^+/A^+}}\right) \tag{3.60}$$

where A^+ is the damping constant, which is determined empirically. To describe Eq. (3.59) in terms of eddy diffusivity for momentum, ε_M is;

$$\frac{\varepsilon_M}{\nu} = \frac{l^2}{\nu}\frac{du}{dy} = \frac{l^{+2}}{\nu}\frac{du^+}{dy^+} \tag{3.61}$$

For the sublayers of the flow in a concentric annulus (see Fig. 3.2), rearranging Eq. (3.61) with the proposed variable von Kármán constant, κ_i, gives the modified eddy diffusivity distributions, ε_M/ν, as the following equations:

(i) <u>For the viscous sublayer of an inner region, the eddy diffusivity distribution</u> is

$$(\varepsilon_M/\nu)_i = \frac{1}{2}[-1 + \{1 + 4\,[\kappa_i \cdot D^+]^2 \zeta^2\,[1 - \exp(-D^+\zeta(\tau_i/\tau_o)^{0.5}/A^+)]^2(\tau/\tau_o)\}^{0.5}] \tag{3.62}$$

$$(0 \le \zeta \le \zeta_{is})$$

where $\kappa_i = \kappa \cdot F(R_i)$ and von Kármán constant, κ, is given as 0.4. ζ is a normalized length between inner wall and outer wall.

(ii) <u>For the viscous sublayer of an outer region, the eddy-diffusivity distribution</u> is;

$$(\varepsilon_M/\nu)_o = \frac{1}{2}[-1+\{1+4(\kappa_o \cdot D^*)^2(1-\zeta)^2[1-\exp(-D^*(1-\zeta)/A^*)]^2(\tau/\tau_o)\}^{0.5}] \qquad (\zeta_{os} \le \zeta \le 1) \tag{3.63}$$

where κ_o is a constant, 0.4. the notations of i and o indicate the inner region and the outer region based on the point of the maximum velocity. The notations *is* and *os* mean the sublayer of the inner region and that of the outer region. These two expressions can be made in dimensionless form (see Appendix D.4).

(B) <u>For the fully turbulent regions; modified Reichardt model</u>

Since the velocity profile outside the viscous sublayer should differ from the law of the wall, the logarithmic law of the wall can not be used. An empirical equation for an entire region outside the viscous sublayer proposed by Reichardt [26] is:

$$\frac{\varepsilon_M}{\nu} = \frac{\kappa \cdot y^+}{6}(1 - \frac{r}{R_o})[1 + 2(\frac{r}{R_o})^2] \tag{3.64}$$

where $r = R_o - y$.

Reichardt's expression for the eddy diffusivity of momentum can be modified for the entire turbulent flow region on both sides of the concentric annulus. From the continuity of the momentum eddy diffusivity at the location of the maximum velocity ($\zeta = \zeta_m$), Reichardt's turbulence model can be modified with the proposed variable von Kármán constant, κ_i, as:

(i) <u>For the region from the inner surface sublayer to the maximum velocity</u> is

$$(\varepsilon_M/\nu)_i = \frac{\kappa_i}{6} D^*(1-\zeta_m) E_c \left[\left(\frac{\zeta_m - \zeta}{\zeta_m} \right)^2 \left\{ 1 - 2\left(\frac{\zeta_m - \zeta}{\zeta_m} \right)^2 \right\} + 1 \right] \tag{3.65}$$

$$(\zeta_{is} \le \zeta \le \zeta_m)$$

where $E_c = (\tau_i/\tau_o)^{0.5} \{\zeta_m/(1-\zeta_m)\}$

(ii) <u>For the region from the maximum velocity to the outer surface sublayer</u> is

$$(\varepsilon_M/\nu)_o = \frac{\kappa_o \cdot D^*}{6} (1-\zeta_m) \left[\left(\frac{\zeta - \zeta_m}{1-\zeta_m} \right)^2 \left\{ 1 - 2\left(\frac{\zeta - \zeta_m}{1-\zeta_m} \right)^2 \right\} + 1 \right] \tag{3.66}$$

$$(\zeta_m \le \zeta \le \zeta_{os})$$

where ζ_m is the location of the maximum velocity. Now that the eddy diffusivity for momentum, $(\frac{\varepsilon_M}{\nu})$, is established for the entire turbulent fluid flow region, the velocity profiles can be derived, using the assumption that zero shear occurs at the radius of maximum velocity. These two expressions can be put in dimensionless form (see Appendix D.4).

If it is assumed that the pressure gradient is constant in the radial direction, a force balance on annular fluid elements between R_i and r_m and between r_m and R_o yields the following equation:

$$\frac{\tau_i}{\tau_o} = \frac{R_o}{R_i} \left(\frac{r_m^2 - R_i^2}{R_o^2 - r_m^2} \right) \tag{3.67}$$

The local shear stress distribution can be obtained also from the force balance made on the annular fluid elements. A force balance invariant of flow position can be established for a given geometry, owing to the fully developed nature of the fluid flow. The basic governing equation, Eq. (3.30), can be rewritten incorporating non-dimensional parameters as:

$$\frac{\tau}{\tau_j} = [1 + (\frac{\varepsilon_M}{\nu})_j]\,(\frac{du^+}{dy^+}) \tag{3.68}$$

Substituting Eqs. (3.65) and (3.66) into Eq. (3.68) with Eq. (3.67), gives the shear stress distribution as:

$$(\tau/\tau_o) = \frac{\{2(R_i^+/D^+)+\zeta_m+\zeta\}\{1+(R_i^+/D^+)\}(\zeta-\zeta_m)}{\{2(R_i^+/D^+)+\zeta_m+1\}\{\zeta+(R_i^+/D^+)\}(1-\zeta_m)}F(\zeta) \tag{3.69}$$

where

$$F(\zeta) = \begin{cases} -1 & (0 \le \zeta \le \zeta_m) \quad \textit{for the inner region} \\ +1 & (\zeta_m \le \zeta \le 1) \quad \textit{for the outer region} \end{cases}$$

Eq. (3.69) in dimensionless form is derived in Appendix D.3.

The two flow regions as shown in Fig. 3.2 are subdivided into viscous sublayers and fully turbulent regions. The velocity at the point of the maximum velocity must be equal in the regions at each side. At the location of the maximum velocity, the boundary conditions in dimensionless parameters are:

$$u_i^* = u_o^*, \qquad \partial u_i^*/\partial\zeta = \partial u_o^*/\partial\zeta = 0 \qquad at\ \zeta = \zeta_m \tag{3.70}$$

The boundary conditions for velocity in dimensionless form, u^*, at the walls are:

$$u^* = 0 \qquad at\ \ \zeta = 0\ \ or\ \ \zeta = 1 \tag{3.71}$$

3.4.3 Friction Coefficient

The friction coefficient is defined as:

$$f_j = \frac{\tau_{wj}}{\frac{1}{2}\rho u_b^2} \tag{3.72}$$

Since it is assumed that the pressure gradient is constant, the force balance yields the following equation:

$$\frac{dp}{dx}\pi(R_o^2 - R_i^2) = 2\pi(\tau_o \cdot R_o + \tau_i \cdot R_i) \tag{3.73}$$

Therefore, the friction coefficient, f, can be obtained from the definition as:

$$f = \frac{(R_o - R_i)}{\rho u_b^2}\left(-\frac{dp}{dx}\right) \tag{3.74}$$

Substituting Eq. (3.73) into Eq. (3.74), and after some rearrangement using dimensionless parameters, the friction coefficient becomes:

$$f = -8\left[\frac{\{1+(\tau_i/\tau_o)\alpha\}(1-\alpha)^2}{(1+\alpha)}\right]\left(\frac{R_o^*}{Re}\right)^2 \tag{3.75}$$

where the shear stress distribution based on shear stress for the outer region is given as;

$$(\tau_i/\tau_o) = \frac{1}{\alpha}\,\frac{\{2(R_i^*/D^*) + \zeta_m\}\zeta_m}{\{2(R_i^*/D^*) + 1 + \zeta_m\}\{1-\zeta_m\}} \tag{3.76}$$

The Reynolds number is defined in the usual way as:

$$Re = \frac{u_b De}{\nu} \tag{3.77}$$

The bulk velocity is derived from the definition as

$$u_b = \frac{1}{\pi(R_o^2-R_i^2)}\left[\int_{R_i}^{R_o} u\,2\pi r dr\right] = 2\left(\frac{\nu}{R_i}\right)\left(\frac{\alpha}{1+\alpha}\right)\left[\int_0^1 u^*(D^*\zeta + R_i^*)\,d\zeta\right] \tag{3.78}$$

Substituting Eq. (3.78) into Eq. (3.77) with some rearrangement yields:

$$Re = 4\left(\frac{1-\alpha}{1+\alpha}\right)\left[\int_0^1 u^*(D+\zeta+R_i^*)d\zeta\right] \tag{3.79}$$

The method of non-dimensionalization for Eq.(3.79) is given in Appendix D.5.

3.4.4 Temperature Distribution

Temperature profiles can be derived from the energy equation governing the transport of heat, given by Eq. (3.29), if the functions for the heat flux and the eddy diffusivity for heat are known. Eq. (3.29) can be written in dimensionless parameters as:

$$\frac{q}{q_i} = \left(\frac{1}{Pr} + \frac{\varepsilon_H}{\nu}\right) \frac{\partial T_j^*}{\partial y_j^*} \tag{3.80}$$

where the dimensionless temperature for each region is defined as:

$$T_j^* = \frac{(T_w - T_j)\rho c_p u_j^*}{q_i} \tag{3.81}$$

where q_i refers to the uniform heat flux at the inner core. The rearrangement of Eq. (3.80) with Eq. (3.81) gives:

$$\frac{\partial T^*}{\partial \zeta} = Pr\, D^* \left[\frac{(q/q_i)}{1 + (Pr/Pr_t)(\varepsilon_M/\nu)}\right] \qquad (0 \le \zeta \le 1) \tag{3.82}$$

The heat flux distribution can be derived from an energy balance made on an element of the flow as:

$$\frac{q}{q_i} = \frac{R_i}{r} \frac{R_o^2 - r^2}{R_o^2 - R_i^2} \tag{3.83}$$

Eq. (3.83) can be further rewritten in a non-dimensional form as:

$$(q/q_i) = \frac{(R_i^+/D^+)\{2(R_i^+/D^+)+1+\zeta)(1-\zeta)}{\{2(R_i^+/D^+)+1\}\{(R_i^+/D^+)+\zeta\}} \qquad (0 \le \zeta \le 1) \tag{3.84}$$

Once the eddy diffusivities for momentum, $(\varepsilon_M/\nu)_j$, are known for the entire fluid region, the temperature profiles can be derived. The method of non-dimensionalization for Eq.(3.84) is given in Appendix D.3.

At the inner wall surface, the dimensionless temperature T^+ must be zero from the definition of T^+. Since it assumed that the outer wall is insulated, the temperature gradient is zero. Therefore, the boundary conditions for temperature in dimensionless form, T^+, at the walls are:

$$\begin{aligned} T^+ &= 0 \qquad at \quad \zeta = 0 \\ dT^+/d\zeta &= 0 \qquad at \quad \zeta = 1 \end{aligned} \tag{3.85}$$

3.4.5 Nusselt Number

The Nusselt number is defined in the usual way as:

$$Nu = \frac{h\,2\,(R_o - R_i)}{k} = \frac{2\,D^+ Pr}{T_b^+} \tag{3.86}$$

and the convective heat transfer coefficient is defined as:

$$h = q_i/(T_i - T_b)$$

The bulk temperature, T_b, is also defined as:

$$T_b = \int_{R_i}^{R_o} r\,u\,T\,dr \Big/ \int_{R_i}^{R_o} r\,u\,dr \tag{3.87}$$

In dimensionless form, T_b becomes as:

$$T_b^* = \frac{(T_i - T_b)\,c_p\,\rho\,u_o^*}{q_i} = \frac{4}{Re}\left(\frac{1-\alpha}{1+\alpha}\right)\left[\int_o^1 u^* T_b^* (D^*\zeta + R_i^*)\,d\zeta\right] \tag{3.88}$$

Therefore, the Nusselt number can be obtained by solving Eq. (3.88). The method of non-dimensionalization is given in Appendix D.5.

3.4.6 Results

The theoretical velocity distributions for three different inner core radii, R_i, at a given Reynolds number with a fixed α of 0.3 are plotted in Figs. 3.12 and for different Reynolds numbers are also given in Fig. 3.13. The calculated results of velocity distributions for two different radius ratios, α, at a given Reynolds number are plotted in Fig. 3.14. The theoretical locations of the maximum velocities compared with correlated expression of others [52, 53, 55] for various values of radius ratios, α, are summarized in Tables 3.5 and 3.6.

The friction coefficients, f, calculated from Eq. (3.75) for two different radii of the inner cores, R_i, with a fixed radius ratio, α (= 0.3), are shown in Fig. 3.15 and the data are summarized in Table 3.7. For three different radius ratios α with a fixed R_i = 12.7 mm, the effect of the radius ratio, α, on the friction coefficient calculated from the present analysis is also shown in Fig. 3.16 and the results are also summarized in Table 3.8.

The calculated momentum eddy diffusivity distributions for three different radii of the inner cores with a fixed radius ratio of $\alpha = 0.3$, at a given Reynolds number are given in Fig. 3.17 and the results are summarized in Table 3.9. For three different radius ratios of α with a fixed inner core radius, the theoretical eddy diffusivity distributions for momentum are shown in Fig. 3.18 and the results are summarized in Table 3.10.

The theoretical temperature distributions for three different radii of inner cores with a fixed radius ratio of $\alpha = 0.3$ are plotted in Fig. 3.19. The calculated results of temperature distributions for three different radius ratios of α, with a fixed inner core radius at a given Reynolds number are plotted in Fig. 3.20. Fig. 3.21 shows the temperature distributions for three different Prandtl numbers with a fixed radius ratio of $\alpha = 0.5$ having a fixed inner core radius at a given Reynolds number.

Fig. 3.22 shows the theoretical Nusselt numbers for two different radii of the inner cores with a fixed radius ratio of $\alpha = 0.3$ and the results are summarized in Table 3.11. The Nusselt numbers calculated from Eq. (3.86) for two different radius ratios of α with a fixed inner core radius are given given in Fig. 3.23 and the results are also summarized in Table 3.12. Figs. 3.24 show the effect of transverse convex curvature, R_i, and radius ratio, α, on the Nusselt number for a given Reynolds number. The effect of Prandtl number on the Nusselt number calculated by the present analysis is also given in Fig. 3.25.

3.5 Analysis: Fully Developed Turbulent Fluid Flow and Heat Transfer in a Concentric Annulus using the Standard k-ε Turbulence Model

Recently, many turbulence models have been developed by investigators [72]. Most of the turbulence models consist of sets of differential equations, associated algebraic equations, and constants to simulate the behaviour of turbulent fluid flows. Computer methods for solving the differential equations of fluid dynamics are also well advanced for three-dimensional, time-dependent turbulent fluid flows. The main obstacles in developing the turbulence model are the difficulty of selecting the set of differential equations which provide universality, the required constants, and functions.

The original k-ε model of turbulence was introduced by Launder, Morse and Spalding [85]. This method considers two differential equations for turbulent quantities, in additional to the equations for the mean flow. One of the modelled equations is an equation for turbulent kinetic energy, k. The second equation is a balance equation for a turbulent kinetic energy dissipation rate, ε. This equation is derived by analogy to the k equation instead of modelling an exact equation of ε derived by manipulating the Navier-Stokes equations. Despite its arbitrariness, the k-ε model had reasonable success in a variety of flows. A limitation of this method is that it can not account for anisotropic turbulent transport known to arise in turbulent shear flows. Therefore, this method can not describe adequately the near wall region of the wall bounded flows. It is usually combined with some version of the "law of the wall", which prescribes a near wall velocity distribution form.

3.5.1 General Equations

Two additional differential transport equations are introduced, one for the turbulent kinetic energy, k, and the other for the dissipation rate of the turbulent kinetic energy, ε. These equations can be developed from the momentum equations using the definitions of k and ε and appropriate manipulations [85]. The turbulence energy, k equation is given as:

$$\frac{Dk}{Dt} = \frac{1}{\rho}\frac{\partial}{\partial x_k}\left(\frac{\mu_t}{\sigma_k}\frac{\partial k}{\partial x_k}\right) + \frac{\mu_t}{\rho}\left(\frac{\partial u_i}{\partial x_k} + \frac{\partial u_k}{\partial x_i}\right)\frac{\partial u_i}{\partial x_k} - \varepsilon \tag{3.89}$$

The left-hand side contains the convective change rate of turbulent kinetic energy. The right-hand side of the equation contains the production and dissipation terms. The term, k, means the production of turbulent kinetic energy by interaction of Reynolds stresses due to the mean velocity gradients. ε is the dissipation rate of the turbulent kinetic energy. The diffusion terms contain a new diffusion coefficient, μ_t / σ_k.

The dissipation equation which was first developed by Hanjalic and Launder [86] is given the following form:

$$\frac{D\varepsilon}{Dt} = \frac{1}{\rho}\frac{\partial}{\partial x_k}\left(\frac{\mu_t}{\sigma_\varepsilon}\frac{\partial \varepsilon}{\partial x_k}\right) + \frac{c_1\mu_t}{\rho}\frac{\varepsilon}{k}\left(\frac{\partial u_i}{\partial x_k} + \frac{\partial u_k}{\partial x_i}\right)\frac{\partial u_i}{\partial x_k} - c_2\frac{\varepsilon^2}{k} \tag{3.90}$$

In Eq. 3.90, the various terms have the same significance as those of the k equation and the diffusion coefficient, $\mu_t / \sigma_\varepsilon$ is introduced. The several empirical constants have been introduced whose values have been estimated through comparisons of model predictions with experimental data. The empirical constants are summarized in Table 3.14. The turbulent viscosity, μ_t, is given as:

$$\mu_t = \frac{c_\mu \rho k^2}{\varepsilon} \tag{3.91}$$

The turbulent viscosity, μ_t, is determined by solution of two turbulent field variables, k and ε. From Eqs. (3.89) to (3.91), the equation sets describing the turbulent flow can be closed.

3.5.2 Boundary Conditions

Before any set of differential equations can be solved, it must be constrained by an appropriate set of boundary conditions. The following section will present the modifications to the various transport equations to account for the presence of the solid wall surface (inner and outer walls).

3.5.2.1 Continuity Equation

The boundary conditions for the continuity equation are imposed by setting all mass fluxes across the boundary of any control volume to zero. This is applied in all equations since the mass flux across control volume boundaries convects all dependent variables into and out of the control volume.

In the case that the fluid flows across the boundaries, this requires a modification to the mass flux allowed through the control volume faces on the peripheries of the solution domain. Once the inlet velocity profile is specified, the approximate mass fluxes are imposed on all control volumes at the inlet. At the outlet, the velocity profile is allowed to develop on its own and no predetermined distribution is imposed. The mass flux from the outlet boundary control volume is calculated based on the velocity at the center of the control volume.

3.5.2.2 Momentum Equations

Two boundary conditions are imposed on the velocity field as shown in Fig. 3.26: (i) the traditional zero penetration; and (ii) the zero slip condition.

The zero penetration condition is applied to the mass flux through all solid boundaries and the zero slip condition is for the shear stress, τ_w, near the wall. The shear stress at the wall is deduced from the "logarithmic law" as given by Spalding [90].

$$\tau_w = \rho u_p c_\mu^{0.25} \frac{\kappa \cdot k^{0.5}}{\ln(E \rho c_\mu^{0.25} k^{0.5} / \mu^{0.5})} \tag{3.92}$$

The shear stress in Eq. (3.92) can be converted to a force that acts as an additional source in the momentum equation for the appropriate control volume. E is a surface roughness parameter and is taken as 9.79 [91]. The von Kármán constant, κ, is about 0.36 to 0.41. For turbulent boundary layers, the length scale is:

$$y^+ = c_\mu^{0.25} \cdot k^{0.5} \cdot \delta y \cdot \rho / \mu \tag{3.93}$$

where Eq. (3.92) is valid for $y^+ > 11.63$ [92]. When $y^+ < 11.63$, the shear stress is based on a linear calculation of the velocity gradient from the near wall node point to the boundary using the following shear stress expression:

$$\tau_w = \mu \left(\frac{\delta u}{\delta y}\right)_p \tag{3.94}$$

3.5.2.3 k and ε Equations

The value of the turbulent kinetic energy, k, at a near wall node point can be calculated using the balance equation for the control volume with the assumption of zero diffusion on the wall. The value of the energy dissipation rate is fixed at the node point by the following:

$$\varepsilon_p = (c_\mu^{0.75} / \kappa)\,(k^{1.5} / \delta y) \tag{3.95}$$

Eq. (3.95) is based on the hypothesis that the turbulent length scale varies linearly with the distance from the wall [72].

3.5.3 Wall Function Method

Close to solid wall surface(s) and other interfaces, the local Reynolds number is so small that viscous effects predominate over turbulent flows. The wall-function method can be used to account for these regions. The wall function method has been proposed by Patankar and Spalding [93]. This method is the one that has been most widely used and is still to be preferred for practical purposes. Its merits are two: (i) it economizes computer time and storage; and (ii) it allows the introduction of additional empirical information in special cases, as when the wall is rough.

Consider the adjacent grid points W and P of the finite difference grid on which the flow is to be computed in Fig. 3.27. In the figure, the point P is sufficiently remote from W, which lies on the wall, so that the viscous effects are entirely overwhelmed by the turbulence. The flux of momentum to the wall has the relation:

$$\frac{u_p}{\sqrt{\tau_w / \rho}} c_\mu^{1/4} k_p^{1/2} = \frac{1}{\kappa} \ln [E_{y_p} \frac{c_\mu^{1/2} k_p^{1/2}}{\nu}] \tag{3.96}$$

Here u_p, τ_w, and y_p are respectively the time average velocity of the fluid at point P along the wall, the shear stress on the wall in the direction of the velocity, u_p, and the distance of the point P from the wall. The wall function reproduces identically the full implications of the "logarithmic velocity profile" when uniform shear stress prevails in the layer W-P, and generation and dissipation of turbulence energy are in balance there and are given the following relation:

$$\tau_w / \rho = c_\mu^{1/2} \cdot k = constant \tag{3.97}$$

3.5.4 Modified Procedure

In the two-equation k-ε model turbulence model for wall flows, these equations are normally used with empirical wall function formulas. However, there is an accuracy problem in predicting the behaviour of fluctuating velocity near the wall. In wall bounded turbulent fluid flows, the k-ε model can not be clearly defined for the wall shear stress. In the literature review [85-90], it was concluded again that there are not any models to predict turbulent fluid flow characteristics near the wall adequately.

In the present study, a force balance was adapted to determine the ratio of shear stress and von Kármán constant, κ, for each region in Eq. (3.92). Reichardt's expression [26] is adapted for the eddy diffusivity of momentum for the entire turbulent flow region on both sides of the concentric annulus.

From the continuity of momentum, the eddy diffusivity at the location of the maximum velocity in the Reichardt turbulence model can be written as:

$$\left(\frac{\varepsilon_M}{\nu}\right)_j = \frac{\kappa_j}{6}\left|(R_j - r_m)\right| \frac{\sqrt{\tau_j/\rho}}{\nu}\left[1 - \left(\frac{r}{R_j}\right)^2\right]\left[1 + 2\left(\frac{r}{R_j}\right)^2\right]\sqrt{\frac{R_j}{r}} \tag{3.98}$$

where the eddy diffusivity for momentum, $(\frac{\varepsilon_M}{\nu})_j$, is established for the entire turbulent fluid flow region using the assumption that zero shear occurs at the radius of maximum velocity.

If it is assumed that the pressure is constant, a balance on the annular fluid elements between R_i and r_m and between r_m and R_o yields the following equation:

$$\frac{\tau_i}{\tau_o} = \frac{R_o}{R_i}\left(\frac{r_m^2 - R_i^2}{R_o^2 - r_m^2}\right) \tag{3.99}$$

Equating the eddy diffusivities at the plane of zero shear gives:

$$\frac{\kappa_0}{\kappa_i} = \frac{r_m - R_i}{R_o - r_m}\sqrt{\frac{\tau_{R_i}}{\tau_{R_o}}} \tag{3.100}$$

where the radius of the maximum velocity, r_m, in the concentric annular duct is determined from the calculation of the velocity distribution directly by the "sorting method" [108].

3.5.5 Algebraic Grid Generation Method

In order numerically to solve the governing partial differential equations of fluid mechanics, approximations of the partial differentials are introduced. These approximations convert the partial derivatives into finite differential expressions which are used to rewrite the partial differential equations. The approximate algebraic equations, i.e. finite difference equations, are subsequently solved at discrete points within the domain of interest. Therefore, a set of grid points within the domain, and the boundaries of the domain, must be specified.

In body-fitted coordinate systems, two coordinate lines, ξ and ζ, are aligned on the surface along the streamwise and circumferential direction, and the third coordinate, η, is normal to the surface [94]. The major advantage of the "algebraic grid generation scheme" is the speed with which a grid can be generated. An algebraic equation is used to relate the grid points in the computational domain to those of the physical domain.

Since the flow near the solid surface has a velocity gradient, accurate computation of the velocity gradients in this region will require many grid points within the domain. Rather than using a uniform grid distribution in the physical domain, grid points would be clustered in this region, which reduces the total number of grid points and increases efficiency. For a physical domain enclosed by lower and upper solid surfaces, clustering at both two surfaces can be considered. For a two-dimensional flow field in a duct, the following algebraic equations are employed:

$$\begin{aligned} \xi &= x \\ \eta &= \alpha + (1 - \alpha)\frac{\ln\{\{\beta + [(2\alpha + 1)y/H] - 2\alpha\}/\{\beta - [(2\alpha + 1)y/H] + 2\alpha\}\}}{\ln[(\beta + 1)/(\beta - 1)]} \end{aligned} \tag{3.101}$$

where ξ and η are the body-fitted coordinates. ξ is aligned streamwise and η is normal to the surface coordinate. H is the height of the physical domain, β is a clustering factor, and α defines where the clustering takes place. When α is zero, the clustering occurs at y = H, and when $\alpha = 0.5$, clustering is distributed equally. The inverse transformation is given as:

$$
\begin{aligned}
x &= \xi \\
y &= H\frac{(2\alpha+\beta)[(\beta+1)/(\beta-1)]^{(\eta-\alpha)/(1-\alpha)}+2\alpha-\beta}{(2\alpha+1)\{1+[\beta+1)/(\beta-1)]^{(\eta-\alpha)/(1-\alpha)}\}}
\end{aligned}
\tag{3.102}
$$

A grid system generated for a domain with 21 x 24 grid points with $\alpha = 0.5$ and $\beta = 1.05$ is shown in Fig. 3.28.

3.5.6 Numerical Solution

3.5.6.1 Procedure

Since there are five differential equations to be solved (p,u,v,w,k, and ε) in general, it would be very convenient if they could be cast in a standard form. This would result in a much shorter computer program since the same simultaneous equation solving algorithm could be used for all six field variables.

Let the dependent variable in the general equation be ϕ. Now, the conservation of ϕ can be expressed by the following differential equation, taken from Patankar [95].

$$\frac{\partial(\rho\phi)}{\partial t} + div(\rho\overline{u_i}\phi) = div(\Gamma\, grad\,\phi) + S \tag{3.103}$$

Since a steady state solution is used in the present study, the first term on the left-hand side disappears. The second term on the left-hand side is the rate of change of ϕ in the elemental control volume due to convection. It equals the net flux of ϕ carried by the flowing fluid. The first term on the right-hand side is the transport of ϕ into the control volume by diffusion and Γ is diffusion coefficient. The last term, S, is a source term. Therefore, Eq. (3.103) becomes:

$$div(\rho \overline{u_i} \phi) - div(\Gamma\, grad\, \phi) = S \tag{3.104}$$

It can be seen that the source of ϕ is balanced by the flux of ϕ out of the control volume by convection and diffusion. All the differential equations used here can be written as:.

$$\frac{\partial(\rho\phi)}{\partial x_i} + \frac{\partial}{\partial x_i}(\Gamma \frac{\partial \phi}{\partial x_i}) = S \tag{3.105}$$

A numerical solution to a differential equation consists of a set of numbers from which the distribution of dependent variables can be reconstructed. The solution domain is divided into a three-dimensional array of control volumes. Within each control volume, the values of the dependent variables are calculated. The governing differential equation must be integrated over these control volumes to yield algebraic equations containing the dependent variable at the current node and at neighboring nodes. This procedure yields a set of algebraic equations that can be solved simultaneously to give the value of the dependent variable in equation at each node. If the original differential equation is nonlinear, the resulting algebraic equation will be a linear equation before a large set of them can be solved simultaneously.

3.5.6.2 Results

The differential equations have been solved by the numerical procedure with the boundary conditions appropriate to the fully developed turbulent flows in concentric annuli. For each flow, 100 cross stream nodes have been employed, together with 10 down stream nodes used to cover the flow area using the "algebraic grid generation scheme". The forward step size in the y-direction was one hundredth of the length between the outer tube and the inner core. To check the numerical accuracy, several calculations have been made with more fine nodes of the grid width. In neither case were the predictions altered seriously. To achieve convergence of the numerical calculation for velocity and turbulence parameters, 2,000 iterations were carried out. Convergence was reached when the relative changes in variables between consecutive iterations were less than 5×10^{-5}.

In Figs. 3.29 and 3.30, the theoretical (k-ε turbulence model) velocity distributions in terms of u^+ versus y^+ coordinates are compared with experimental results for two different radii of inner cores, R_i = 16.7 mm and 8.57 mm having a fixed radius ratio, α, of 0.3 at various Reynolds numbers, respectively.

The theoretical velocity distributions for three different radii of inner cores having a fixed radius ratio, α (= 0.5) at a given Reynolds number of 40,000 are plotted in Fig. 3.31.

In Fig. 3.32, the theoretical (k-ε model) eddy diffusivity distribution is compared with the experimental results for three inner core radii, R_i = 8.57, 16.7, and 25.4 mm, with a fixed radius ratio of 0.3. at a given Reynolds number, respectively.

The turbulent intensities of the present study (k-ε turbulent model) and the experimental results of Brighton and Jones [56] for a inner core radius of 51 mm with a radius ratio, $\alpha = 0.562$ and Park [4] for a inner core radius of 21 mm with a radius ratio of $\alpha = 0.43$ at a Reynolds number of 44,000 are shown in Fig. 3.33.

CHAPTER 4
EXPERIMENTAL STUDY

4.0 Objective

In Chapter 3, the analytical results were theoretically presented for the effect of transverse convex surface curvature on the momentum and heat transfer characteristics for (i) turbulent boundary layer flow and heat transfer on a circular cylinder; and (ii) fully developed turbulent flow and heat transfer in a concentric annular duct.

In this experimental study, the main objective is also to determine experimentally the effects of the transverse convex curvature on the fluid flow and heat transfer characteristics for (i) turbulent boundary layer flows on circular cylinders and (ii) fully developed turbulent flows in concentric annular ducts. The former experiment, a preliminary experimental study of the transverse convex wall curvature, was carried out by Lee and Kim [45,46]. The experimental data have been analysed and recompiled in the present thesis.

Velocity profiles, friction coefficients, eddy diffusivities for momentum, temperature profiles, and Nusselt numbers for the fully developed turbulent air flows in concentric annular ducts were obtained from the new experimental set-up, specifically constructed for the stated objectives.

The data obtained experimentally are compared with the results of the theoretical analyses outlined in the previous Chapter 3.

4.1 Turbulent Boundary Layer Flow and Heat Transfer over a Circular Cylinder

As pointed out above, the experimental study with regard to the effects of the transverse convex surface curvature on turbulent boundary layer flows over circular cylinders was carried out by Lee and Kim [45,46]. It was presented for the case of $\delta/R_i \approx O(1)$ which had a wide range of application in engineering practice. Tests were carried out with free stream air velocities between 7.5 m/s and 30 m/s inside the wind tunnel. For the heat transfer study, the electrical power supplied to the test cylinder was controlled so that the difference between the average surface temperature and the free air stream temperature was between 15°C and 30°C. Velocity and temperature profiles were measured by either a static pitot-tube or a thermocouple probe, respectively.

4.1.1 Apparatus

4.1.1.1 Wind Tunnel

The wind tunnel used is the low speed, open circuit Eiffel type system currently in a University of Ottawa laboratory. It consists of six separate sections; the entrance, contraction, test section, diffuser, flexible coupling and a fan as shown in Fig. 4.1.

The entrance section is 1.53 m x 2.44 m in length and has four screens made of 1.4 mm mesh. A contraction section is 2.14 m in length with a contraction ratio of 4.0. The test-section portion is 3.66 m in length with a rectangular cross-section of 0.91 m x 0.61 m. A rectangular diffuser, with about a 6.5 degree angle, is converted to a regular octagon with a length of 2.29 m, and then changed to a sixteen sided polygon with a length of 1.07 m. A flexible connection made of rubber sheet, about 300 mm wide, is used to reduce the vibration caused by the fan. The Buffalo axial flow fan, type S-54C-9, has a diameter of 1.45 m, and a maximum capacity of 25.5 m^3/s at 89 mm of water gauge static pressure and the maximum r.p.m. is 1170. The fan motor has a full load of 27.6 KW, and is controlled by an adjustable speed magnetic drive.

The blockage effect is negligible on the pressure distribution within the test-sections because the area ratio of the cross-section of the test cylinders to that of the wind tunnel at the test section area is less than 0.4%. No blockage correction, therefore, is needed for the measured pressure data.

4.1.1.2 Test Sections

The three test cylinders with direct electrical resistance heating were made of stainless steel, type SS 304. They have different diameters. The essential dimensions are included in Table 4.1.

For measuring the temperature of core heaters, twelve copper-constantan thermocouples (T-type, S.W.G 30) were installed using the "split-junction" method [99] along the inner wall periphery of the test cylinders. Several additional thermocouples were positioned on the inner wall to check the symmetry of the temperature distributions. All thermocouples were calibrated in situ. Boundary-layer tripping wires were used for all the test cylinders at $x = 0$. The diameter of the tripping wires was 1.6 mm.

Test sections were positioned in the wind tunnel using two kinds of fixtures: one rigid and fixed for the down stream, and the other free, made of piano wire. The alignment of the test cylinders with the mean air flows were checked using a survey level and a 3-hole yaw tube.

4.1.2 Measurements

(1) Velocity Measurement

For the measurement of velocity distribution, the pressure signal from the specially designed static pitot-tube was recorded with two MKS Baraton pressure transducers. The pressure transducers have full scale pressure heads of 133.4 Pa (1 torr) and 1.334 kPa (10 torr), respectively, with not more than 0.1% error at full scale. The direct current signal from the pressure tranducer was connected to the data acquisition system that consisted of a Hewlett-Packard (HP) desk top computer and four other HP instruments: a HP 3455A Digital Voltmeter, a HP 3495A scanner, a HP 98035 Real Time Clock and a HP 7245 Printer/Plotter.

(2) Temperature Measurement

The wall temperature distribution was measured with thermocouples, T-type (S.W.G 30), placed along the test cylinders. For the measurement of the radial temperature distribution, a traversing thermocouple probe made of 36 S.W.G. "T" type (copper-constantan) thermocouple was mounted across the 1.9 mm gap of the "fork" shape, made of electrically non-conducting vinyl rod.

(3) Heat Flux Measurement

The wall of the test cylinder acts as a resistance heating element. Because of the high electric current required, the electrical power to the test heater tube was supplied via two transformers; a power-stat transformer (variable transformer, 13.4 KVA, Superior Electric Co.), and a step-down transformer (Dry Type, 15 KVA, Marcus Co.). The power dissipated in the test cylinders was determined by measuring the electric potential drops and currents individually along the test section. For the measurements of the electrical potential drops, the wires of the wall thermocouples were used.

4.1.3 Data Reduction

In measuring the local temperature of the fluid flow, the hot junction of the thermocouple-probe senses the temperature difference from the actual temperature at that point. For computing the true temperature of the air from the reading of a thermocouple probe placed in the air stream with a given heat flux at the wall, the convection heat transfer between the fluid and the hot junction of a thermocouple probe, the radiation heat transfer between the hot junction and the wall, and the conduction heat transfer along the thermocouple wires, should be considered.

For the heat transfer study, the power input to the test cylinder was regulated so that the difference between the average surface temperature and the free-stream air temperature was between 15 - 20°C. At the location on the cylinder wall where the maximum heat transfer rate occurred, the temperature difference was only about 6-7°C. With the uncertainties in the temperature measurements, the corresponding uncertainties in the Nusselt number were about ±1 %.

Because of axial heat conduction due to the different flow regimes, the condition of constant heat flux is no longer applicable, especially at the small value of x, even with electrical resistance heating. Local heat transfer, therefore, was deduced from the following Eq. (4.1), which was obtained from the energy balance made on the elements of the test cylinders.

$$h_x = \frac{\left(\dot{q} + k\dfrac{d^2T}{dx^2}\right)b}{(T_w - T_\infty)} - \epsilon(T_w^2 + T_\infty^2)(T_w + T_\infty) \tag{4.1}$$

where b is the wall thickness and ϵ is the emissivity. The values of the second derivatives of temperature were determined from the experimental results of the axial temperature distributions. The maximum error introduced in the final value of the heat transfer coefficients, by neglecting the axial heat conduction was less than 1%. The maximum effect of radiation was seen to be about 0.4%.

4.1.4 Experimental Results

(1) Velocity Distribution

The results of dimensionless velocity profiles at a fixed value of x as a function of radius, R_i, from the experimental results of Willmarth et al. [31] and Lee and Kim [45,46] are summarized in Tables 4.2. In Fig 4.2, velocity profiles are plotted as the dimensionless velocity, u^+, versus the dimensionless radial distance, y^+ for the two different radii of the circular cylinders, R_i: 0.51 mm and 25.4 mm at free stream velocity, u_∞ (= 15 m/s). Theoretical results are also included in this figure for comparison.

(2) Local Skin Friction Coefficient

The skin friction coefficients and local Reynolds numbers were calculated from the definitions:

$$C_{f,x} = \frac{\tau_{w,x}}{\frac{1}{2}\,\rho\, u_x^2} \tag{4.2}$$

and

$$Re_x = \frac{x\, u_\infty}{\nu} \tag{4.3}$$

The skin friction coefficient was deduced by curve fitting data obtained from the velocity measurement to Rao's "law of the wall" [38] given as:

$$u^{+} = \frac{1}{k}\ln\left[R_i^{+}\ln\left(\frac{r^{+}}{R_i^{+}}\right)\right] + C \tag{4.4}$$

The deduced results of skin friction coefficients for a range of the Reynolds number based on the axial distance Re_x from the experimental results of Lee and Kim [45,46] are summarized in Table 4.3. Fig 4.3 is the plot of the local skin friction factor deduced from the experimental data for the three different radii of circular cylinders, R_i: 6.35 mm, 12.7 mm, and 25.4 mm at free stream velocity, u_∞ (= 15 m/s).

(3) Temperature Distribution

The deduced results of temperature profiles at a fixed value of x as a function of radius, R_i, from the experimental results of Lee and Kim [45,46] are summarized in Table 4.4. The plot of the dimensionless temperature distribution for the circular cylinder with 6.35 mm radius at free stream velocity, u_∞ (= 30 m/s), is shown in Fig. 4.4. The theoretical results are again shown in the figure for reference. In Fig 4.5, the temperature profiles are plotted for three different turbulent Prandtl numbers, Pr_t: 1.0, 0.9, and 0.8, respectively.

(4) Local Nusselt Number

The local Nusselt number is defined as:

$$Nu_x = \frac{h\,x}{k} \tag{4.5}$$

The deduced results of the local Nusselt number for a range of the length Reynolds number Re_x from the experimental results of Lee and Kim [45,46] are summarized in Table 4.5. Fig 4.6 is the plot of experimental local Nusselt numbers deduced from experimental data for the two different radii of the circular cylinders, R_i : 6.35 mm and 25.4 mm at free stream velocity, u_∞ (= 30 m/s).

4.2 Fully Developed Turbulent Fluid Flow and Heat Transfer in a Concentric Annular Duct

The objective of this particular experimental study is to determine experimentally the effects of the transverse convex surface curvature for fully developed turbulent fluid flow and heat transfer in concentric annular ducts. The velocity profiles, friction coefficients, temperature profiles, and Nusselt numbers were obtained. The experimental data were compared to the theoretical analysis results demonstrated in Chapter 3.

To test the validity of the experimental apparatus, a series of tests on a pipe without any inner core tubes were carried out, and the data obtained were carefully examined against the existing correlations for circular tubes to establish confidence in the apparatus. Then, three annuli having three different inner radii, R_i = 16.7 mm, 8.57 mm and 3.98 mm, with the same fixed radius ratio, α, of about 0.3, were studied over a Reynolds number range of about 20,000 to 60,000 with air as the working fluid. All the experimental work was carried out under steady-state conditions which were usually attained in about one to two hours. Most of the tests were run a second time to confirm the reproducibility of the experimental results.

The main annulus assembly and instrumentation used in this present investigation are described in the following sections. Some details of the calibration methods for the orifice, pitot tube and thermocouples are also described.

4.2.1 Apparatus

The main annulus assembly is schematically shown in Fig. 4.7. The essential dimensions are included in Table 4.6.

The available hydrodynamic equivalent dimensionless test length, x/De, should be long enough to ensure fully developed turbulent flow both hydrodynamically and thermally. The hydrodynamic entrance lengths are supposed to be about 30 to 50 equivalent diameters for the ranges of the radius ratios and Reynolds numbers covered in the present study according to the related literature [56, 96-98]. The test-section lengths of the present annulus assemblies were between about 70 and 100 equivalent diameters so that they were considered long enough to reach fully developed turbulent flows .

In Fig. 4.8, air was drawn through a flow measuring orifice, 8 cm orifices [100], into a settling chamber and through a bell-mouthed contraction section into the test section by a blower located at the end. The settling chamber consisted of filters, screens and flow straighteners. The screens were made of 2.0 mm mesh. The bell-mouthed section was machined from a 30.5cm x 30.5 cm x 20.3 cm Plexiglas block. The two blower fans used were rated 0.9 m^3/min and 8.5 m^3/min. at 50.8 cm of water gage static pressure. The details of the entrance section are shown in Fig. 4.9.

Along the test section, provisions were made for the measurements of pressure drops and velocity and temperature fields at various sections. The locations of the measuring sections and static pressure taps for each test section are shown in Figs.4.10 and 4.11. Shown in Figs. 4.12 and 4.13 are the positions of the thermocouples embedded in the wall of the three core tubes. A specially designed traversing mechanism as shown in Fig.4.14 carried the measuring instruments: a pitot-static tube and a thermocouple-probe for the measurement of the local velocity and temperature profile, respectively. With this mechanism, the radial displacement of the probe was measured within 0.025 mm by a position gage (Starret model No. 25-4041).

The electrically heated core tubes were supported at three points by electrically insulated three-point carriers at four places along the outer tube. The predicted deflection rate was to be less than 2% with four supporters (see Appendix E). The carriers provided radial adjustment of the core tubes are shown in Figs. 4.15 and 4.16 which illustrate the details of the wire and the rod support mechanisms, respectively. In Fig. 4.15 (a), a stainless-steel wire (piano wire gage 30) was provided to hold the rod to reduce flow disturbance in the flow region. For the latter, a revolving steel ball was provided at the tip of each rod support to allow for the axial thermal expansion of the core tube when it is heated. The position of the core tube against the outer tube was determined by depth micrometer gauge (Starrett) through the several openings provided along the length and around the circumference of the outer tubes. In this way, the maximum eccentricity measured was found to be less than 3% (see Appendix E). An eccentricity caused by the deflection of the inner core was negligible because an eccentricity of less than 3% was seen not to affect the flow and heat transfer characteristics for the fully developed turbulent region of the concentric annular duct [4,96].

To reduce axial misalignment, all the flanges were clamped together for drilling and reaming simultaneously during the manufacturing stage. The entire outside sections of the outer tubes were covered with fibreglass insulation to reduce the radial heat loss. The heat loss through the insulation was measured by means of heat-meters consisting of two thermocouples whose junctions were set at a known radial distance apart. Also, provision was made for checking the amount of the conduction heat loss from the core heater tube to the electric lead cable. Three pairs of thermocouples were at known position on the cable near each tube end.

The assembled test section was mounted horizontally on four movable carbon-steel supports. Provision was made on the feet of these supports to provide a fine adjustment of height by screw mechanisms. The horizontal alignment of the whole assembly was accomplished by adjusting these screw mechanisms and was checked by a surveying level. The maximum misalignment was less than ±5 mm for each test section.

There were three different diameters of outer tubes used in this experiment. To connect between the settling box and the outer tube, conical diffusers were manufactured. The angle of the conical diffuser was less than seven degrees to reduce the effect of the flow separation [80]. To reduce the vibration effect from the blower, a conical diffuser and a flexible tube were used to connect the annular duct assembly to the blower as shown in Fig. 4.7.

Having the apparatus assembled, all the outside sections of the outer tube were wrapped with 2.54 cm thickness fibreglass to reduce the radial heat leakage. The heat leakage was measured with a heat meter made of thermocouples, T-type S.W.G. 30, described in Section 4.2.2.2. For boundary layer tripping, two steel wires of A.W.G. 11 and A.W.G. 24 were used.

The inlet geometry, as shown in Fig. 4.7, was constructed to correspond as close as possible to the idealized model illustrated in Fig. 4.17.

4.2.2 Instrumentation

4.2.2.1 Pitot Tube and Pressure Measurement Systems

A pitot tube was manufactured from a stainless steel hypodermic needle (1 mm O.D. and 0.7 mm I.D.) as shown in Figs. 4.18 (a) and (b), and was used for flow field investigation. To reduce flow interference, making the diameter of the support tube small (3.2 mm O.D., Stainless Steel Tube) was desirable because of the dimensions of the annular passages used in the present study.

To measure the main stream velocity profiles with a pitot tube, measuring ports of 9.5 mm in diameter were provided along the surface of the outer tubes and static pressure taps of 1.6 mm in diameter were also provided. These were made by drilling through the wall from the outside and by carefully removing the burrs on the inside. A length (38 mm) of brass tubing (about 6.35 mm O.D.) was carefully soldered over each hole.

Pressures were read on either a differential micro-manometer (R. Fuess Model F7409) or a long slender manometer (T.E.M. Instruments Limited) depending on the head of the pressure and are shown in Figs. 4.19 (a) and (b). For measuring pressure, only an estimate of the average readout has been made because of the rapid random fluctuations in pressure readouts. The error introduced in this manner was estimated to be less than ± 0.5 % considering the maximum and minimum values of the instantaneous readouts. A micro-manometer in Fig. 4.19 (a) was rated to be accurate within about ±0.025 mm of the manometer fluid and the accuracy of the slender long manometer in Fig. 4.19 (b) was ±0.06 mm. The specific gravity of the manometer fluid (95 % alcohol) used was 0.81.

4.2.2.2 Temperature Measurement Systems

To measure the radial temperature distribution, enamel and vinyl insulated copper-constantan thermocouples, T-type wires (S.W.G. 30, Omega Inc.), were used to make the thermocouple probe shown in Figs.4.20 (a) and (b), and used with calibrated precision mercury-in-glass thermometers. The junctions of the thermocouple probes were made by arc welding the two ends of wires in a Thermocouple Welder (Model Fisher 416). In the welding process, argon gas was used to prevent oxidation of the junctions of the thermocouples. The thermocouple junction was mounted across the gap of the 1.9 mm fork as seen in Fig. 4.20. A fork was made of vinyl rod to reduce heat transfer via the metal stem of the probe.

To measure the axial wall temperature distribution, 10 - 14 thermocouples were embedded in the wall of the heating core tubes as shown in Figs. 4.12 (a) to (c). To check the possible circumferential variation of the wall temperature, three pairs of thermocouples were installed at both ends of each heating core tube. All the thermocouple junctions along the test heaters were made by using a "split junction" method [99] which is illustrated in Figs. 4.21. By using this method, the shorting of the two thermocouple wires in the tube could be prevented.

The ambient and settling box temperatures were also read using thermocouples. All the thermocouples were connected to the digital thermometers (Omega model DP 460 and Leeds & Northrup Model 914) using two 16 points rotary selector switches (N.R. Model 8248) for convenience and rapidity of temperature measurements.

4.2.2.3 Power and its Measurement Systems

In this experiment, the wall of the inner core tube was used as a resistance heating element. Because of the high electric current required for heating the test heater tube, the power was applied by two transformers; a power-stat transformer (variable transformer 13.4 KVA Super Electric Co.), and a step-down transformer (Dry Type 15 KVA Marcus Co.) as shown in Fig. 4.22. The power supply and instrumentation circuits are illustrated in Fig. 4.23.

The power dissipated in the heated core tube was determined by measuring the voltage drop across the two known points along the test section. For the voltage drop measurement, the copper wires of the wall thermocouples were used. Voltage drops were read by a voltmeter (HP 427A) with full-scale sensitivities ranging from 10 mV to 300 V AC, which was rated with a measuring accuracy of ±2% of full scale and a digital multimeter (Smart 22-183). The digital multimeter (Smart 22-183) was used to measure the electric current of the heater core tube using current transformer (GE JP-1) due to its high current flow (up to 1000 Amp.).

4.2.2.4 Orifice Plate

To measure the mean velocity in each run, a B.S. 8 cm orifice [100] was manufactured. An orifice was calibrated against a pitot tube traversing across the annular duct. An orifice plate was placed at the inlet section of the settling chamber as shown in Fig. 4.7.

4.2.3 Calibrations of Instruments

4.2.3.1 Orifice Plate

Mean flow velocities measured from the pitot tube traversing mentioned in Section 4.2.2.4, were used to calibrate the orifice. Velocity distribution measurements were taken from about twenty cross-sections of the channel (the outer tube only) for a wide range of Reynolds numbers. The results of the calibration are shown in Fig. 4.24. The accuracy of the orifice was estimated as ±1% for the range of Reynolds numbers studied.

4.2.3.2 Thermocouples

Temperature was measured with copper-constantan, T-type wires (S.W.G. 30, Omega Inc.). The thermocouples used in this study were calibrated by means of the "fixed points method" [101]. For calibration, water and ice made of the same distilled water were used as the fixed-points of 0°C and 100°C. A precision mercury-in-glass thermometer set (Fisher Nr.15-155) was used as a secondary thermometer in a constant temperature oil bath that was the part of viscometer (M&LTest Equipment 4510). Measurement error was seen within ±1% and the results of the calibration are shown in Figs.

4.25 (a) and (b).

4.2.4 Experimental Procedure

Before starting the main series of tests, the outer tube only was used to verify the validity of the test apparatus without any inner core tube. The main purposes of this initial procedure were: (i) to test the apparatus by checking the friction and velocity data for the fully developed turbulent flow against well-established circular tube data, and (ii) to establish a basis for comparison of the data which would be obtained in subsequent experiments.

After the apparatus was assembled and aligned, the concentricity of the inner core in relation to the outer tube was checked by depth micrometer gauge (Starrett). The core tubes were supported by three-point carriers as previous mentioned so that radial adjustments of the inner core tubes were accomplished. The maximum eccentricity was about ±0.5 % for the test section 2 (see Appendix E). Therefore, the eccentricity due to the lack of straightness of the inner core tube was seen to be negligible.

4.2.4.1 Preliminary Test

The outer tubes of the annulus assemblies were used without any inner core tube. The tests were run under steady state conditions. The temperatures in the room and the settling box were read via the digital thermometers (Omega model DP 460 and Leeds & Northrup Model 914).

The velocity profiles were measured with a Pitot-static tube at Reynolds numbers of about 20,000 and 40,000 in each channel.

Pressure drop data were obtained from the pressure taps. Velocity profiles and friction factors at each test section were measured by the static pressure taps and pitot tube for a range of Reynolds number from about 20,000 to 50,000. The experimental results of the friction factors in the fully developed region of a circular tube compared against the Blasius equation [26] are shown in Fig. 4.26.

4.2.4.2 Velocity Profile and Pressure Drop Measurements

Before making any measurements for the velocity profile, the apparatus should reach steady-state conditions until the reading of the manometer on the orifice does not change. It took about one hour to reach the steady-state.

The velocity profiles were measured with a Pitot-static tube at a Reynolds numbers of about 20,000 and 40,000 in each annular duct. The Pitot-static tube was corrected near the walls to compensate for the effects of velocity gradient error. The details of the correction are given in Section 4.2.5.

The pressure drop data were obtained over the entire accessible range of Reynolds numbers which depended on the capacity of the blower. The manifolds for the pressure taps were arranged so that the pressure difference between two desired pressure taps could be measured. To obtain the data for the fully developed turbulent flow, the data of pressure drop were taken in the region where there was no significant variation in pressure gradient. To check the reproducibility of the experimental data, tests were often repeated.

4.2.4.3 Temperature Profile Measurement

Power was supplied to the inner core tube for heating and was adjusted so that the temperature difference between the walls of core tubes and the inlet air was about 20 - 50°C. The power dissipated was determined by measuring the electric potential drops and current individually along the test section. For the measurement of the electrical potential drops, the three wires of the wall thermocouples were used and were recorded.

Before making measurements for the temperature profiles, the apparatus should reach thermally steady-state conditions; i.e., the reading of temperature in the inner tube wall should not change as a function of time. It took about one hour to reach a thermal steady-state. The room temperature and the temperature in the settling chamber were checked every 10 minutes and the room temperature was maintained relatively constant by adjusting the room ventilation system. The average temperature variation in the room was within ± 0.5°C during the period of each test.

All temperatures were recorded from thermocouples and thermocouple-probes via the digital thermometers in conjunction with a precision mercury-in-glass thermometer. The electrical potential differences along the thermocouple locations were also recorded.

During the test, when the heat flux was changed, getting the potential difference between the two known locations was difficult because of the fluctuation in the main electricity current. Therefore, if the temperature change of the core wall was more than 0.5°C, the test was repeated.

The temperature profiles across the channel were measured with a thermocouple-probe made for this study at a Reynolds number of about 20,000 and 40,000 for each annular duct. Some measurements were repeated to check the reproducibility of the experimental data.

4.2.5 Reduction and Correction of Experiment Data

4.2.5.1 Thermocouple Probe

When a thermocouple probe is placed in an annulus to measure the local temperature of the fluid flow, the hot junction of the thermocouple-probe senses a temperature different from the actual temperature in that point. For computing the true temperature of a fluid from the reading of a thermocouple probe placed in a fluid flow of an annular passage with a given heat flux at the wall, the following corrections must be made for:

(i) the convection heat transfer between the fluid and the hot junction,

(ii) the radiation heat transfer between the hot junction and the wall, and

(iii) the conduction heat transfer along the thermocouple wires.

If the conduction heat loss along the thermocouple wires is negligible compared with the convection and radiation heat transfer, then the following energy balance can be made for the hot junction:

$$h\,A\,(T_{fluid} - T_{junction}) = \sigma\,A\,F_{\epsilon}\,F_{g}\,(T_{w}^{4} - T_{junction}^{4}) \tag{4.6}$$

where

h = convection heat transfer coefficient from the fluid to the hot junction

A = surface area of the hot junction

σ = Stefan-Boltzmann constant (5.669 x 10^{8} W/m^2 K^4)

F_{ϵ} = surface emissivity of the hot junction

F_g = radiation geometry factor

The value of $h_{junction}$ can be calculated from a simplified equation for the heat transfer from a small cylinder transverse to a fluid flow [102] gives as:

$$h = 0.11\, c_p\, G^{0.6} / D^{0.4} \tag{4.7}$$

where

G = mass flow rate of the fluid, i.e., air

D = diameter of a hot junction

As an example, for the experiment of Test Section 1 (Re = 26,000), where the velocity was 7.5 m/sec at y = 0.96 cm, the temperature reading was 20°C and the wall temperature was 43.5°C. The diameter of the junction was about 0.1 mm. Then, the heat transfer coefficient, $h_{junction}$, calculated from Eq. (4.7) was 426 W/m^2°C. Assuming that the emissivity, F_ϵ, of the oxidized thermocouple junction is 0.5 and the area factor, F_g, is unity (the maximum error), the thermocouple error for the above example was:

$$(T_{fluid} - T_{junction}) = 0.5 \times 5.669 \times 10^{-8} \times (316.5^4 - 293^4) / 426 = 0.17\ ^\circ C$$

Although the thermocouple error in the present study will vary at different radial positions and at different Reynolds numbers, the order of the error is about the same as that given for the example above. Therefore, it can be ignored.

The error due to the conduction along the thermocouple wires has been studied by Schneider [102]. Lee [65] reported that the errors at y = 0.2 and 0.5 mm were about 0.4°C and 0.17°C, respectively for his experiments with $\alpha = 0.6$ and Re = 40,000. To reduce the conduction heat loss along the thermocouple wires in the present study, the hot junction was mounted across the gap of a fork made of a vinyl rod. The error from the conduction loss was assumed to be negligibly small.

4.2.5.2 Heat Losses

The heat flux from the core tube wall was corrected for the radiation heat loss and the heat leakage through the insulation of the outer tube and through the electric lead wires. The radiation heat flux q between the hot core surface and the outer tube wall can be estimated by the following equation:

$$q = \frac{\sigma}{(1/\epsilon_1) + (A_1/A_2)(1/\epsilon_2 - 1)} (T_2^4 - T_1^4) \tag{4.8}$$

where

A = surface area of the core or outer tube

σ = Stefan-Boltzmann constant (5.669×10^{8} W/m^2 K^4)

ϵ = surface emissivity

For the experiment of the test section 2 (Re = 43,000), where $T_1 = 43\,°C$, $T_2 = 26°C$ and ϵ_1 = 0.074 for polished stainless steels and $\epsilon_2 = 0.052$ for commercial polished coppers [103], the radiation heat flux q calculated from the above equation is about 50.5 W/m^2. Since the heat flux by electric power of the heater core was about 1,457 W/m^2, the heat loss due to the radiation effect was about 3%.

The heat leakage through the insulation of the outer tube was determined by measuring the conduction heat transfer through the fibre glass insulation. Two thermocouples whose hot junctions were set one inch apart were used to obtain the radial temperature gradient across the 2.54 cm thick insulation. Three such pairs were used at known positions along the insulation and the average radial temperature gradient was obtained.

The conduction heat flow rate, q, through a hollow cylinder is:

$$q = \frac{2\pi k L}{\ln(R_o / R_i)} (T_i - T_o) \tag{4.9}$$

For the above experiment, the heat loss calculated was approximately 1.5 W and the electric power to the test section was about 967 W. The loss due to conduction through the fibre glass insulation was, therefore, about 0.15 %. The heat leakage through the electric lead wire was calculated from the measured temperature gradient. Three thermocouples were placed 30 cm apart into the lead wire surface. The heat loss calculated from the simple heat conduction equation was usually less than 0.3 W. The heat fluxes used to calculate the heat transfer coefficients were corrected for these heat losses: radiation, conduction through the insulation, and conduction through the lead cable.

4.2.5.3 Pitot Tube

The pitot tube is used to measure the velocities of fluid flow. Certain errors arise because the effective center of the tube does not coincide with the geometric center. These displacement effects are due to the shear stress of the wall. A study of the displacement effects on circular pitot tubes has been made by MacMillan [104], and for rectangular mouthed pitot tubes by Quarmby and Das [105]. Their results for the displacement effects on a set of five rectangular mouthed pitot tubes of a constant thickness ratio 0.6 show that the displacement, Δ, due to shear stress, is given by:

$$\frac{\Delta}{b} = 0.19 \pm 0.01 \tag{4.10}$$

where

Δ = displacement toward the region of higher velocity

b = outside thickness of pitot tube.

When this relation was applied to the pitot tube used for the velocity measurements in the present study, the effective displacement was about 0.1 mm. Young and Maas [106] have introduced a displacement of the effective core center, Δ, occurred toward the higher velocity region. They presented the following empirical relation for the effective displacement, Δ:

$$\begin{aligned} \frac{\Delta}{D_o} &= 0.18 && \textit{where} \quad \frac{D_i}{D_o} = 0.6 \\ \frac{\Delta}{D_o} &= 0.131 + 0.082\,\frac{D_i}{D_o} && \textit{where} \quad 0 \le \frac{D_i}{D_o} \le 1 \end{aligned} \tag{4.11}$$

where

$$\frac{D_o}{p} \cdot \frac{dp}{dx} = 0.1 - 0.2$$

and p is the impact pressure of the stream at the geometric center. When this relation was applied to the pitot tube used for the velocity measurement, the effective displacement was about 0.1 mm away from the wall and the calculation of the maximum error was less than 1% [65].

4.2.6 Uncertainty Analysis

A method used here for estimating uncertainty in experimental results was presented by Kline and McClinton [107]. The method is based on a specification of the uncertainties in the various primary experimental measurements.

Suppose a set of measurements is made and the uncertainty in each measurement may be expressed with the same odds. These measurements are used to calculate some desired result of the experiments. Therefore, the calculated uncertainty is based on the uncertainties in the primary measurements. The result R is a given function of the independent variables: $x_1, x_2, x_3, \cdots\cdots, x_n$. Thus

$$R = R\,(x_1, x_2, x_3, \cdots\cdots, x_n) \tag{4.12}$$

Let w_R be the uncertainty in the result and $w_1, w_2, w_3, \cdots\cdots, w_n$ be the uncertainties in the independent variables. If the uncertainties in the independent variables are given with the same odds, then the uncertainty in the result having these odds is given as:

$$w_R = \left[\left(\frac{\partial R}{\partial x_1} w_1\right)^2 + \left(\frac{\partial R}{\partial x_2} w_2\right)^2 + \cdots\cdots + \left(\frac{\partial R}{\partial x_n} w_n\right)^2\right]^{\frac{1}{2}} \tag{4.13}$$

4.2.6.1 Uncertainty in Friction Coefficient

The definition of friction factor, f, is

$$f = \frac{\tau}{\frac{1}{2}\rho \bar{u}^2} \tag{4.14}$$

The shear stress calculated from the measured pressure drop over the test section and its accuracy was within ± 1% : an accuracy of the micro-manometer used was about 0.2 % and the reading error was about 0.7%. The average velocity was calculated from the flow rate measured by the orifice plate located in front of the test apparatus. From the calibration curve shown in Fig. 4.24, the accuracy of the average velocity was taken to be ± 1.5 %. The uncertainty of the density was estimated as ± 1% [65].

From Eq. (4.13), the uncertainty in the friction coefficient can be expressed in the dimensionless form as:

$$\left(\frac{w_R}{R}\right)_f = \left[\left(\frac{w_\tau}{\tau}\right)^2 + \left(\frac{w_\rho}{\rho}\right)^2 + \left(\frac{2\,w_{\bar{u}}}{\bar{u}}\right)^2\right]^{\frac{1}{2}} \tag{4.15}$$

Therefore, the uncertainty in the friction coefficient was about ±3.3 % from Eq. (4.15).

4.2.6.2 Uncertainty in Reynolds Number

The definition of the Reynolds number in a concentric annulus is:

$$Re = \frac{De \cdot \bar{u}}{\nu} \tag{4.16}$$

For the equivalent diameter, De, the uncertainty was about ±0.2 %. The uncertainty for estimating dynamic viscosity, ν, was ± 1.5 % [65]. The uncertainty in Reynolds number can be expressed in the non-dimensional form as:

$$\left(\frac{w_R}{R}\right)_{Re} = \left[\left(\frac{w_{De}}{De}\right)^2 + \left(\frac{w_\nu}{\nu}\right)^2 + \left(\frac{w_{\bar{u}}}{\bar{u}}\right)^2\right]^{\frac{1}{2}} \tag{4.17}$$

The uncertainty in the Reynolds number was estimated from Eq. (4.17) to be about ±2.2 %.

4.2.6.3 Uncertainty in Nusselt Number

The definition of the Nusselt number is

$$Nu = \frac{h \cdot De}{k} = \frac{q_w \cdot De}{k\,(T_w - T_b)} \tag{4.18}$$

where

$$T_w - T_b = T_w - \left(T_{air} + \frac{2\pi R_i \cdot L \cdot q_w}{\rho \cdot c_p \cdot Q}\right)$$

The uncertainty in the Nusselt number can be expressed in the non-dimensional form as:

$$\left(\frac{w_R}{R}\right)_{Nu} = \left[\left(\frac{w_{De}}{De}\right)^2 + \left(\frac{w_{q_w}}{q_w}\right)^2 + \left(\frac{w_k}{k}\right)^2 + \left(\frac{w_{T_w - T_b}}{T_w - T_b}\right)^2\right]^{\frac{1}{2}} \tag{4.19}$$

and

$$\left(\frac{w_R}{R}\right)^2_{T_w - T_b} = \left(\frac{w_{De}}{De}\right)^2 + \left(\frac{w_{R_i}}{R_i}\right)^2 + \left(\frac{w_L}{L}\right)^2 + \left(\frac{w_{q_w}}{q_w}\right)^2 + \left(\frac{w_k}{k}\right)^2 + \left(\frac{w_\rho}{\rho}\right)^2 + \left(\frac{w_Q}{Q}\right)^2 + \left(\frac{w_{T_w}}{T_w}\right)^2 + \left(\frac{w_{T_{air}}}{T_{air}}\right)^2 \quad (4.20)$$

The thermal conductivity, k, of air is known to be within ± 2 % and the specific heat at constant pressure, c_p, could be evaluated to a high accuracy and was ignored [65]. The uncertainties in the radius, R_i, and length, L, were about ± 0.2%. The uncertainty in the flow rate measurement, Q, was about ± 1.5% and that in the fluid density was ± 1.0 %.

The uncertainty in the inlet temperature measurement, T_{air}, was estimated to be about ± 1%. The wall temperature at the test section was measured by 10-14 thermocouples, and the average value was used in the calculation. The uncertainty in the wall temperature, T_w, was about ± 0.5 % including the instrument error.

The wall heat flux, q_w, was calculated from the power input with a correction for the heat leakage to the surroundings. The uncertainty in the wall heat flux was about ± 4 % including the uncertainties in the input transformer, step-down current transformer, digital voltage metre, core tube wall thickness and length.

Considering the given numeric values of uncertainties, the uncertainty of (T_w - T_b) was about ± 4.4 % from Eq. (4.20). Therefore, the uncertainty in the Nusselt number is about ± 6.3 %.

4.2.7 Experimental Results

4.2.7.1 Velocity Distribution and Friction Coefficient

Velocity distributions were obtained for a range of Reynolds number between about 20,000 and

60,000 in concentric annular ducts with two different radii, R_i = 16.7 mm and 8.57 mm, respectively, with a fixed radius ratio of $\alpha = 0.3$. Experimental Reynolds numbers were based on the "equivalent diameter", De, and the observed mean velocity. To obtain the mean velocity, the local velocity profiles measured were integrated around the annular cross-section and divided by the cross-sectional area of the concentric annular duct. While measuring the local velocity, the pitot tube could not sense the stagnation pressure at the centre of the pitot tube near solid walls. The correction of data for this is discussed in Section 4.2.5.3.

Figs 4.27 (a) through (d) and Figs. 4.28 (a) through (d) are some plots of the measured velocity profiles obtained for the radius ratio of $\alpha = 0.3$ with R_i = 16.7 mm and 8.57 mm, respectively, where the dimensionless velocity, u^+, is plotted versus the non-dimensional distance between the inner core tube and the outer tube, $(r - R_i) / (R_o - R_i)$, respectively. The effects of Reynolds numbers on velocity distributions can be deduced from these figures.

Velocity distributions taken in the inner and outer regions of each annular duct, for the radius ratio of $\alpha = 0.3$ with R_i = 16.7 mm and 8.57 mm are also plotted in Figs. 4.29 and 4.30, respectively.

The radius of the maximum velocity, r_m, in the concentric annular duct is important for calculating the wall shear stress. However, the flatness of the velocity profiles in the vicinity of the maximum velocity makes it difficult to find r_m accurately. For measuring r_m, a double pitot tube was manufactured from two stainless steel hypodermic needles (1 mm O.D. and 0.7 mm I.D.) that were 1.5 mm apart as shown in Fig. 4.18 (b). The location of the maximum velocity could be found by measuring the pressure difference between pitot tubes, and finding the location where the pressure difference was zero. It was, however, difficult to determine the precise location of the maximum velocity due to the fluctuation of pressure [67]. For comparison, the radius of the maximum velocity was calculated from the velocity distributions. The velocity gradient, du/dy, was computed by Lagrangian interpolation of polynomials [108]. The typical velocity gradient curves in the vicinity of the maximum velocity are shown in Figs. 4.31. In Fig. 4.32, the radii of maximum velocities obtained from experimental and theoretical results with a inner core radius of 16.7 mm and 8.57 mm, are plotted for a Reynolds number of 26,000.

In Figs 4.33 through 4.35, the measured friction factors are plotted for three different radii of inner cores, R_i = 3.98 mm, 8.57 mm, and 16.7 mm, respectively, with a fixed radius ratio of $\alpha = 0.3$. The results of the present analysis are also included in these figures for comparison. In Fig. 4.36, the effect of transverse convex curvature on the friction coefficient for two different radii, R_i = 16.7 mm and 8.57 mm is shown together with the theoretical results.

4.2.7.2 Eddy Diffusivity for Momentum

The experimental eddy diffusivities for momentum, ε_M, for fully developed turbulent flows in concentric annular ducts were evaluated from the velocity profiles and pressure gradients obtained experimentally.

The dimensionless eddy diffusivity for momentum, ε_M/ν, can be expressed as:

$$\left(\frac{\varepsilon_M}{\nu}\right)_j = \left[\frac{(\tau/\rho)_j/\nu}{(du/dr)_j}\right] - 1.0 \qquad (4.21)$$

and the wall shear stress from the measured pressure gradient can be calculated by:

$$\tau_j = (dp/dx)\left|\frac{r_m^2 - R_j^2}{2R_j}\right| \qquad (4.22)$$

From Eqs. (4.21) and (4.22), the experimental value of ε_M/ν can be calculated from the velocity distributions and measured pressure gradients. In the vicinity of the maximum velocity, it is difficult to obtain the accurate velocity gradients, because the local velocity gradients becomes nearly zero. To obtain the gradients of velocity distribution, the Lagrangian interpolation of polynomials [108] was used to obtain the velocity gradients in the vicinity of the maximum velocity.

In Fig. 4.37, the experimental eddy diffusivities for momentum are plotted for a Reynolds numbers of 26,000 and 44,000 with inner core radius, R_i, of 16.7 mm with a fixed radius ratio, α of about 0.3 with the predicted results. Experimental eddy diffusivities for momentum at the Reynolds numbers, Re: 26,600 and 48,000 for the inner core radius, R_i, of 8.57 mm with a fixed radius ratio, α (about 0.3), are also plotted in Fig. 4.38 with the theoretical results.

The effect of the transverse convex curvature in terms of R_i on the eddy diffusivity for momentum are plotted in Figs. 4.39 and 4.40 for two different radii, R_i = 16.7 mm and 8.57 mm with Reynolds numbers of 26,000 and 47,000, respectively.

4.2.7.3 Temperature Distribution and Nusselt Number

In Fig. 4.41, the temperature distributions are plotted with non-dimensional temperature, T^+, versus non-dimensional radial distance, $(r - R_i) / (R_o - R_i)$, for Prandtl number 0.71 and the radius ratio, α (= 0.3) with R_i ; 16.7 mm and 8.57 mm, respectively. The results from the present analytical results are also included in these figures for comparison.

Fig. 4.42 shows the effect of the transverse convex wall curvature on the temperature profile for the inner radii, R_i, of 16.7 mm and 8.57 mm at the given Reynolds numbers and Prandtl number 0.71.

In Figs 4.43 through 4.45, the Nusselt numbers deduced from Eq. (3.86) are plotted for three different radii of inner cores, R_i = 3.98 mm, 8.57 mm, and 16.7 mm, respectively, with a fixed radius ratio of $\alpha = 0.3$, having Pr = 0.71. The Nusselt numbers for two different inner core radii, R_i = 3.98 mm and 8.57 mm with Pr = 0.71 are plotted along with the theoretical results in Fig. 4.46. Fig. 4.47 shows the effect of the transverse convex wall curvature on the Nusselt number for three different Reynolds numbers with Prandtl number 0.71.

CHAPTER 5
DISCUSSION OF RESULTS

5.0 General Overview

The characteristics of turbulent flow and heat transfer can be evaluated through theoretical and experimental studies. In the present study, the effect of transverse convex curvature on the fluid flow characteristics with regard to the velocity profile, friction coefficient, eddy diffusivity, temperature profile, and heat transfer coefficient were investigated for both: (i) the turbulent boundary layer flow and heat transfer on heated circular cylinders and (ii) the fully developed turbulent flow and heat transfer in concentric annular ducts with smooth surfaces for uniform heat generated within the heated boundary.

In the analytical study, i.e. Chapter 3, the analytical results are obtained through a mathematical model for turbulence models based on a <u>variable von Kármán constant, κ_i</u>, proposed for the first time in the present study. The standard k-ε turbulence model applied to concentric annuli is also investigated.

An experimental study as given in Chapter 4 has been also conducted on the effects of the inner radius, R_i, with three annuli having different radii of the inner cores: 3.98 mm, 8.57 mm, and 16.7 mm with a fixed radius ratio, α (about 0.3) over a range of the Reynolds number between about 20,000 and 60,000. Air (Prandtl number ≈ 0.71) was used as the working fluid.

For the purpose of clarity, the cases of circular cylinders and concentric annular ducts are individually discussed in this chapter.

5.1 Turbulent Boundary Layer Flows and Heat Transfer over Circular Cylinders

5.1.1 Velocity Distribution

The present theoretical velocity profiles for the turbulent boundary layer flows over circular cylinders with different radii, R_i, of the circular cylinders at a given local Reynolds number are shown in Fig. 3.4. It illustrates that the velocity profiles become flatter as the radius, R_i, becomes smaller, and are always flatter than those of fluid flows over a flat plate at a given local Reynolds.

In the Fig 4.2, the experimental velocity profiles with our theoretical results are plotted for two different radii of circular cylinders, $R_i = 0.51$ mm and 25.4 mm at a given free stream velocity, u_∞ (= 15 m/s). It is seen that there is in a good agreement between the experimental data of Willmarth et. al. [31] and Lee and Kim [45,46] and the present analysis. The velocity profile has the same trend as the analytical results shown in Fig. 3.4. In the Fig. 4.2, the velocity gradient, $(\partial u/\partial y)$, near the wall surface becomes flatter as the cylinder radius, R_i, becomes smaller, and always flatter, than that of the flows over a flat plate at a given local Reynolds number, Re_x. This implies that the thickness of the momentum boundary layer becomes thinner as the value of the cylinder radius, R_i, decreases at a fixed axial position, x, for the same free stream air velocity as shown in the figure. The result also shows that the wall shear stress, τ_w, increases with decreasing cylinder radius, R_i. In the figure, the slope in the logarithmic region of the dimensionless velocity profiles physically represents that the value of the von Kármán constant, κ, increases with a decreasing value of the cylinder radius, R_i. It can be seen that for the ratio of the boundary layer thickness to the cylinder radius, $\delta/R_i \approx O(1)$, the length scale distribution of turbulent eddy which is a function of wall shear stress, τ_w, is strongly affected by the change in the value of the cylinder radius, R_i, i.e., the transverse convex surface curvature.

Consequently, the effect of the transverse convex surface curvature on the velocity development in the normal direction to the wall becomes greater with a decrease in the cylinder radius, R_i. As the radius of the circular cylinder becomes smaller, the diffusion of the turbulent kinetic energy produced at the wall becomes less in the normal direction to the wall than that for the case of two dimensional flow.

5.1.2 Skin Friction Coefficient

The theoretical skin friction coefficients for the turbulent boundary layer flows over circular cylinders for various radii of cylinders, R_i, are given in Fig. 3.5. The local skin friction coefficients normalized by those of the flat plate are also shown in Fig. 3.6. In the figures, it can be seen that, as the radius of the circular cylinder, R_i, becomes smaller, the local skin friction coefficient, $C_{f,x}$, increases. It is also seen that the local friction factor for the turbulent boundary layer flow over a circular cylinder is always higher than that for a corresponding flat plate flow, indicating that $C_{f,x}$ is definitely affected by the transverse convex surface curvature, R_i.

In Fig. 4.3, the experimental skin friction coefficients deduced from the velocity profiles are shown together with that of a flow over a flat plate for a range of Re_x between $5x10^5$ and $2.5x10^6$. There is a good agreement between the experimental data of Lee and Kim [45,46] and the present analysis. It is also seen that the local friction coefficient for the turbulent boundary layer flow over a cylinder is always higher than that for a corresponding flat plate flow and the trend is the same as that of the present analysis shown in Fig. 3.5. The smaller the radius of the cylinder, R_i, i.e., the higher the transverse convex surface curvature, the higher the local skin friction coefficient, $C_{f,x}$. This conclusion is in good agreement with those of Willmarth et al. [31] and Rao [38]. The effect of the transverse convex surface curvature is accentuated at large local Reynolds number, Re_x, and at a transverse convex surface curvature is accentuated at large local Reynolds number, Re_x, and at a small radius of the circular cylinder, R_i. This is more clearly illustrated in Fig. 3.6. It can be seen that the local friction coefficient, C_{fx}, strongly depends upon R_i, and less on the local Reynolds number, Re_x. These trends may be due to the differences in the flow field over a circular cylinder from that over a flat plate, as discussed previously. When the hydrodynamic (momentum) boundary layer thickness is very thin relative to the cylinder radius, i.e. δ/R_i is small, there is a correspondingly small area change across the boundary layer, and the cylinder behaves like a flat plate. On the other hand, when the boundary layer is thick compared with the cylinder radius, R_i, there is a substantial area change and a large difference between the flat plate and the cylinder. Thus, there are two elements involved in establishing the magnitude of the cylinder geometry effect. The first is the boundary layer thickness, δ, and the second is the cylinder radius, R_i, i.e., the transverse convex wall curvature. In the previous figures, the thickness of the boundary layer increases with axial distance rapidly at first and then more slowly far downstream. Therefore, the larger the local Reynolds number, Re_x, the thicker the hydrodynamic boundary layer and the greater the effect of cylindrical geometry. Likewise, the smaller the cylinder radius, R_i, the greater the transverse convex curvature effect, $1/R_i$.

As was seen in the velocity profiles, the velocity gradient, $(\partial u/\partial y)$, near the wall surface becomes steeper as the cylinder radius, R_i, becomes smaller. This means that the turbulence production, $-\rho\overline{u'v'}\,(\partial u/\partial y)$, also increases with a decreasing value of cylinder radius, R_i. And since the longitudinal as well as transverse diffusion terms are negligibly small relative to the production term with local equilibrium (production = dissipation), the skin friction coefficient must increase with decreasing values of the cylinder radius, R_i.

To characterize the effect of the transverse convex surface curvature as discussed in Section 1.1, the Reynolds number based on the cylinder radius, Re_{Ri}, can not characterize the transverse convex surface curvature of a circular cylinder as implied by Patel et al. [2], Sparrow et al. [36], and Cebeci [37]. There are a number of skin friction coefficient data for the turbulent boundary layer flows over the circular cylinders available in the literature, but the attempt to compare them with the present study has failed because of the lack of the pertinent information such as R_i^* and Re_{Ri}. The Re_{Ri} can not itself represent the transverse convex curvature effect as discussed in Section 1.1.

Patel et al. [2] and Cebeci [37] suggested that the effect of the transverse convex wall curvature on the axisymmetric turbulent boundary layer is similar to that of favourable pressure gradients. They also suggested that the velocity profile becomes steeper and the value of the skin friction coefficient, C_f, becomes greater than those over a flat plate when $dp/dx = 0$.

From the present results of both the experiment and the analysis, it can be seen that the skin friction coefficient, C_{fx}, strongly depends upon the radius of the circular cylinder, R_i, i.e., the transverse convex wall curvature and less on the local Reynolds number, Re_x.

5.1.3 Temperature Distribution

In Fig. 3.7, the theoretical temperature profiles for the turbulent boundary layer flows over circular cylinders for different radii, R_i, at a given local Reynolds number are plotted in terms of the dimensionless temperature, T^+, versus non-dimensional radial distance, y^+. The figure illustrates that, for a given Prandtl number, the temperature profiles become flatter as the radius, R_i, becomes smaller, and always flatter than those of fluid flows over a flat plate at a given local Reynolds number.

Fig. 3.8 shows the effect of the Prandtl number on the temperature profiles. It is seen that, as the Prandtl number increases, the effect of the cylinder radius, i.e., the transverse convex curvature, seems to diminish. In the figure, the changes of temperature profiles between the flat plate and circular cylinders are much greater for Pr = 0.7 than for Pr = 1. This is because the thermal boundary layer thickness decreases with increasing Prandtl number. Therefore, the fluids of higher Prandtl number are less susceptible to the effects of the transverse convex curvature, i.e., the cylinder radius, R_i, than for the fluids of lower Prandtl number.

A representation of the temperature profiles obtained from the present analysis and experiment is shown in Fig. 4.4 for R_i (= 6.35 mm), Re_{Ri} (= 6,070) and Pr (= 0.71). It is seen that there is a good agreement between the experimental data of Lee and Kim [45,46] and the present analysis. In such comparison as shown in Fig. 4.4, it is seen that the temperature profiles become flatter with decreasing values of R_i just as the velocity profiles become flatter than those of the flows over a flat plate at a given local Reynolds number. This is because, as was for the case of the momentum transfer discussed in Section 5.1.2, the production term of turbulent heat convection, $-c_p \rho \overline{v'T'} (\partial T / \partial y)$, at a given fixed value of x, becomes greater as the value of cylinder radius, R_i, decreases, resulting in greater heat transfer near the wall surface. These are essentially the same characteristics that have already been discussed for the velocity profiles. It is seen that the agreement between the present analysis and experimental results is very good.

Fig. 4.5 shows the effect of turbulent Prandtl number on temperature profiles. For the present theoretical calculation, the turbulent Prandtl number is set to unity, which was determined from the correlated expression of Gräber [81]. It is seen that agreement between the experimental and the theoretical results is best when the turbulent Prandtl number is unity. As the turbulent Prandtl number decreases, the deviation of temperature profile decreases. This is because the eddy diffusion for heat is greater than that of momentum. Therefore, turbulent heat convection, $-c_p \rho \overline{v'T'}(\partial T/\partial y)$, at a given fixed value of x, becomes greater as the turbulent Prandtl number decreases, resulting in greater heat transfer near the wall surface.

5.1.4 Nusselt Number

The heat transfer in terms of the Nusselt number based on the distance x, Nu_x versus the local Reynolds number, Re_x, at a given Prandtl number of 0.71 from the present analysis is shown in Fig. 3.9 for three different cylinder radii as an illustration. The effect of the transverse convex surface curvature on the Nusselt number is very similar to that for the skin friction coefficient as discussed in Section 5.1.2. The increase in heat transfer under the corresponding flow condition becomes pronounced with a decrease in the transverse convex surface curvature, i.e., R_i, and the length Reynolds number, Re_x. This is more clearly illustrated in Fig. 3.10, where the local Nusselt numbers of the circular cylinders are normalized by that of a flat plate. It can be seen that Nu_x strongly depends upon R_i, and less on the local Reynolds number, Re_x. The effect of the Prandtl number, Pr, combined with that of the transverse convex surface curvature on heat transfer is shown in Fig. 3.11. For the same value of the local Reynolds number, Re_x, it is seen that the normalized Nusselt number increases with an increasing Prandtl number or a decreasing value of the inner core radius. This is understandable because the thickness of the thermal boundary layer decreases with an increasing Prandtl number, Pr or a decreasing R_i.

The experimental results of Lee and Kim [45, 46] are compared with the results of the present analysis in Fig. 4.6 in terms of the local Nusselt number, Nu_x, versus the local Reynolds number, Re_x

for two radii of circular cylinders, 6.35 and 25.4 mm, respectively. The agreement between the present analytical and experimental Nusselt numbers is very reasonable. The results indicate that the effect of the circular cylinder radius, R_i, is very similar to that for the skin friction coefficients, and Nusselt number for the circular cylinder is always greater than that for a flat plate under the corresponding flow conditions. The increase in heat transfer is accentuated at large values of the length Reynolds number, Re_x, i.e., in thick boundary layers and at small radii of cylinder, R_i. The physical interpretation of these trends in heat transfer is the same as that already given in connection with the skin friction results in Section 5.1.2.

5.2 Fully Developed Turbulent Flow and Heat Transfer in a Concentric Annular Duct

In the present study, it has been assumed that the surface of the channel is "hydrodynamically or aerodynamically smooth", because the surface roughness of the channel affects the characteristics of the turbulent fluid flow and heat transfer [26]. To test the validity of the assumption of aerodynamically smooth surface, the friction coefficient data obtained from the tests on the turbulent flows without inner cores were compared against the friction coefficient of Blasius [26] for circular tubes in Fig. 4.26. The friction coefficients were obtained for a range of Reynolds number between about 10,000 and 50,000 for the three circular channels having three different radii, 48.7 mm, 24.6 mm, and 13.0 mm. All experimental works were carried out under the steady-state conditions which were discussed in Section 4.2.4.1. As can be seen in the figure, the friction coefficients obtained from the present experimental data are in a good agreement with the Blasius' correlation for the fully developed turbulent channel flows. This verifies that the surfaces of the channels used in the present study are hydrodynamically smooth.

The entrance length in terms of the equivalent diameters, x/De, are between 50 and 70 at the measured station due to the different lengths of the annuli (see Section 4.2.1). These values are long enough to attain fully developed turbulent flow as compared to the experimental results of 30 to 40 equivalent diameters obtained by other investigators [4,56,62,63]

5.2.1 Velocity Distribution

Velocity profiles were obtained for the fully developed turbulent flows in concentric annular ducts for a range of the Reynolds numbers from about 20,000 to 60,000 with a fixed radius ratio, α (about 0.3), having two different radii of inner cores, R_i = 16.7 mm and 8.57 mm, respectively.

Most of the velocity profiles are plotted as dimensionless velocity, u_j^+, in order to plot all curves on the same basis. For fully developed turbulent flows in concentric annular ducts, since the shear stresses on the walls of both tubes are constant, the friction velocities, u_j^*, for the inner and the outer region of the flow field can be determined. The conventional dimensionless parameters, u_i^+, u_o^+, y_i^+, and y_o^+ can be obtained from these friction velocities.

In Fig. 3.12, the theoretical velocity distributions for three different radii of the inner cores, R_i, at a given Reynolds number are shown where α is kept at 0.3. It shows that in the outer region, the velocity profiles deviate very little from the "logarithmic law" of the circular tube. However, the velocity fields in the inner region deviate with changes in the inner core radius, R_i. The deviation of the inner portion from the outer region is greater with the smaller inner core radius, R_i. This trend is the same as was with the case of the previous turbulent boundary layer flow over circular cylinders given in Section 5.1.1. The deviations of the velocity profiles for the inner region from those for the outer region may be explained as a result of the increase in the effect of the transverse convex wall curvature, R_i, due to the increased radial convexity associated with a decrease in the inner core radius, R_i. For different Reynolds numbers, the theoretical velocity distributions for three different radii of the inner cores are also given in Fig. 3.13. It illustrates that the velocity fields in the inner region also deviate with changes in the Reynolds number.

The effect of the radius ratio, α, on velocity profile is also shown in Fig. 3.14 for two radius ratios at a given Reynolds number of 20,000. It illustrates that the velocity profile in the outer region deviates very little with a change of the radius ratio, α, but in the inner region, the velocity field deviates with a change of the radius ratio. The deviation of the inner portion from the outer is greater with the smaller radius ratio, α, which is generally in accord with the previous studies [4,53,56,62-66,99].

Figs 4.27 and 4.28 are representative plots of the measured velocity profiles together with those of the present analysis obtained for two different radii of the inner cores, R_i : 16.7 mm and 8.57 mm, respectively, having a fixed radius ratio, α, of 0.3 at the given Reynolds number. The figures also show that the approximate position of the shift in the location of the maximum velocity from that for the fully developed turbulent circular duct flow. The shift is increased as the inner core radius, R_i decreases. The agreement of experimental velocity profiles with the theoretical analysis is good for all concentric annular ducts investigated.

In Figs. 4.29 and 4.30, the experimental velocity distributions in u^+ versus y^+ coordinates are plotted for a fixed radius ratio, α, of 0.3 with R_i; 16.7 and 8.57 mm, respectively, at the Reynolds numbers of 26,000, 31,000, 44,000 and 48,000. The experimental results are in good agreement with those of the present analysis, calculated from Eq. (3.59).

Throughout the evaluation of both theoretical and experimental velocity distribution, it is concluded that:

(i) the velocity profile deviates from that of the fully developed turbulent flow in a circular duct with a decreasing value of the inner core radius, R_i, but in the outer region there is hardly any deviation,

(ii) while the effect of the transverse concave surface curvature on the turbulence mechanism is very little, that of the convex surface curvature is seen to be important for transverse convex surfaces, and

(iii) the transverse convex surface curvature is also one of factors to affect the characteristics of turbulent fluid flow in addition to the radius ratio, α, and the Reynolds number, Re.

5.2.2 Radius of Maximum Velocity

One of the major difficulties in the analysis of turbulent fluid flows in annular ducts has been the determination of the shear stress ratio between the two wall surfaces (inner core and outer tube walls), which requires the knowledge of the radius of the maximum velocity. It is also often assumed that the radius of the maximum velocity is the same as the point of zero shear.

The theoretical locations of the maximum velocities calculated from our analysis given as Eq. (3.59) are compared against the empirical correlations of Lamb [52] and Kays and Leung [55] for various radius ratios, α, and are summarized in Tables 3.5 and 3.6. It is seen that the radius of the maximum velocity in the present analysis lies somewhere between Lamb's [52] and Kays and Leung's [55]. Note that Knudsen and Katz [50] and Rothfus et al.[51] have reported that the radius of the maximum velocity for the turbulent flow in annuli is nearly the same as that for laminar flow. However, the radii of the maximum velocity investigated in the present study and by other investigators [53, 56, 62] are less than those for laminar flow.

The velocity gradient curves in the vicinity of the maximum velocity are shown in Figs. 4.31 (a) and (b). The radii of the maximum velocities for two different radii of 16.7 mm and 8.57 mm are shown with the theoretical results and other investigators, Park's [4] and Kays and Leung's [55]. The radii of the maximum velocity in the concentric annuli from the present measurements are less than those of Kays' [55], but greater than Park's [4] (α = 0.27). Park's smaller value may be partially due to the smaller radius ratio, i.e., α = 0.27: as discussed in Section 5.2.1, when α is smaller, the radius of the maximum velocity in a concentric annulus shifts to the inner region. The discrepancy between our values of r_m and those of Kays and Leung [55] could be because their empirical correlation does not consider the effect of the Reynolds number [62].

Fig. 4.32 illustrates the effect of the transverse convex surface curvature, R_i, on the radius of the maximum velocity. As the inner radius, R_i, decreases, the point of the maximum velocity moves toward the inner wall. This is because as R_i decreases, the ratio of the shear stress at the inner wall to that at the outer wall increases as discussed in Section 5.2.1.

5.2.3 Friction Coefficient

The friction coefficients, f, calculated from Eq. (3.75) for two different radii of the inner cores, R_i, with a fixed radius ratio of $\alpha = 0.3$, are shown in Fig. 3.15. It shows that the friction coefficient, f, increases with a decreasing value of the inner core radius, R_i. This implies that as R_i decreases, the shear stress at the inner wall increases for a given Reynolds number at a fixed value of α. This must be due to the fact that, since the velocity gradient, $(\partial u/\partial y)$, near the wall surface for the inner region becomes flatter as the inner core radius, R_i, becomes smaller, the wall shear stress of the inner core, $\tau_{w,i}$, increases with a decreasing value of the inner core radius, R_i, as discussed in Section 5.2.1. The turbulence production, $-\rho\overline{u'v'}\,(\partial u/\partial y)$, increases with a decreasing value of R_i, because the velocity gradient, $(\partial u/\partial y)$, near the wall surface of the inner core becomes flatter with a decreasing value of R_i.

In Fig. 3.16, the effect of the radius ratio, α, on the friction coefficient calculated from the present analysis is also shown for three different values of radius ratios, α, with a fixed R_i. The figure illustrates that the friction coefficient is greater with a larger radius ratio, α, and the trend is in accord with previous studies [4,53,56,62,63,66,99].

In Figs. 4.33 through 4.35, the friction coefficients obtained from measured velocity profiles and pressure drops for the fully developed turbulent flow are plotted for three different radii of inner cores: 3.98 mm, 8.57 mm, and 16.7 mm, respectively, with a fixed radius ratio of $\alpha = 0.3$. The trend is the same as those of the present analysis in Fig. 3.15. The experimental friction coefficients for three annuli having radii of inner cores = 3.98 mm, 8.57 mm, and 16.7 mm with a fixed radius ratio $\alpha = 0.3$, agree with the present analysis very closely. They also show that the friction coefficients for the fully developed turbulent flow in concentric annular ducts are always greater than those of Deissler [8] for the fully developed turbulent pipe flow. In the figure, the results of Park's [4] is less than those of the present analysis, since he used the inner core radius of 23.6 mm which is greater than R_i used in the present experiment. As stated above, as the inner core radius, R_i, increases, the friction coefficient decreases. Therefore, the friction coefficients of Park [4] are less than those of the present study.

Fig. 4.36 illustrates the effect of the transverse convex surface curvature on the friction coefficient for two different radii of 3.98 and 8.57 mm with the fixed radius ratio, α , of 0.3. It demonstrates clearly that the friction coefficient decreases with an increasing value of R_i for the fixed radius ratio. The agreement between the present theory and experiment is very good, considering the difficulties involved in the measurement of the pressure losses in turbulent flows.

5.2.4 Eddy Diffusivity for Momentum

The eddy diffusivity for momentum, ε_M, can be determined as:

$$\varepsilon_M = \frac{\Delta p}{2L} \frac{\left|\frac{r_m^2 - r^2}{r}\right|}{\rho \frac{du}{dr}} - \nu \tag{5.2}$$

To determine the eddy diffusivity for momentum, the pressure gradient and the local velocity gradient for fully developed turbulent flow are required. The pressure gradient was directly determined from the measurement of the pressure drop at the static pressure taps provided along the annular test sections and the local velocity gradient was determined graphically. In the vicinity of the maximum velocity, a large amount of uncertainty in the momentum eddy diffusivity, ε_M, may arise as the radial distance approaches r_m, because the local velocity gradient becomes almost zero at that point.

In Fig. 3.17, the effect of the transverse convex surface curvature on the eddy diffusivity distribution calculated from Eqs. (3.61) through (3.65) is shown for three different radii of the inner cores with a fixed radius ratio of $\alpha = 0.3$, at a given Reynolds number. The figure illustrates that the eddy diffusivity distribution in the outer and inner regions of the annulus has different peak values for each region. It is noted that, in the inner region, the eddy diffusivity for momentum increases with a decreasing value of the inner core radius, R_i, while the change of the eddy diffusivity in the outer region is very little. This implies that, while in the outer region the effect of the transverse concave curvature on the turbulent diffusion is negligible, the effect of transverse convex surface curvature is significant with the change of the inner core radius, R_i. It is seen that the change of the momentum eddy diffusivity distribution in the inner region is due to the increased radial convexity associated with a decreasing inner core radius, R_i.

Fig. 3.18 shows the effect of the radius ratio, α, on the eddy diffusivity distribution for a given Reynolds number at the value of R_i set at 7.5 mm. It seems that the radius ratio, α, has little effect on the relative magnitude of the eddy diffusivity distributions for momentum in the inner and outer regions, although its absolute value increases with an increasing α.

The experimental values of ε_M/ν are deduced from Eq. (5.2) with the measured velocity distributions and pressure gradients. In Figs. 4.37, the eddy diffusivities for momentum are plotted for the Reynolds numbers of 26,000 and 44,000 with the inner core radius, R_i, of 16.7 mm and a fixed radius ratio, $\alpha = 0.3$. The eddy diffusivity distribution for the inner core radius, R_i, of 8.57 mm at the Reynolds numbers of 26,600 and 48,000 are also shown in Figs. 4.38. The inspection of both the theoretical and the experimental results illustrates that the eddy diffusivity distribution for momentum increases to a peak on both regions and decreases near the boundary layer edge, i.e. near the radius of the maximum velocity. Since it is difficult to obtain the velocity gradient accurately in the vicinity of the maximum velocity due to the flatness of the velocity distribution, the experimental result in this region is, therefore, less reliable. However, within both the inner and the outer regions, the agreement between the theoretical and experimental results is reasonably good. In Figs. 4.38 which is for an R_i of 8.57 mm, the peak value of eddy diffusivity for momentum in the inner region is shifted a little to the core wall from that shown in Figs. 4.37, which is for an R_i of 16.7 mm as was seen in the analytical results already shown in Fig. 3.17. The experimental results are, in general, in good agreement with the present analysis except near the vicinity of the maximum velocity, because the velocity gradient becomes indeterminate in that situation. The figures also show that as the Reynolds number becomes greater, the turbulent length scale is greater. This implies that the higher the Reynolds number, the longer the turbulent eddy moving out into the fully turbulent layer from the sublayer.

In Figs. 4.39 and 4.40, the effect of transverse convex surface curvature on the eddy diffusivity for momentum is shown for two different radii of the inner cores, R_i = 16.7 mm and 8.57 mm, respectively, at Reynolds numbers of 26,000 and 47,000. The figure shows that, as R_i becomes smaller, the eddy diffusivity becomes greater. This implies that, as the inner core radius, R_i, is smaller, the turbulent stress, $-\overline{u'\upsilon'}$, becomes greater.

5.2.5 Temperature Distribution

Temperature profiles were measured with a thermocouple probe, which was manufactured for the present study as described in Section 4.2.2.2, at Reynolds numbers of about 20,000 and 50,000 with air as a working fluid (Prandtl number ≈ 0.71) in each concentric annular duct.

Since annuli of different inner core radii, R_i, and radius ratios, α, are considered, the abscissa of the curve in the figures is chosen to be a non-dimensional distance, $(r - R_i) / (R_o - R_i)$, in order to plot all curves on the same basis.

In Fig. 3.19, the effect of the transverse convex surface curvature, $1/R_i$, from the present analysis on temperature distribution is shown for different radii of the inner cores with a fixed radius ratio of $\alpha = 0.3$ and $Pr = 0.71$ for the fully developed turbulent flow in concentric annuli. The figure illustrates that, as the inner core radius, R_i, becomes smaller, the value of the bulk temperature, T_b^+, becomes smaller and always less than that of parallel planes for a given α, Pr, and Re, implying that the turbulent heat transfer becomes more vigorous.

The effect of radius ratio, α, on temperature distribution is also shown in Fig. 3.20 for different radius ratios, α, at a given Reynolds number. The figure shows that the higher the value of α, the higher the bulk temperature, T_b^*. The trend of this result is in a good agreement with other investigators [4, 55, 63]

Fig. 3.21 shows the effect of the Prandtl number, Pr, on temperature distribution at a given Reynolds number of 30,000 with R_i (= 12.5 mm). It depicts that the effect of increasing the Prandtl number is to give a more squared temperature profile, while a low Prandtl number yields a more rounded profile which is similar to that for laminar flow. This illustrates that at higher Prandtl numbers, the thermal resistance is in the sublayer, whereas at a low Prandtl number it is distributed over the entire flow cross section. The reasons for these differences can be seen in the total thermal conductance term in the energy equation, $(1/Pr + \varepsilon_H/\nu)$, where the turbulent and molecular diffusions are seen to depend on the Prandtl number. At a low Prandtl number, the temperature profile is similar to the laminar profile, because the conduction term dominates everywhere. At a higher Prandtl number, the heat is diffused rapidly over the entire fluid. In the figure, it is also seen that at high Prandtl numbers, the temperature distribution is more sensitive to the sublayer diffusivity, and rather insensitive in the outer region.

In Figs. 4.41, a comparison between the present analytical and experimental investigation on the effect of the Reynolds number on temperature distribution is shown for the Prandtl number 0.71, and R_i of 16.7 mm and 8.57 mm, respectively with a fixed radius ratio, α, of 0.3. It illustrates that, as the Reynolds number increases, the production term of turbulent heat convection, $-c_p\rho\overline{\upsilon' T'}(\partial T/\partial y)$, becomes greater, resulting in greater heat transfer near the wall surface. This implies that the effect of increased Reynolds number is to decrease the thickness of the sublayer and increase the eddy diffusivity for heat in the outer region. This conclusion is in a good agreement with the present analysis and other studies [4, 55, 63]. The agreement between the theoretical and experimental results for Pr = 0.71 is good.

The comparison between the present analytical and experimental investigation on the effect of the transverse convex surface curvature on temperature distribution is also shown in Figs. 4.42 for a Prandtl number of 0.71, and R_i = 16.7 mm and 8.57 mm with a fixed radius ratio of $\alpha = 0.3$, respectively, at Reynolds numbers of about 32,000 and 47,000. It illustrates that the smaller the value of the inner core radius, R_i, the smaller the bulk temperature, T_b^*. This is because, as discussed in Section 5.1.3, the production term of turbulent heat convection, $-c_p\rho\overline{v'T'}(\partial T/\partial y)$, at a given fixed value of α, Pr and Re, becomes greater as the value of the inner core radius R_i decreases. It also shows that the effect of the transverse convex curvature in the Fig. 4.42 (b) is more notable than that in the Fig. 4.42 (a). The physical reasoning as discussed in Section 5.2.1 is that the Reynolds number effect is more pronounced for the lower values of the inner core radius, R_i. As may be seen in Figs. 4.42, the agreement between the theoretical and experimental results is good.

5.2.6 Nusselt Number

The analytical results on the effect of the transverse convex surface curvature, R_i, on the fully developed heat transfer coefficients in terms of the Nusselt number for fully developed turbulent flow in concentric annuli are shown in Fig. 3.22. The theoretical Nusselt number are calculated from Eq. (3.86) for two different annuli having different radii of the inner core with a fixed radius ratio of $\alpha = 0.3$, and Prandtl number, Pr = 0.71, at a Reynolds number range between about 10,000 and 50,000. It shows that the effect of the transverse convex surface curvature is similar to the case of the friction coefficient: as the radius of the inner core is smaller, the heat transfer rate is higher. This is because, as discussed in previous Section 5.2.5, the smaller the value of the inner core radius, R_i, the smaller the bulk temperature, T_b^* due to the increase of the production term of turbulent heat convection, $-c_p\rho\overline{v'T'}(\partial T/\partial y)$, at a given fixed value of α, Pr and Re, resulting in greater heat transfer near the wall surface. Therefore, the Nusselt number for the fully developed turbulent flows in concentric annular ducts with the smaller inner core diameter is always greater than that of the annulus with the larger inner core radius. It also shows that the Nusselt numbers for the fully developed turbulent flows in concentric annular ducts are always greater than those of parallel planes.

In Fig. 3.23, the theoretical Nusselt number calculated from Eq. (3.86) for two radius ratios, α, with Prandtl number, Pr = 0.71, is shown. It illustrates that as the radius ratio, α, increases, the Nusselt number increases.

Figs. 3.24 (a) and (b) show the effect of both the transverse convex curvature, R_i, and the radius ratio, α, on the Nusselt number for fully developed turbulent flow in concentric annuli at a given Reynolds number of 31,000. The figures illustrate that as the convex surface curvature, R_i, decreases or the radius ratio, α, decreases, the Nusselt number increases. Fig. 3.24 (b) also shows that the trend is similar to that of α in Fig. 3.24 (a). Comparing the results in Fig. 3.24 (a), the percentage changes in the normalized Nusselt number, Nu/Nu_{pp}, for $\alpha = 0.9$ at a Reynolds number of 31,000 for air, Pr $\approx$ 0.71 between R_i = 1 mm and R_i = 99 mm is about 32%, while that for $\alpha = 0.1$ is about 24%.

The effect of the Prandtl number, Pr, is shown in Fig. 3.25 for three Prandtl numbers with a fixed radius ratio, $\alpha = 0.5$ (R_i = 12.7 mm). It shows that when the Prandtl number increases, the heat transfer is higher. This is because the turbulent thermal diffusion is higher for an increasing value of the Prandtl number as discussed in Section 5.2.5.

In Figs. 4.43 through 4.45, a comparison between the present analysis and experiment on the Nusselt numbers is shown for three different radii of inner cores; 3.98 mm, 8.57 mm, and 16.7 mm, respectively, with a fixed radius ratio, $\alpha = 0.3$ for air, $Pr \approx 0.71$ as a working fluid. It is seen that the agreement is very good. The figures also demonstrate that the Nusselt numbers for the fully developed turbulent flow in concentric annular ducts are always greater than those for parallel planes.

Fig. 4.46 illustrates the effect of the transverse convex surface curvature on the Nusselt number, Nu. It clearly shows that the Nusselt number increases with decreasing values of R_i for a fixed radius ratio of $\alpha = 0.3$. This is because, as discussed in Fig. 3.20, the smaller the value of the inner core radius, R_i, the smaller the bulk temperature, T_b^* due to the increase of the production term of turbulent heat convection, $-c_p\rho\overline{v'T'}(\partial T/\partial y)$, at a given fixed value of α, Pr and Re.

In Fig. 4.47, the effects of the transverse convex curvature and the Reynolds number, Re, on the Nusselt number with a fixed radius ratio, α, are shown. As is seen in the figure, the higher the Reynolds number or the smaller R_i, the higher the heat transfer. The physical meaning was already discussed in previous related figures.

The comparison between the results for the turbulent boundary layer flow and those for the fully developed turbulent flow reveals that the effect of the convex surface curvature on the turbulent fluid flow and heat transfer should be greater for the turbulent boundary layer flows on circular cylinders than for the fully developed turbulent fluid flows in concentric annular ducts. This is because, whereas only the convex surface exists for the turbulent boundary layer flow over a circular cylinder, the fully developed turbulent annular flow is subject to two surfaces, i.e., a concave and a convex. Since the concave surface curvature has negligible effect on the turbulent fluid flow and heat transfer, when the radius ratio, α, is small, the significance of the convex surface curvature effect diminishes. Even with large a radius ratio, the presence of the concave surface, whose effect is negligible, would reduce the effect of the convex surface curvature in a concentric annuli.

5.3 Fully Developed Turbulent Flow in a Concentric Annular Duct: the Standard k-ε Model of Turbulence

5.3.1 Velocity Distribution

Figs. 3.29 and 3.30 show the comparisons between the theoretical (standard k-ε turbulence model) and experimental velocity distributions for two different radii of the inner cores, R_i = 16.7 mm and 8.57 mm, respectively, having a fixed radius ratio, α, of 0.3 at a given Reynolds number. Most of the velocity distributions in the outer region are in good agreement, but those in the inner region have a deviation between the theoretical and the experimental results. This implies that the k-ε model can not identify the effect of the transverse convex surface curvature for the fully developed turbulent fluid flows in concentric annular ducts. This shows more clearly in Fig. 3.31. As can be seen in the figure, the k-ε model with the constants given can not show any effect of the transverse convex surface curvature, even though the difference between the velocity distribution in the outer region and that of the inner region. The velocity distribution in the inner region was identified by Lee and Park [4, 63] who have used a simple modified mixing length turbulence model in their analysis.

5.3.2 Eddy Diffusivity for Momentum

The eddy diffusivity distribution for momentum is also investigated using the k-ε model of turbulence for two different radii of the inner cores, R_i = 16.7 mm and 8.57 mm, respectively, having a fixed radius ratio, α, of 0.3 at a given Reynolds number as shown in Fig. 3.32. It also illustrates the same point as in Section 5.3.1., i.e, the k-ε model can not identify the effect of the transverse convex surface curvature for the fully developed turbulent fluid flows in concentric annular ducts.

Figs. 3.33 show that the theoretical (standard k-ε turbulence model) and experimental turbulent intensity distribution for two inner core radii; R_i = 51 mm (α = 0.562) and 21 mm (α = 0.46) at a given Reynolds number. From the figures, it can be seen that the deviation of the experiment from the prediction is greater for the larger inner radius, R_i (= 51 mm), whose convex curvature effect is small as can be seen in Fig. 3.33 (a), than that for the smaller inner radius, R_i (= 21 mm), indicating that the standard k-ε turbulence model fails to describe the turbulent intensity distribution when the inner core radius , R_i , changes.

Since the momentum transfer by the k-ε model failed to identify the effect of the transverse convex surface curvature, no further attempt was made to apply the k-ε model for the heat transfer calculation. It could be stated that the standard k-ε model could be modified without any particular advantage over the present simple turbulence model used in the present study. It is also believed that this is beyond the scope of the present study.

CHAPTER 6
CONCLUSIONS

6.0 General Layout

The present study investigated the effect of transverse convex surface curvature, not only on turbulent boundary layer flows and heat transfer over heated circular cylinders, but also on fully developed turbulent flows and heat transfer in concentric annular ducts with smooth surfaces. Both analytical and experimental studies were carried out.

For the analytical study, the effects of the transverse convex surface curvature on the fluid flow and heat transfer, i.e., velocity distribution, friction coefficient, eddy diffusivity distribution, temperature distribution, and heat transfer coefficient, have been studied. The analytical predictions were obtained by a mathematical model for the turbulence models based on adaption of the variable von Kármán constant, κ_i, proposed for the first time in the present thesis.

The computer program developed for the present study employs an iterative process to match the velocity and temperature profiles with force and energy balances and calculates the desired momentum and thermal characteristics. It was assumed that the thermodynamic fluid properties in the analysis were independent of temperature. The standard k-ε turbulence model with the modified procedure is also investigated.

Experimental study has been also conducted on the effect of the inner radius, R_i, of the transverse convex surface curvature on the fully developed turbulent fluid flow and heat transfer in concentric annular ducts. Air was used as the working fluid. Three annuli having three different radii of the inner cores, R_i = 3.98 mm, 8.57 mm, and 16.7 mm with a fixed radius ratio, α (about 0.3), were used over a range of the Reynolds number between about 20,000 and 60,000. The maximum axial lengths available for the experiment were between about 70 and 100 equivalent diameters depending on the respective radius of each core tube. Inner cores were heated electrically to provide the constant heat fluxes throughout the test sections and instrumented for temperature and power measurements. The outer tubes were insulated to minimize the leakage of heat. In the case of the experimental study for the turbulent boundary layer flows and heat transfer on circular cylinders, the experimental data of Willmarth et al. [31] and Kim and Lee [45, 46] were recompiled for the present study.

For the purpose of clarity, the conclusion for the cases of the turbulent boundary layer flow over circular cylinders and fully developed turbulent flow in concentric annular ducts are individually made in the followings.

6.1 Turbulent Boundary Layer Flow and Heat Transfer on a Circular Cylinder

The effects of the transverse convex surface curvature on both fluid flow and heat transfer for turbulent boundary layer flows over the heated circular cylinders were identified. The study demonstrates that:

(1) The turbulence model with the variable von Kármán constant, κ_i, was seen to predict correctly the momentum and heat transfer for the turbulent boundary layer flows over circular cylinders. The analytical results using the turbulent model with the variable von Kármán constant, κ_i, proposed for the first time in the present thesis, were in good agreement with the experimental results of other investigators [31,45,46].

(2) Both the friction coefficient and the Nusselt number increase with a decreasing value of the cylinder radius and their values are always greater than those for the flows over a flat plate for the ranges of parameter studied.

(3) The cylinder radius, R_i, and Reynolds number, Re_x, are the two dominant parameters in describing the effect of transverse convex wall curvature.

(4) The effect of transverse convex wall curvature on heat transfer increases with an increasing Prandtl number.

6.2 Fully Developed Turbulent Flow and Heat Transfer in a Concentric Annular Duct

The following conclusions are reached from the present study on the effect of the transverse convex surface curvature for the fully developed turbulent flows and heat transfer in concentric annular ducts.

(1) The turbulence model which adapted the variable von Kármán constant, κ_i, proposed for the first time in the present thesis, is seen to predict correctly the momentum and heat transfer for fully developed turbulent flows and heat transfer in concentric annular ducts.

(2) Substantial agreements were obtained between the analytical and experimental results for the ranges of Reynolds numbers considered. Both the friction coefficient and heat transfer increase with a decreasing value of the inner core radius and their values are always greater than those for the flows in parallel planes or pipes for the ranges of parameter studied.

(3) From the present study and other past investigations, it is seen that while the effect of transverse concave curvature on fluid flow and heat transfer is negligible, that of transverse convex curvature is significant.

(4) It is demonstrated that the standard k-ε turbulence model can not identify the effect of transverse convex surface curvature for fully developed turbulent fluid flows in concentric annular ducts. However, the standard k-ε model could be modified without any particular advantage over the present simple turbulence model used in the present study.

6.3 An Additional Deductive Conclusion

The following additional conclusions are also deduced from the present study.

(1) It is seen from the limited literature that the transverse convex surface curvature also influences the values of CHF (Critical Heat Flux) from experiments in concentric annuli. The CHF for a concave surface (the outer surface) seems to be significantly higher than that for a convex surface (the inner core). This and the present study indicate that the tube-based CHF correlations should not be applied to flow outside of tube bundles or in a subchannel whose heated surfaces are convex.

(2) Since no workable theoretical model other than the present study exists, nor are there experimental results to quantify the effect of transverse convex curvature on fluid flow, heat transfer and especially CHF, any experimental verification of the fluid flow and heat transfer (including CHF) for such critical applications as nuclear reactor cores must come from experimental simulations in a 1:1 bundle lattice geometry for fuel bundles.

APPENDIX A
Dimensional Analysis

There are several methods of reducing a number of dimensional variable into a small number of dimensionless groups. The scheme used here is that of Buckingham [72] which is now called the Buckingham pi (Π) Theorem. The name pi comes from the mathematical notation Π, meaning a product of variables. The dimensionless variable groups found from the theorem are power products denoted by Π_1, Π_2, Π_3, etc.

A.1 Turbulent Boundary-Layer Flow on a Circular Cylinder

A.1.1 Fluid Flow

Considering three groups contained eight variables to express the governing relationship of fluid flow character for turbulent boundary-layer fluid flow:

$$\text{Fluid flow character} = f(\rho, u_\infty, \mu, \tau_w, x, y, R_i, \delta)$$

1. Geometrical Parameters: R_i, x, y
2. Physical properties of working fluid: ρ, μ
3. Experimental variables: u_∞, δ, τ_w

Suppose that three basic dimensions and four primary variables are selected as:

Fundamental dimensions: M, L, T

Primary variables: ρ, μ, u_∞

The pi groups required are:

Number of dimensional groups, n: 8

Number of dimensionless variable k: 3

Reduced dimensionless variables expected, j: n - k

Therefore, we can expect five dimensionless variables or 5 (= 8 - 3) pis.

Then the five pi groups are formed by power products of these three primary variables and additional variables as:

$\Pi_1 = [\mu^a \ \rho^b \ u_\infty^c \ \tau_w] = [\tau_w / \rho \, u_\infty^{\ 2}] = C_f$

or $\qquad = [u^* / u_\infty]^2 \quad = u^+$

$\Pi_2 = [\mu^a \ \rho^b \ u_\infty^c \ x] \ = [\rho \, u_\infty \, x / \mu] = Re_x$

$\Pi_3 = [\mu^a \ \rho^b \ u_\infty^c \ y] \ = [\rho \, u_\infty \, y / \mu]$

$\Pi_4 = [\mu^a \ \rho^b \ u_\infty^c \ R_i] \ = [\rho \, u_\infty \, R_i / \mu] = Re_{Ri}$

$\Pi_5 = [\mu^a \ \rho^b \ u_\infty^c \ \delta] \ = [\rho \, u_\infty \, \delta / \mu]$

$\Pi_6 = \Pi_3 \cdot \Pi_1^{\frac{1}{2}} = [y \, u^* / \nu] = y^+$

$\Pi_7 = \Pi_2 / \Pi_4 = x / R_i$

$\Pi_8 = \Pi_5 / \Pi_3 = \delta / y$

Finally, governing relationship of fluid flow character for turbulent boundary-layer flow is:

$$f_1 \, (C_f, Re_{Ri}, Re_x, x/R_i, \delta/y) = 0$$

or

$$f_2 \, (u^+, y^+, Re_{Ri}, Re_x, x/R_i, \delta/y) = 0$$

Therefore, the functional relationship of fluid flow character is;

$$C_f = f_1 \, (Re_{Ri}, Re_x, x/R_i, \delta/y)$$

or

$$u^+ = f_2 \, (y^+, Re_{Ri}, Re_x, x/R_i, \delta/y)$$

A.1.2 Heat Transfer

Considering three groups contained eleven variables to express the governing relationship of heat transfer for turbulent boundary-layer fluid flow:

$$\text{Heat Transfer} = f(\rho, \bar{u}, \mu, k, c_p, \Delta T, q_w, x, y, R_i, \Delta)$$

1. Geometrical Parameters: R_i, x, y
2. Physical properties of working fluid: ρ, μ, k, c_p
3. Experimental variables: $u_\infty, \delta, \Delta T, q_w$

Suppose that four basic dimensions and four primary variables are selected as:

Fundamental dimensions: M, L, T, Θ

Primary variables: $\rho, u_\infty, x, \Delta T$

The pi groups required are:

Number of dimensional groups, n: 10

Number of dimensionless variable k: 4

Reduced dimensionless variables expected, j: n - k

Therefore, we can expect seven dimensionless variables or 7 (= 11- 4) pis.

Then the seven pi groups are formed by power products of these four primary variables and additional variables as:

$$\Pi_1 = [u_\infty^{\,a}\ \rho^{\,b}\ x^{\,c}\ \Delta T^{d}\,\mu] = [u_\infty x/\nu]^{-1} = [Re_x]^{-1}$$

$$\Pi_2 = [u_\infty^{\,a}\ \rho^{\,b}\ x^{\,c}\ \Delta T^{d}\,k] = [k\,\Delta T / u_\infty^{3}\rho\, x]$$

$$\Pi_3 = [u_\infty^{\,a}\ \rho^{\,b}\ x^{\,c}\ \Delta T^{d}\,c_p] = [c_p\,\Delta T / u_\infty^{2}]$$

$$\Pi_4 = [u_\infty^{\,a}\ \rho^{\,b}\ x^{\,c}\ \Delta T^{d}\,q_w] = [q_w / \rho\, u_\infty^{3}]$$

$$\Pi_5 = [u_\infty^{\,a}\ \rho^{\,b}\ x^{\,c}\ \Delta T^{d}\,R_i] = [x / R_i]^{-1}$$

$$\Pi_6 = [u_\infty^{\,a}\ \rho^{\,b}\ x^{\,c}\ \Delta T^{d}\,y] = [y/x]$$

$$\Pi_7 = [u_\infty^{a}\ \rho^{b}\ x^{c}\ \Delta T^{d}\ \Delta] = [\Delta / x]$$

$$\Pi_8 = \Pi_4 / \Pi_2 = q_w\, x / k\, \Delta T = Nu$$

$$\Pi_9 = \Pi_3 / (\Pi_1 \cdot \Pi_2) = \nu / \alpha = Pr$$

$$\Pi_{10} = \Pi_7 / \Pi_6 = \Delta / y$$

Finally, the heat transfer functional relationship is:

$$f\,(Nu, Pr, Re_x, x/R_i, \Delta/y) = 0$$

or

$$Nu = f\,(Pr, Re_x, x/R_i, \Delta/y)$$

A.2 Fully Developed Turbulent Fluid Flow in a Concentric Annulus with Smooth Surfaces

A.2.1 Friction Coefficient

Considering three groups contained eight variables to express the governing relationship of fluid flow character for turbulent boundary-layer fluid flow: for fully developed turbulent flow:

$$\text{Fluid flow character} = f(\rho, \bar{u}, \mu, \tau_w, y, D_e, D_i, D_o)$$

1. Geometrical Parameters: D_e, D_i, D_o, y
2. Physical properties of working fluid: ρ, μ
3. Experimental flow variables: $\bar{u}, \tau_w$

Suppose that three basic dimensions and three primary variables are selected as:

Fundamental dimensions: M, L, T

Primary variables: $\rho, \bar{u}, \mu$

The pi groups required are:

Number of dimensional groups, n: 8

Number of dimensionless variable k: 3

Reduced dimensionless variables expected, j: n - k

Therefore, we can expect five dimensionless variables or 5 (= 8 - 3) pis.

The five pi groups are formed by power products of these four primary variables and additional variables as:

$$\Pi_1 = [\mu^a \ \rho^b \ \bar{u}^c \ \tau_w] = [\tau_w/\rho u^2] = f$$

$$\text{or} \qquad = [u_\tau/u]^2 = u^+$$

$$\Pi_2 = [\bar{u}^a \ \rho^b \ \mu^c \ De] = [\bar{u}\,De/\nu]^{-1} = [Re_{De}]^{-1}$$

$$\Pi_3 = [\bar{u}^a \ \rho^b \ \mu^c \ D_i] = [\bar{u}\,D_i/\nu]^{-1} = [Re_{Di}]^{-1}$$

$$\Pi_4 = [\bar{u}^a \ \rho^b \ \mu^c \ D_o] = [\bar{u}\,D_o/\nu]^{-1} = [Re_{Do}]^{-1}$$

$$\Pi_5 = [\mu^a \ \rho^b \ \bar{u}^c \ y] = [\rho\bar{u}\,y/\mu]$$

$\Pi_6 \quad = \Pi_3 / \Pi_4 = \alpha$

$\Pi_7 \quad = \Pi_1^{1/2} \cdot \Pi_5 = y^+$

Finally, the governing relationship of fluid flow character for fully developed turbulent flow is:

$$f\,(f,\ \alpha,\ Re_{De},\ Re_{Di} \text{ or } Re_{Do}) = 0$$

or

$$f\,(u^+,\ y^+,\ \alpha,\ Re_{De},\ Re_{Di},\ Re_{Do}) = 0$$

This may be rewritten

$$f = f\,(\alpha,\ Re_{De},\ Re_{Di} \text{ or } Re_{Do})$$

or

$$u^+ = f\,(y^+,\ \alpha,\ Re_{De},\ Re_{Di},\ Re_{Do})$$

A.2.2 Heat Transfer

Considering three groups contained nine variables to express the governing relationship of heat transfer function for fully developed turbulent flow:

$$\text{Heat Transfer} = f\,(\rho,\ \bar{u},\ k,\ \mu,\ c_p,\ \Delta T,\ q_w,\ D_e,\ D_i \text{ or } D_o)$$

1. Geometrical Parameters: D_e, D_i or D_o
2. Physical properties of working fluid: ρ, k, μ, c_p
3. Experimental flow variables: $\bar{u}$, ΔT, q_w

Suppose that four basic dimensions and four primary variables are selected as:

Fundamental dimensions: M, L, T, Θ

Primary variables: ρ, $\bar{u}$, De, ΔT

The pi groups required are:

Number of dimensional groups, n: 9

Number of dimensionless variable k: 4

Reduced dimensionless variables expected, j: n - k

Therefore, we can expect five dimensionless variables or 5 (= 9 - 4) pis.

Then the five pi groups are formed by power products of these four primary variables and additional variables as:

$\Pi_1 = [\bar{u}^a \ \rho^b \ De^c \ \Delta T^d \mu] = [\bar{u}\, De / \nu]^{-1} = [Re_{De}]^{-1}$

$\Pi_2 = [\bar{u}^a \ \rho^b \ De^c \ \Delta T^d k] = [k\, \Delta T / \bar{u}^3 \rho\, De]$

$\Pi_3 = [\bar{u}^a \ \rho^b \ De^c \ \Delta T^d c_p] = [c_p \Delta T / \bar{u}^2]$

$\Pi_4 = [\bar{u}^a \ \rho^b \ De^c \ \Delta T^d q_w] = [q_w / \rho \bar{u}^3]$

$\Pi_5 = [\bar{u}^a \ \rho^b \ De^c \ \Delta T^d D_i] = [D_i / De]$ or $\Pi_5 = [\bar{u}^a \ \rho^b \ De^c \ \Delta T^d D_o] = [D_o/De]$

$\Pi_6 = \Pi_4 \cdot \Pi_5 / \Pi_2 = Nu$

$\Pi_7 = \Pi_5 / \Pi_6 = \alpha$

$\Pi_8 = \Pi_1 \cdot \Pi_3 / \Pi_2 = Pr$

$\Pi_9 = [\Pi_1 / \Pi_6]^{-1} = Re_{Di}$ or $\Pi_9 = [\Pi_1 / \Pi_7]^{-1} = Re_{Do}$

Finally, the heat transfer functional relationship is:

$$f\,(Nu, \alpha, Pr, Re_{De}, Re_{Di} \text{ or } Re_{Do}) = 0$$

or

$$Nu = f\,(\alpha, Pr, Re_{De}, Re_{Di}, Re_{Do})$$

APPENDIX B
Sample Comparison

The heat transfer relationship for fully developed turbulent fluid flow in a concentric annulus as shown in Appendix A may be expressed as:

$$Nu = Nu\ (Re_{De}, Pr, \alpha = R_i/R_o, Re_{Ri}) \qquad \text{(B.1)}$$

Re_{Ri} can be made by an infinite number of the combinations between R_i and $d\bar{u}$ for a given value of Re_{Ri} as following examples;

If Re_{Ri} ($= u_{avg} \cdot R_i / \nu$) is 1,000, it can be made for a given fluid with $\nu = 1$ by:

$u_{avg} = 1{,}000$	$R_i = 1;$
$u_{avg} = 100$	$R_i = 10;$
$u_{avg} = 10$	$R_i = 100;$
$u_{avg} = 1$	$R_i = 1{,}000;$
.	.
.	.

This implies that the parameter Re_{Ri} itself cannot characterize the transverse convex curvature of the wall surfaces of a concentric annulus. Therefore, the radius of an inner core, R_i, may be used in place of Re_{Ri} ($= R_i.\bar{u}/\nu$) in Eq. (B.1).

$$Nu = Nu\ (Re_{De}, Pr, \alpha = R_i/R_o \text{ and } R_i) \qquad \text{(B.2)}$$

APPENDIX C.1

Distribution of Shear Stress and Radial Heat Flux of Circular Cylinder Geometry

C.1.1 Shear Stress Distribution

The schematic geometry of a circular cylinder surface is shown in Fig. 3.1. The force applied to the control volume is shown in Figure C1.1.

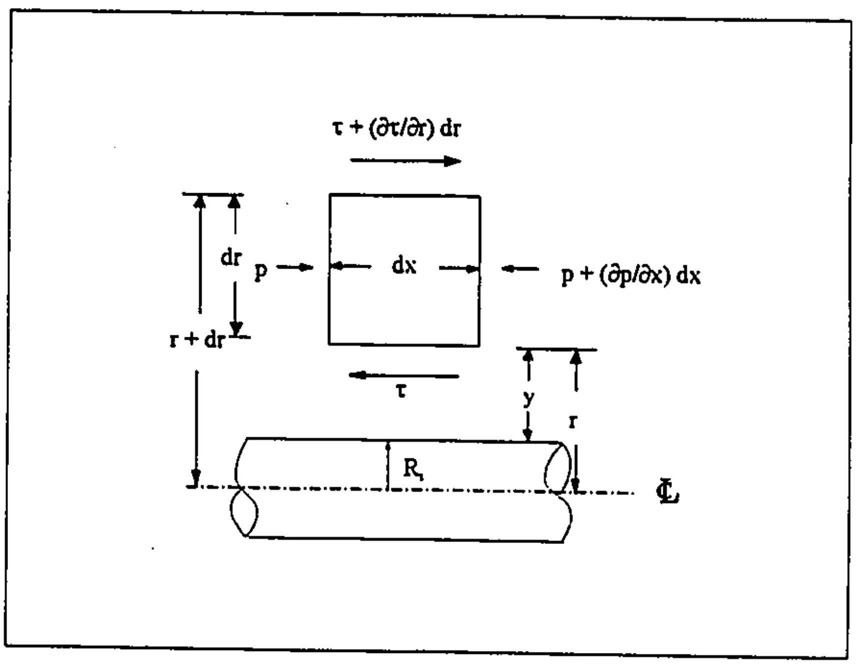

Figure C1.1 Control Volume for a Circular Geometry

The force balance equation yields:

$$- \tau 2 \pi r dx + p 2 \pi r dr = (\tau + \frac{\partial \tau}{\partial r} dr) 2 \pi (r + dr) dx - (p + \frac{\partial p}{\partial x} dx) 2 \pi r dr \tag{C1.1}$$

On simplifying Eq. (C1.1) as:

$$\frac{\partial}{\partial r}(\tau \cdot r) = \frac{\partial p}{\partial x} r \tag{C1.2}$$

and integrating

$$\tau \cdot r = \frac{\partial p}{\partial x} \int_0^r r \, dr \tag{C1.3}$$

and

$$\tau \cdot r = - \frac{\partial p}{\partial x} \frac{r^2}{2} + C \tag{C1.4}$$

where $r = R_i + y$.

If it is assumed that there is no pressure gradient, then the equation can be simplified with the boundary condition $\tau = \tau_w$ at $r = R_i$ as:

$$\frac{\tau}{\tau_w} = \frac{R_i}{R_i + y} \tag{C1.5}$$

In dimensionless parameters, Eq. (C1.5) becomes as:

$$\frac{\tau}{\tau_w} = \frac{R_i^+}{R_i^+ + y^+} \tag{C1.6}$$

C.1.2 Heat Flux Distribution

The heating condition is that the core surface is heated with a constant heat flux. The analysis can be carried out by calculating the heat balance. The control volume for the heat balance is shown in Fig. C1.2 below.

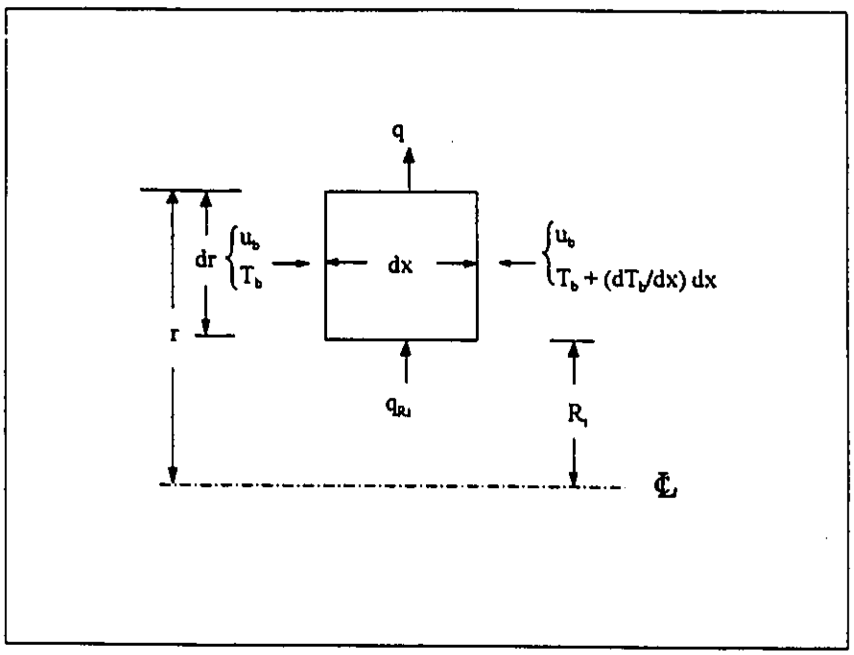

Figure C1.2 Control Volume for Circular Cylinder Geometry

The law of conservation of energy can be expressed for the control volume as:

$$\rho c_p T_b u_b (r^2 - R_i^2) + q_{R_i} 2\pi R_i dx = q_{R_i} 2\pi r dr + \rho c_p u_b (r^2 - R_i^2)(T_b + \frac{\partial T_b}{\partial x} dx)$$

The equation can be simplified as:

$$\rho c_p (r^2 - R_i^2)(\frac{u_b}{2})(\frac{\partial T_b}{\partial x}) = q_{R_i} R_i - q r \tag{C1.7}$$

If the convection term is negligible within a boundary layer, then the equation yields:

$$\frac{q}{q_{R_i}} = \frac{q}{q_w} = \frac{R_i}{r} = \frac{R_i}{R_i + y} \tag{C1.8}$$

APPENDIX C.2

Non-Dimensionalized Forms of the Velocity and Temperature Equation for a Circular Cylinder

C.2.1 Velocity Profile

The radial velocity of fluid, u(r), can be derived from the definition of the total shear stress as:

$$\tau = \mu \frac{\partial u}{\partial y} - \rho \overline{u'v'} \tag{C2.1}$$

From the Prandtl mixing length hypothesis, the turbulent fluctuation term becomes:

$$- \overline{u'v'} = l^2 \left| \frac{\partial u}{\partial y} \right|^2 \tag{C2.2}$$

Substituting Eq. (C2.2) into Eq. (C2.1) becomes :

$$\frac{\tau}{\rho} = \nu \frac{\partial u}{\partial y} + l^2 \left| \frac{\partial u}{\partial y} \right|^2 \tag{C2.3}$$

The definition of friction velocity, u^* is:

$$u^* = (\frac{\tau_w}{\rho})^{1/2}$$

Substitution of Eq. (C2.2) into (C2.1) and from the definition of the non-dimensional parameter can be made:

$$\tau^{*} = \frac{\partial u^{+}}{\partial y^{+}} + l^{+2}\left(\frac{\partial u^{+}}{\partial y^{+}}\right)^{2} \tag{C2.4}$$

where the shear-stress ratio, τ^{*}, is defined as:

$$\tau^{*} = \frac{\tau}{\tau_w}$$

and the dimensionless radial length, y^{+}, is:

$$y^{+} = \frac{y u^{*}}{\nu}$$

Eq. (C2.4) is an equation that is a form of an incomplete square polynomial about $\partial u^{+} / \partial y^{+}$:

$$a x^{2} + b x + c = 0$$

Thus the roots of above equation are:

$$x = \frac{\partial u^{+}}{\partial y^{+}}; \quad a = l^{+2}; \quad b = 1; \quad c = -\tau^{*}$$

The positive root of the polynomial is:

$$\frac{\partial u^+}{\partial y^+} = \frac{-1 + \sqrt{1 + 4 l^{+2} \tau^+}}{2 l^{+2}} \tag{C2.5}$$

Finally, Eq. (C2.5) can be further simplified as:

$$\frac{\partial u^+}{\partial y^+} = \frac{2 \tau^+}{1 + \sqrt{1 + 4 l^{+2} \tau^+}} \tag{C2.6}$$

C.2.2 Temperature Profile

The equation of temperature profiles across the flow cross-section can be derived from the basic heat transport equation in Eq. (3.23), as:

$$-\frac{q}{\rho c_p} = (\alpha + \varepsilon_H) \frac{\partial T}{\partial r} \tag{C2.7}$$

where α is the thermal diffusivity.

Eq. (C2.7) can be made dimensionless by introducing a non-dimensionalized temperature, T^+:

$$T^+ = \frac{(T_w - T) \rho c_p u^*}{q_w} \tag{C2.8}$$

Using Eq. (C2.8), the partial derivative for T can be transformed as:

$$\frac{\partial T}{\partial r} = \pm \frac{q_w}{\rho c_p u^*} \frac{\partial T^+}{\partial r} \tag{C2.9}$$

where $r = R_j \pm y$

Substitution of Eq.(C2.9) into (C2.7) can be made:

$$\frac{\partial T^+}{\partial y^+} = Pr \frac{q/q_w}{1 + \frac{Pr}{Pr_t}(\frac{\varepsilon_M}{\nu})} \tag{C2.10}$$

And the eddy viscosity can be defined as:

$$\frac{\varepsilon_M}{\nu} = l^{+2} \frac{\partial u^+}{\partial y^+} \tag{C2.11}$$

APPENDIX C.3

Non-Dimensionalized Forms of Other Fluid Parameters for Circular Cylinder Geometry

C.3.1 Momentum Defect (Thickness) Area, θ

From the integral momentum equation for the axisymmetric boundary equation, the momentum defect (or momentum thickness) area[1] in an axisymmetric flow for constant pressure, p, and constant density, ρ, is:

$$\frac{d\theta}{dx} = \frac{2\,\pi\,a}{\rho\,u_\infty^2}\,\tau_w \tag{C3.1}$$

where the momentum defect area, θ, is defined as:

$$\theta = 2\,\pi \int_{R_i}^{\delta + R_i} \frac{u}{u_\infty}\,(1 - \frac{u}{u_\infty})\;r\,dr \tag{C3.2}$$

Eq.(C3.2) can be rearranged using $r = R_i + y$ as:

$$\theta = 2\,\pi \int_0^{\delta} \frac{u}{u_\infty}\,(1 - \frac{u}{u_\infty})\,(R_i + y)\,dy \tag{C3.3}$$

Eq. (C3.3) in dimensionless form yields:

---

[1] Momentum thickness or defect is a measure of total plate drag. von Kármán noted that the drag equals the integrated wall shear along the plate [74].

$$\theta = 2\pi R_i \left(\frac{\nu}{u^*}\right) \frac{1}{u_\infty^+} \int_0^{\delta^+} u^+ \left(1 - \frac{u^+}{u_\infty^+}\right)\left(1 + \frac{y^+}{R_i^+}\right) dy^+ \tag{C3.4}$$

In Eq. (C3.4), the integral part is given as:

$$I = \int_0^{\delta^+} u^+ \left(1 - \frac{u^+}{u_\infty^+}\right)\left(1 + \frac{y^+}{R_i^+}\right) dy^+ \tag{C3.5}$$

Thus, Eq. (C3.5) becomes:

$$\theta = 2\pi R_i \left(\frac{\nu}{u^*}\right) \frac{1}{u_\infty^+} I \tag{C3.6}$$

Differentiation of Eq.(C3.6) yields:

$$d\theta = 2\pi R_i \left(\frac{\nu}{u^*}\right) \frac{1}{u_\infty^+} dI \tag{C3.7}$$

Substitution of Eq. (C3.6) into (C3.1) yields:

$$x^+ = u_\infty^+ I \tag{C3.8}$$

C.3.2 Reynolds Number

The length Reynolds number, Re_x, may be expressed from the definition as:

$$Re_x = \frac{u_\infty x}{\nu} = u_\infty^+ x^+ \qquad \text{(C3.9)}$$

With Eq. (C3.8) and Eq. (C3.9) this becomes:

$$\frac{dRe_x}{dI} = u_\infty^{+2} \qquad \text{(C3.10)}$$

where the integral function is given as:

$$I(u_\infty^+ , R_i^+) = \int_0^{\delta^+} u^+ \left(1 - \frac{u^+}{u_\infty^+}\right) \left(1 + \frac{y^+}{R_i^+}\right) dy^+$$

Integration of Eq. (C3.10) yields:

$$Re_x = u_\infty^+ I - 2 \int_0^{u_\infty^{+}} u_\infty^{+\prime} I \, du_\infty^{+\prime} \qquad \text{(C3.11)}$$

C.3.3 Friction Coefficient

The friction coefficient is defined by:

$$c_{fx} = \frac{\tau_w}{\frac{1}{2} \rho u_x^2} \qquad \text{(C3.12)}$$

In dimensionless parameters,

$$c_{fx} = \frac{\frac{\tau_w}{\rho}}{\frac{1}{2} u_x^2} = \frac{2}{u_x^{+2}} \qquad \text{(C3.13)}$$

C.3.4 Enthalpy Defect (thickness) Area, Δ

The integral energy equation for the axisymmetric boundary equation is expressed in terms of enthalpy defect (or thickness) area. The problem of defining a thickness of the thermal boundary layer is similar to that posed by the momentum boundary layer and it becomes:

$$\frac{d\Delta}{dx} = \frac{2\pi a}{\rho c_p u_\infty (T_w - T_\infty)} q_w \tag{C3.14}$$

where the enthalpy defect area, Δ, is defined for a constant-property flow of a perfect gas with no chemical reaction [18]. The heat flux is defined as:

$$q_w = \frac{d}{dy} \int_0^\infty \rho c_p u (t - t_\infty) dy \tag{C3.15}$$

Substitution of Eq. (C3.15) into Eq.(C3.14) yields:

$$\Delta = 2\pi \int_{R_i}^{\delta_H + R_i} \frac{u}{u_\infty} \frac{(T - T_w)}{(T_w - T_\infty)} r\, dr \tag{C3.16}$$

In dimensionless parameters, Eq. (C3.16) can be rearranged for the case of uniform heat flux at the wall surface as:

$$\Delta = 2\pi R_i \left(\frac{\nu}{u^*} \right) \int_0^{\delta_H^+} \frac{u^+}{u_\infty^+} \frac{(T_\infty^+ - T^+)}{T_\infty^+} \left(1 + \frac{y^+}{R_i^+} \right) dy \tag{C3.17}$$

Substitution Eq.(C3.15) into (C3.17) yields:

$$x^{*} = \int_{0}^{\delta_H^{*}} u^{*} (T_\infty^{*} - T^{*}) \left(1 + \frac{y^{*}}{R_i^{*}} \right) dy^{*} \tag{C3.18}$$

Thus, from the definition of local Reynolds number, the local Reynolds number can be given as:

$$Re_x = x^{*} u_\infty^{*} \tag{C3.19}$$

Differentiation of Eq. (C3.19) yields:

$$\frac{dRe_x}{dI_H} = 1 \tag{C3.20}$$

where the integral function is:

$$I_H = \int_{0}^{\delta_H^{*}} u^{*} u_\infty^{*} (T_\infty^{*} - T^{*}) (1 + \frac{y^{*}}{R_i^{*}}) dy^{*}$$

Therefore, Eq. (C5.20) can be rewritten as;

$$Re_x = \int_{0}^{\delta_H^{*}} u^{*} u_\infty^{*} (T_\infty^{*} - T^{*}) (1 + \frac{y^{*}}{R_i^{*}}) dy^{*} \tag{C3.21}$$

C.3.5 Local Nusselt Number, Nu_x

Eq.(C3.21) can be rearranged as:

$$Re_x = \int_{0}^{\delta_H^{*}} u^{*} u_\infty^{*} T_\infty^{*} (1 + \frac{y^{*}}{R_i^{*}}) dy^{*} - \int_{0}^{\delta_H^{*}} u^{*} u_\infty^{*} T^{*} (1 + \frac{y^{*}}{R_i^{*}}) dy^{*} \tag{C3.22}$$

The temperature can be obtained, in dimensionless form, as:

$$T_\infty^+ = \frac{\frac{Re_x}{u_\infty^+} + \int_0^{\delta_H^+} u^+ T^+ (1 + \frac{y^+}{R_i^+}) dy^+}{\int_0^{\delta_H^+} u^+ (1 + \frac{y^+}{R_i^+}) dy^+} \tag{C3.23}$$

C.3.6 Local Nusselt Number, Nu_x

The Nusselt number is defined as:

$$Nu_x = \frac{h x}{k} \tag{C3.24}$$

where the convective heat transfer coefficient, h, is:

$$h = \frac{q_w}{T_w - T_b} \tag{C3.25}$$

Substitution Eq. (C3.25) into (C3.24) yields:

$$Nu_x = \frac{2x}{\left(k \frac{T^+}{c_p \rho u^+} \right)} \tag{C3.26}$$

Eq. (C3.26) can be further reduced with dimensionless parameters:

$$Nu_x = \frac{Pr \cdot Re_x}{T_\infty^+ \cdot u_\infty^+} \tag{C3.27}$$

APPENDIX D.1

Distribution of Shear Stress and Radial Heat Flux in Concentric Annular Flow

D.1.1 Shear Stress Distribution

The schematic geometry of a concentric annulus with smooth surfaces is shown in Figure D1.1 below.

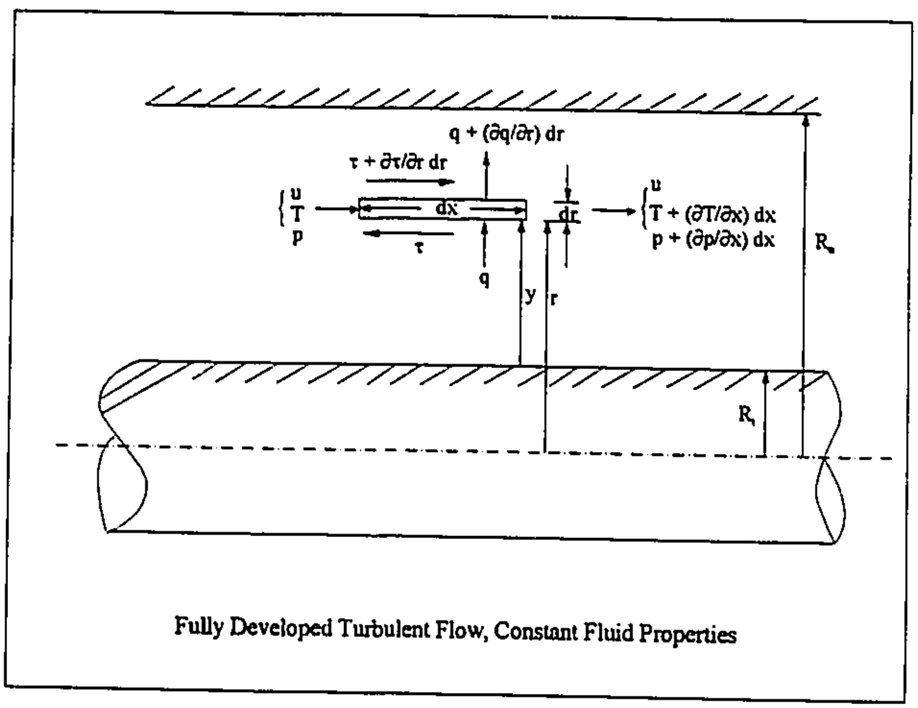

Figure D1.1 Shear Stress and Heat Flux Distribution in Annular Flow

The distribution of the shear stress, τ, is derived using the momentum equation. Referring to Fig. D1.1, a force balance for a cylindrical fluid element is

$$-\tau(2\pi r dx) + (\tau + \frac{\partial \tau}{\partial r}dr)2\pi(r+dr)dx + p2\pi r dr - (p + \frac{\partial p}{\partial x}dx)2\pi r dr = 0 \qquad \text{(D1.1)}$$

On simplifying Eq. (D1.1) as:

$$\frac{\partial}{\partial r}(\tau \cdot r) = \frac{\partial p}{\partial x} r \qquad \text{(D1.2)}$$

and integrating

$$\tau \cdot r = \frac{\partial p}{\partial x}\int_0^r r\,dr \qquad \text{(D1.3)}$$

and

$$\tau \cdot r = \frac{\partial p}{\partial x}\frac{r^2}{2} + C \qquad \text{(D1.4)}$$

To determine the integration constant in Eq. (D1.4), some assumption concerning the position of zero stress must be made. In the case of axisymmetric flow in a pipe, zero stress occurs at zero radius based on the centerline because of symmetry and it coincides with the position of the maximum velocity. In the asymmetrical velocity field of the annular flow, it will be assumed that zero stress occurs at the radius of the maximum velocity, i.e., at r_m.

Therefore, with the boundary condition $\tau_m = 0$ at $r = r_m$, Eq. (D1.4) becomes:

$$\tau = \frac{1}{2}\frac{\partial p}{\partial x}\frac{r^2 - r_m^2}{r} \tag{D1.5}$$

or

$$\tau = \frac{\Delta p}{2L}\left|\frac{r^2 - r_m^2}{r}\right| \tag{D1.6}$$

From Eq. (D1.6) the ratio of the shear stress, τ_i/τ_o can easily obtained as:

$$\frac{\tau}{\tau_i} = \frac{R_i}{r}\left(\frac{r_m^2 - r^2}{r_m^2 - R_i^2}\right) \tag{D1.7}$$

and

$$\frac{\tau}{\tau_o} = \frac{R_o}{r}\left(\frac{r^2 - r_m^2}{R_o^2 - r_m^2}\right) \tag{D1.8}$$

therefore

$$\frac{\tau_i}{\tau_o} = \frac{R_o}{R_i}\left(\frac{r_m^2 - R_i^2}{R_o^2 - r_m^2}\right) \tag{D1.9}$$

D.1.2 Radial Heat Flux Distribution

In a concentric annulus, the heating condition considered is that the core surface is heated with the outer surface insulated. The heat analysis can be carried out by calculating the heat balance. The control volume for the heat balance is also expressed in Fig. D1.1.

Consider a small cylindrical control volume as indicated in Fig. D.1. If axial thermal diffusion is negligible, according to the steady flow energy equation, the net heat transfer equals the enthalpy change in the present case as:

$$\begin{aligned} \rho c_p u T 2\pi r dr + q 2\pi r dx = \rho c_p u \left(T + \frac{\partial T}{\partial x} dx\right) 2\pi r dr \\ + \left(q + \frac{\partial q}{\partial r} dr\right) 2\pi (r + dr) dx \end{aligned} \tag{D1.10}$$

On simplifying Eq. (D1.10) as:

$$-\frac{\partial}{\partial r}(q \cdot r) = \rho c_p r u \frac{\partial T}{\partial x} \tag{D1.11}$$

In a flow which is fully developed both hydrodynamically and thermally with the inner boundary heat flux, q_w, uniform in the x direction,

$$\frac{\partial T}{\partial x} = \frac{\partial T_b}{\partial x} = constant \tag{D1.12}$$

Eq. (D1.11) then becomes

$$-\frac{\partial}{\partial r}(q\cdot r) = \rho\, c_p\, r\, u\, \frac{\partial T_b}{\partial x} \tag{D1.13}$$

From a heat balance,

$$q_w\, 2\,\pi\, R_i\, dx = \pi\,(R_o^2 - R_i^2)\,\bar{u}\,\rho\, c_p\, dT_b \tag{D1.14}$$

therefore

$$\frac{\partial T_b}{\partial x} = \frac{2\, q_w\, R_i}{(R_o^2 - R_i^2)\,\bar{u}\, c_p\, \rho} \tag{D1.15}$$

Integration of Eq. (D1.13) with Eq. (D1.15) gives

$$q = q_w\, \frac{2\,\pi\, R_i\, \rho}{W\, r} \int_r^{R_o} u\, r\, dr \tag{D1.16}$$

where W is the mass flow of fluid through the annulus cross section.

Clearly, the radial distribution of heat flux q is dependent on the velocity distribution u = u (r). If the local velocity u (r) is constant and equal to the average velocity, $\bar{u}$. Then,

$$q = q_w\, \frac{2\,\pi\, R_i\, \rho}{W\, r}\, \bar{u} \int_r^{R_o} r\, dr \tag{D1.17}$$

and

$$\frac{q}{q_w} = \frac{R_i}{r} \left(\frac{R_o^2 - r^2}{R_o^2 - R_i^2} \right) \tag{D1.18}$$

Since q / q_w is dependent on the velocity distribution, i.e. u = u (r), it is necessary to make some assumption concerning the velocity distribution. This matter has been studied by Barrow [53] in the fully developed flow in an annulus. He has shown that the more realistic velocity distribution predicted heat fluxes in the outer region of the maximum velocity of the annulus samller than those calculated from Eq. (D1.18). However, since the heat fluxes are already very small in the outer region of the annulus, the assumption concerning the velocity field is not critical to the evaluation of q (r). Therefore the effect of u (r) on q / q_w has a very minor effect.

APPENDIX D.2

Non-Dimensionalized Forms of the Velocity and Temperature Equation for Concentric Annular Geometry

D.2.1 Velocity Profile

The axial velocity of the fluid, u(r), can be derived from the definition of total shear stress as:

$$\frac{\tau_j}{\rho} = (\nu + \varepsilon_{M,j}) \frac{\partial u_j}{\partial r} \tag{D2.1}$$

Rearranging Eq. (D2.1) the velocity gradient becomes:

$$\frac{\partial u_j}{\partial r} = \frac{\tau_j}{\rho} \frac{1}{\nu} \frac{1}{1 + (\frac{\varepsilon_M}{\nu})_j} \tag{D2.2}$$

Now the friction velocity, u_j^* is:

$$u_j^* = \sqrt{\frac{\tau_{w,j}}{\rho}} \tag{D2.3}$$

Substitution of Eq. (D2.3) into (D2.2) yields:

$$\frac{\partial u_j}{\partial y} = u_j^{*2} \frac{1}{\nu} \frac{1}{1 + (\frac{\varepsilon_M}{\nu})_j} \tag{D2.4}$$

In dimensionless parameters Eq. (D2.4) becomes:

$$\frac{\partial u_j^+}{\partial \zeta} = D^+ \frac{\tau/\tau_o}{1 + (\frac{\varepsilon_M}{\nu})_j} \tag{D2.5}$$

D.2.2 Temperature Profile

The equation of a temperature profile across the flow cross-section can be derived from the basic heat transport equation, Eq. (3.23) as:

$$-\frac{q}{\rho c_p} = (\alpha + \varepsilon_H)\frac{\partial T}{\partial r} \tag{D2.6}$$

where α is the thermal diffusivity.

In dimensionless temperature, T_j^+, as:

$$\frac{\partial T_j}{\partial r} = \pm \frac{q_j}{\rho c_p u_j^*} \frac{\partial T_j^+}{\partial r} \tag{D2.7}$$

where the radial distance $r = R_j \pm y_j$. Eq. (D2.7) can be expressed with the normalized distance parameter, ζ, as:

$$\frac{\partial T_j^+}{\partial \zeta_j} = \pm D^+ \cdot Pr \frac{q/q_j}{1 + \frac{Pr}{Pr_t}(\frac{\varepsilon_M}{\nu})_j} \tag{D2.8}$$

where + sign applies for $j = i$ and - sign for $j = o$. Pr_t is the turbulent Prandtl number.

APPENDIX D.3

Non-Dimensionalized Forms of Momentum and Energy Equation for a Concentric Annular Geometry

D.3.1 Shear Stress Ratio

From the force balance in Appendix D.1, the shear stress ratio was derived as:

$$\frac{\tau}{\tau_o} = \frac{R_o}{r}\left(\frac{r^2 - r_m^2}{R_o^2 - r_m^2}\right) \tag{D3.1}$$

which can be rearranged as:

$$\frac{\tau}{\tau_o} = \frac{R_o}{y + R_i}\left[\frac{\left(\frac{R_i + y}{D}\right)^2 - \left(\frac{R_i + y_m}{D}\right)^2}{\left(\frac{R_o}{D}\right)^2 - \left(\frac{R_i + y_m}{D}\right)^2}\right] \tag{D3.2}$$

Using non-dimensional parameters, Eq. (D3.2) can be rewritten as:

$$\frac{\tau}{\tau_o} = \frac{(D^+ + R_i^+)(\zeta - \zeta_m)\left(2\frac{R_i^+}{D^+} + \zeta + \zeta_m\right)}{(\zeta D^+ + R_i^+)(1 - \zeta_m)\left(2\frac{R_i^+}{D^+} + 1 + \zeta_m\right)} \tag{D3.3}$$

Eq. (D3.3) can be further reduced to:

$$\frac{\tau}{\tau_o} = \frac{\left(1 + \frac{R_i^*}{D^*}\right)(\zeta - \zeta_m)\left(2\frac{R_i^*}{D^*} + \zeta + \zeta_m\right)}{\left(\zeta + \frac{R_i^*}{D^*}\right)(1 - \zeta_m)\left(2\frac{R_i^*}{D^*} + 1 + \zeta_m\right)} \tag{D3.4}$$

In the same manner, the shear stress ratio, τ / τ_i, becomes

$$\frac{\tau}{\tau_i} = \frac{\left(\frac{R_i^*}{D^*}\right)(\zeta_m - \zeta)\left(2\frac{R_i^*}{D^*} + \zeta + \zeta_m\right)}{\left(\zeta + \frac{R_i^*}{D^*}\right)\zeta_m\left(2\frac{R_i^*}{D^*} + \zeta_m\right)} \tag{D3.5}$$

or

$$\frac{\tau_i}{\tau_o} = \frac{1}{\alpha}\frac{\zeta_m\left(2\frac{R_i^*}{D^*} + \zeta_m\right)}{(1 - \zeta_m)\left(2\frac{R_i^*}{D^*} + \zeta_m + 1\right)} \tag{D3.6}$$

D.3.2 Heat Flux Ratio

From the heat balance given in Appendix D.1, the heat flux ratio was derived as:

$$\frac{q}{q_i} = \left(\frac{R_i}{r}\right)\left(\frac{R_o^2 - r^2}{R_o^2 - R_i^2}\right) \tag{D3.7}$$

which can be rearranged as:

$$\frac{q}{q_i} = \frac{\left(\frac{R_i}{D}\right)}{\left(\frac{R_i + y}{D}\right)} \left[\frac{\left(\frac{R_o}{D}\right)^2 - \left(\frac{R_i + y}{D}\right)^2}{\left(\frac{R_o}{D}\right)^2 - \left(\frac{R_i}{D}\right)^2}\right] \tag{D3.8}$$

Eq. (D3.8) can be further reduced as:

$$\frac{q}{q_i} = \frac{\left(\frac{R_i}{D}\right)}{\left(\frac{R_i + y}{D}\right)} \frac{(D - y)\,(D + y + 2R_i)}{D\,(D + 2R_i)} \tag{D3.9}$$

In non-dimensional parameters, Eq. (D3.9) can be rewritten as:

$$\frac{q}{q_i} = \frac{\left(\frac{R_i^*}{D^*}\right)}{\left(\frac{R_i^*}{D^*} + \zeta\right)} \frac{\left[(1 - \zeta)\,(1 + \zeta + 2\frac{R_i^*}{D^*})\right]}{\left[(1 + 2\frac{R_i^*}{D^*})\right]} \tag{D3.10}$$

APPENDIX D.4

Non-Dimensionalized Forms of Turbulence Model for a Concentric Annular Geometry

To solve the closure problems that arise in the turbulence fluctuation terms, the eddy viscosity term, ε_M/ν, requires mathematical modeling because it cannot be determined analytically. The term will exhibit the different behavior, depending on the state of the boundary layers. Usually, the boundary layer can be regarded as consisting of two layers. The first one, the viscous sublayer, is confined to a region of the flow near a solid boundary. Beyond of the viscous sublayer lays the fully turbulent regions. Therefore, both regions require the turbulence models, respectively.

D.4.1 Viscous Sublayer

In the viscous sublayer, the turbulence model proposed by van Driest [8] is used in the present analysis. The van Driest hypothesis [26] is a sublayer scheme that provides for an eddy diffusivity that is zero at y = 0. It has the virtue that it allows a continuous calculation through the sublayer and into the fully turbulent region with no discontinuity. In this scheme, the Prandtl mixing length [26] can be used to the wall instead of truncating it to zero at an assumed outer edge of the sublayer with a damping function.van Driest proposed that;

$$l = \kappa \cdot y \left(1 - \frac{1}{e^{y^+/A^+}}\right) \tag{D4.1}$$

where A^* is a constant determined empirically. Eq. (D4.1) in a form of eddy viscosity, ε_M / ν,

$$\frac{\varepsilon_M}{\nu} = \frac{l^2}{\nu}\frac{du}{dy} = \frac{l^{+2}}{\nu}\frac{du^+}{dy^+} \qquad \text{(D4.2)}$$

The combination of Eqs. (D4.1) and (D4.2) yields:

$$\frac{\varepsilon_M}{\nu} = (\kappa_j \cdot y_j^+)^2 \left[1 - \exp\left(-\frac{y_j^+}{A^+}\right)\right]^2 \left|\frac{\partial u_j}{\partial y_j}\right| \qquad \text{(D4.3)}$$

Substitution of Eq. (D4.2) into Eq. (D4.3) gives:

$$\left(\frac{\varepsilon_M}{\nu}\right)^2 + \frac{\varepsilon_M}{\nu} = (\kappa_j \cdot y_j^+)^2 \left[1 - \exp\left(-\frac{y_j^+}{A^+}\right)\right]^2 \left|\frac{\left(\frac{\tau}{\tau_R}\right)_j}{\left(1 + \frac{\epsilon_M}{\nu}\right)_j}\right| \qquad \text{(D4.4)}$$

Eq. (D4.4) is a form of an incomplete square polynomial about ε_M / ν:

$$ax^2 + bx + c = 0$$

The solutions are:

$$x = \frac{\varepsilon_M}{\nu}; \quad a = 1; \quad b = 1$$

and

$$c = (\kappa_j \cdot y_j^+)^2 \left[1 - \exp\left(-\frac{y_j^+}{A^+} \right) \right]^2 \left| \left(\frac{\tau}{\tau_j} \right) \right|$$

The positive root of the polynomial is:

$$\frac{\varepsilon_M}{\nu} = \frac{1}{2} \left[-1 + \sqrt{ 1 + 4 (\kappa_j \cdot y_j^+)^2 \left[1 - \exp\left(-\frac{y_j^+}{A^+} \right) \right]^2 \left| \left(\frac{\tau}{\tau_R} \right)_j \right| } \right] \tag{D4.5}$$

For further simplification of Eq. (D4.5) with the dimensionless parameter D^+, it becomes:

For viscous sublayer of the inner region of the annular flow:

$$\left(\frac{\varepsilon_M}{\nu} \right)_i = \frac{1}{2} \left[-1 + \sqrt{ 1 + 4 (\kappa_i \cdot D^+ \zeta)^2 \left[1 - \exp\left(-\frac{D^+ \zeta}{A^+} \left(\frac{\tau_i}{\tau_o} \right)^{0.5} \right) \right]^2 \left(\frac{\tau}{\tau_o} \right) } \right] \tag{D4.6}$$

For viscous sublayer of the outer region of the annular flow:

$$\left(\frac{\varepsilon_M}{\nu} \right)_o = \frac{1}{2} \left[-1 + \sqrt{ 1 + 4 \{\kappa \cdot D^+ (1 - \zeta)\}^2 \left[1 - \exp\left(-\frac{D^+ (1 - \zeta)}{A^+} \right) \right]^2 \left(\frac{\tau}{\tau_o} \right) } \right] \tag{D4.7}$$

With the variable von Kármán constant, κ_i, proposed for the first time in the present study, the expression of $(\frac{\varepsilon_M}{\nu})_j$ becomes:

(i) For the viscous sublayer of an inner region;

$$\left(\frac{\varepsilon_M}{\nu}\right)_i = \frac{1}{2}\left[-1 + \sqrt{1 + 4\{\kappa\cdot F(R_i)D^+\zeta\}^2\left[1 - \exp\left(-\frac{D^+\zeta}{A^+}\left(\frac{\tau_i}{\tau_o}\right)^{0.5}\right)\right]^2\left(\frac{\tau}{\tau_o}\right)}\,\right] \quad (D4.8)$$

$$0 \le \zeta \le \zeta_{is}$$

(ii) For the viscous sublayer of an outer region;

$$\left(\frac{\varepsilon_M}{\nu}\right)_o = \frac{1}{2}\left[-1 + \sqrt{1 + 4\{\kappa\cdot D^+(1-\zeta)\}^2\left[1 - \exp\left(-\frac{D^+(1-\zeta)}{A^+}\right)\right]^2\left(\frac{\tau}{\tau_o}\right)}\,\right] \quad (D4.9)$$

$$\zeta_{os} \le \zeta \le 1$$

D.4.2 Fully Turbulent Regions

Since the velocity profiles outside the viscous sublayers should differ from the law of the wall, the logarithmic law of the wall cannot be used. In the fully turbulent regions, the empirical model originally proposed by Reichadt [9] is used in a modified form as:

$$\left(\frac{\varepsilon_M}{\nu}\right)_j = \frac{\kappa_j\cdot y_j^+}{6}\left[1 - \left(\frac{r - r_m}{R_j - r_m}\right)^2\right]\left[1 + 2\left(\frac{r - r_m}{R_j - r_m}\right)^2\right] \quad (D4.10)$$

From the continuity of the momentum eddy diffusivity at the location of the maximum velocity at $\zeta = \zeta_m$, the Reichardt turbulence model can be rewritten as:

(a) For the fully turbulent layer of an inner region:

$$\left(\frac{\varepsilon_M}{\nu}\right)_i = \frac{\kappa_i \cdot y_m^+}{6}\sqrt{\frac{\tau_i}{\tau_o}}\left[1 - \left(\frac{y_m - y}{y_m}\right)^2\right]\left[1 + 2\left(\frac{y_m - y}{y_m}\right)^2\right] \qquad for \;\; y_{ts} \le y \le y_m \qquad \text{(D4.11)}$$

where variable von Kármán constant, $\kappa_i = \kappa \cdot F(R_i)$ proposed in Section 3.2. Eq. (D4.11) can be further simplified in non-dimensional parameters as:

$$\left(\frac{\varepsilon_M}{\nu}\right)_i = \frac{\kappa \cdot D^+}{6}(1-\zeta_m)E_c\left[\left(\frac{\zeta_m-\zeta}{\zeta_m}\right)^2\left\{1-2\left(\frac{\zeta_m-\zeta}{\zeta_m}\right)^2\right\}+1\right] \qquad for \;\zeta_{ts} \le \zeta \le \zeta_m \qquad \text{(D4.12)}$$

where $E_c = F(R_i)\,(\tau_i/\tau_o)^{0.5}\,\{\zeta_m/(1-\zeta_m)\}$

(b) For the fully turbulent layer of an outer region:

$$\left(\frac{\varepsilon_M}{\nu}\right)_o = \frac{\kappa_o}{6}(D-y_m)\left[1 - \left(\frac{y - y_m}{D - y_m}\right)^2\right]\left[1 + 2\left(\frac{y - y_m}{D - y_m}\right)^2\right] \qquad for \;\; y_{ts} \le y \le y_m \qquad \text{(D4.13)}$$

where κ_o is a constant, i.e., 0.4. Eq. (D4.13) can be further simplified using non-dimensional parameters:

$$\left(\frac{\varepsilon_M}{\nu}\right)_o = \frac{\kappa_o \cdot D^+}{6}(1-\zeta_m)\left[\left(\frac{\zeta-\zeta_m}{1-\zeta_m}\right)^2\left\{1-2\left(\frac{\zeta-\zeta_m}{1-\zeta_m}\right)^2\right\}+1\right] \qquad for \;\zeta_m \le \zeta \le \zeta_{os} \qquad \text{(D4.14)}$$

APPENDIX D.5

Non-Dimensionalized Forms of Other Fluid Parameters for a Concentric Annular Geometry

D.5.1 Bulk Velocity

The bulk velocity of the fluid across the concentric annulus cross-section is defined as:

$$u_b = \frac{\int_{R_i}^{R_o} u(r)\, 2\pi r\, dr}{\int_{R_i}^{R_o} 2\pi r\, dr} = \frac{2}{(R_o^2 - R_i^2)} \left[\int_{R_i}^{R_m} u(r)\, r\, dr + \int_{R_m}^{R_o} u(r)\, r\, dr \right] \tag{D5.1}$$

Eq. (D5.1) can be rearranged in dimensionless parameters as:

$$u_b = 2 \left(\frac{\nu}{R_i} \right) \left(\frac{\alpha}{1+\alpha} \right) \left[\int_0^1 u^+ (D^+ \zeta + R_i^+)\, d\zeta \right] \tag{D5.2}$$

or

$$u_b = 2 u_o^* \left(\frac{D^+}{R_i^+} \right) \left(\frac{\alpha}{1+\alpha} \right) \left[\int_0^1 u^+ \left(\zeta + \frac{R_i^+}{D^+} \right) d\zeta \right] \tag{D5.3}$$

D.5.2 Reynolds Number

The Reynolds number for a concentric annulus cross section is defined as:

$$Re_{De} = \frac{u_b De}{\nu} = \frac{u_b 2 (R_o - R_i)}{\nu} \tag{D5.4}$$

Eq. (D5.4) can be further reduced as:

$$Re_{De} = \frac{u_b 2 R_i (1 - \alpha)}{\alpha \nu} \tag{D5.5}$$

Substituting the bulk velocity, u_b, given in Eq. (D5.3) into Eq. (D5.5) and rearranging it in dimensionless terms yields:

$$\begin{aligned} Re_{De} &= \frac{4 R_i^* (1 - \alpha)}{\alpha} \left(\frac{D^*}{R_i^*} \right) \left(\frac{\alpha}{1+\alpha} \right) \left[\int_0^1 u^* \left(\zeta + \frac{R_i^*}{D^*} \right) d\zeta \right] \\ &= \frac{4 D^* (1 - \alpha)}{(1 + \alpha)} \left[\int_0^1 u^* \left(\zeta + \frac{R_i^*}{D^*} \right) d\zeta \right] \end{aligned} \tag{D5.6}$$

or

$$Re_{De} = \frac{4 (1 - \alpha)}{(1 + \alpha)} \left[\int_0^1 u^* (D^* \zeta + R_i^*) \, d\zeta \right] \tag{D5.7}$$

D.5.3 Friction Coefficient

The friction coefficient is defined as:

$$f = \frac{\tau_w}{\frac{1}{2}\rho u_b^2} \tag{D5.8}$$

For a concentric annulus cross-section, it becomes:

$$f = \frac{(R_o - R_i)}{\rho u_b^2}\left(-\frac{dp}{dx}\right) \tag{D5.9}$$

A force balance made for an element of fluid in the annlus gives:

$$\frac{dp}{dx}\pi(R_o^2 - R_i^2) = 2\pi(\tau_o R_o + \tau_i R_i) \tag{D5.10}$$

Substituting Eq. (D5.10) into Eq. (D5.9) yields:

$$f = -\frac{(R_o - R_i)}{\rho u_b^2}\frac{2(\tau_o R_o + \tau_i R_i)}{(R_o^2 - R_i^2)} \tag{D5.11}$$

where the bulk velocity, u_b, can be expressed as:

$$u_b = \frac{Re_{De} \cdot \nu}{2(R_o - R_i)} \tag{D5.12}$$

Substituting Eq. (D5.12) into Eq. (D5.11) gives:

$$f = -\frac{4(R_o - R_i)(R_o - R_i)^2}{\rho\, Re^2 \nu^2}\;\frac{2(\tau_o R_o + \tau_i R_i)}{(R_o^2 - R_i^2)}$$

$$= -\frac{8(R_o - R_i)^2}{\rho\, Re^2 \nu^2}\;\frac{(\tau_o R_o + \tau_i R_i)}{(R_o + R_i)}$$

$$= -\frac{8(R_o - R_i)}{Re^2}\left[R_i + \left(\frac{\tau_o}{\tau_i}\right)R_o\right]\left(\frac{\tau_i/\rho}{\nu^2}\right) \qquad \text{(D5.13)}$$

$$= -\frac{8(1-\alpha)}{Re^2\,\alpha}\,R_i^2\left[1 + \left(\frac{\tau_o}{\tau_i}\right)\alpha\right]\left(\frac{\tau_i/\rho}{\nu^2}\right)$$

where Re means Re_{De}.

Finally, the last expression of Eq. (D5.13) can be rearranged in dimensionless form as:

$$f = -8\left[\frac{\{1 + (\tau_i/\tau_o)\,\alpha\}\,(1-\alpha)^2}{(1+\alpha)}\right]\left(\frac{R_o^*}{Re}\right)^2 \qquad \text{(D5.14)}$$

where the shear stress distribution in dimensionless parameters is given as:

$$(\tau_i/\tau_o) = \frac{1}{\alpha}\;\frac{\{2(R_i^*/D^*) + \zeta_m\}\,\zeta_m}{\{2(R_i^*/D^*) + 1 + \zeta_m\}\{1-\zeta_m\}} \qquad \text{(D5.15)}$$

D.5.4 Bulk Temperature

The bulk temperature of the fluid across the concentric annulus cross-section is defined as:

$$T_b = \frac{\int_{R_i}^{R_o} u(r)\, T\, 2\pi r\, dr}{\int_{R_i}^{R_o} u(r)\, 2\pi r\, dr} \tag{D5.16}$$

A dimensionless temperature T_j^+ is defined as:

$$T^+ = \frac{(T_w - T)\, c_p\, \rho\, u_o^*}{q_i} \tag{D5.17}$$

Substitution of Eq. (D5.17) into Eq. (D5.16) and rearranging would yield:

$$T_b = \frac{T_w \int_{R_i}^{R_o} u(r)\, r\, dr}{\int_{R_i}^{R_o} u(r)\, r\, dr} - \frac{q_i}{\rho\, c_p\, u_o^*} \frac{\int_{R_i}^{R_o} u(r)\, T^+\, r\, dr}{\int_{R_i}^{R_o} u(r)\, r\, dr} \tag{D5.18}$$

which can be reduced to:

$$T_b = T_w - \frac{q_i}{\rho\, c_p\, u_o^*} \frac{\int_{R_i}^{R_o} u(r)\, T^+\, r\, dr}{\int_{R_i}^{R_o} u(r)\, r\, dr} \tag{D5.19}$$

Now, the bulk velocity, u_b, is:

$$u_b = \frac{2}{(R_o^2 - R_i^2)} \left[\int_{R_i}^{R_o} u(r)\, r\, dr \right] \tag{D5.20}$$

and

$$\int_{R_i}^{R_o} u(r)\, r\, dr = \frac{u_b 2\,(R_o^2 - R_i^2)}{2} = \frac{u_b 2\,(R_o - R_i)}{\nu} \frac{(R_o + R_i)\,\nu}{4} = Re \cdot \nu \cdot R_o \cdot \frac{1 + \alpha}{4} \tag{D5.21}$$

Also,

$$\frac{q_i}{c_p\, \rho\, u_o^*} \int_{R_i}^{R_o} u(r)\, T^*\, dr = \frac{q_i}{c_p \rho} (R_o - R_i)^2 \left[\int_0^1 \left(\zeta + \frac{R_i^*}{D^*} \right) u^*\, T^*\, d\zeta \right] \tag{D5.22}$$

Finally, substitution of Eqs. (D5.18) and (D5.19) into (D5.16) yields:

$$T_b^* = \frac{4\, D^*\, (R_o - R_i)}{Re\, R_o (1 + \alpha)} \int_0^1 (\zeta + \frac{R_i^*}{D^*})\, u^*\, T^*\, d\zeta \tag{D5.23}$$

Eq. (D5.23) can be further reduced to:

$$T_b^* = \frac{4}{Re} \frac{(1 - \alpha)}{(1 + \alpha)} \int_0^1 (D^* \zeta + R_i^*)\, u^*\, T^*\, d\zeta \tag{D5.24}$$

D.5.5 Nusselt Number

The Nusselt number is defined as:

$$Nu = \frac{h\,De}{k} = \frac{h\,2\,(R_o - R_i)}{k} \tag{D5.25}$$

where h is defined as:

$$h = \frac{q_i}{T - T_b} \tag{D5.26}$$

Substitution of Eq. (D5.26) into Eq.(D5.25) yields:

$$Nu = \frac{2\,(R_o - R_i)}{\left(k\,\dfrac{T_b^*}{c_p\,\rho\,u_o^*}\right)} \tag{D5.27}$$

Eq. (D5.27) can be further reduced as:

$$Nu = \frac{2\,D^*}{T_b^*}\,Pr \tag{D5.28}$$

APPENDIX E
Calculations of Deflection Rate for Inner Core

The electrically heated core tubes are supported at four points by the electrically insulated 3-point carriers which provide the radial adjustment of the core tubes as shown in Fig. E.1, as well as in Figs. 4.15 (a) and (b).

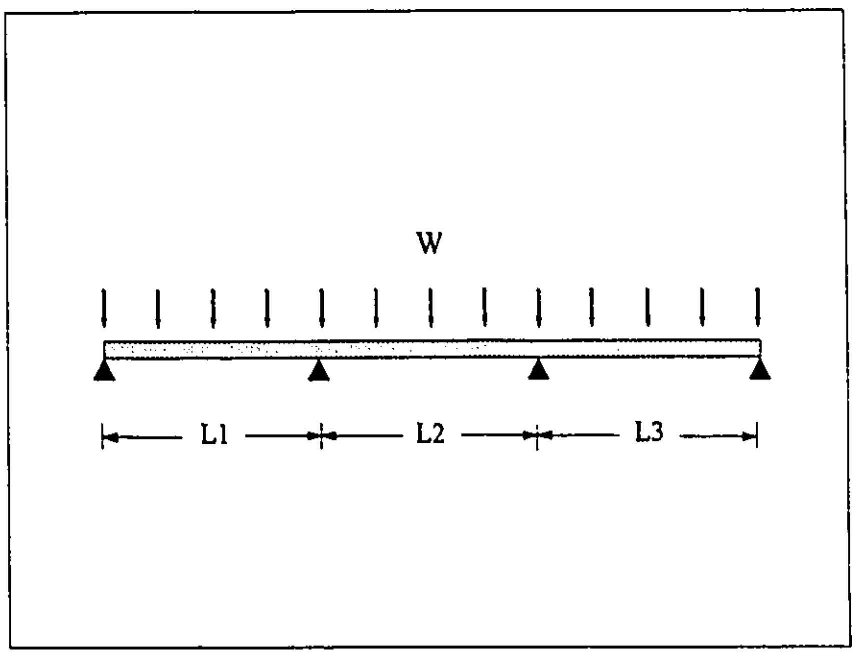

Figure E.1 The Schematic Drawing for Supported Inner Core

A stainless-steel wire (piano wire gage 30) is also provided to hold the rod in order to minimize flow disturbance in the developing flow region. A revolving steel ball is provided at the tip of each rod support to accommodate the axial expansion of the core tube when it is heated.

Consider the core as a simply supported beam as in Fig. E.2.

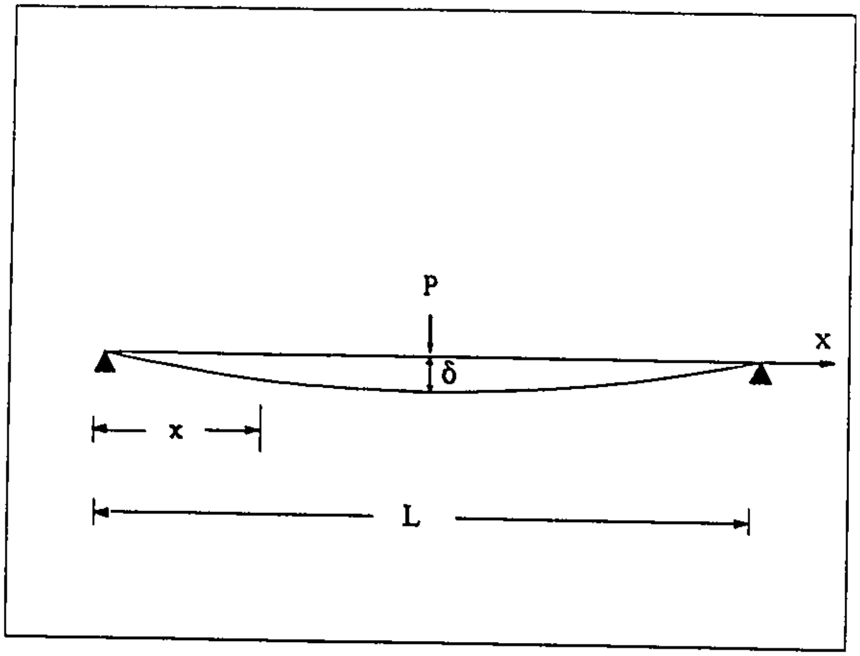

Figure E.2 Schematic Diagram of Simply Supported Beam

The deflection curve has the form of a half sine wave [109] as:

$$y = \delta \sin \frac{\pi x}{L} \tag{E.1}$$

In order to find the total strain energy stored in the beam, differentiating Eq. (E.1) twice with respect to x yields:

$$\frac{d^2y}{dx^2} = -\frac{\delta \pi^2}{L^2} \sin \frac{\pi x}{L} \tag{E.2}$$

The strain energy becomes :

$$U = \frac{EI}{2}\int_0^l \left(\frac{d^2y}{dx^2}\right)^2 dx = \frac{EI\pi^4\delta^2}{4L^3} \tag{E.3}$$

Equating this strain energy to the work done by the applied load is:

$$WL = \frac{EI\pi^4\delta^2}{4L^3} \tag{E.4}$$

Therefore the deflection is:

$$\delta^2 = \frac{4WL^4}{EI\pi^4} \tag{E.5}$$

and the equation for the moment of inertia is :

$$I = \frac{\pi(D_o^4 - D_i^4)}{64} \qquad [m^4] \tag{E.6}$$

The values of each variable are given as:E = 2.07 x 10^{11} N/m^2 for stainless steel 304, and the weight per unit length, W, 7.8 x 10^{-3} kg/cm^3 [109].

Using Eqs. (E.1), (E.2) and (E.3), the deflection rates for each test section are calculated and are listed in Table E.1. The measured deflection rates are listed in Table E.2.

Table E.1 Theoretical Deflection Rates for Test Sections

Test Section	Deflection Rate, m	Rate of Eccentricity
1	6.59×10^{-3}	1.00 %
2	4.28×10^{-3}	1.27 %
3	6.74×10^{-3}	0.56 %

Table E.2 Measured Deflection Rates for Test Sections

Position		Deflection Rate		
		Test Section 1	Test Section 2	Test Section 3
Midway	Top (0°)	0.08 %	0.23 %	0.28 %
	Left (120°)	0.01 %	0.48 %	0. 48 %
	Right (270°)	0.04 %	0.27 %	0.37 %

APPENDIX F
Numerical Computation and Sample Calculation

Most of the theoretical calculation requires numerical integration where accuracy of the computation is very important.In most cases, Simpson's rule was used for the numerical integration and was checked by repeating the integration process with varying mesh sizes. For the numerical calculations in the present study, using FORTRAN language, a number of computer programs were prepared for the numerical evaluation of the theoretical expressions for the various parameters in Chatpers 3. Sample flow diagrams of numerical computation for the friction coefficient in Eq. (3.75) and the Nusselt number in Eq. (3.86) are shown in Figs. F.1 and F.2.

To clarify the procedure for the computation of the results presented in Chapter 5, one of typical experiment with the annulus having a radius ratio of 0.3 (R_i = 16.7 mm) has been chosen as an illustration.

F.1. Pressure Drop Experiment (Test Section 1)

(1) Initial Conditions:

$\alpha = 0.3$

$R_i = 16.7$ mm

$R_o = 48.7$ mm

$De = 2 \cdot (R_o - R_i) = 64$ mm

Temperature = 20°C

(2) Flow Rate

$$Q = 0.768\sqrt{manometer\ reading} = 3.46\ [m^3/\text{min}]$$

Manometer reading measures pressure drop across the edge orifice inlet to the annulus apparatus. The manometer is read in mm alcohol.

(3) Average Velocity in Annulus

$$\bar{u} = 0.768\,\frac{\sqrt{manometer\ reading}}{60A} = 8.78\ [m/\text{sec}]$$

where A is the area of the annular cross section.

(4) Reynolds Number

$$Re = \frac{\bar{u}\,De}{\nu} = 39{,}700$$

(5) Shear Stress

$$\tau = \frac{De}{4}\frac{dp}{dx}$$

$$\frac{dp}{dx} = 17.55\ [N/m^3]$$

$$\tau = 0.2813\ [kg/m^2]$$

(6) Overall Friction Factor

$$f = \frac{\tau}{0.5\,\rho\,\bar{u}^2} = 0.0062$$

(7) Eddy diffusivity for momentum

$$\frac{\varepsilon_M}{\nu} = \frac{\left(\dfrac{\tau_i}{\rho_{air}}\right)}{\left(\dfrac{du}{dy}\,\nu\right)} - 1 = 21.1$$

F.2. Heat Transfer Experiment (Test Section 1)

(1) Initial Conditions:

$\alpha = 0.3$

$R_i = 16.7$ mm

$R_o = 48.7$ mm

$De = 2 \cdot (R_o - R_i) = 64$ mm

Temperature = 20°C

(2) Flow Rate

$$Q = 0.768\,\sqrt{manometer\ reading} = 3.46\ [m^3/\text{min}]$$

(3) Reynolds Number

$$Re = \frac{\bar{u}\,De}{\nu} = 39{,}700$$

(4) Heat Flux (calculated from electrical power input less heat loss through outer wall)

$$q = \frac{I\,E}{\pi \cdot D_i \cdot dx} - q_{loss} = 1{,}534 \;\; [W/m]$$

(5) Inlet Temperature of Air = 20°C

(6) Bulk Temperature

$$T_b = \frac{q}{\pi\,(R_o^2 - R_i^2)\,u_b\,c_p\,\rho_{air}\,3600} + T_{air} = 23.5 \;\; [°C]$$

(7) Heat Transfer Coefficient

$$h = \frac{q}{2\,\pi\,R_i\,(T_w - T_b)} = 30.5 \;\; [W/m^2 \cdot °C]$$

(8) Nusselt Number

$$Nu = \frac{h\,De}{k} = 82.53$$

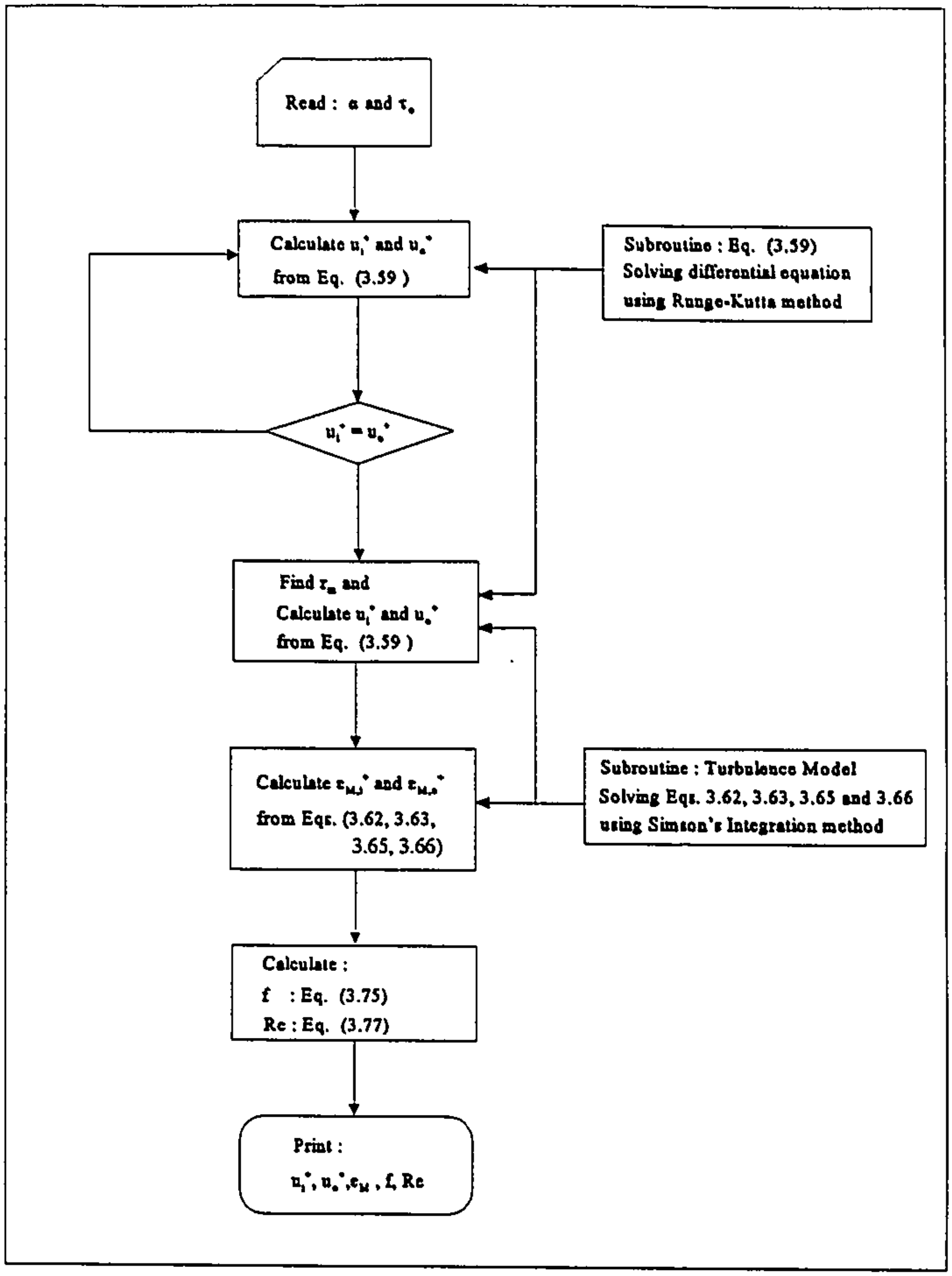

Figure F.1 Simplified Flow Diagram of Friction Factor

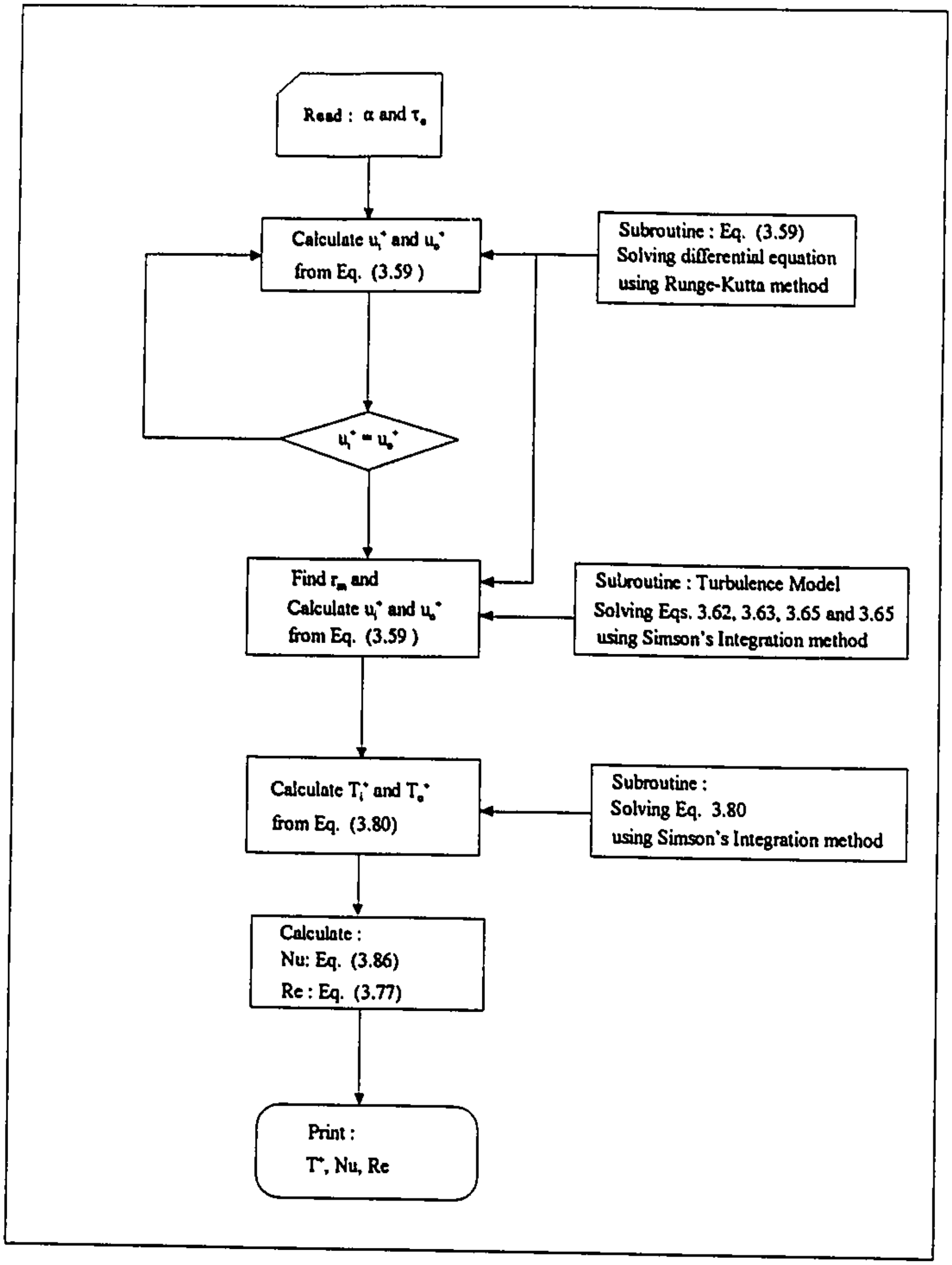

Figure F.2 Simplified Flow Diagram of Nusselt Number Calculation

REFERENCES

1. Prandtl, L., "Über Flüssig keitsbewegung bei sehr kleiner Reibung", Proc. 3rd. Int. Math. Cong. Heidelberg, (1904); Reprinted in NACA TM 452, (1928).
2. Patel, V.C. et al, "Measurements in the Thick Axisymmetric Turbulent Boundary Layer near the Tail of a Body of Revolution", J. Fluid Mech., **63**, 345-367, (1974).
3. Shigechi,T., Kawae, N., and Lee, Y., "Turbulent Fluid Flow and Heat Transfer in Concentric Annuli with Moving Core", Int. J. Heat Mass Transfer, **33**, 2029-2037, (1990).
4. Park, S.D., "Developing Turbulent Flow in Concentric Annuli: An Analytical and Experimental Study", Ph.D. Thesis, Univ. Of Ottawa, (1971).
5. Barrow, H., Lee Y., and Roberts A., "The Similarity Hypothesis Applied to Turbulent Flow in An Annulus, Int. J. Heat Mass Transfer, **8**, 1499-1505, (1965).
6. Jonsson, V.K. and Sparrow, W., "Experiments on Turbulent Flow Phenomena in Eccentric Annular Ducts", J. Fluid Mech., **25**, 65-86, (1965).
7. Hornby, R.P., Mistry, J. and Barrow, H., "A Mixing Length Model for Turbulent Flow in Constant Cross Section Duct", Wärme-und Stoffübertragung, **10**, 125-129, (1977).
8. van Driest, E. R., "On Turbulent Flow Near a Wall", J. Aero. Sci., **23**, 1007-1012, (1956).
9. Reichardt, H., "Die Wärmeübertragung in turbulenten Reibungschichten", Z. Angew. Math. Mech., 20, 297, (1940) (Available in English translation as NACA TM1047, (1943).

10. Moser, R.D. and Moin, P., "Direct Numerical Simulation of Curved Turbulence Channel Flow", NASA TM 85974, (1984).

11. Neves, et al., "Effects of Convex Transverse Curvarture on Wall Bounded Turbulence. Part 2. The Pressure Fluctuations", J. Fluid Mech., **272**, 383-406, (1994).

12. Spalart, P., "Direct Simulation of a Turbulent Boundary Layer up to R_θ = 1410", J. Fluid Mech., **187**, 61-98, (1988).

13. Moin, P. and Kim, J., "On the Numerical Solution of time- dependent viscous incompressible fluid flows involving solid boundaries", J. Comp. Phys., **35**, 381-392, (1980).

14. Moin, P. and Kim, J., "Numerical Investigation of Turbulent Channel Flow", J. Fluid Mech., **118**, 341-377, (1982).

15. Moin, P. and Kim, J., "The Structure of the Vorticity Field in Turbulent Channel Flow. Part 1. Analysis of Instantaneous Fields and Statistical Correlations", J. Fluid Mech., **155**, 441-464, (1985).

16. Deissler, R.G., "Analytical Investigation of Turbulent Flow in Smooth Tubes with Heat Transfer with Variable Fluid Properties for Prandtl Number of 1", NACA TN-2242, December, (1950).

17. Laufer, J., "Investigation of Turbulent Flow in a Two-dimensional Channel", NACA Rep. 1053, (1951).

18. Barbin, A.R. and Jones, J.B., "Turbulent Flow in the Inlet Region of a Smooth Pipe", Journal of Basic Engng., Trans. ASME, **85**, 29-34, (1963).

19. Clark, J.A., "A Study of Incompressible Turbulent Boundary Layers in Channel Flow", J. Basic Engng., Trans. ASME, **90**, 455-468, (1968).

20. Eckelmann, H., "The Structure of the Viscous Sublayer and the Adjacent Wall Region in a Turbulent Channel Flow", J. Fluid Mech., **65**, 439-459, (1974).

21. Hussain, A.K.M.F. and Reynolds, W.C., "Measurements in Fully Developed Turbulent Channel Flow", J. Fluids Engng., Trans. ASME, **97**, 568-580, (1975).

22. Johansson, A.V. and Alfredsson, P.H., "On the Structure of Turbulent Channel Flow", J. Fluid Mech., **122**, 295-314, (1982).

23. Johansson,A.V. and Alfredsson, P.H., "Effects of Imperfect Spatial Resolution on Measurement of Wall-bounded Turbulent Shear Flows", J. Fluid Mech., **137**, 409-421, (1983).

24. Kim, J. et al., "Turbulence Statistics in Fully Developed Channel Flow at Low Reynolds Number", J. Fluid Mech., **177**, 133-166, (1987).

25. Landweber, L., "Effect of Transverse Curvature on Frictional Resistance", Dawd Taylor Model Basin Report 689, (1949).

26. Kays, W. and Crawford, M., Convective Heat and Mass Transfer, McGraw-Hill, 2nd ed. New York, (1980).

27. Eckert, E.R.G, Hantnett, J.P and Birkerak, R, "Simplified Equations for Calculating Local and Total Heat Flux to Non-isothermal Surface", J. Aerospace Science, 24, 549-551, (1957).

28. Glauert, H.B. and Lighthill, M.J., "Axisymmetric Boundary-layer on A Long Cylinder", Proceeding of Royal Society, London, Series A, 230, 188, (1955).

29. Coles, D.," The Law of the Wake in the Turbulent Boundary Layer", J. Fluid Mechanics, **1**, 191-226, (1956).

30. Yu, Y. S., "Effect of Transverse Curvarture on Turbulent Boundary Layer Characteristics", J. Ship Research, **2**, 33-51, (1958).

31. Willmarth, W.W. and Yang, C.S., "Wall Pressure Fluctuations beneath Turbulent Boundary Layers on a Flat Plate and a Cylinder", J. Fluid Mech., **41**, 47-80, (1970).

32. Patel, V.C., "Calibration of the Preston Tube and Limitations on Its Use in Pressure Gradients", J. Fluid Mech., **23**, 185-208, (1965).

33. Yasuhara, M, "Experiment of Axisymmetric Boundary Layers along a Cylinder in Compressible Fows", Trans. Japan Soc. of Aerospace Sciences, **2**, 33-72, (1959).

34. Lueptow, R.M., Leehey, P. and Stellinger, T., "The Thick, Turbulent Boundary Layer on a Cylinder: Mean and Fluctuating Velocities", Phys. Fluids, **28**, 3495-3505, (1985).

35. Lueptow, M.R. and Haritonidis, J.H., "The Structure of Turbulent Boundary Layer on a Cylinder in Axial Flow", Phys. Fluid, **30**, 2993-3005, (1987).

36. Sparrow, E.M., Eckert, E.R.G. and Minkowycs, W.J., "Heat Transfer and Skin Friction for Turbulent Boundary Layer Flow Longitudinal to a Circular Cylinder", J. Appl. Mech., Trans. ASME, **83**, 37-43, (1963).

37. Cebeci, T. et al., "Solution of the Incompressible Turbulent Boundary Layers Equations with Heat Transferon", J. Heat Transfer, Trans. ASME., **92**, 133-143, (1970).

38. Rao, G.N.V., "The Law of the Wall in a Thick AxisymmetricTturbulent Boundary Layer", J. Appl. Mech., **34**, 237-238, (1967).

39. Rao, G.N.V. and Keshavan, N.R., "Axisymmetric Turbulent Boundary Layers in Zero Pressure Gradient Flows", J. Appl. Mech., **39**, 25-32, (1972).

40. White, F.M., Lessmann, G.H. and Christoph, G.H., "Analysis of Turbulent Skin Friction in Thick Axisymmetric Boundary Layers", AIAA J., **11**, 821-825, (1973).

41. Bradshaw, P. and Cebeci, T., "Comment on Mean Velocity Profile of a Thick Turbulent Boundary Layer along a Circular Cylinder", AIAA J., **11**, 893-895, (1973).

42. Afzal, N. and Narasimha, R., "Axisymmetric Turbulent Boundary Layer along a Circular Cylinder at Constant Pressure", J. Fluid Mechanics, **74**, 113-128, (1976).

43. Afzal, N. and Narasimha, R., "Asymptotic Analysis of Thick Axisymmetric Turbulent Boundary Layers", AIAA J., **23**, 963-965, (1985).

44. Denli, N. and Landweber, "Thick Axisymmetric Turbulent Boundary-Layer on a Circular Cylinder", J. Hydronautic, **13**, 92-104, (1979).

45. Kim, K.C., Lee, Y. and Ma, E, "Effect of Transverse Convex Curvature on Turbulent Flow and Heat Transfer", First International Symposium on Experimental and Computational Aerothermodynamics of Internal Flows, Beijing, 202-207, (1990).

46. Lee, Y. and Kim, K.C., "An Analysis on Effect of Transverse Convex Curvature on Turbulent Flow and Heat Transfer", Wärme-und Stoffübertragung, **28**, 89-95, (1993).

47. Kim, K.C. and Lee, Y., "Effect of Transverse Convex Curvature on Heat Transfer from Heated Cylinders with Axisymmetric Backward-facing Steps", Int. J. Heat Mass Transfer, **39**, 1763-1767, (1996).

48. Deardorff, J.W., "A Numerical Study of Three-dimensional Turbulent Channel Flow at Large Reynolds Number", J. Fluid Mech., **41**, 453-480, (1970).

49. Moin, P. and Kim, J., "On the numerical solution of time- dependent viscous incompressible fluid flows involving solid boundaries", J. Comp. Phys., **35**, 381-392, (1980).

50. Knudsen, J. G. and Katz, D. L., Fluid Dynamics and Heat Transfer, McGraw-Hill, New York, Chapter 8, (1950).

51. R.R. Rothfus, C.C.Monrad, and V.E. Senecal, "Velocity Distribution and Fluid Friction in Smooth Concentric Annuli", Industrial and Engineering Chemistry, **42**, 2511-2520, (1950).

52. Lamb, H., Hydodynamics, 5th Ed., Canbridge Univ. Press., London, (1924).

53. Lee, Y.and Barrow, H., "Turbulent Flow and Heat Transfer in Concentric and Eccentric Annuli", I Mech. E, **178**, 1-16, (1963).

54. Lawn, C.J. and Elliot, C.J., "Fully Developed Turbulent Flow through Concentric Annuli", J. Mech. Eng. Sci., **14**, 195-204, (1972).

55. Kays, W.M. and Leung, E.Y., "Heat Transfer in Annular Passages Hydrodynamicaly Developed Turbulent Flow with Arbitrarily Prescribed Heat Flux", J. Heat Mass Transfer, **6**, 537-557, (1963).

56. Brighton , J.A. and Jones, J.B., "Fully Developed Turbulent Flow in Annuli", J. Basic Eng., Trans. ASME, **86**, 835-844, (1964).

57. Beck, H., "Warmeübergang und Druck erlust in konzentrischen und exzentrischen Ringspalten bei erzwungener Strömung und freier Konvektion", Dr.-Ing. Dissertation, Technische Hochschule Karlsruhe, Germany, (1960).

58. Reynolds, W.C., Lundberg, R.E., and McCuen, P.A., "Heat Transfer in Annular Passages. General Formulation of the Problem for Arbitrarily Prescribed Wall Temperatures or Heat Fluxes", J. Heat Mass Transfer, **6**, 483-493, (1963).

59. Mizushina, T., "Analogy between Fluid Friction and Heat Transfer in Annuli", General Discussion on Heat Transfer, Inst. Mech. Eng., 191, (1951).

60. Levy, S., "Turbulent Flow in an Annulus", J. of Heat transfer, Trans. ASME, **89**, 25-31, (1967).

61. Wilson, N.W. and Medwell, J.O., "An Analysis of the Developing Turbulent Hydrodynamic and Thermal Boundary Layers in an Internally Heated Annulus", Paper No.70-HT-9, Trans. ASME, 1-7, (1970).

62. Quarmby, A., and Anard, R.K., "Fully Developed Turbulent Heat Transfer in Concentric Annuli with Uniform Wall Heat Fluxes", Chem. Eng. Sci., **24**, 171-187, (1969).

63. Lee, Y. and Park, S.D., "Developing Turbulent Flow in Concentric Annuli: An Analytical and Experimental Study", Wärme-und Stoffübertragung, **4**, 156-166, (1971).

64. Bailey, R. V., "Heat Transfer to Liquid Metals in Concentric Annuli", Oak Ridge Nat. Lab. Report ORNL-521, (1950).

65. Lee, Y., "Turbulent Flow and Heat Transfer in Concentric and Eccentric Annuli", Ph.D. Thesis, Univ. of Liverpool, (1964).

66. Rehem, K., "Turbulent Flow in Smooth Concentric Annuli with Small Radius Ratio", J. Fluid Mech., **64**, 263-287, (1974).

67. Quarmby, A., "An Experimental Study of Turbulent Flow through Concentric Annuli", Int. J. Mech. Sci., **9**, 205-221, (1967).

68. Lorenz, F.R., "On Turbulent Flow through Annular Passage", Communications, Institute of Fluid Mechanics, Karlsruhe, (1932) (Data are reported in Ref. 57).

69. Owen, W.M., "Experimental Study of Water Flow in Annular Pipes", Proc. ASCE, 77, Separate No. 88, (1951) (Data are reported in Ref. 57).

70. Ivey, C.M., "The Position of Maximum Velocity in Annular Flow", M.Sc. Thesis, University of Windsor, Canada, (1965) (Data are reported in Ref. 55).

71. Jones, W.P. and Launder, B.E., "The Prediction of Laminarization with a Two-equation Model of Turbulence", Int. J. Heat Mass Transfer, **15**, 301-314, (1972).

72. Launder, B.E. and Spalding, D.B., "The Numerical Computation of Turbulent Flow", Comp. Methods in App. Mech. Eng., **3**, 269-289, (1974).

73. Ng, K.H. and Spalding D.B., "Predictions of Two-dimensional Boundary-layes on Smooth walls with a Two-equation Model of Turbulence", Int. J. Heat Mass Transfer, **19**, 1161-1171, (1976).

74. Leschziner, M.A. and Rodi, W., "Calculation of Annular and Twin Parallel Jets Using Various Discretization Schemes and Turbulence Model Variations", J. Fluid Eng., **103**, 352-360, (1981).

75. Lee, B.K., Cho, N.H. and Choi, Y.D., "Analysis of Periodically Fully Developed Turbulent Flow and Heat Transfer by k-ε Equation Model in Arificially Roughened Annulus", Int. J. Heat Mass transfer, **31**, 1797-1806, (1988).

76. Fujji, S., Akino, N., Kawamura, H. and Sanokawa, K., "Experimental and Theoritical Investigations on Heat Transfer of Strongly Heated Turbulent Gas Flow in an Annular Duct', Int. J. JSME series II, **34**, 348-354, (1991).

77. Torii, S., Shimizu, H., Hasegawa, S. and Kusama, N., "Laminarization of Strongly Heated Annular Gas Flow", Int. J. JSME, Series II, **34**, 157-168, (1991).

78. Dasai, C.P. and Vafai, K., "An Investigation and Comparative Analysis of Two- and Three-dimensional Turbulent Natural Convection in a Horizontal Annulus', Int. J. Heat Mass Transfer, **37**, 2475-2504, (1994).

79. Schlichting, H., Boundary Layer Theory, 6th ed., McGraw-Hill, New York, 408-445, (1968).

80. White, F. M., Fluid Mechanics, 2nd ed., McGraw-Hill, Singapore, 330-332, (1968).

81. Gräber, H., "Der Wärmeübergang in glatten Rohren, zwischen parallelen Platten, in Ringspalten and längs Rohrbündeln bei exponentieller Wärmeflussverteilung in erzwungener laminarer oder turbulenter Strömung", Int. J. Heat Mass Transfer, **13**, 1645-1703, (1970).

82. McEligot, D.H. and Taylor, M.F., "The Turbulent Prandtl Number in the Near-Wall Region for Low-Prandtl-number Gas Mixtures", Int. J. Heat Mass Transfer, **39**, 1287-1295, (1996).

83. Reynolds A.J., "The Prediction of Turbulent Prandtl and Schmidt Numbers", Int. J. Heat Mass Transfer, **18**, 1055-1069, (1975).

84. Young, A.D., Boundary Layers, BSP Professional Books, London, 37-47, (1989).

85. Launder, B.E., Morse, A. and Spalding, D.B., "The Prediction of Free Shear Stress Flows-A Comparision of the Performance of Six Turbulence Models", Proc. Langley Free Shear Flows Conference, NASA SP321, (1973).

86. Hanjalic, K and Launder, B.E., "A Reynolds-strss Model of Turbulence and Its Application to Asymmetric Shear Flows", J. Fluid Mechanics, **52**, 609-638, (1972).

87. Wyngaard, J.C., Arya, S.P.S. and Coté, O.R., "Some Aspects of the Structure of Convective Planetary Boundary Layers", J. Atmos. Sci., **31**, 747, (1974).

88. Launder, B.E., Reece, G.J. and Rodi, W., "Progress in the Development of A Reynolds Stress Turbulence Closure", J. Fluid Mechanics, **68**, 537-566, (1975).

89. Gibson, M.M. and Launder, B.E., "Ground Effect on Pressure Fluctuations in the Atmospheric Boundary-Layer", J. Fluid Mechanics , **86**, 491-511, (1978).

90. Spalding, D.B., Turbulence Models, Imperical College of Science and Technology, London, (1982).

91. Restivo, A.M.O., "Turbulent Flow in Ventillated Rooms", Ph.D. Thesis, Imperical College, London, (1979).

92. Chieng, C.C. and Launder, B.E., "On the Calculation of Turbulent Heat Transport Downstream from Abrupt Pipe Expansion", The Winter Annual Meeting of the ASME, Chicago, I11, Nov., 16-21, (1980).

93. Patankar, S.V. and Spalding, D.B., "A Calculation Procedure for Heat Mass and Momentum Transfer in Three-dimensional Parabolic Flows", Int. J. Heat Mass Transfer, **15**, 1787, (1972).

94. Hoffmann, K.A., Computational Fluid Dynamics for Engineer, Engineering Education System, Austin, Tx, U.S.A., 248-303, (1989).

95. Patankar, S.V., Numerical Heat Transfer and Fluid Flow, McGraw-Hill, New York, (1980).

96. Olson, R.M., and Sparrow, E.M., "Measurements of Turbulent Flow Development in Tubes and Annuli with Square of Rounded Entrances", A.I.Ch.E. J., **9**, 776-770, (1963).

97. Okishi, T.H. and Sarovy, G.K., "An Experimental Study of the Turbulent Flow Boundary-Layer Development in Smooth Annuli", J. Basic Eng. Trans ASME, **89**, 823-836, (1967).

98. Lee, Y., "Turbulent Heat Transfer from the Core Tube in Thermal Entrance Regions of Concentric Annuli", Int. J. Heat Mass Transfer, **11**, 509-522, (1968).

99. Lee, Y. and Mital, U., "A Two-phase Closed Thermosyphone", Int. J. Heat Mass Transfer, **15**, 1695-1707, (1972).

100. British Standard Code, Orifice Plate with Corner Tapping, B.S. 1042: Part 1, 107, (1964).

101. ASTM STP 470A, Manual on the Use of Thermocouples in Temperature Measurement, 3rd, ASTM, U.S.A., (1979).

102. McAdams, W.H., Heat Transmission, McGraw-Hill, New York, (1954). (Content is refered in the book)

103. Holman, J.P., Heat Transfer, 7th Ed., McGraw-Hill, New York, (1990).

104. MacMillane, F.A., Experiments on Pitot Tubes in Shear Flow, A.R.C., R&M 3028, (1957).

105. Quarmby, A. and Das, M.K., "Displacement Effects on Pitot Tubes with Rectanggular Mouths", The Aeronautical Quarterly, (1961).

106. Young, A.D. and Maas, J.N., The Behaviour of a Pitot Tube in a Transverse Pressure Gradient, A.R.C., R&M 1770, (1937).

107. Holman, J.P., Experimental Mothods for Engineers, 3rd Ed., McGraw-Hill, New York, (1985).

108. Hilderbrand, F.B., "Introduction on Numerical Analysis", McGraw-Hill, New York, 64-68, (1956).

109. Crandall, S.H., Dahl, N.C. and Lardner, T.J., An Introduction to the Mechanics of Solids, 2nd, McGraw-Hill, Tokyo, (1978).

110. Eckert, E.R.G. and Drake, R.M., Heat and Mass Transfer, McGraw-Hill, New York, (1959).

Table 2.1 Similarity Laws for the Axisymmetric, Turbulent Boundary Layer Flow

Author	Sublayer	Law of wall	Outer law
Planar Law [26]	$u^+ = y^+$	$u^+ = A \ln (y^+) + B$ A, B universal	$(u_\infty - u)/u^* = C \ln (y/\delta) + D$ C, D : universal
Richmond [26]		$u^+ = A \ln \{y^+ [1+(y/2 R_i)]\} + B$ A, B universal	
Yu [30]		$u^+ = A \ln (y^+) + B$ A : universal B : function of Re_{R_i}	$(u_\infty - u)/u^* = C \ln (y/L) + D$ C : universal D : function of Re_{R_i} L : based on u^* and ν
Rao [38]	$u^+ = R_i^+ \ln (r/R_i)$	$u^+ = A \ln [R_i^+ \ln (r/R_i)] + B$ A, B : functions of Re_{R_i}, R_i^+	
Bradshaw and Patel [41]		$u^+ = A \ln \{4y^+/[1+(r/R_i)^{0.5}]^2\}+B$ A : universal B : function of R_i^+	
Afzal and Narasima [42]		$u^+ = A \ln (y^+) + B (1/R_i^+)$ $u^+ = A \ln (y^+) + D (\delta/R_i)$ A : universal B : function of $1/R_i^+$ D : function of δ/R_i, R_i^+	
Denli and Landweber [44]		$u^+ = A \ln [R_i^+ (r/R_i)^{0.5} \ln (r/R_i)] +B$ A : universal B : function of R_i^+	

Table 2.2 Major Experiments for a Concentric Annulus

Author	Radius Ratio α ($=R_i/R_o$)	Tube Diameter (mm)		Working Fluid
		Inner	Outer	
Rheme [66]	0.02	1.98	99.97	Air
	0.04	3.96		
	0.1	9.98		
Lee and Barrow [53]	0.258	25.4	101.6	Air
	0.387	38.7		
	0.613	60.3		
Brighton and Jones [56]	0.0625	12.7	203.2	Air, water
	0.125	25.4		
	0.375	76.2		
	0.562	114.3		
Lawn and Elliot [54]	0.088	12.7	144.3	Air
	0.176	25.4		
	0.396	57.1		
Quarmby [67]	0.107	8.0	73.2	Air
	0.174	12.7		
	0.347	25.4		
Lee and Park [63]	0.065	6.4	97.4	Air
	0.261	25.4		
	0.433	42.2		
	0.621	60.3		

Table 3.1 Variable von Kármán Constant, κ_i

R_i (m)	κ_i
0.01*	0.958
0.02*	0.921
0.063*	0.768
0.125*	0.606
0.25*	0.366
0.5*	0.419
1.0*	0.303
0.25**	0.548
0.5**	0.52
1.0**	0.443

* Deduced from experimental data [45]

** Deduced from experimental data [31]

Table 3.2 Theoretical Local Skin Friction Coefficient, $C_{f,x}$, Turbulent Boundary Layer Flow, u_∞ = 15 m/s

	$C_{f,x}$		
Re_x	R_i = 6.35 mm	R_i = 12.7 mm	R_i = 25.4 mm
	Re_{Ri} = 6,500	Re_{Ri} = 13,000	Re_{Ri} = 26,000
50,000	0.0078125	0.0075055	0.0073013
60,000	0.0076193	0.0072538	0.0070311
70,000	0.0074266	0.0070505	0.0068267
80,000	0.0072790	0.0068847	0.0066531
90,000	0.0071480	0.0067416	0.0065018
100,000	0.0070385	0.0066248	0.0063711
110,000	0.0069433	0.0065110	0.0062644
120,000	0.0068615	0.0064262	0.0061651
130,000	0.0067812	0.0063379	0.0060778
140,000	0.0066634	0.0062616	0.0059971
150,000	0.0066578	0.0061965	0.0059226
160,000	0.0065974	0.0061324	0.0058539
170,000	0.0065486	0.0060694	0.0057954
180,000	0.0065003	0.0060215	0.0057422
190,000	0.0064578	0.0059695	0.0056853
200,000	0.0064105	0.0059228	0.0056336

Table 3.3 Theoretical Local Nusselt Number, Nu_x, Turbulent Boundary Layer Flow, Pr = 0.71 (u_∞ = 15 m/s)

Nu_x			
Re_x	R_i = 6.35 mm	R_i = 12.7 mm	R_i = 25.4 mm
	Re_{Ri} = 6,500	Re_{Ri} = 13,000	Re_{Ri} = 26,000
50,000	136.15	113.45	100.06
60,000	156.80	134.23	118.00
70,000	181.22	154.51	135.55
80,000	204.86	174.54	152.96
90,000	229.06	195.15	170.93
100,000	252.68	214.33	188.38
110,000	275.64	235.11	205.58
120,000	299.08	253.74	221.99
130,000	322.55	273.56	238.83
140,000	366.37	293.09	256.59
150,000	368.51	312.38	273.33
160,000	392.06	331.69	289.28
170,000	414.91	351.03	306.57
180,000	439.50	369.64	322.54
190,000	461.39	390.44	339.85
200,000	486.50	409.37	355.85

Table 3.4 Theoretical Local Nusselt Number, Nu_x, Turbulent Boundary Layer Flow, u_∞ = 15 m/s

R_i = 6.35 mm				
Re_x	Pr = 0.01	Pr = 0.7	Pr = 1	Pr = 10
	Nu_x	Nu_x	Nu_x	Nu_x
50,000	13.96	136.15	166.24	487.70
60,000	16.40	156.80	191.40	561.04
70,000	19.04	181.22	221.17	647.74
80,000	21.70	204.86	249.98	731.61
90,000	24.25	229.06	279.47	817.39
100,000	27.01	252.68	308.25	901.09
110,000	29.53	275.64	336.23	982.42
120,000	32.10	299.08	364.78	1065.42
130,000	34.85	322.55	393.38	1148.46
140,000	37.26	366.37	423.31	1235.41
150,000	39.85	368.51	449.36	1311.06
160,000	42.44	392.06	478.04	1394.31
170,000	45.26	414.91	505.87	1475.09
180,000	47.78	439.50	535.82	1562.04
190,000	50.30	461.39	562.47	1639.36
200,000	53.26	486.50	565.81	1728.05

Table 3.5 Theoretical Radius of Maximum Velocity, r_m, Fully Developed Turbulent Flow
$\alpha = 0.3$, Re = 20,000

$\zeta_m = \frac{r_m - R_i}{R_o - R_i}$	R_i		
	16.7 mm	8.57 mm	3.98 mm
ζ_m	0.432	0.440	0.443

Table 3.6 Theoretical Radius of Maximum Velocity, r_m, Fully Developed Turbulent Flow,
Re = 20,000

α	$(r_m - R_i) / (R_o - r_m)$				
	Lamb[1][46] (Laminar)	Present Analysis	Kays and Leung[2] [55]	Lee and Barrow[3] [46]	Equal Shear[4]
0.05	0.605	0.349	0.358	-	0.224
0.1	0.678	0.552	0.454	-	0.316
0.3	0.817	0.733	0.662	0.771	0.547
0.5	0.891	0.838	0.788	0.843	0.707
0.7	0.942	0.923	0.885	0.892	0.837

Table 3.7 Theoretical Friction Coefficient, f, Fully Developed Turbulent Flow, $\alpha = 0.3$

R_i (mm)	Re					
	15,000	20,000	30,000	40,000	50,000	60,000
16.7	0.00830	0.00755	0.00668	0.00618	0.00583	0.00556
8.57	0.00835	0.00757	0.00669	0.00619	0.00584	0.00558
3.98	0.00844	0.00764	0.00678	0.00625	0.00590	0.00565

Table 3.8 Theoretical Friction Coefficient, f, Fully Developed Turbulent Flow

α	Re				
	10,000	20,000	30,000	40,000	50,000
0.001	0.00802	0.00639	0.00572	0.00527	0.00497
0.01	0.00822	0.00653	0.00586	0.00541	0.00512
0.05	0.00837	0.00670	0.00602	0.00559	0.00529
0.1	0.00877	0.00700	0.00628	0.00582	0.00551
0.3	0.00926	0.00733	0.00656	0.00606	0.00573
0.5	0.00944	0.00742	0.00663	0.00612	0.00578
0.7	0.00955	0.00748	0.00668	0.00619	0.00581
0.9	0.00955	0.00745	0.00664	0.00611	0.00577

Table 3.9 Theoretical Eddy Diffusivity for Momentum, ε_M/ν, Fully Developed Turbulent Flow, $\alpha = 0.3$ (Re = 21,000)

$\frac{r - R_i}{R_o - R_i}$	R_i = 16.7 mm	R_i = 8.57 mm	R_i = 3.98 mm
	ε_M/ν	ε_M/ν	ε_M/ν
0.00	0.000	0.000	0.000
0.05	9.414	10.653	12.908
0.10	17.448	19.324	22.851
0.14	21.083	23.095	26.944
0.20	22.938	24.792	28.423
0.25	23.127	24.608	27.619
0.30	22.561	23.571	25.781
0.35	22.012	22.620	24.144
0.40	21.672	21.539	22.615
0.45	21.707	21.621	21.976
0.50	21.665	21.578	21.938
0.55	21.892	21.803	22.170
0.60	22.360	22.269	22.647
0.65	22.719	22.626	23.013
0.71	22.850	22.755	23.149
0.75	22.421	22.327	22.717
0.81	20.760	20.672	21.039
0.85	18.135	18.056	18.383
0.91	12.617	12.559	12.800
0.95	5.899	5.866	6.002
1.00	0.000	0.000	0.000

Table 3.10 Theoretical Eddy Diffusivity for Momentum, ε_M/ν, Fully Developed Turbulent Flow, Re = 21,000

$\dfrac{r - R_i}{R_o - R_i}$	$\alpha = 0.1$	$\alpha = 0.5$	$\alpha = 0.9$
	ε_M/ν	ε_M/ν	ε_M/ν
0.00	0.00	0.00	0.00
0.05	15.51	8.51	8.07
0.10	27.31	17.79	15.65
0.15	30.41	21.98	20.09
0.20	30.23	24.06	22.21
0.24	28.65	24.21	22.77
0.30	26.50	23.41	22.38
0.35	25.60	22.48	21.54
0.40	25.48	21.58	20.66
0.45	25.66	21.27	20.01
0.51	26.06	21.13	19.76
0.56	26.56	21.24	19.63
0.60	26.89	21.63	19.83
0.65	27.11	22.01	20.23
0.70	26.81	22.31	20.59
0.75	25.70	22.03	20.58
0.80	23.39	20.69	19.77
0.85	19.49	18.44	17.63
0.91	13.51	13.58	13.57
0.96	4.80	7.56	6.85
1.00	0.00	0.00	0.00

Table 3.11 Theoretical Nusselt Number, Nu, Fully Developed Turbulent Flow in Concentric Annulus, $\alpha = 0.3$

	$R_i = 16.7$ mm			$R_i = 8.57$ mm			$R_i = 3.98$ mm		
	Re			Re			Re		
Pr	10,000	30,000	50,000	10,000	30,000	50,000	10,000	30,000	50,000
0.01	7.69	8.46	9.46	7.75	8.49	9.54	8.12	9.07	10.19
0.7	41.07	66.91	99.52	43.16	67.88	102.11	45.91	76.70	112.01
1.0	50.10	82.74	124.10	52.62	83.78	127.07	55.72	94.30	138.70
5.0	112.53	193.66	298.24	117.61	194.19	302.30	122.05	214.58	322.89
10.0	150.99	262.61	407.36	157.51	262.49	411.50	162.41	288.31	436.48
100.0	331.24	586.07	919.99	344.42	582.63	923.93	351.36	633.46	968.53

Table 3.12 Theoretical Nusselt Number, Nu, Fully Developed Turbulent Flow in Concentric Annulus, $\alpha = 0.5$

	Eq. (3.86)				Kays and Leung [55]			Lee and Barrow [46]		
	Re				Re			Re		
Pr	10,000	30,000	50,000	100,000	10,000	30,000	100,000	10,000	30,000	100,000
0.001	6.35	6.46	6.57	6.78	6.28	6.30	6.30	-	-	-
0.01	6.89	7.87	8.80	10.8	6.37	6.45	7.30	-	-	-
0.7	30.9	65.0	95.7	163	30.9	66.0	166	31.6	65.5	188.6
1.0	37.5	80.2	120	205	38.2	83.5	212	38.7	82.6	192.2
3.0	65.6	148.0	224	393	66.8	152	402	78.4	178	437.5
10.0	110	258	397	707	106	260	715	204.4	477.3	1206.7
100.0	242	579	902	1627	220	558	1600	-	-	-

Table 3.13 Theoretical Nusselt Number, Nu, Fully Developed Turbulent Flow, Pr = 0.71

α	Re				
	10,000	20,000	30,000	40,000	50,000
0.1	51.0	81.0	106.6	133.3	158.5
0.3	35.2	56.1	73.9	92.5	110.0
0.5	31.2	49.6	65.3	81.7	97.1
0.7	29.4	46.6	61.3	79.0	91.1
0.9	28.4	44.9	59.0	73.8	87.6

Table 3.14 Empirical Constants for the k-ε Model of Turbulence

	Launder and Spalding [72]	Jones and Launder [71]	Hanjalić and Launder [86]	Wyngaard et al. [87]	Launder et al. [88]	Gibson and Launder [89]
c_μ	0.09	0.09	0.09	0.09	0.09	0.09
$c_{\varepsilon 1}$	1.55	1.45	1.45	1.50	1.44	1.45
$c_{\varepsilon 2}$	2.00	1.90	2.00	2.00	1.90	1.90
σ_k	1.00	1.00	1.00	1.00	1.00	1.00
σ_ε	1.30	1.30	1.30	1.30	1.30	1.30

Table 4.1 Essential Dimensions of Test Cylinders, Circular Cylinder

No.	OD, mm	ID, mm	L, mm	Material
1	50.8	44.7	1,270	S..S. 304
2	12.7	20.6	1,016	S.S. 304
3	6.35	10.9	1,016	S.S. 304

Table 4.2 Velocity Distributions for Turbulent Boundary Layer Flows over Circular Cylinders*

$x = 61$ cm, $u_\infty = 15$ m/s					
$R_1 = 6.35$ mm		$R_1 = 12.7$ mm		$R_1 = 25.4$ mm	
$\delta/R_1 = 2.52$		$\delta/R_1 = 1.34$		$\delta/R_1 = 0.71$	
y^+	u^+	y^+	u^+	y^+	u^+
30	13.6	25	13.1	32.8	14.1
37	14.2	35	14.4	43.7	14.7
44	14.3	48	15.0	58.2	15.0
51	14.5	61	15.2	69.4	15.2
64	15.0	75	15.7	86.6	15.9
77	15.3	91	16.2	104.4	16.2
92	15.7	114	16.4	125.9	16.5
110	16.1	135	16.6	145.3	17.1
120	16.3	155	17.0	165.9	17.4
140	16.4	180	17.3	195.7	17.9
160	16.7	210	17.5	218.5	18.0
180	16.8	230	17.5	249.3	18.1
200	17.2	270	18.0	278.4	18.4
230	17.4	290	18.2	314.3	18.9
260	17.5	330	18.3	358.7	19.0
300	17.6	360	18.4	400.4	19.2
350	17.8	400	18.5	447.1	19.3
420	18.05	440	18.6	510.3	19.5
480	18.1	500	18.9	570	19.8
580	18.2	550	19.0	622.2	19.8

* Experimental Data of Kim and Lee [45,46]

Table 4.3 Local Skin Friction Coefficients for Turbulent Boundary Layer Flow over a Circular Cylinder*

$u_\infty = 15$ m/s $(x = 61$ cm$)$					
$R_i = 25.4$mm		$R_i = 12.7$mm		$R_i = 6.35$mm	
Re_x	$C_{f,x}$	Re_x	$C_{f,x}$	Re_x	$C_{f,x}$
5.5×10^5	0.00445	5.5×10^5	0.00510	5.5×10^5	0.00585
7.7×10^5	0.00455	7.7×10^5	0.00527	7.7×10^5	0.00597
9.6×10^5	0.00445	9.6×10^5	0.00525	9.6×10^5	0.00595
1.17×10^6	0.00430	1.17×10^6	0.00516	1.36×10^6	0.00573
1.36×10^6	0.00439	1.58×10^6	0.00492	1.60×10^6	0.00565
1.60×10^6	0.00433	1.87×10^6	0.00483	1.87×10^6	0.00549

* Experimental Data of Kim and Lee [45,46]

Table 4.4 Temperature Distribution for Turbulent Boundary Layer Flow over a Circular Cylinder*

R_i = 16.1 cm,			
u_∞ = 30 m/s, Pr=0.71 (δ/R_i =2.52, x = 61 cm)			
y^+	T^+	y^+	T^+
7.5	5.0	210	13.9
13	7.7	300	14.0
22	9.7	340	14.3
30	9.9	400	14.8
40	11.0	440	15.0
55	11.5	500	15.2
70	12.0	600	15.3
80	12.3	670	15.5
90	12.7	740	15.6
100	12.9	800	15.8
120	13.0	840	16.0
150	13.1	940	16.0
190	13.7	-	-

* Experimental Data of Kim and Lee [45,46]

Table 4.5 Local Nusselt Numbers for Turbulent Boundary Layer Flow over Circular Cylinders*

u_∞=30 m/s (x = 61 cm)			
R_i = 6.35mm		R_i = 12.7mm	
Re_x	Nu_x	Re_x	Nu_x
3.6×10^5	1411.2	7.4×10^5	1445.2
3.8×10^5	1423.1	7.5×10^5	1454.3
5.4×10^5	1417.5	1.0×10^6	1862.0
9.8×10^5	2023.7	1.3×10^6	2320.5
1.36×10^6	1779.8	1.50×10^6	2635.5
1.50×10^6	2992.5	1.80×10^6	3112.2
1.60×10^6	3248.0	-	-
1.80×10^6	3565.8	-	-
1.96×10^6	3910.2	-	-
2.10×10^6	4263.0	-	-

* Experimental Data of Kim and Lee [45,46]

Table 4.6 Essential Dimensions of Test Sections, Concentric Annular Duct

Tube	α	O.D. (mm)	Effective length (m)	Material	L/D_e
Outer tube 1	0.32	101.5	-	Copper	73.8
Inner tube 1		32.5	5.18	S.S. 304	
Outer tube 2	0.32	53.8	-	Copper	69.6
Inner tube 2		17.2	2.53	S.S. 304	
Outer tube 3	0.31	28.6	-	Copper	102.5
Inner tube 3		7.95	2.17	S.S. 304	

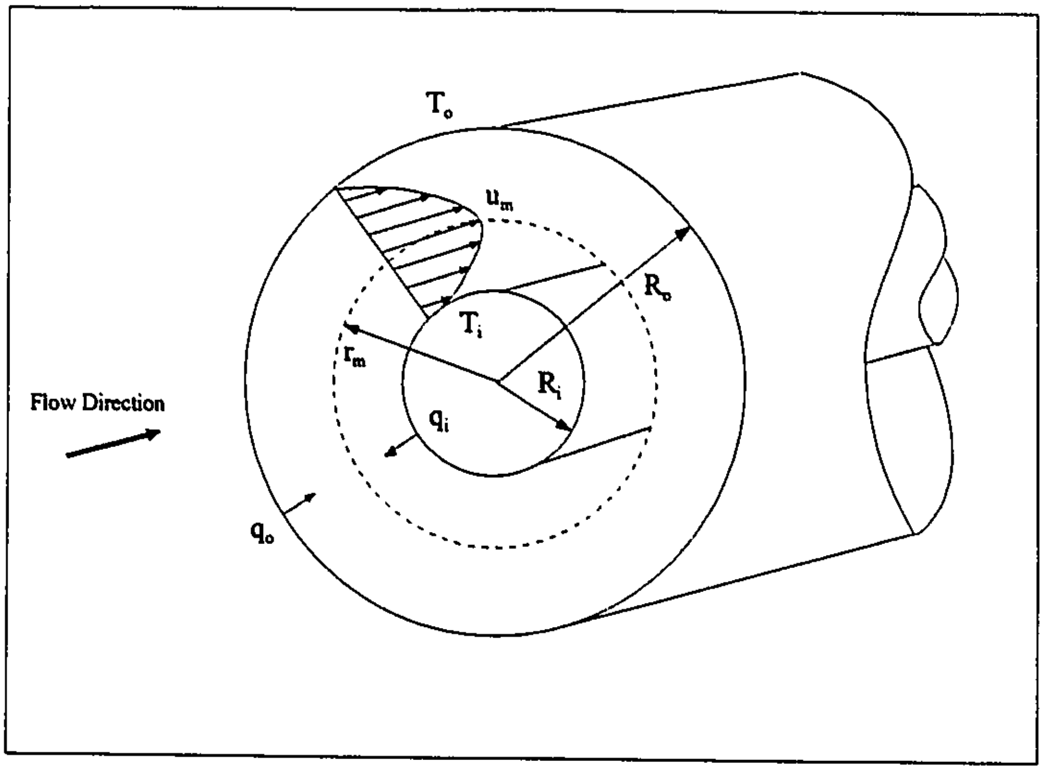

Figure 1.1 Concentric Annulus: Nomenclature

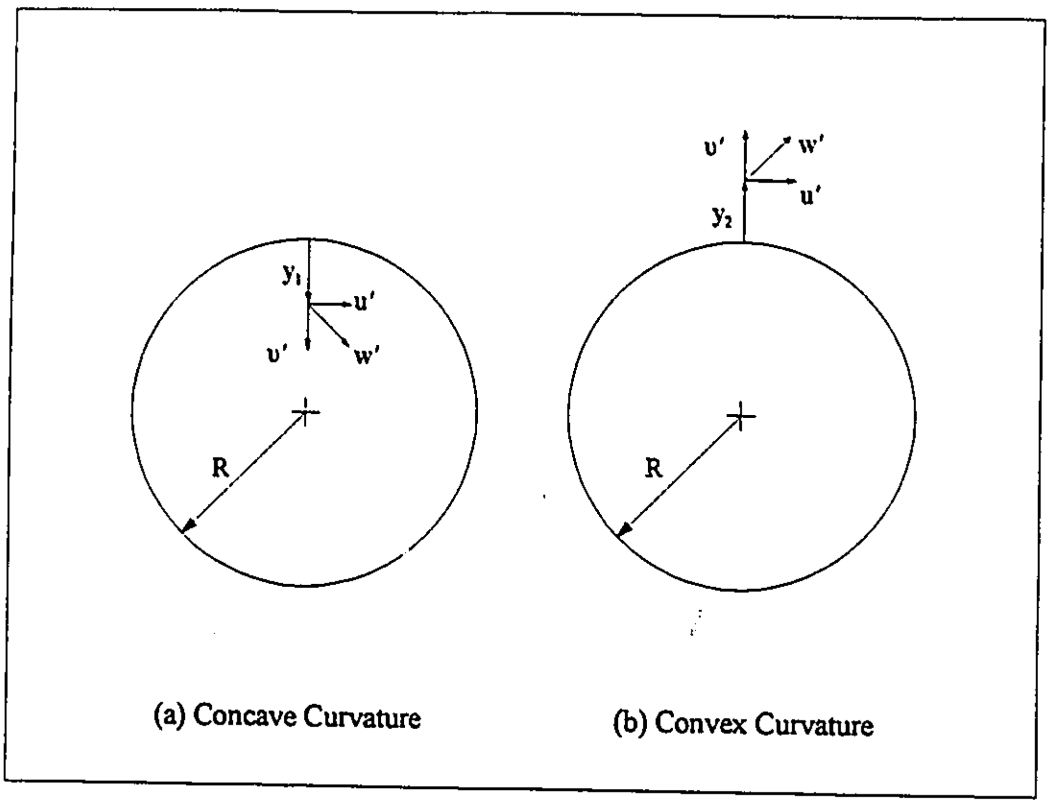

Figure 1.2 Transverse Surface Curvature

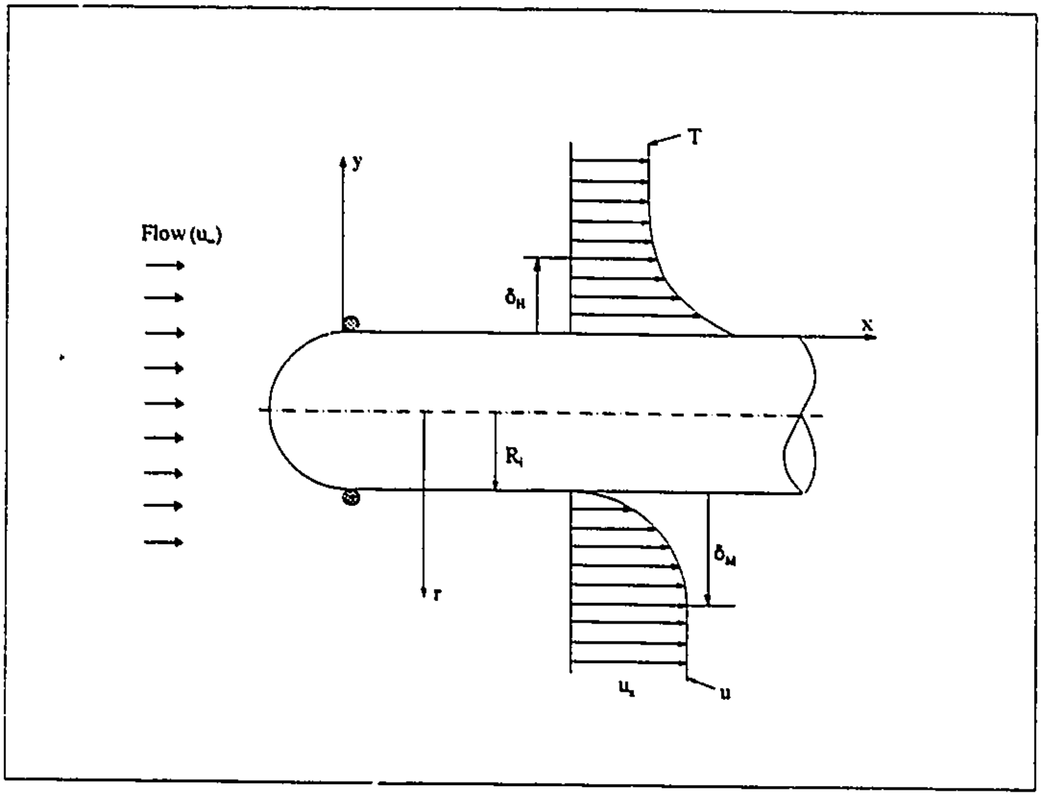

Figure 3.1 Idealized Model for Circular Cylinder: Nomenclature

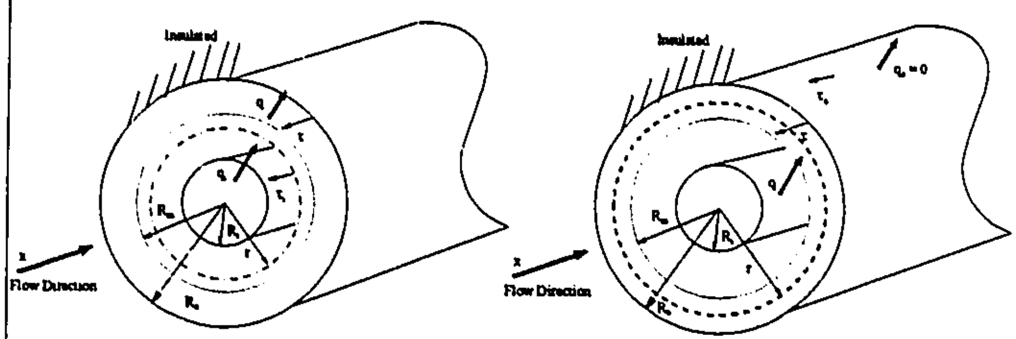

(a) Inner Region (b) Outer Region

Figure 3.2 Idealized Model for a Concentric Annular Duct: Nomenclature

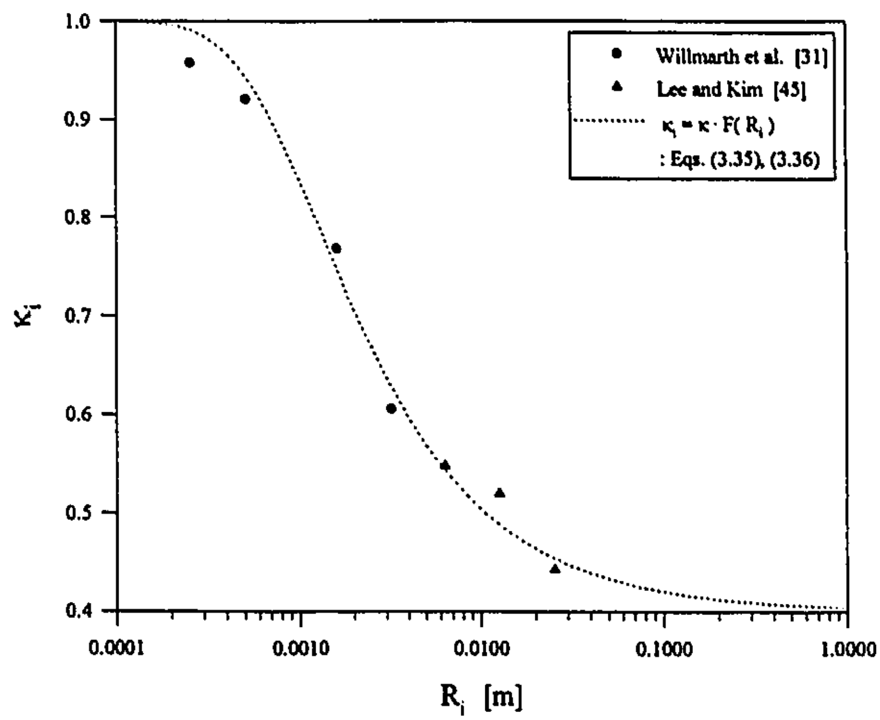

Figure 3.3 Effect of Transverse Convex Surface Curvature on von Kármán Constant, κ_i

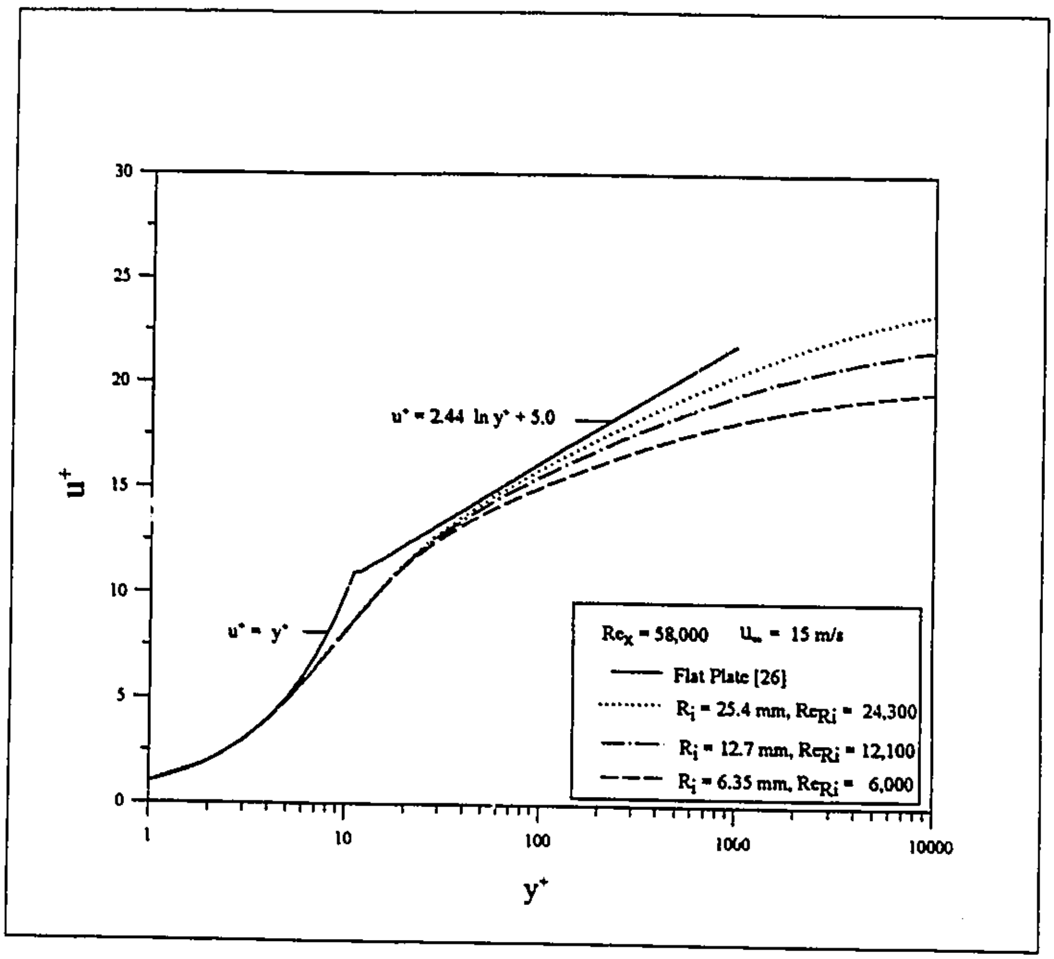

Figure 3.4 Effect of Transverse Convex Curvature on Velocity Distribution, Turbulent Boundary Layer Flow; Theory

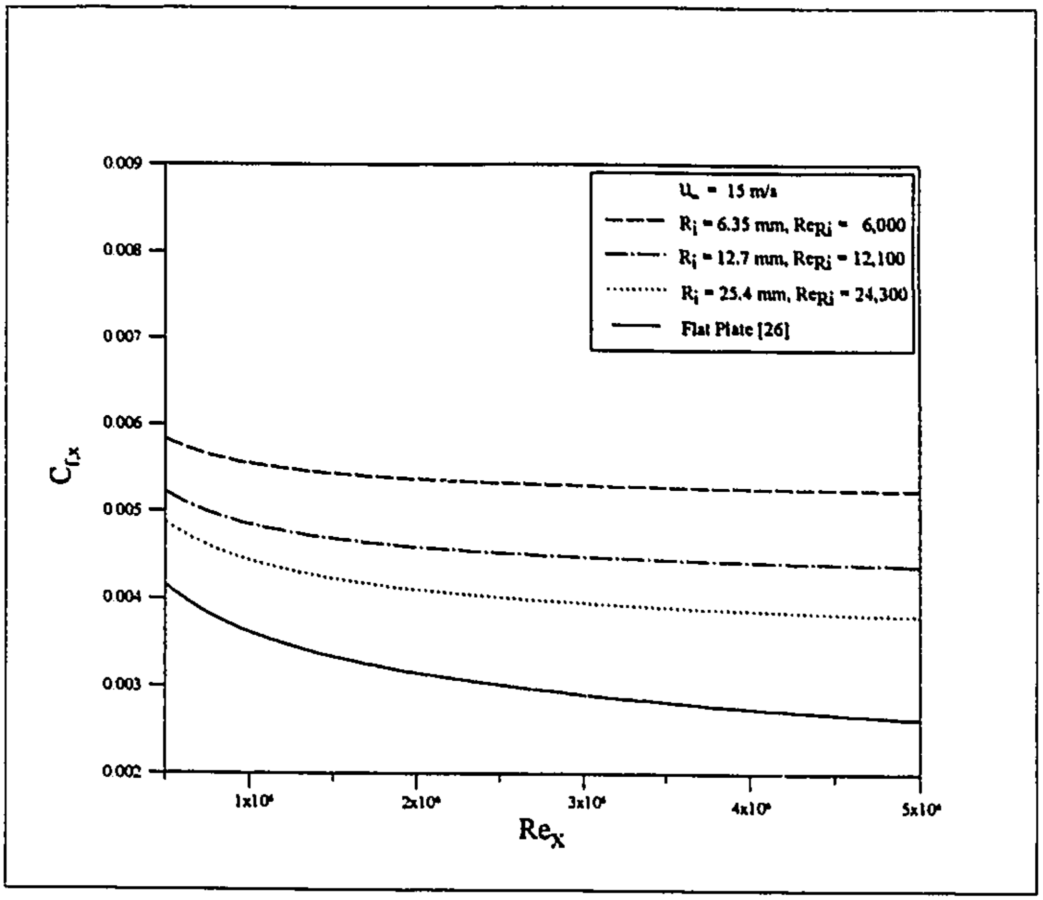

Figure 3.5 Effect of Transverse Convex Curvature on Skin Friction Coefficient, Turbulent Boundary Layer Flow; Theory

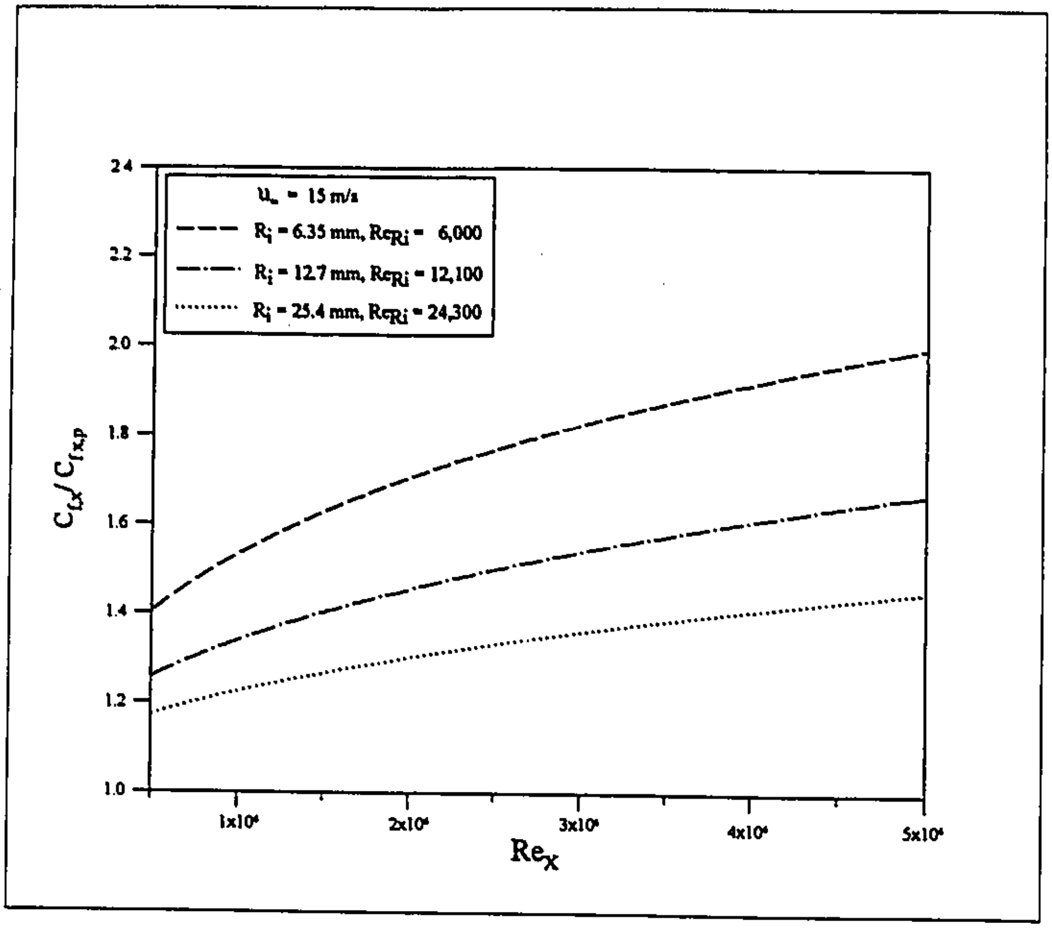

Figure 3.6 Normalized Skin Friction Coefficient, Turbulent Boundary Layer Flow; Theory

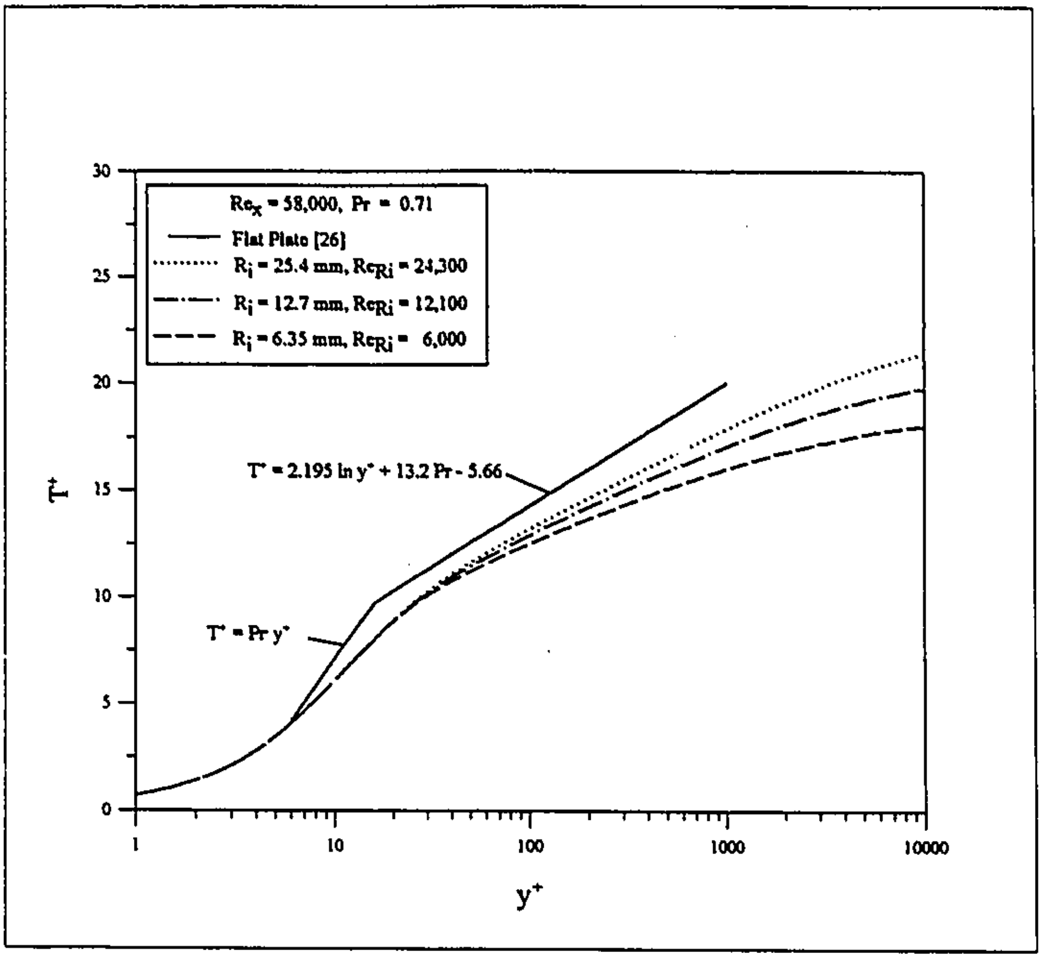

Figure 3.7 Effect of Transverse Convex Curvature on Temperature Distribution, Cylinder Wall Heated, Turbulent Boundary Layer Flow; Theory

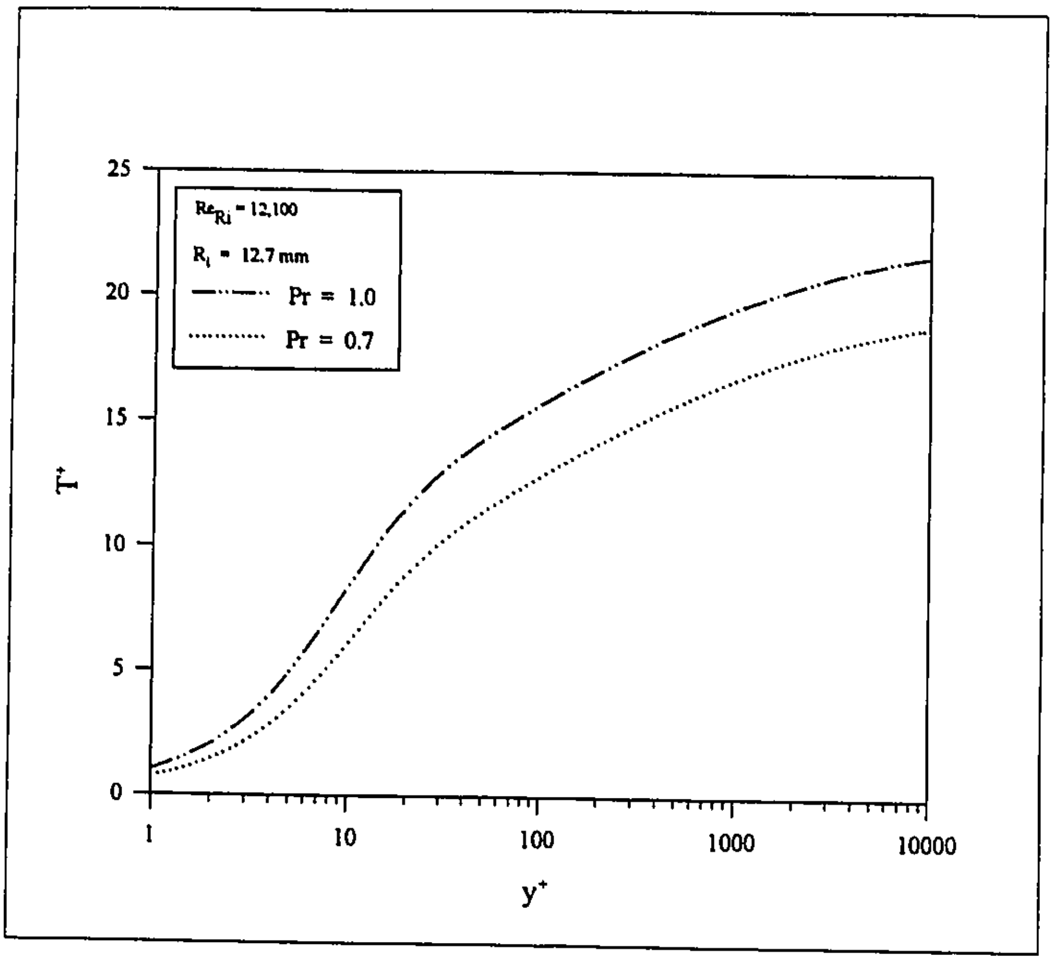

Figure 3.8 Effect of Prandtl Number, Pr, on Temperature Distribution, Cylinder Wall Heated, Turbulent Boundary Layer Flow; Theory

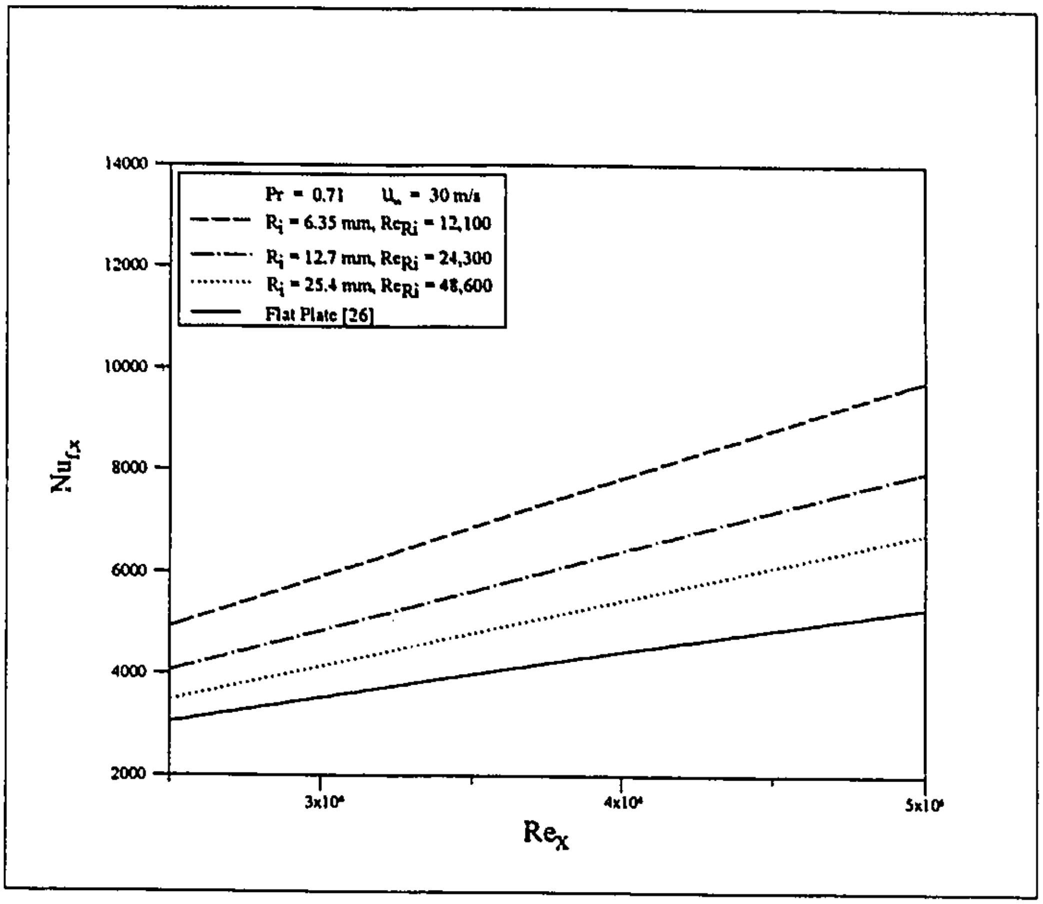

Figure 3.9 Effect of Transverse Convex Curvature on Nusselt Number, Cylinder Wall Heated, Turbulent Boundary Layer Flow; Theory

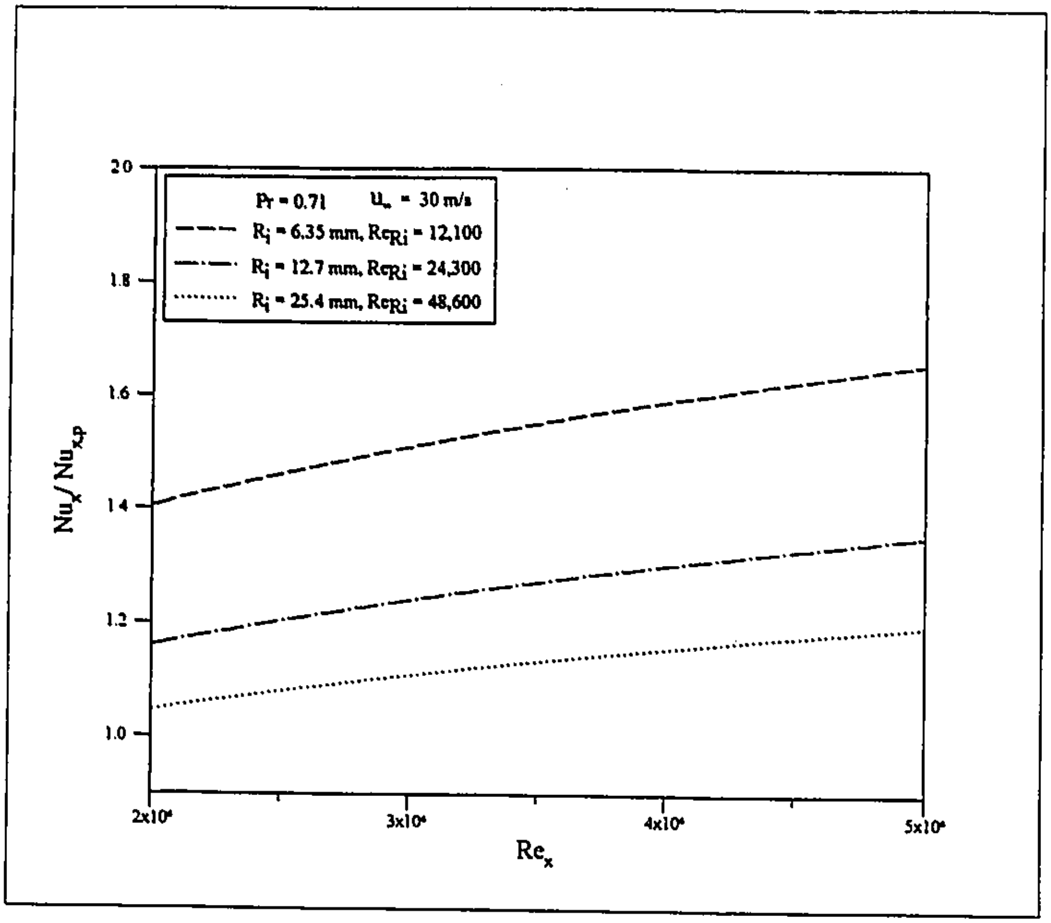

Figure 3.10 Normalized Nusselt Number, Cylinder Wall Heated, Turbulent Boundary Layer Flow; Theory

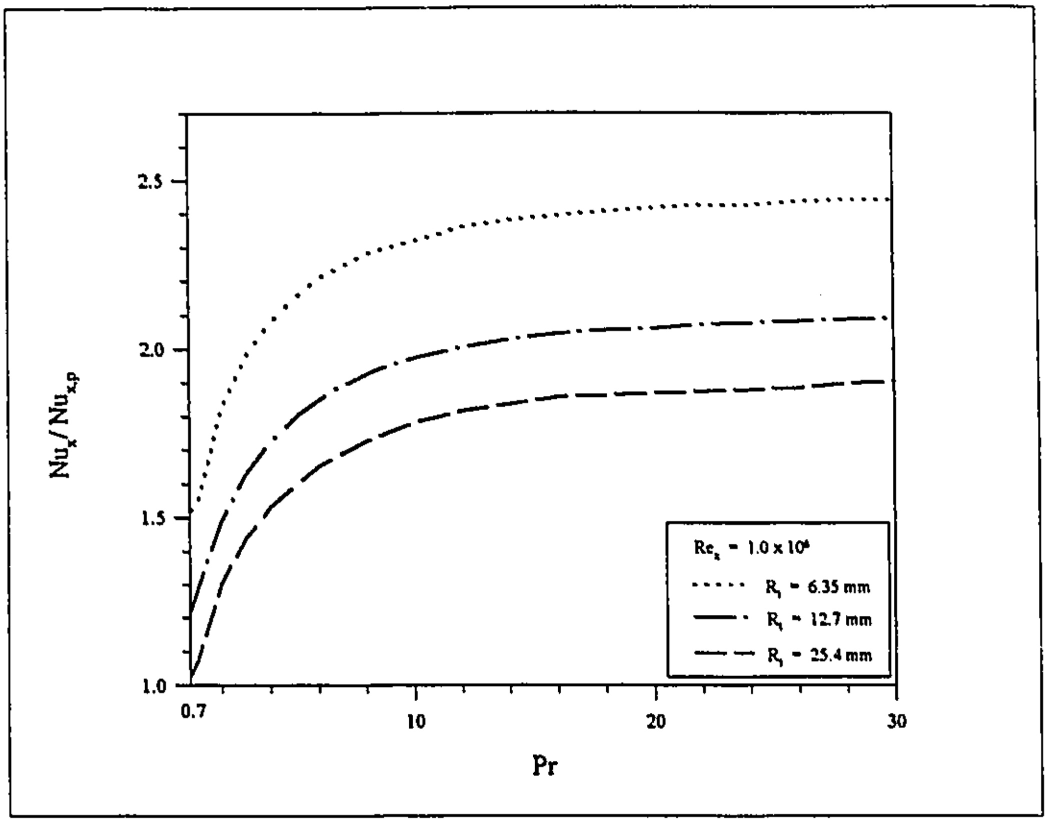

Figure 3.11 Effect of Transverse Convex Curvature and Prandtl Number on Nusselt Number, Cylinder Wall Heated, Turbulent Boundary Layer Flow; Theory

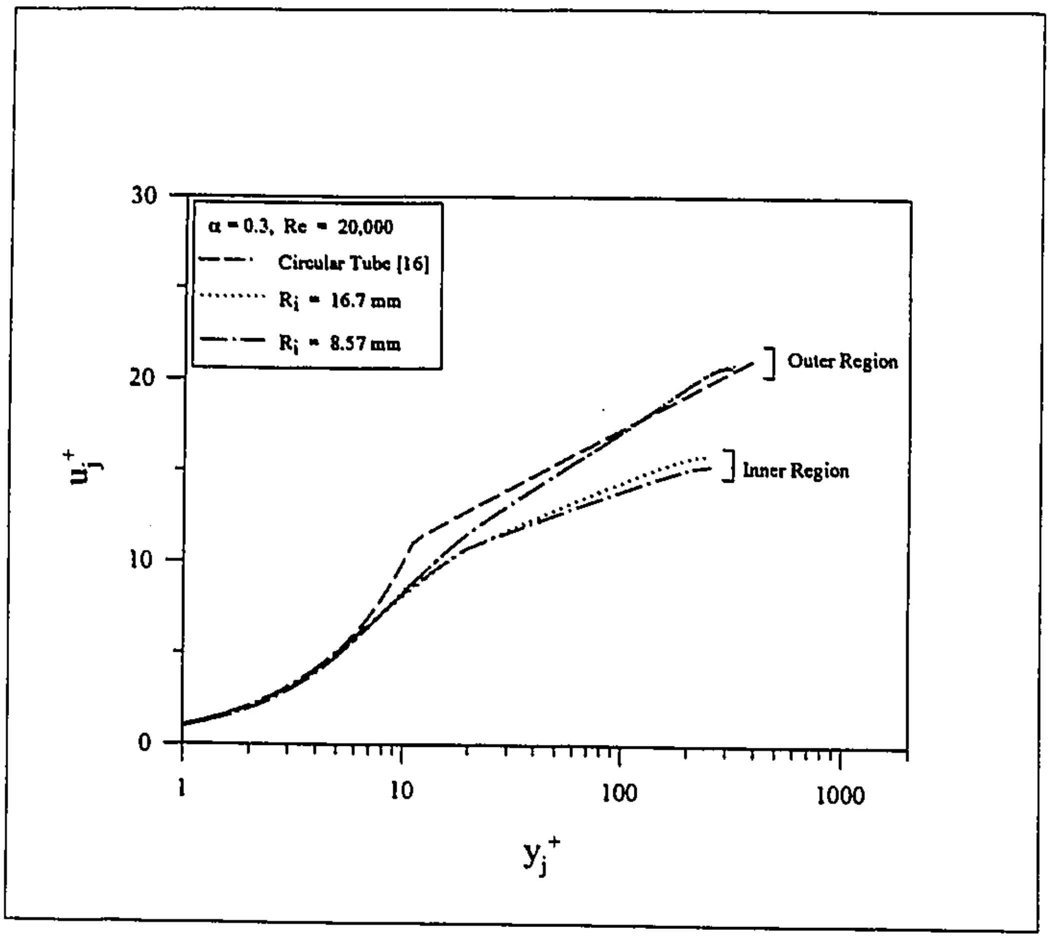

Figure 3.12 Effect of Transverse Convex Curvature on Velocity Distribution, Fully Developed Turbulent Flow in Concentric Annulus; Theory

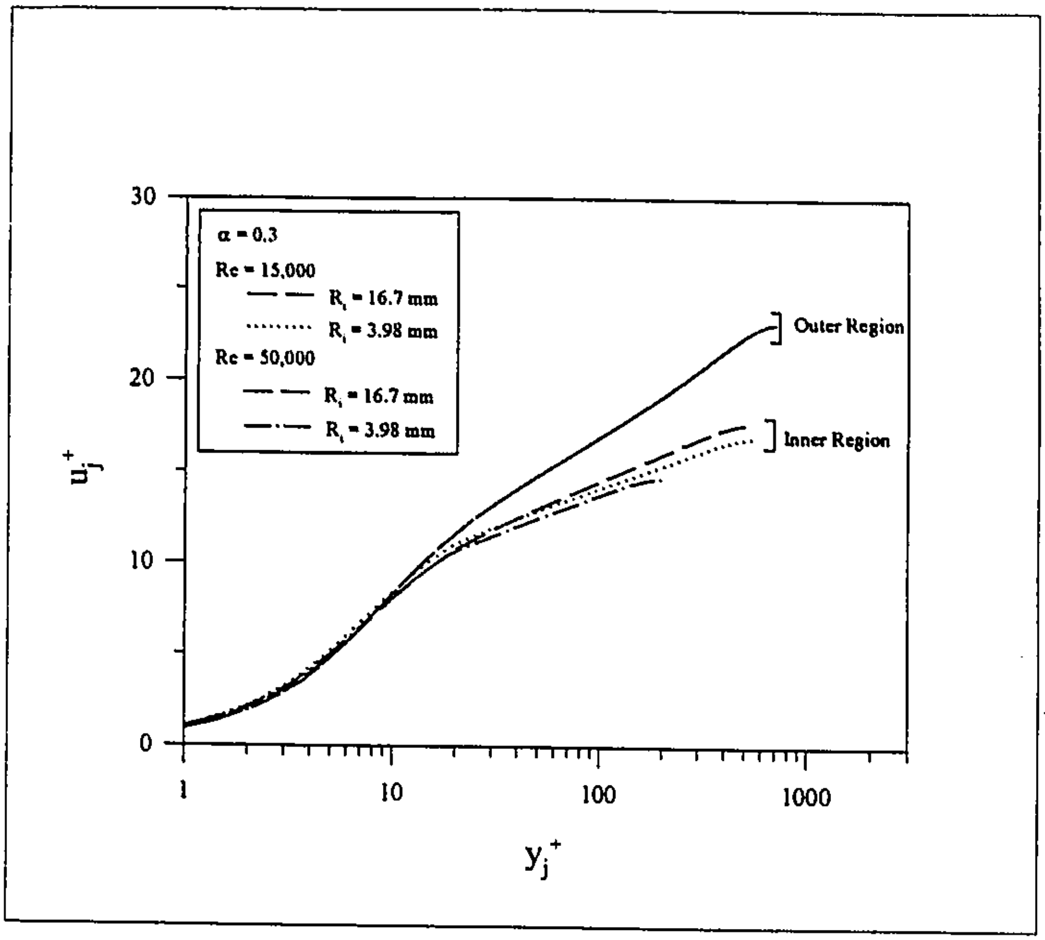

Figure 3.13 Effect of Transverse Convex Curvature and Reynolds Number on Velocity Distribution, Fully Developed; Theory

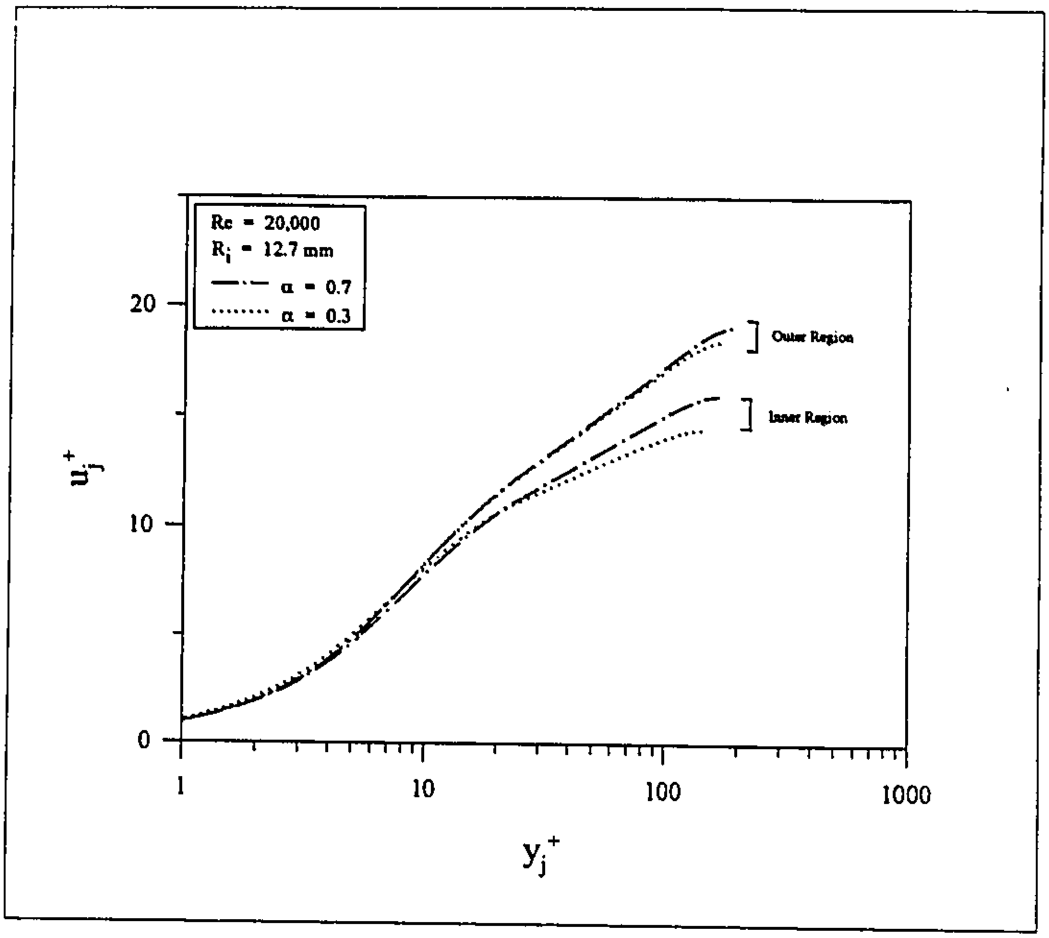

Figure 3.14 Effect of Radius Ratio with Transverse Convex Curvature on Velocity Distribution, Fully Developed; Theory

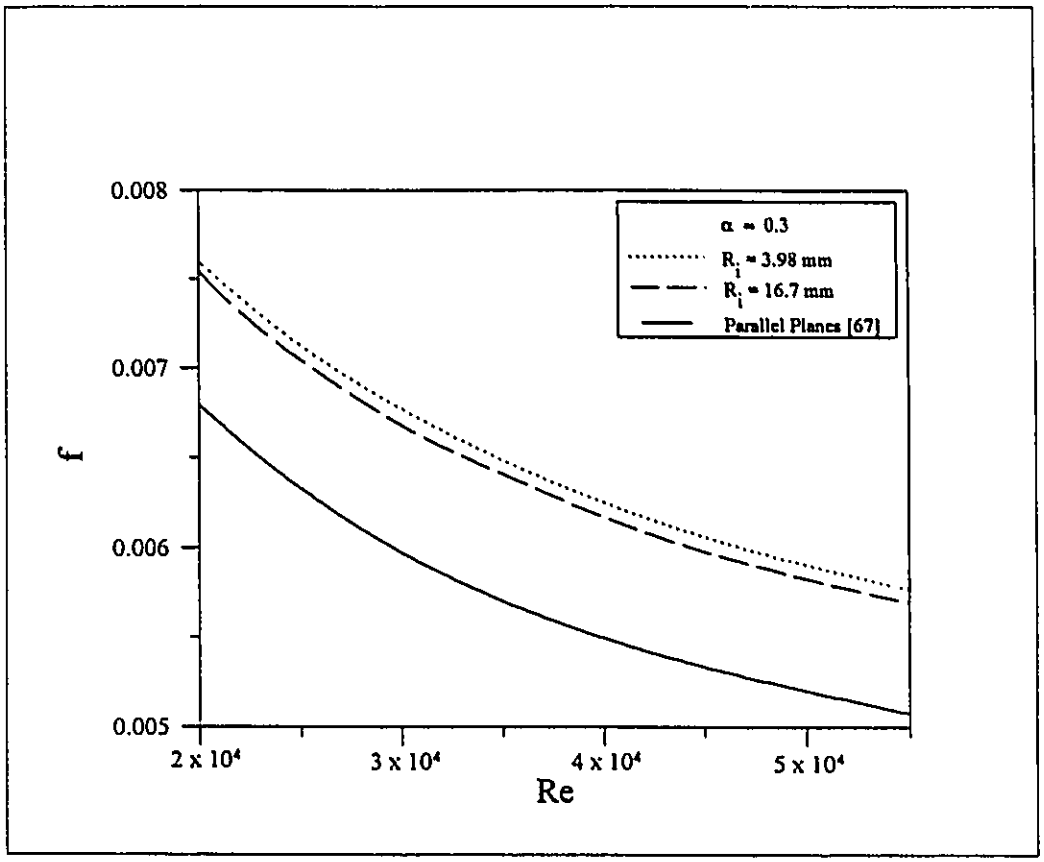

Figure 3.15 Effect of Transverse Convex Curvature on Friction Coefficient, Fully Developed Turbulent Flow; Theory

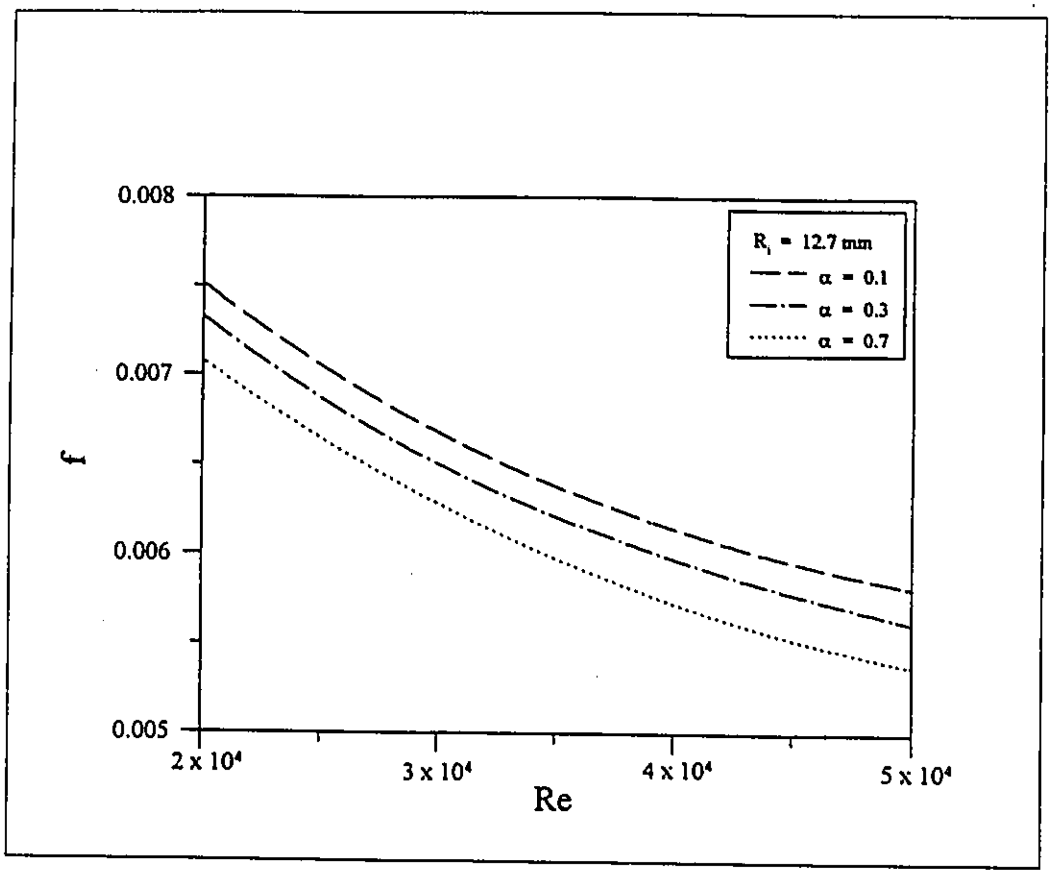

Figure 3.16 Effect of Radius Ratio with Transverse Convex Curvature on Friction Coefficient, Fully Developed; Theory

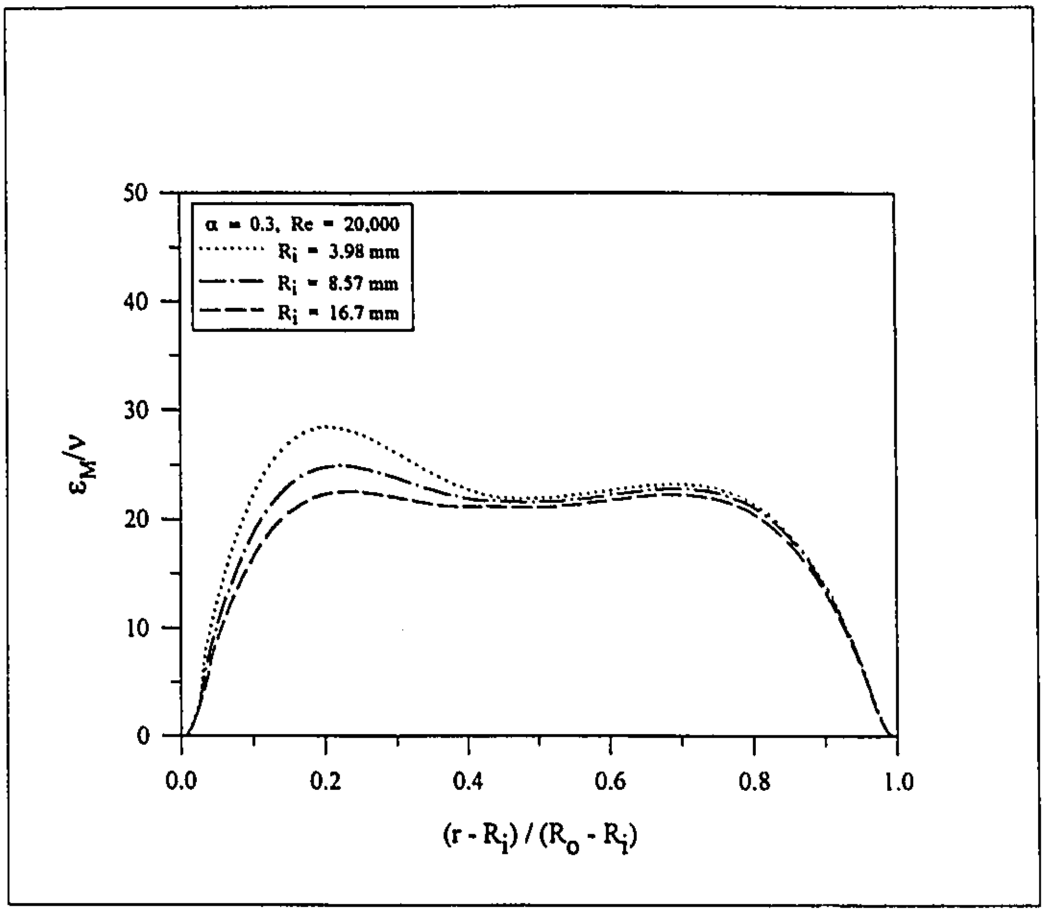

Figure 3.17 Effect of Transverse Convex Curvature on Eddy Diffusivity For Momentum, Fully Developed Turbulent Flow; Theory

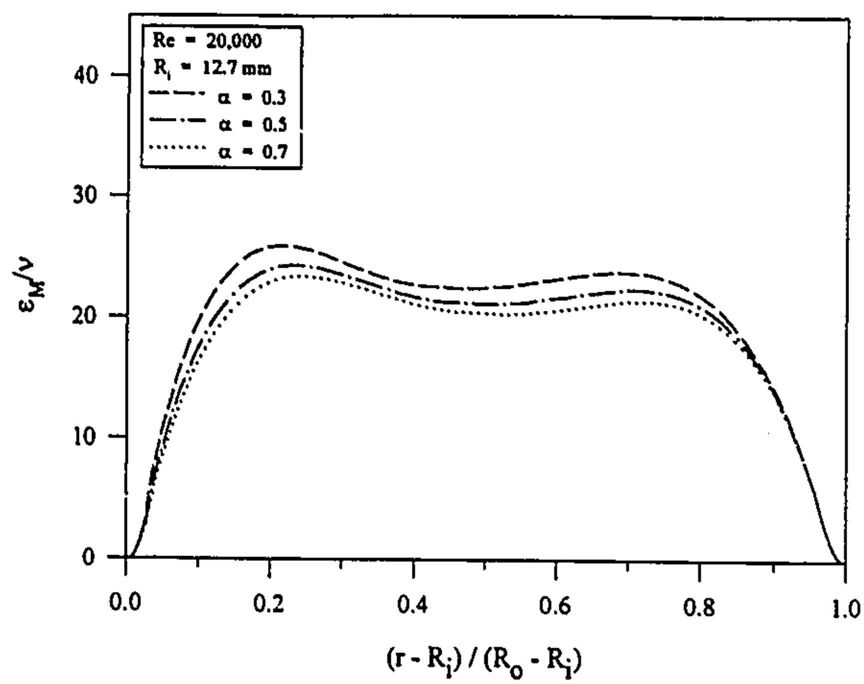

Figure 3.18 Effect of Radius Ratio with Transverse Convex Curvature on Eddy Diffusivity for Momentum, Fully Developed Turbulent Flow; Theory

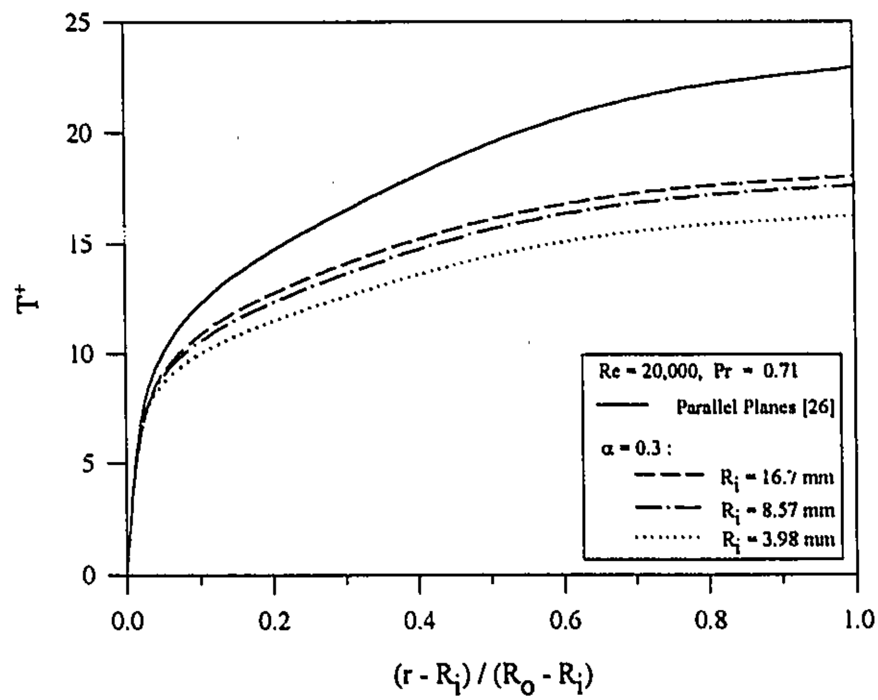

Figure 3.19 Effect of Transverse Convex Curvature on Temperature Distribution, Fully Developed Region, Inner Core Wall Heated, Outer Tube wall Insulated; Theory

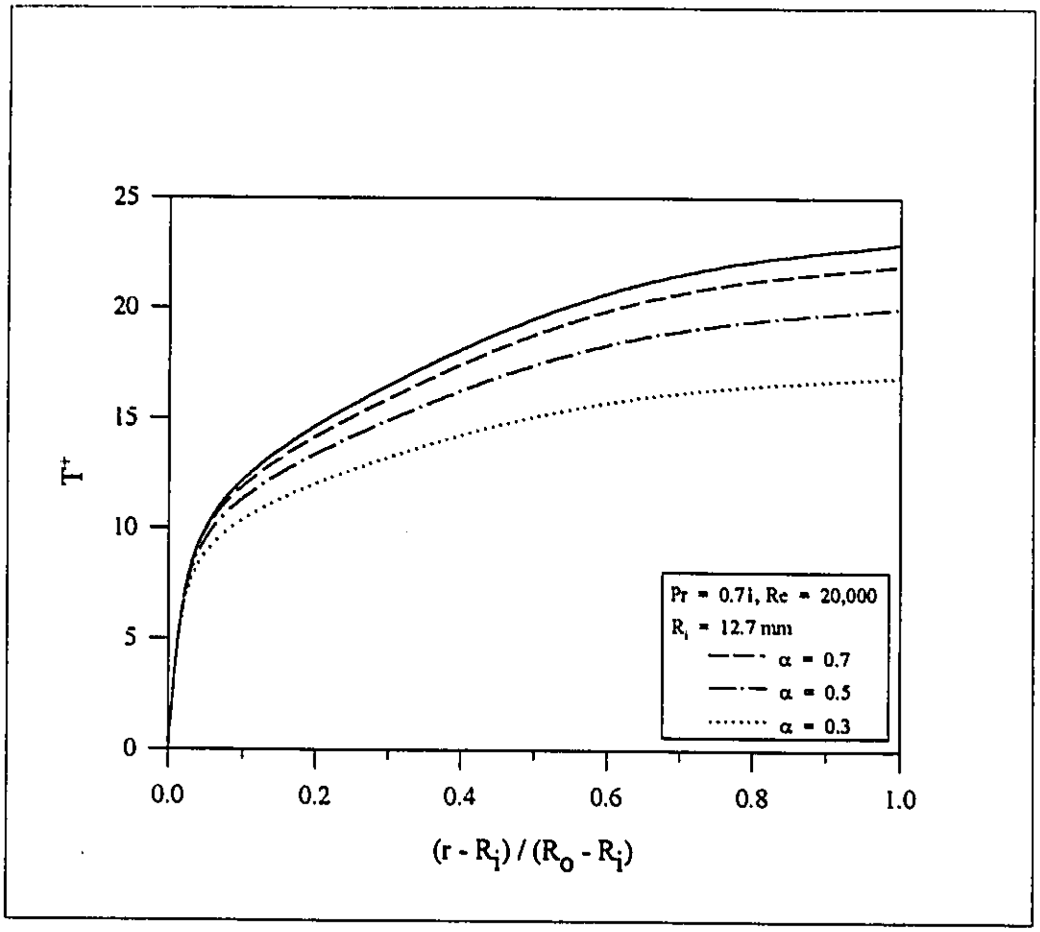

Figure 3.20 Effect of Radius Ratio with Transverse Convex Curvature on Temperature Distribution, Fully Developed Region, Inner Core Wall Heated, Outer Tube Wall Insulated; Theory

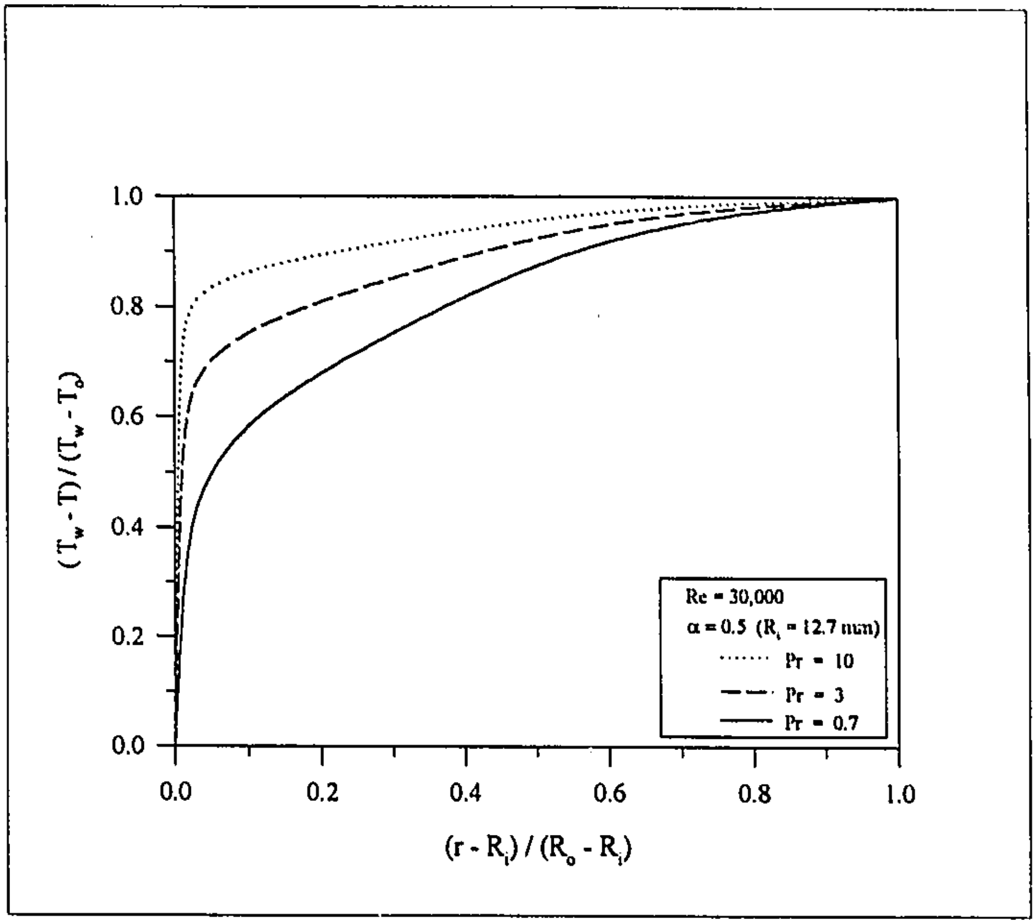

Figure 3.21 Effect of Prandtl Number on Temperature Distribution, Fully Developed Region, Inner Core Wall Heated, Outer Tube Wall Insulated; Theory

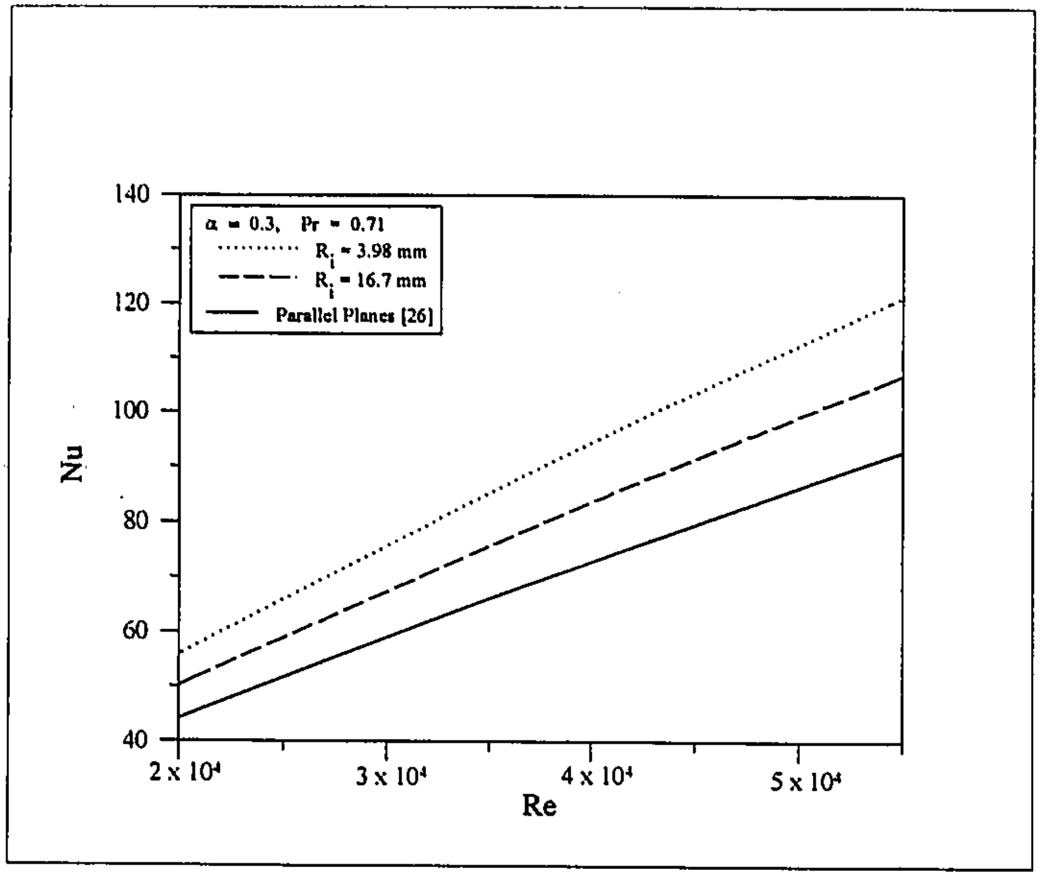

Figure 3.22 Effect of Transverse Convex Curvature on Nusselt Number, Fully Developed Region, Inner Core Wall Heated, Outer Tube Wall Insulated; Theory

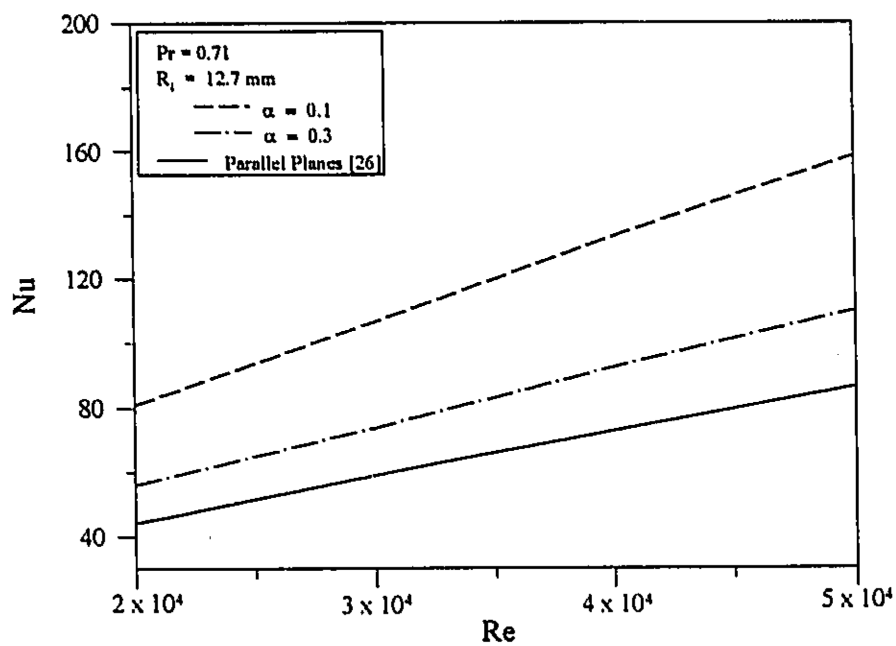

Figure 3.23 Effect of Radius Ratio with Transverse Convex Curvature on Nusselt Number, Fully Developed Region, Inner Core Wall Heated, Outer Tube Wall Insulated; Theory

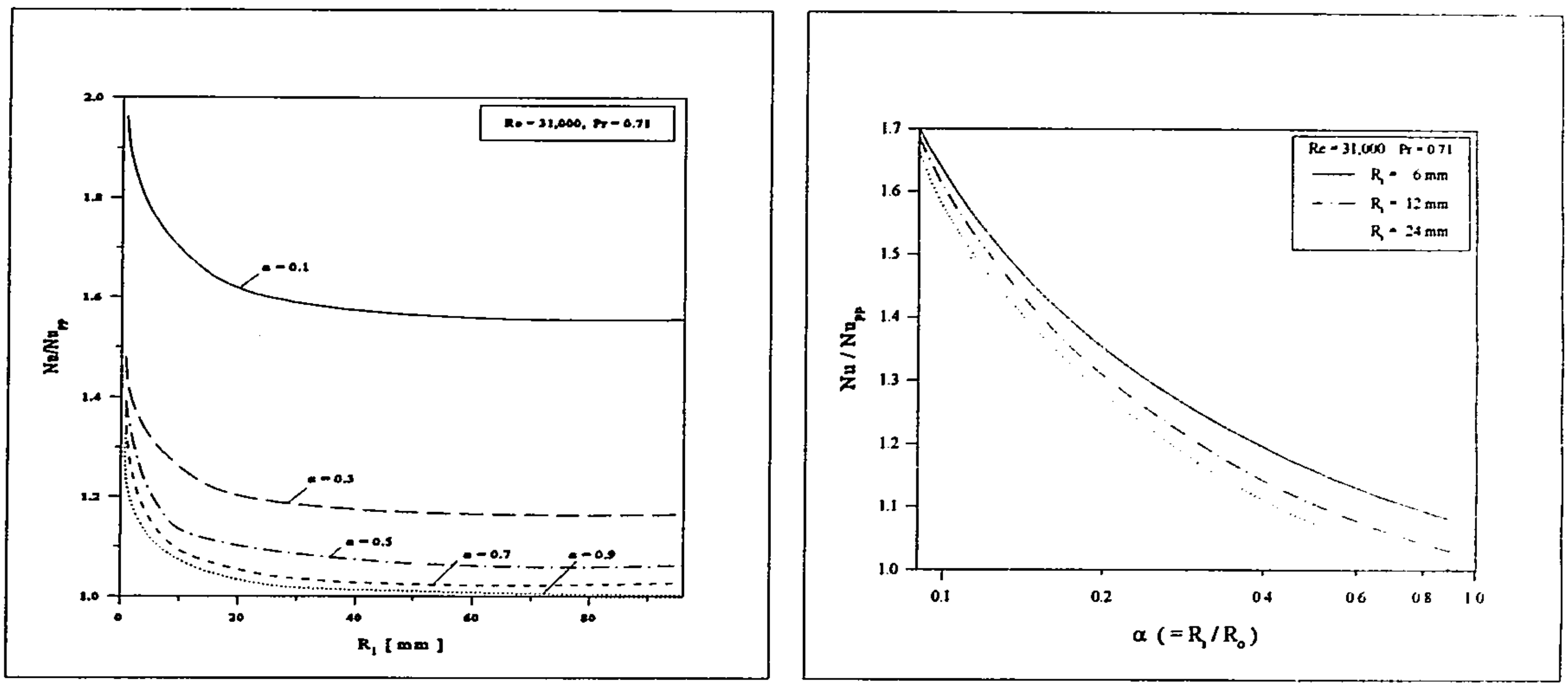

(a) (b)

Figure 3.24 Effect of Transverse Convex Curvature and Radius Ratio on Nusselt Number, Fully Developed Turbulent Flow, Inner Core Wall Heated, Outer Tube Wall Insulated; Theory

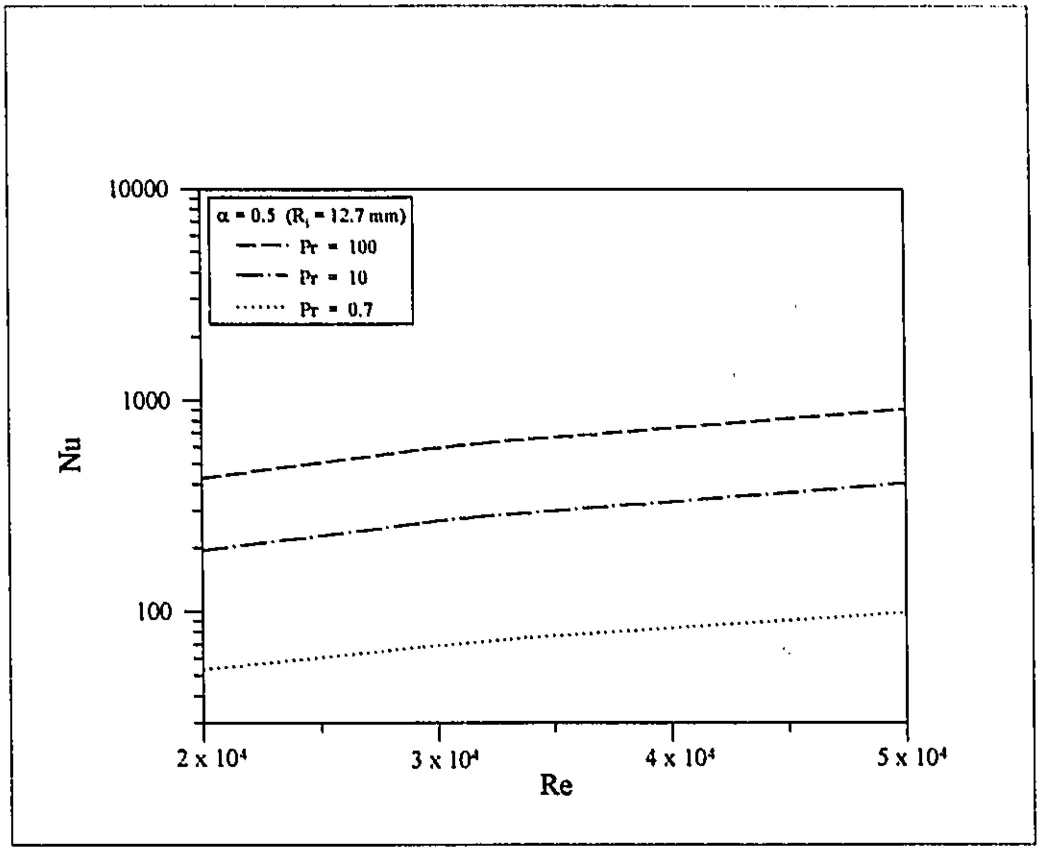

Figure 3.25 Effect of Prandtl Number on Nusselt Number, Fully Developed Region, Inner Wall Heated, Outer Wall Insulated; Theory

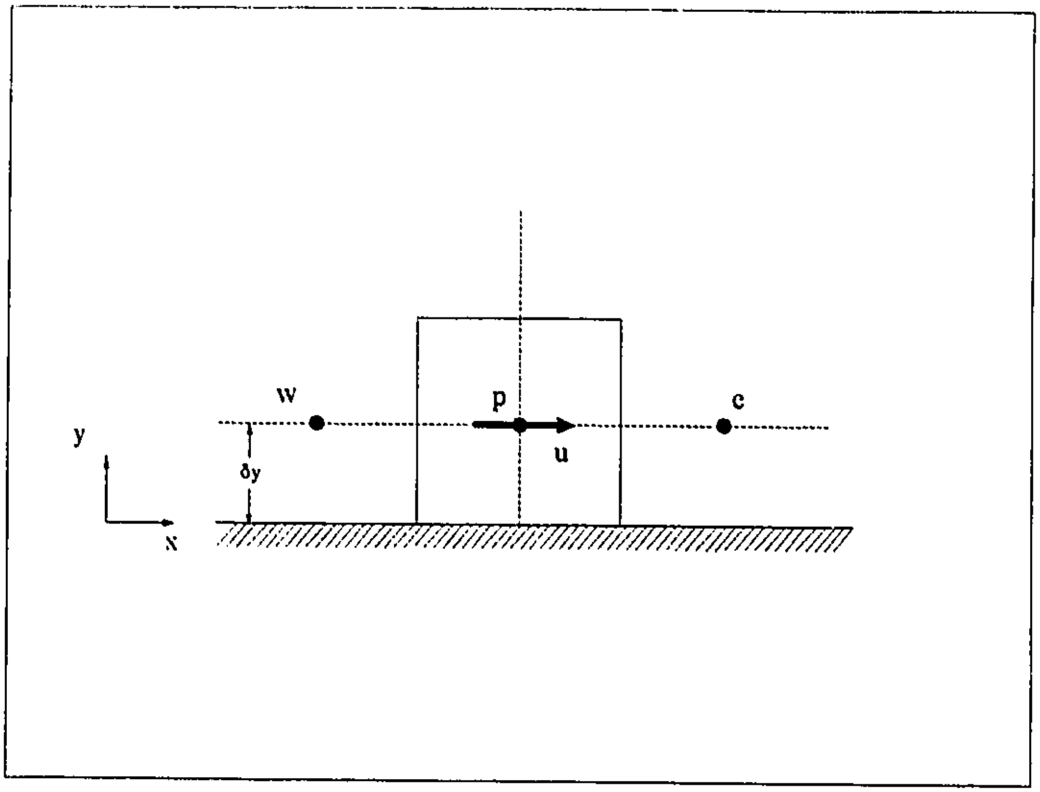

Figure 3.26 Momentum Boundary Conditions at Node: Nomenclature

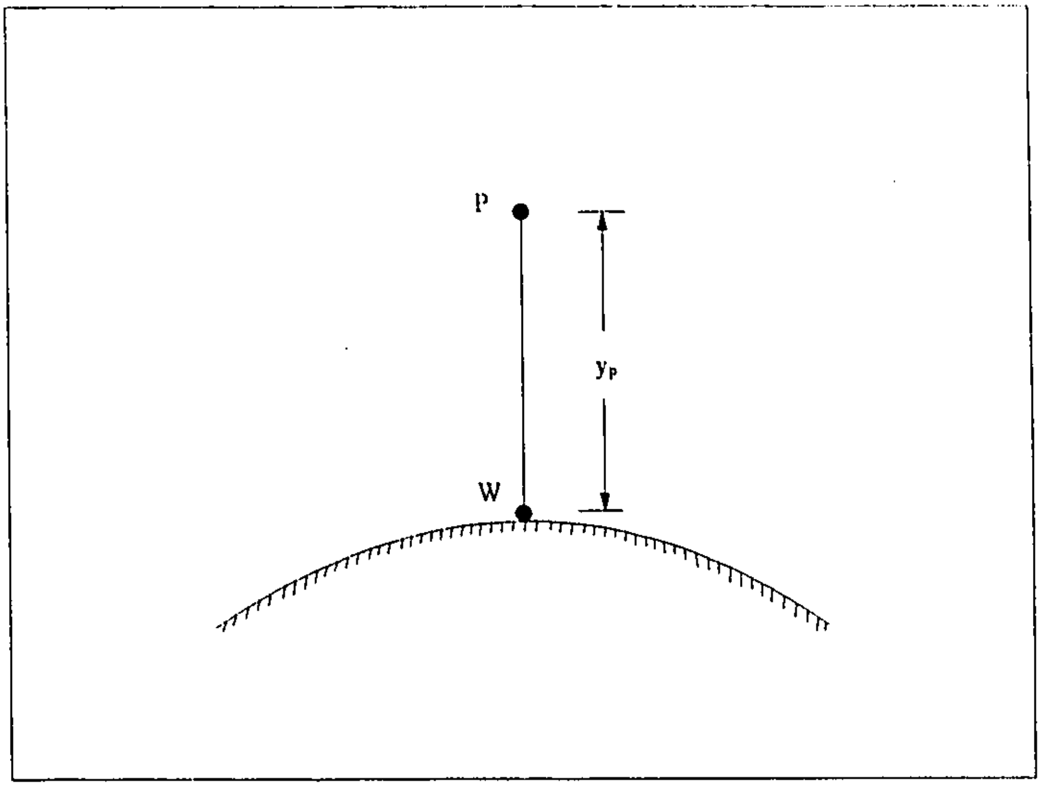

Figure 3.27 Near Wall Node Model: Nomenclature

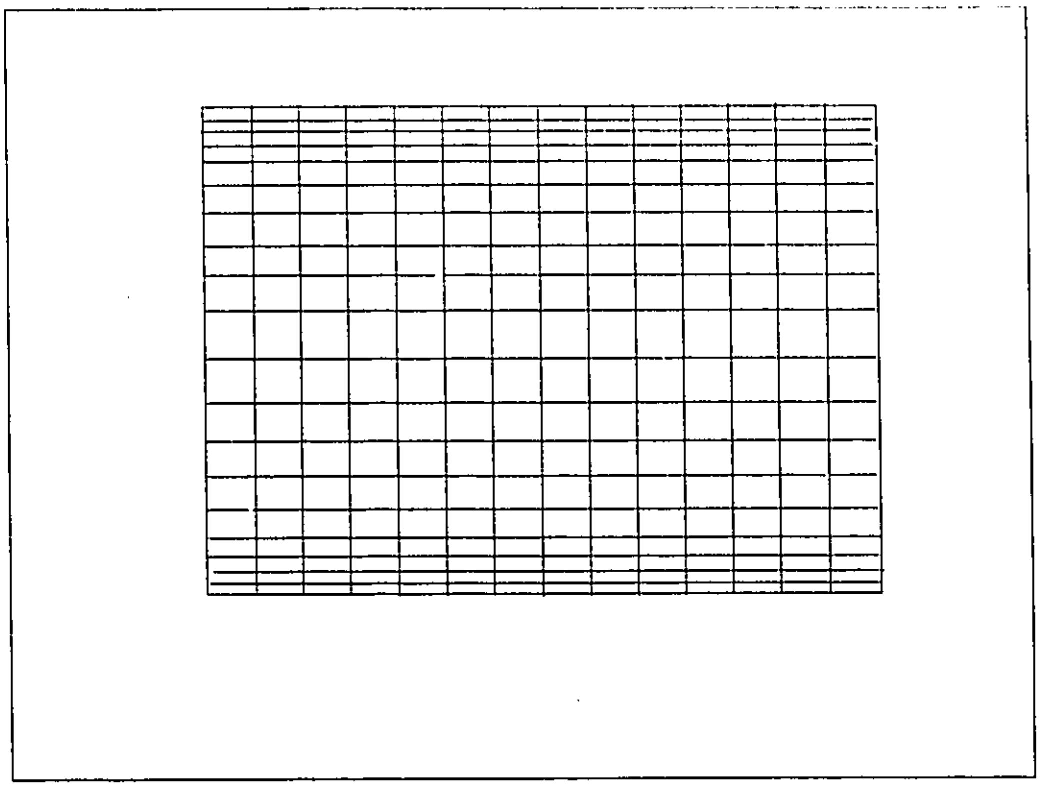

Figure 3.28 Grid System Generated by the Transformation Function as $\beta = 1.05$

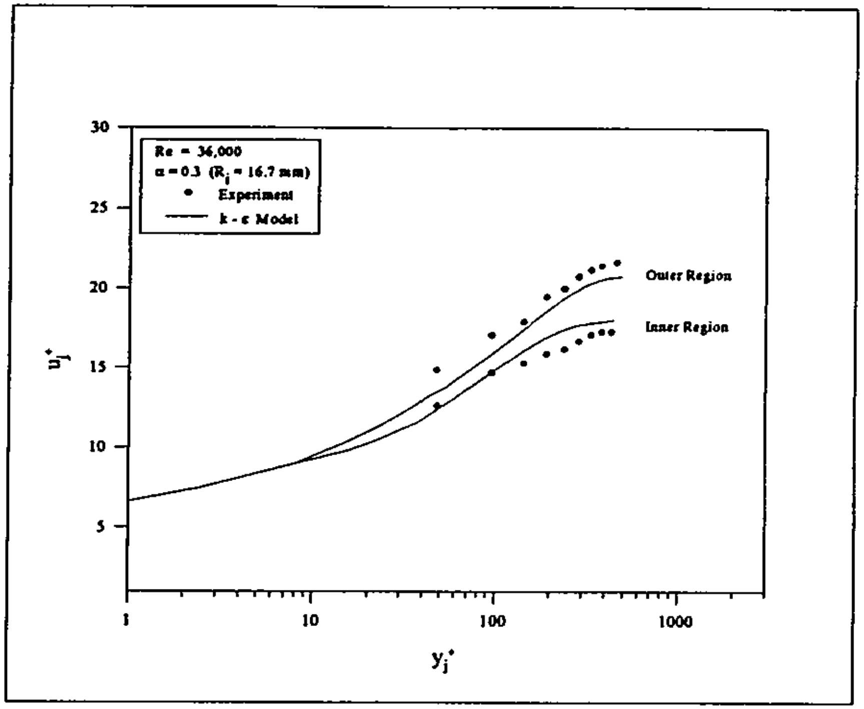

(a) Re = 36,000

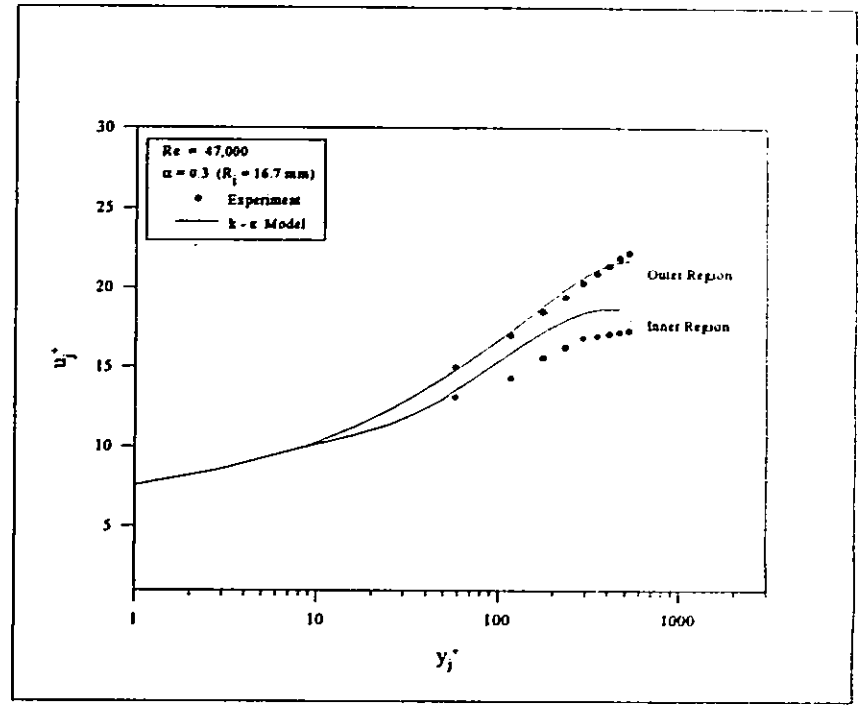

(b) Re = 47,000

Figure 3.29 Theoretical (k-ε Turbulence Model) and Experimental Velocity Distributions, Fully Developed, $\alpha = 0.3$ ($R_i = 16.7$ mm)

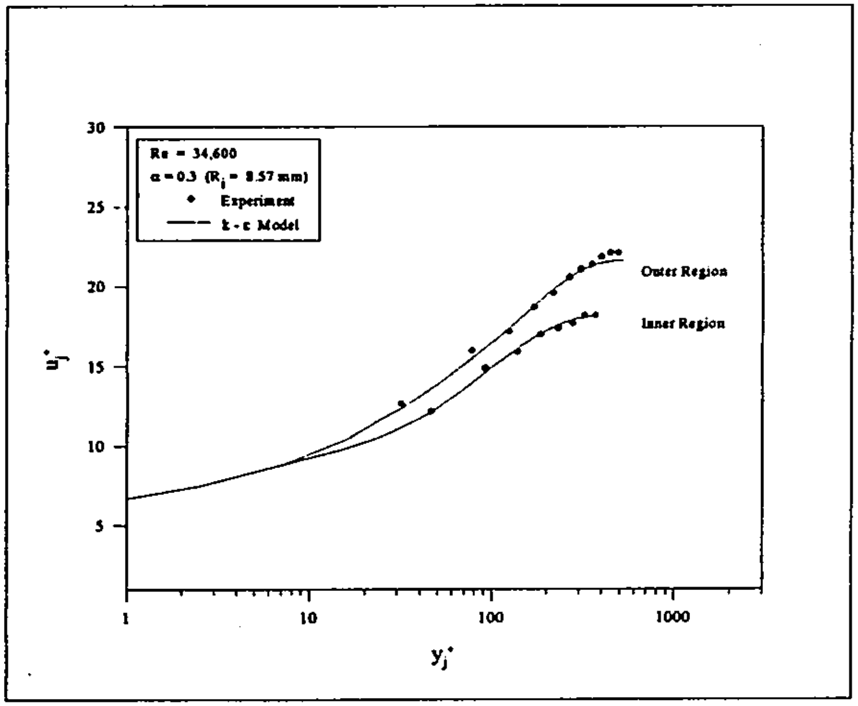

(a) Re = 34,600

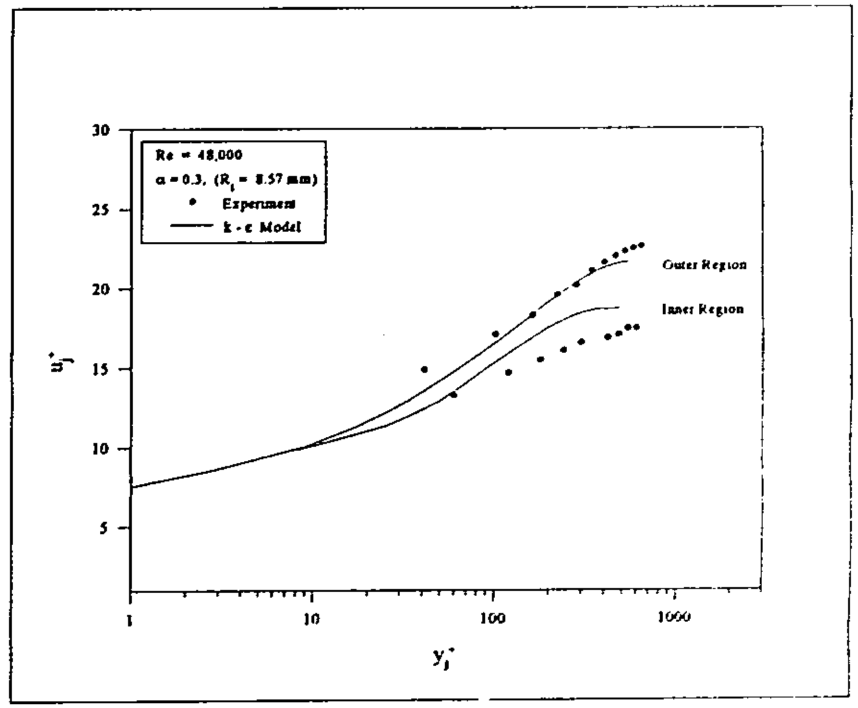

(b) Re = 48,000

Figure 3.30 Theoretical (k-ε Turbulence Model) and Experimental Velocity Distributions, Fully Developed, $\alpha = 0.3$ ($R_i = 8.57$ mm)

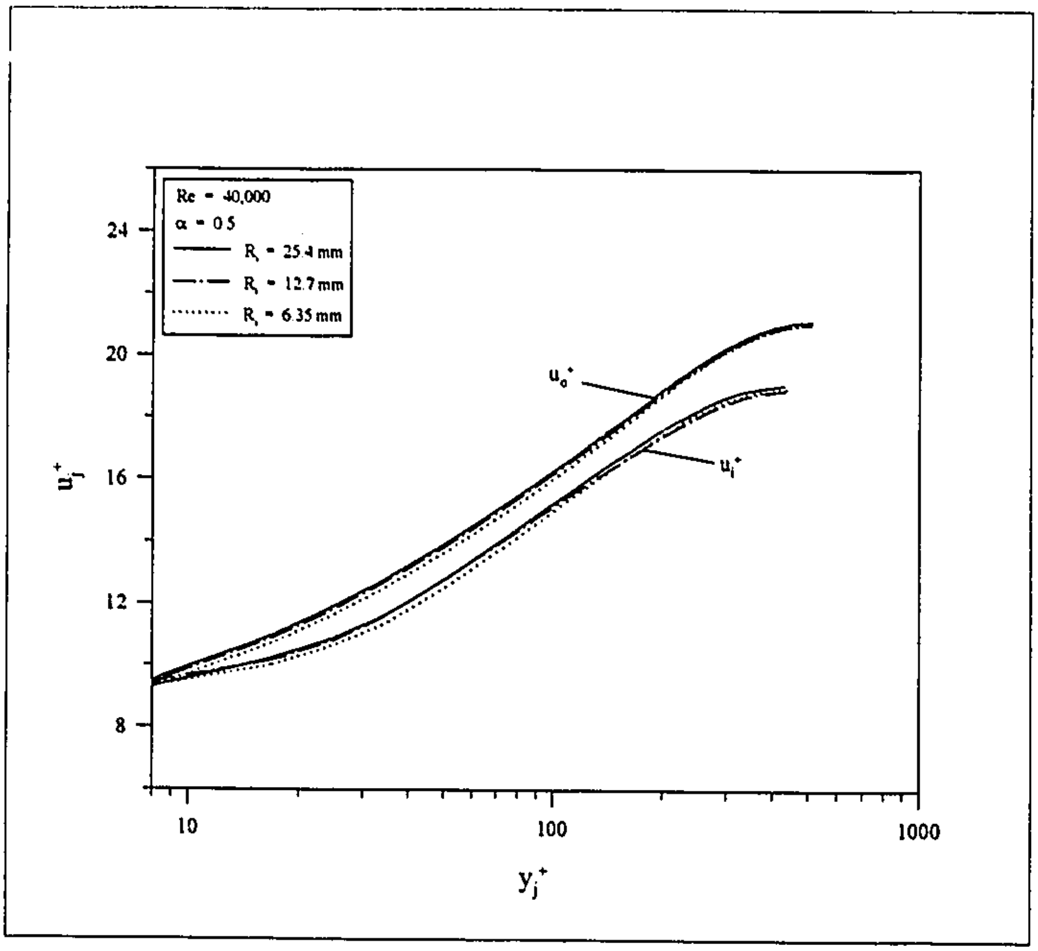

Figure 3.31 Theoretical (k-ε Turbulence Model) Velocity Distributions, Fully Developed, $\alpha = 0.5$, Re = 40,000

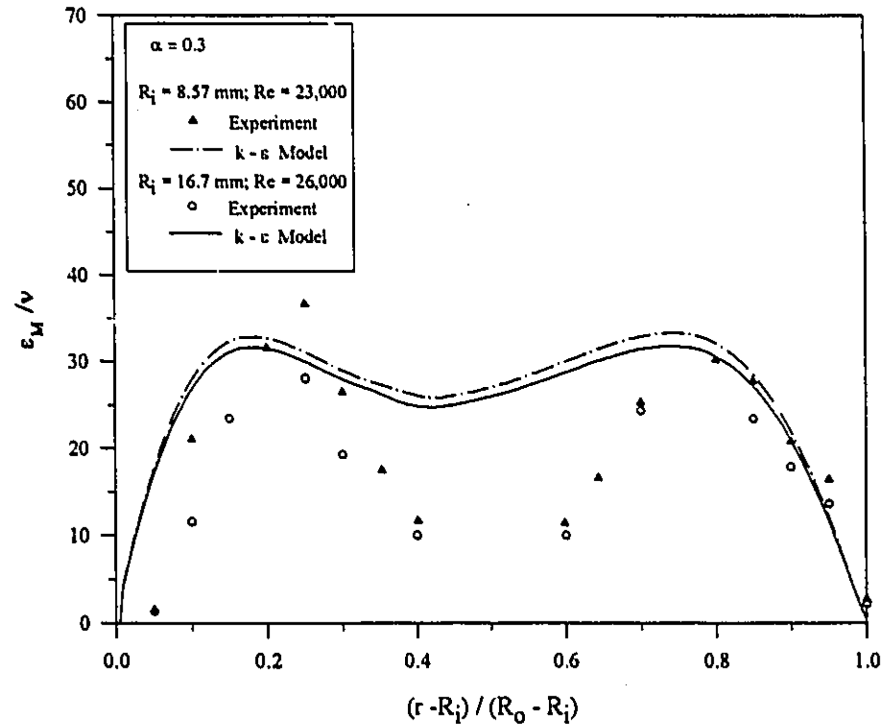

Figure 3.32 Theoretical (k-ε Turbulence Model) and Experimental Eddy Diffusivity Distributions for Momentum, Fully Developed Turbulent Flow

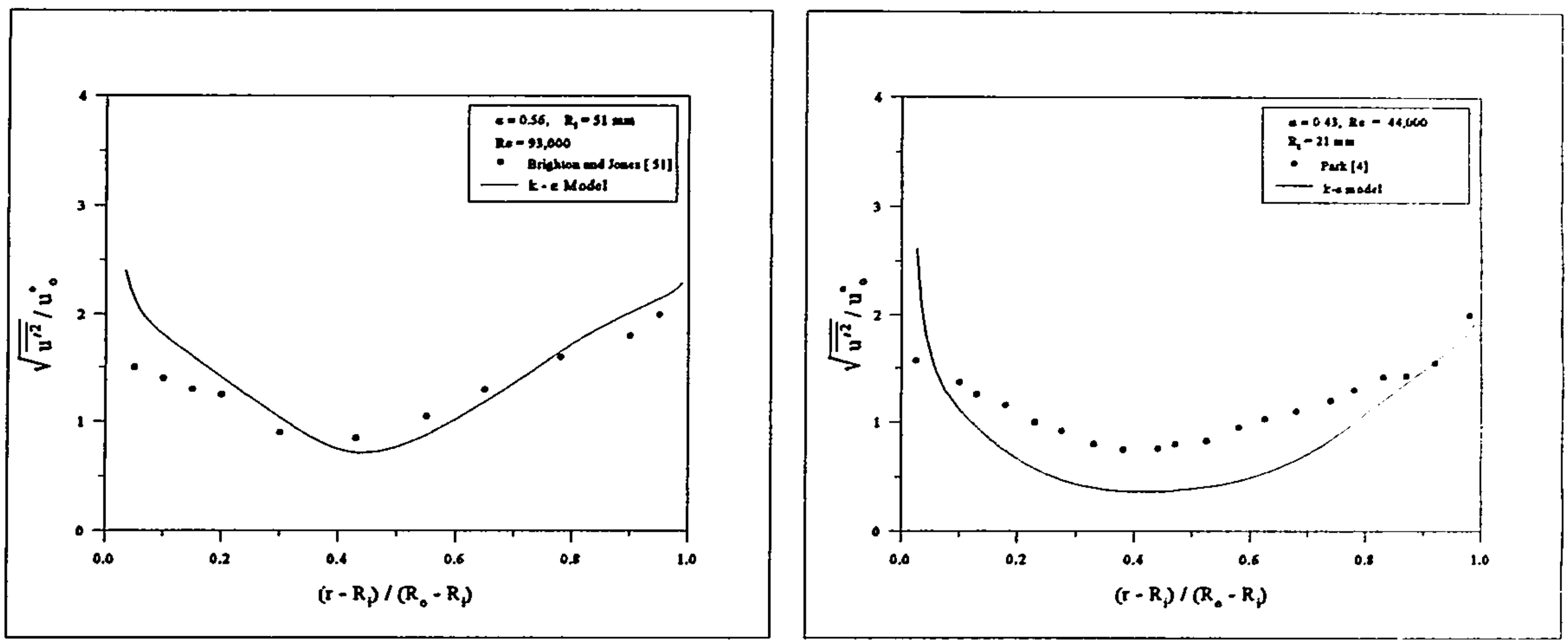

(a) Re = 93,000

(b) Re = 44,000

Figure 3.33 Theoretical (k-ε Turbulence Model) and Experimental Turbulent Intensity Distributions, Fully Developed Turbulent Flow

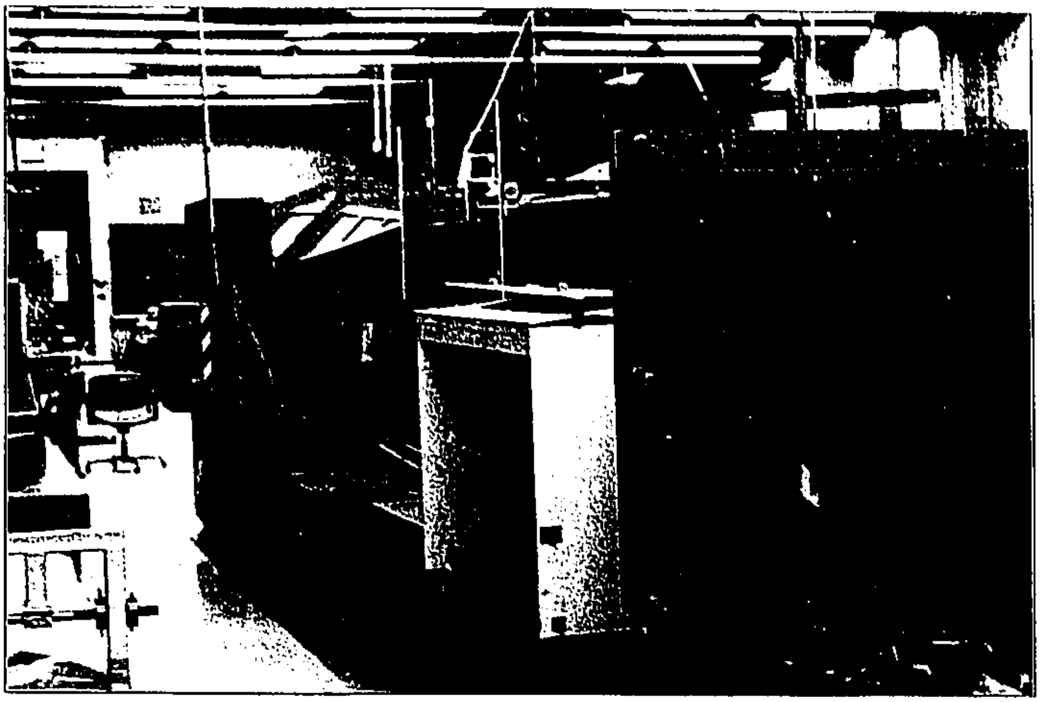

Figure 4.1 Wind Tunnel

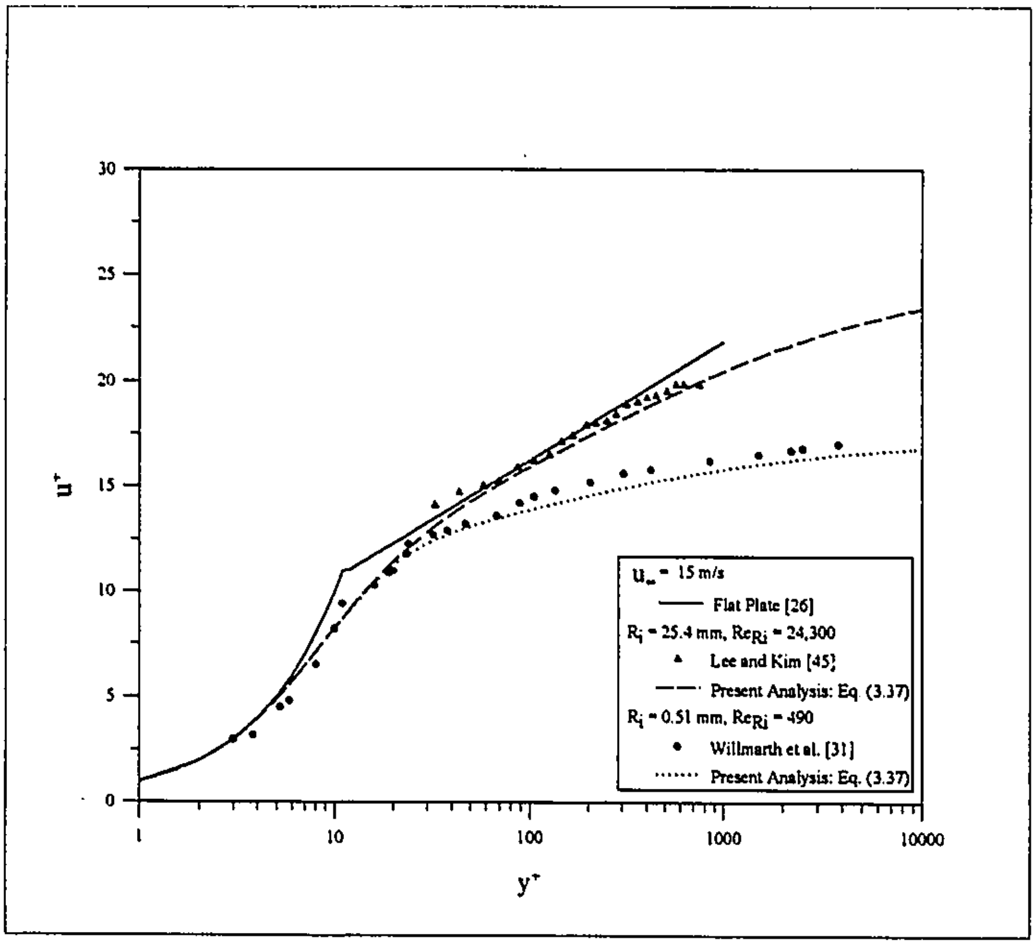

Figure 4.2 Effect of Transverse Convex Curvature on Velocity Distribution, Turbulent Boundary Layer Flow

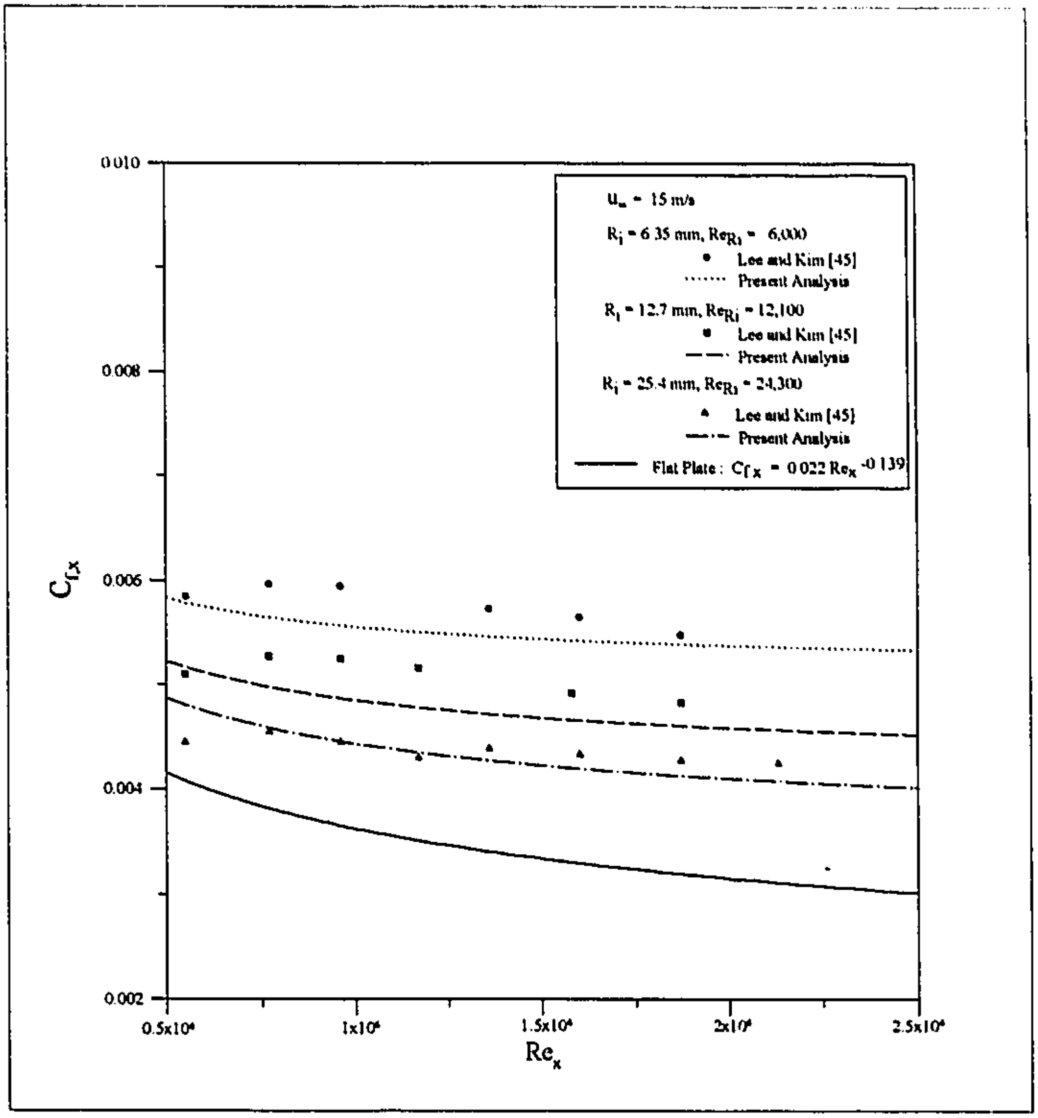

Figure 4.3 Effect of Transverse Convex Curvature on Skin Friction Coefficient, Turbulent Boundary Layer Flow

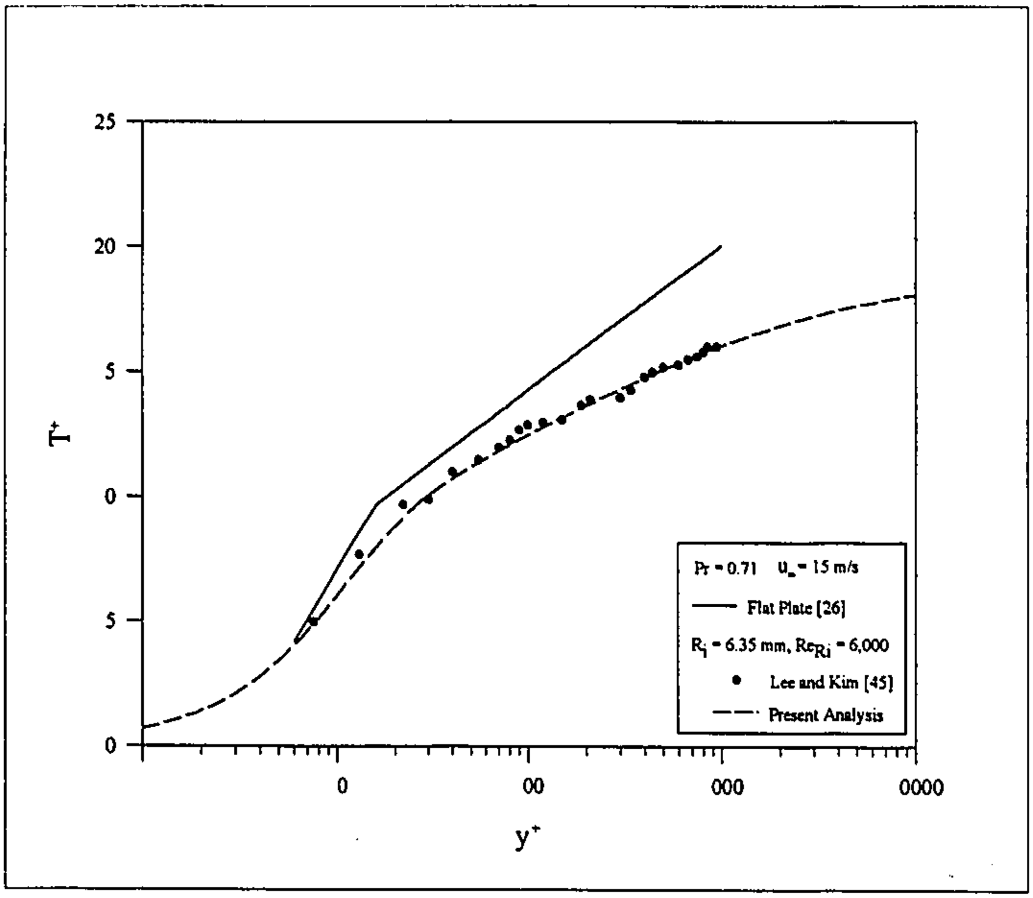

Figure 4.4 Temperature Distribution, Cylinder Wall Heated, Turbulent Boundary Layer Flow

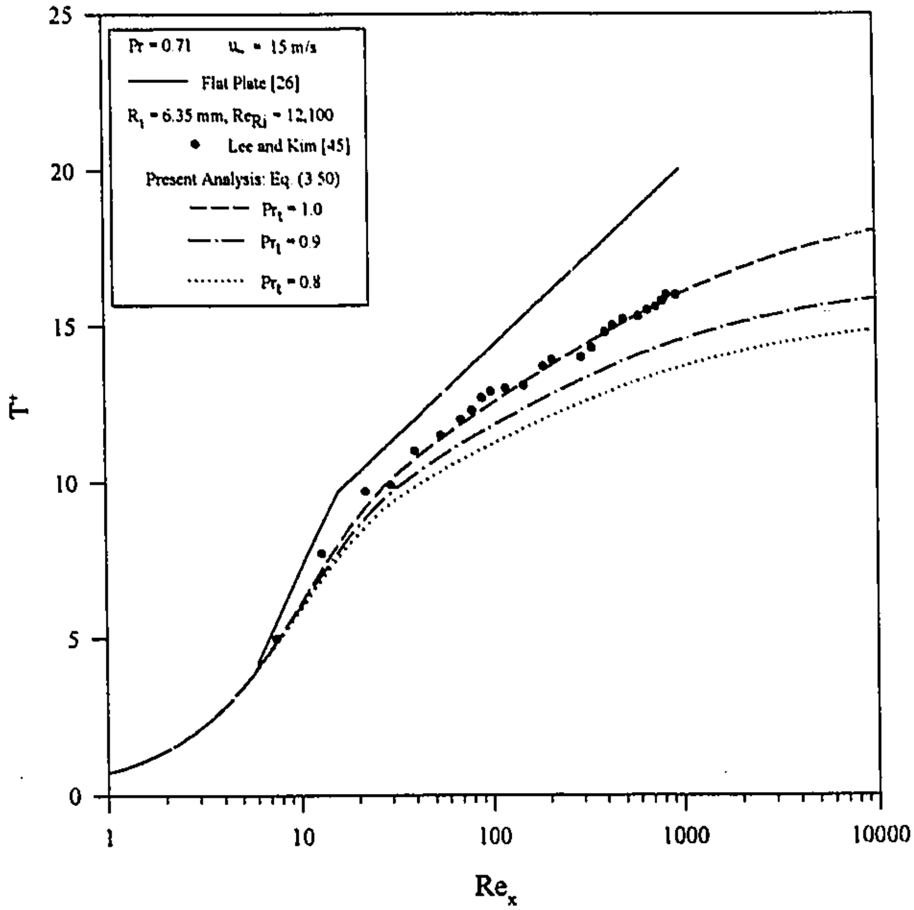

Figure 4.5 Effect of Turbulent Prandtl Number, Pr_t, on Temperature Distribution, Cylinder Wall Heated, Turbulent Boundary Layer Flow

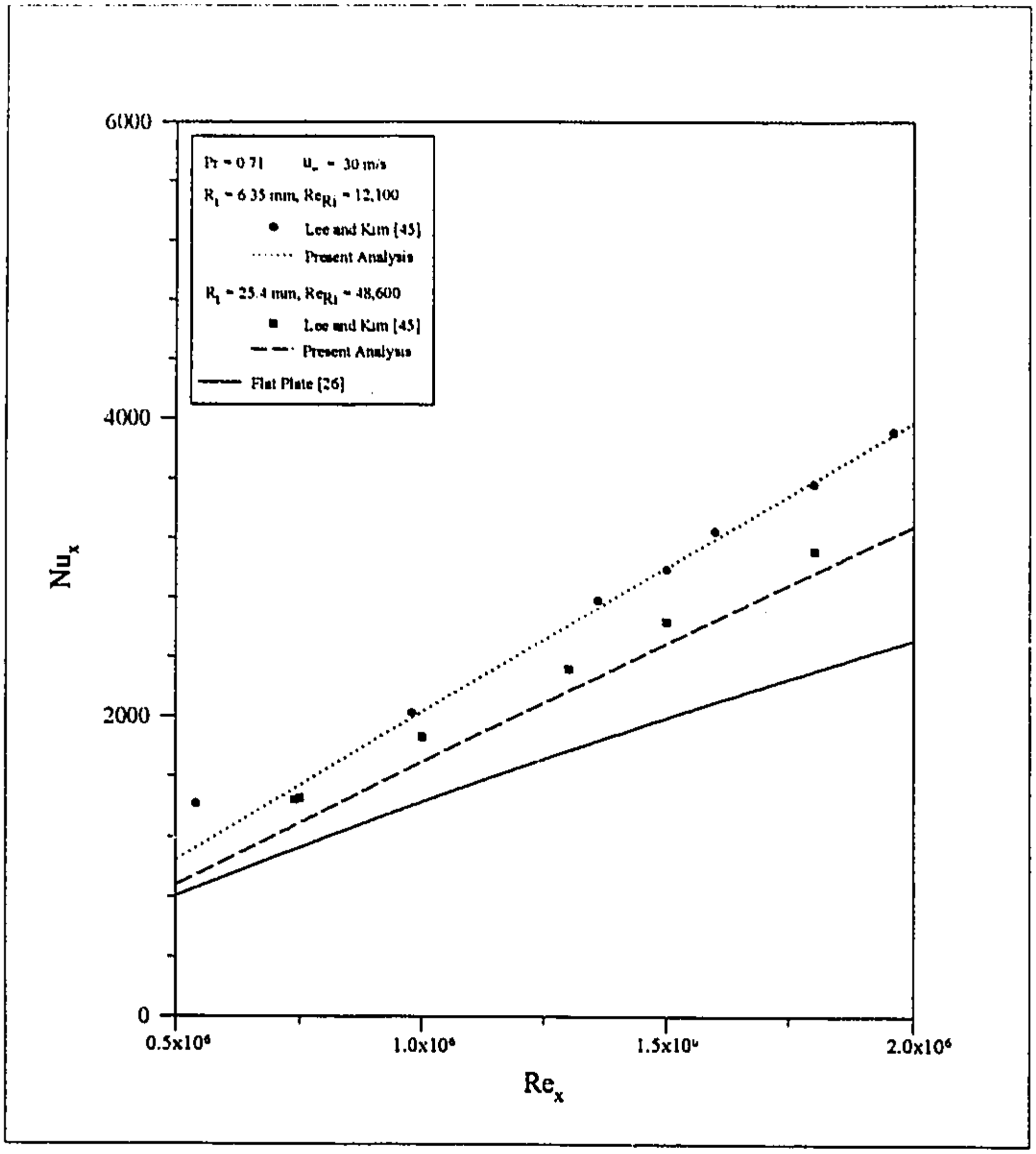

Figure 4.6 Effect of Transverse Convex Curvature on Nusselt Number, Cylinder Wall Heated, Turbulent Boundary Layer Flow

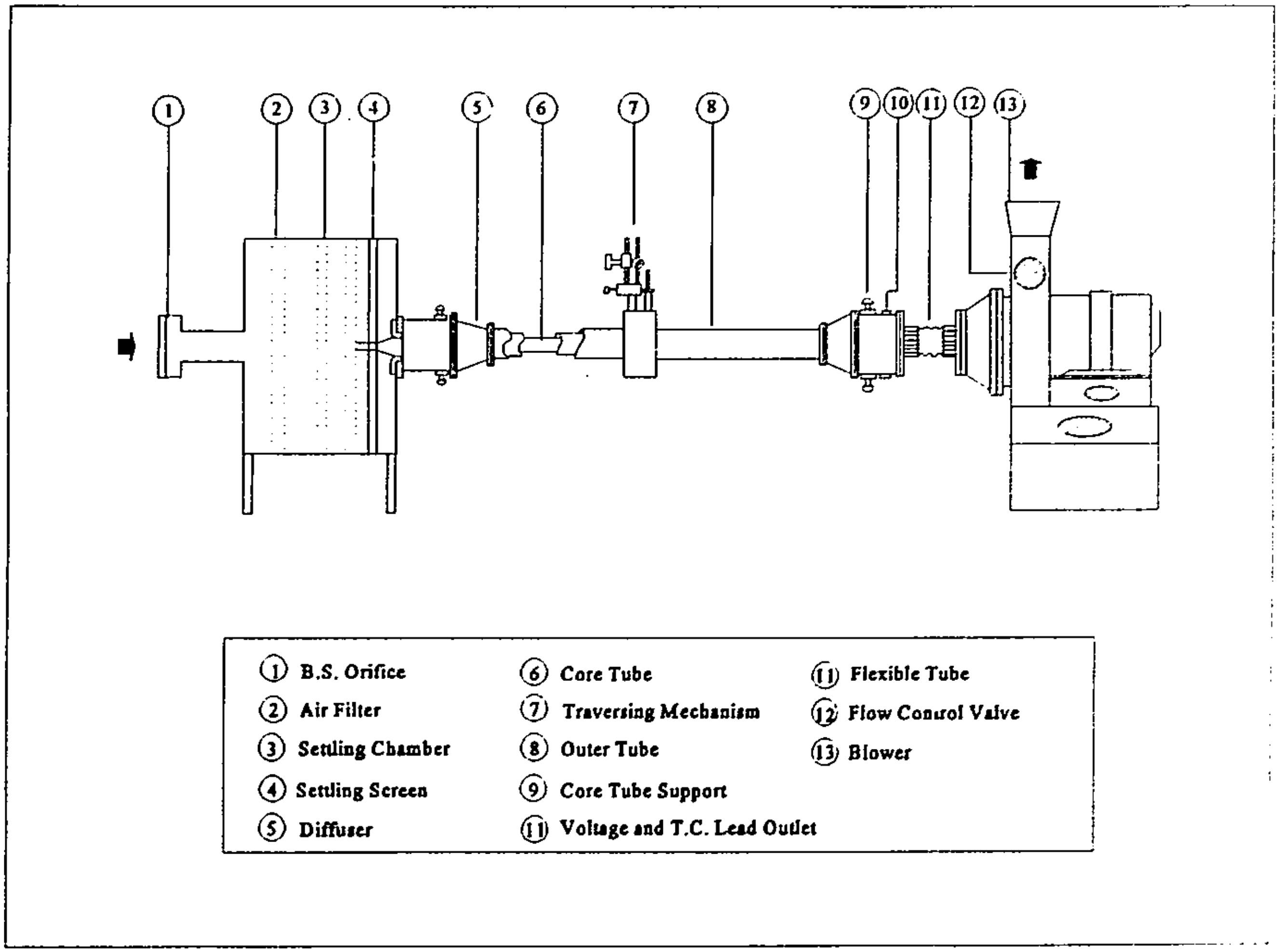

Figure 4.7 Schematic Diagram of Test Assembly

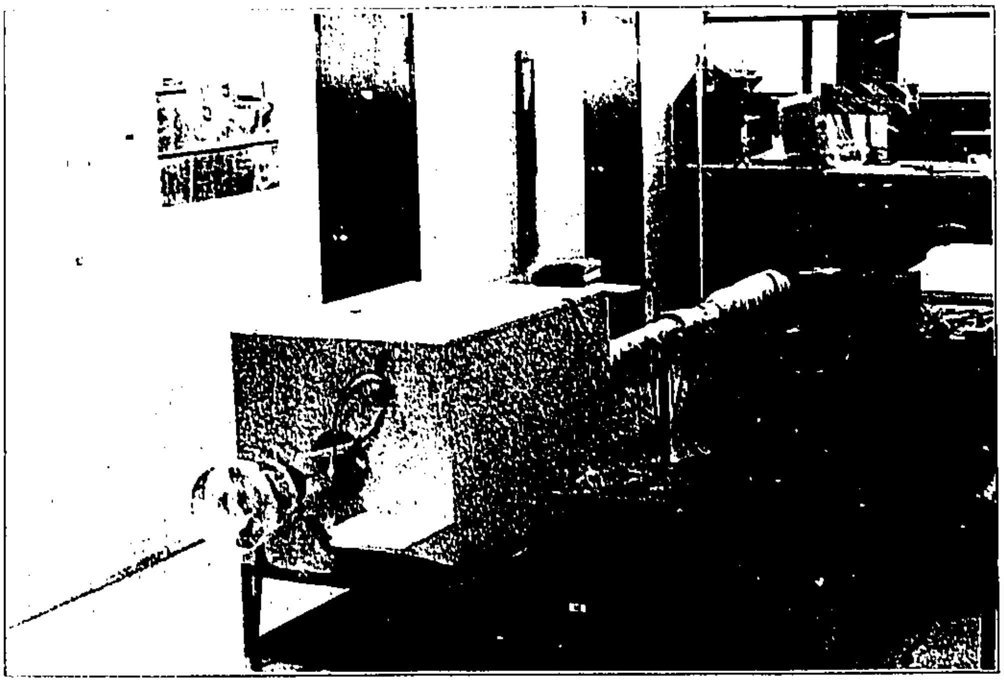

Figure 4.8 Experimental Apparatus From Inlet End

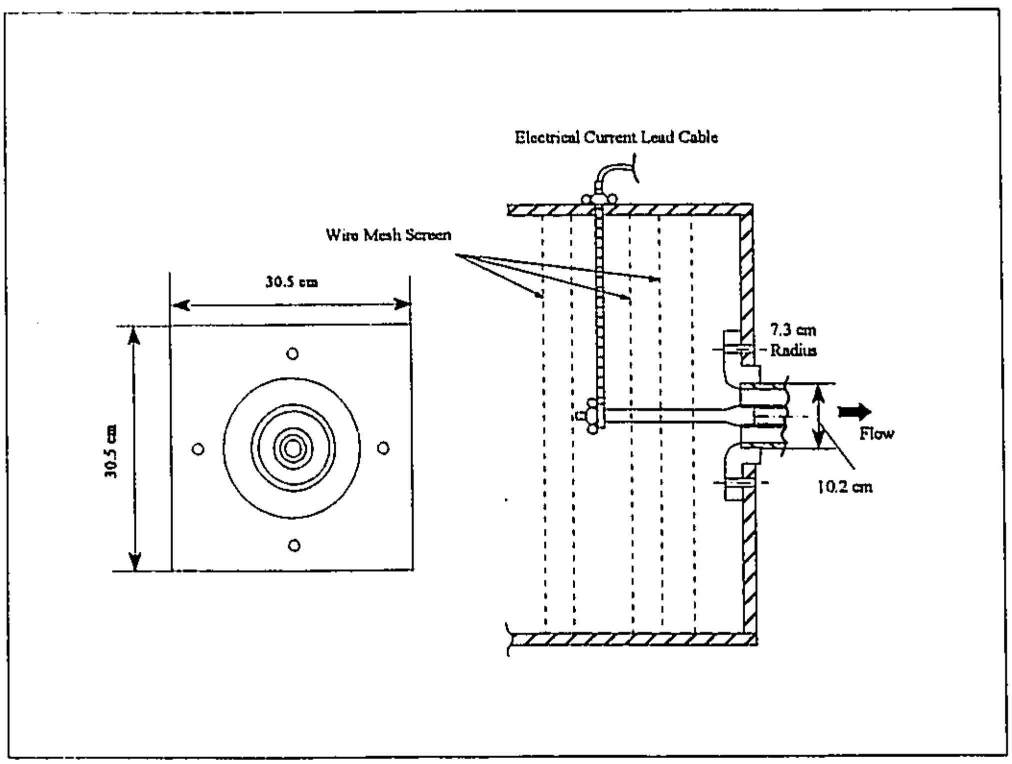

Figure 4.9 Details of Annular Duct Entrance

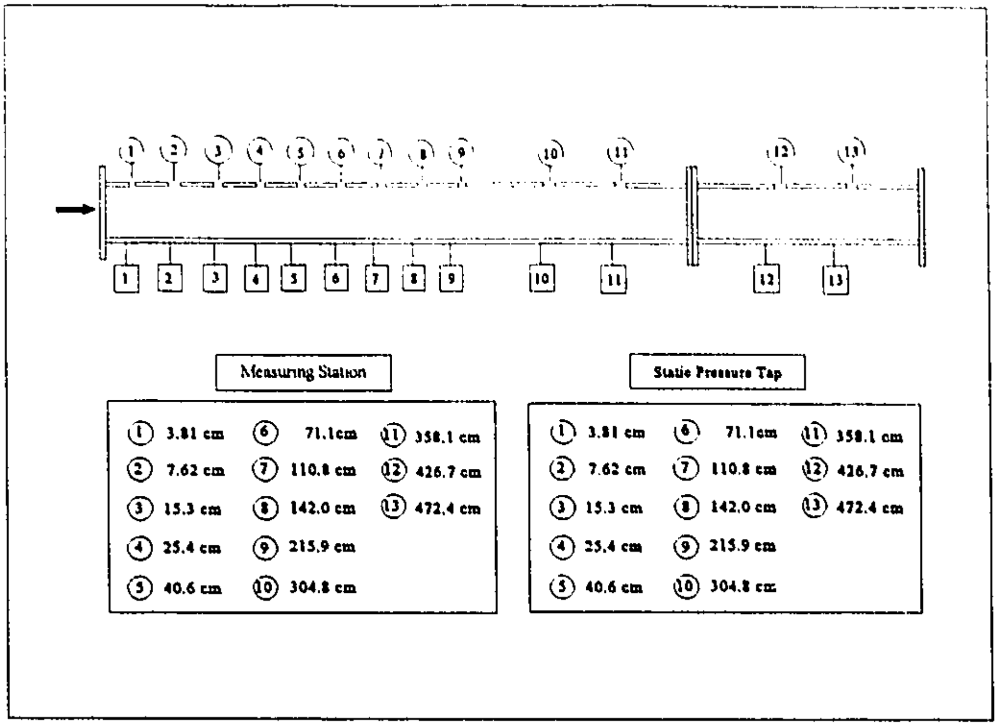

Figure 4.10 (a) Measuring Stations and Static Pressure Taps on Outer Tube for Test Section 1

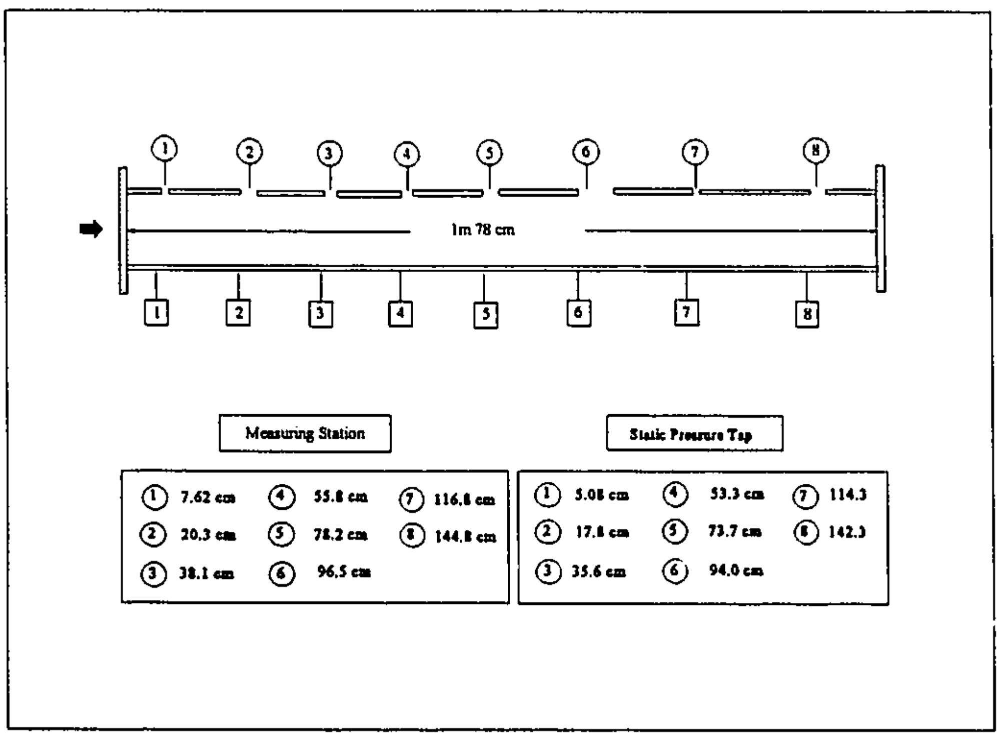

Figure 4.10 (b) Measuring Stations and Static Pressure Taps on Outer Tube for Test Section 2

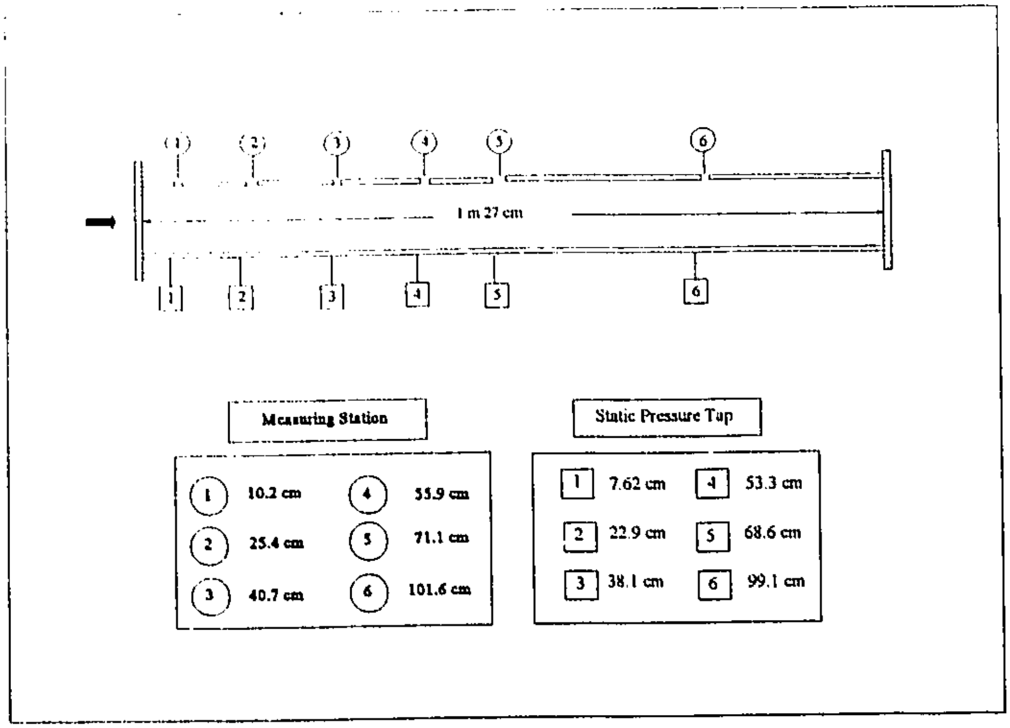

Figure 4.10 (c) Measuring Stations and Static Pressure Taps on Outer Tube for Test Section 3

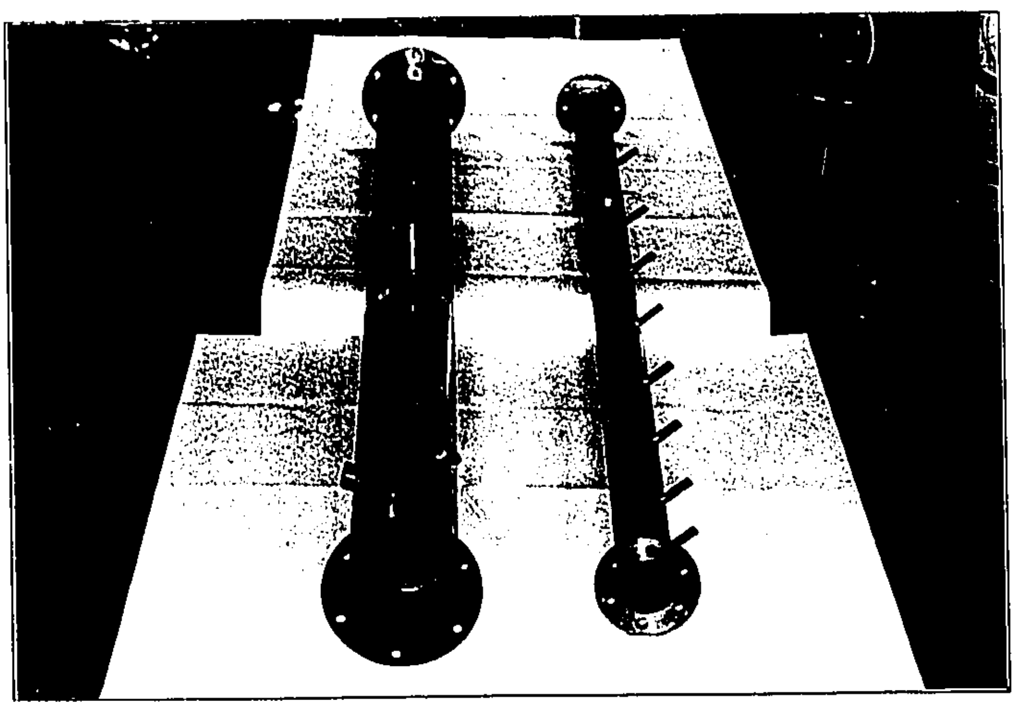

Figure 4.11 Outer Tubes of Test Sections

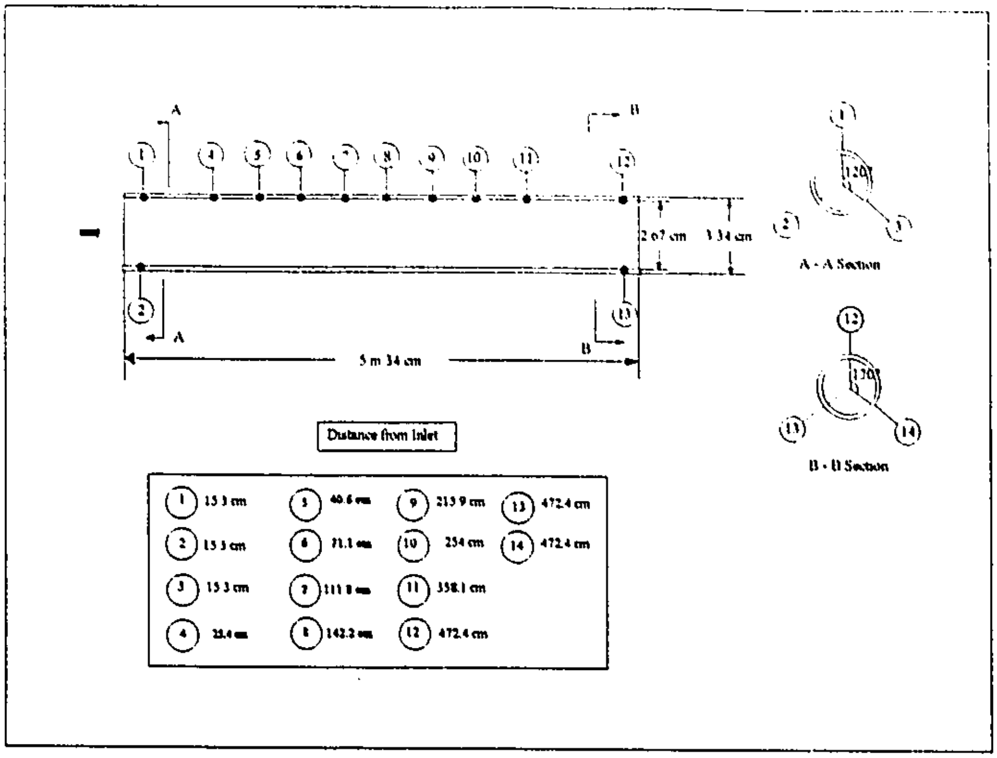

Figure 4.12 (a) Thermocouple Locations in Core Tube for Test Section 1

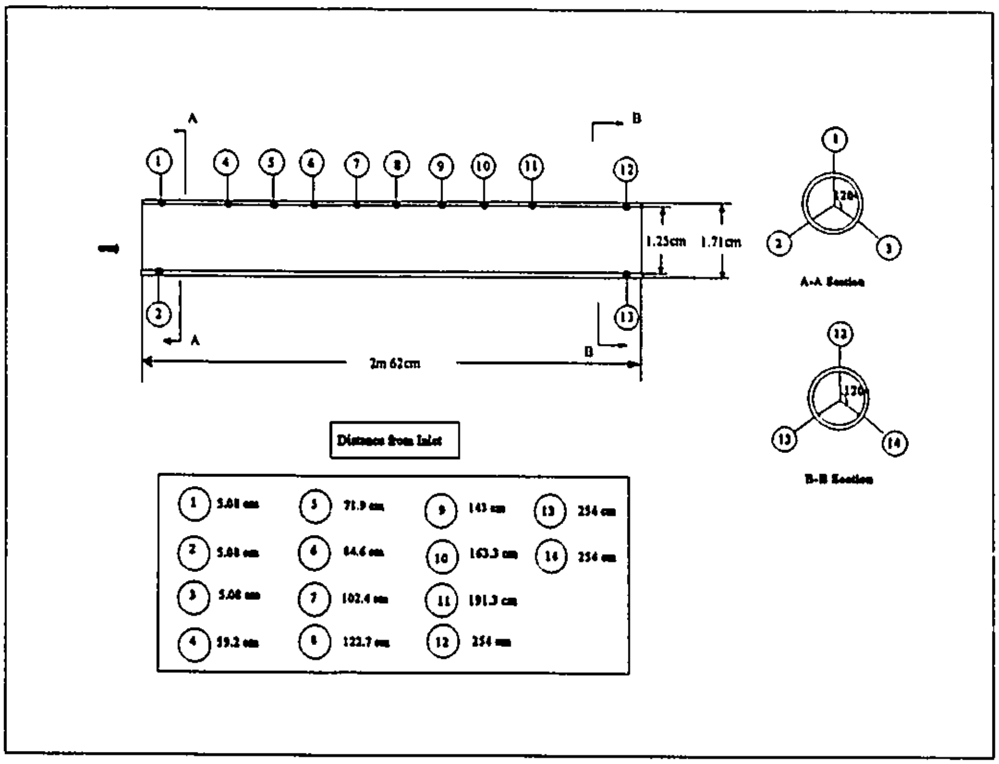

Figure 4.12 (b) Thermocouple Locations in Core Tube for Test Section 2

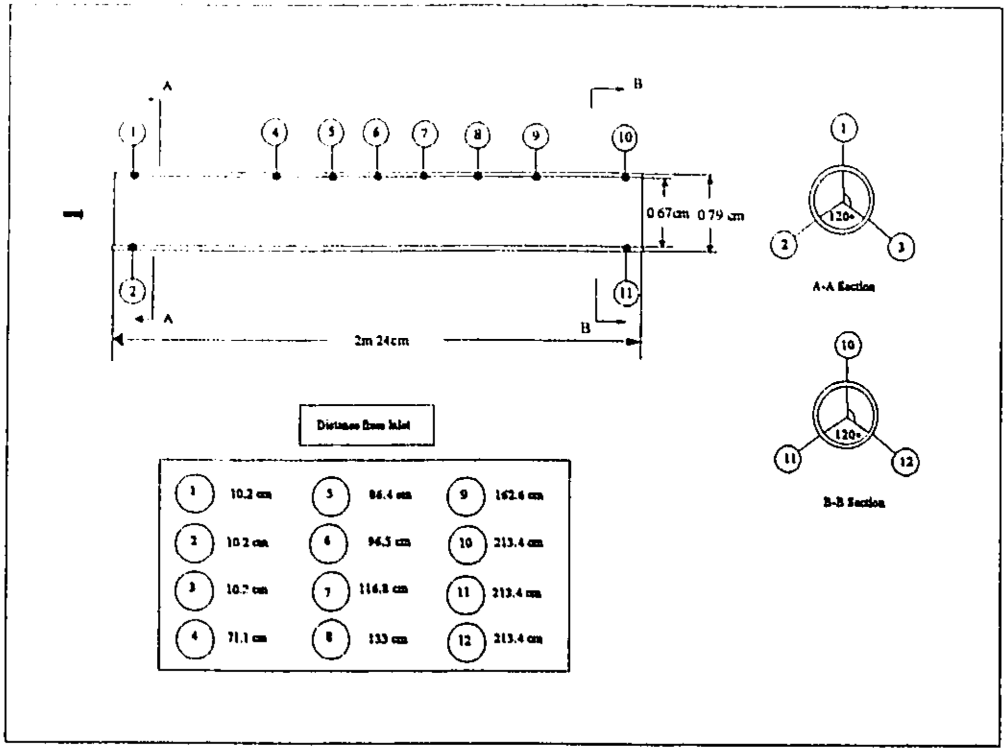

Figure 4.12 (c) Thermocouple Locations in Core Tube for Test Section 3

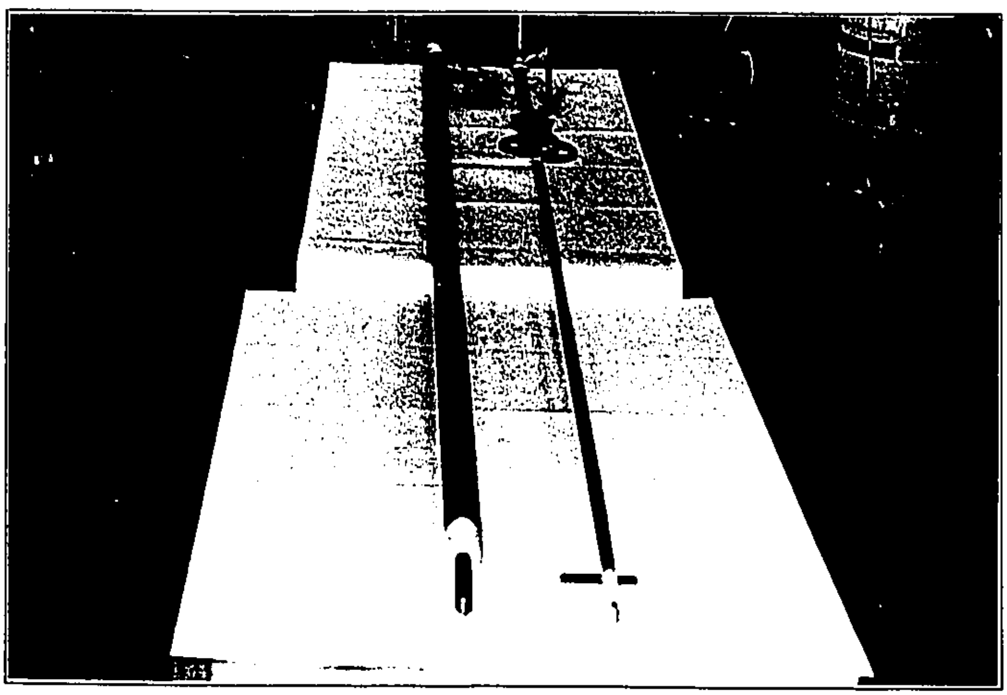

Figure 4.13 Inner Core Tubes of Test Sections

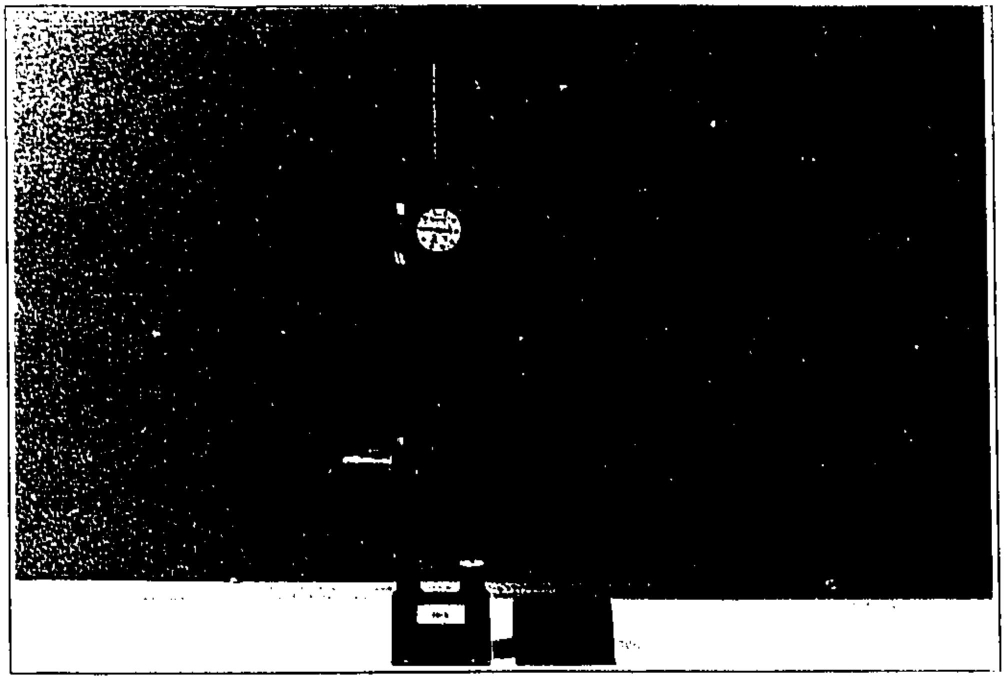

Figure 4.14 Traversing Mechanism

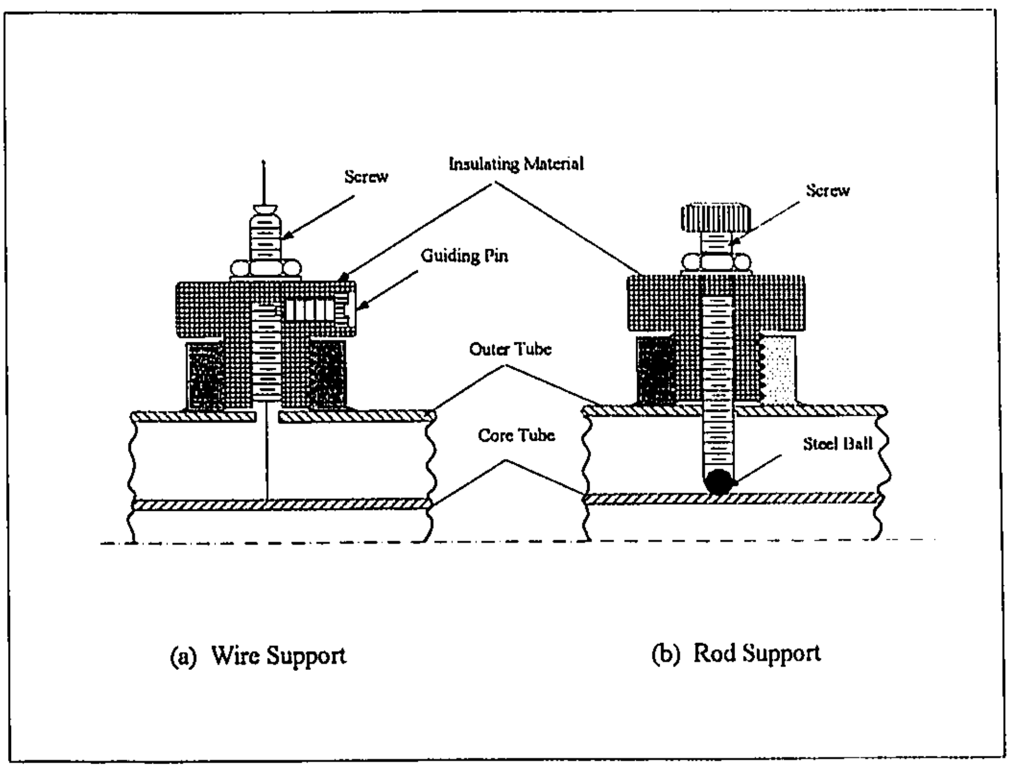

Figure 4.15 Details of Inner Core Support

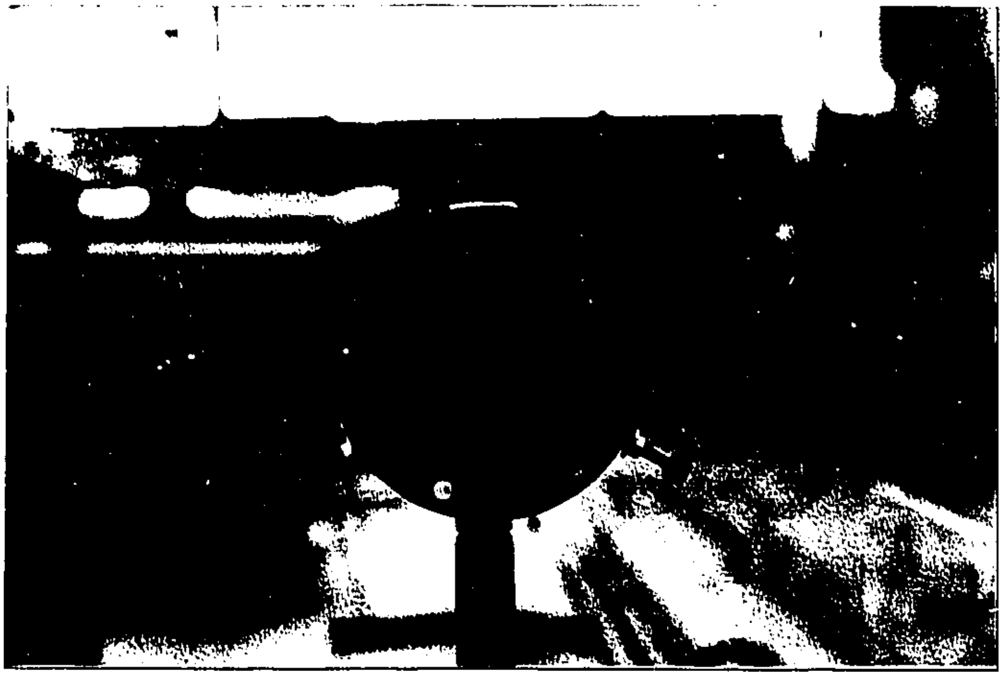

Figure 4.16 Inner Core Tube Support (Rod Type)

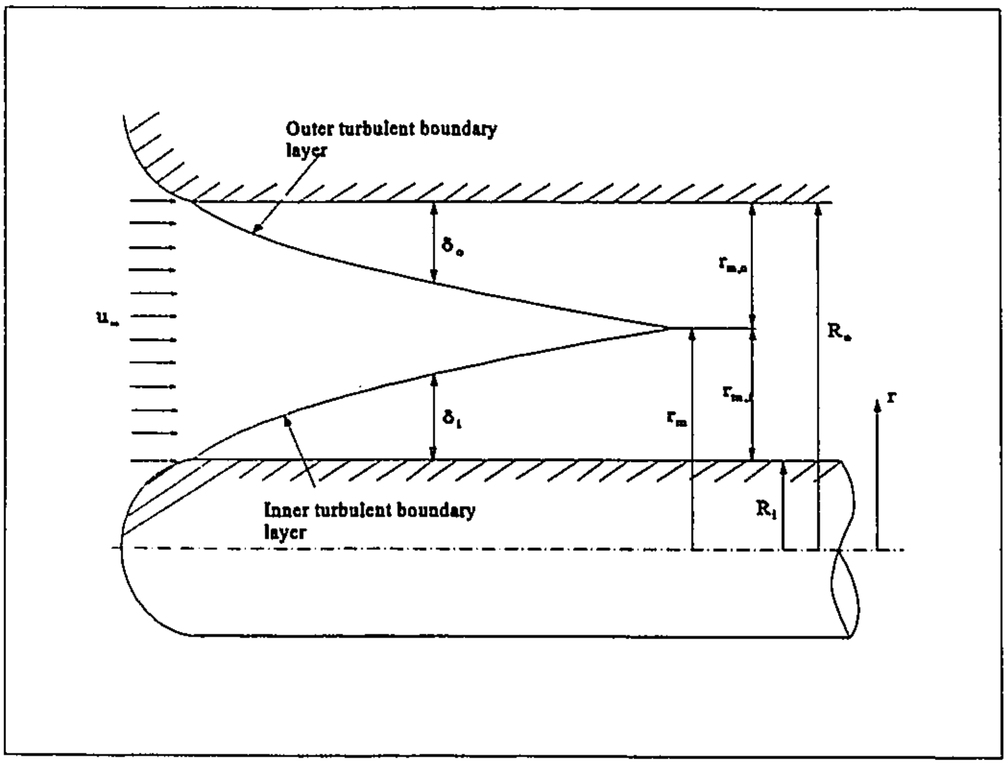

Figure 4.17 Entrance Region of Concentric Annular Duct

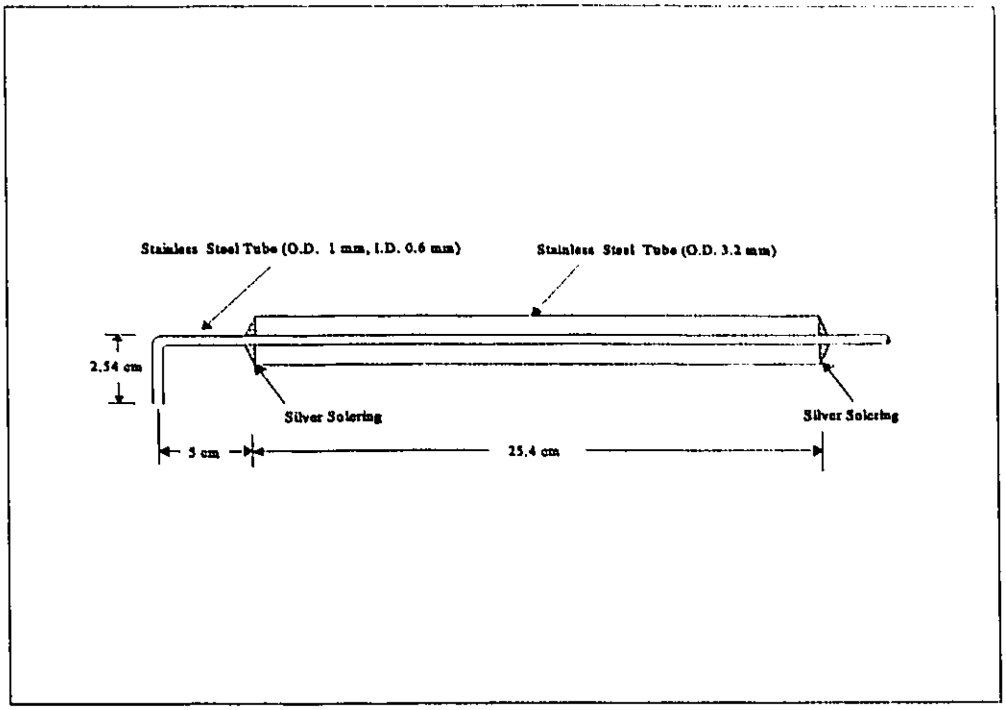

(a) Details

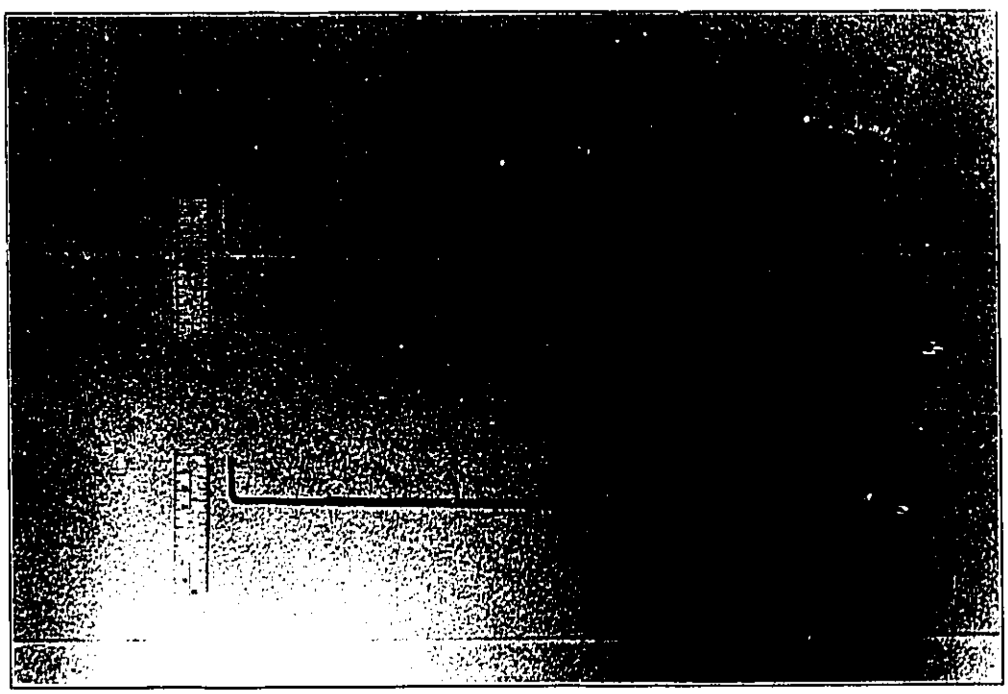

(b)

Figure 4.18 Total Pressure Probe (Pitot Tube)

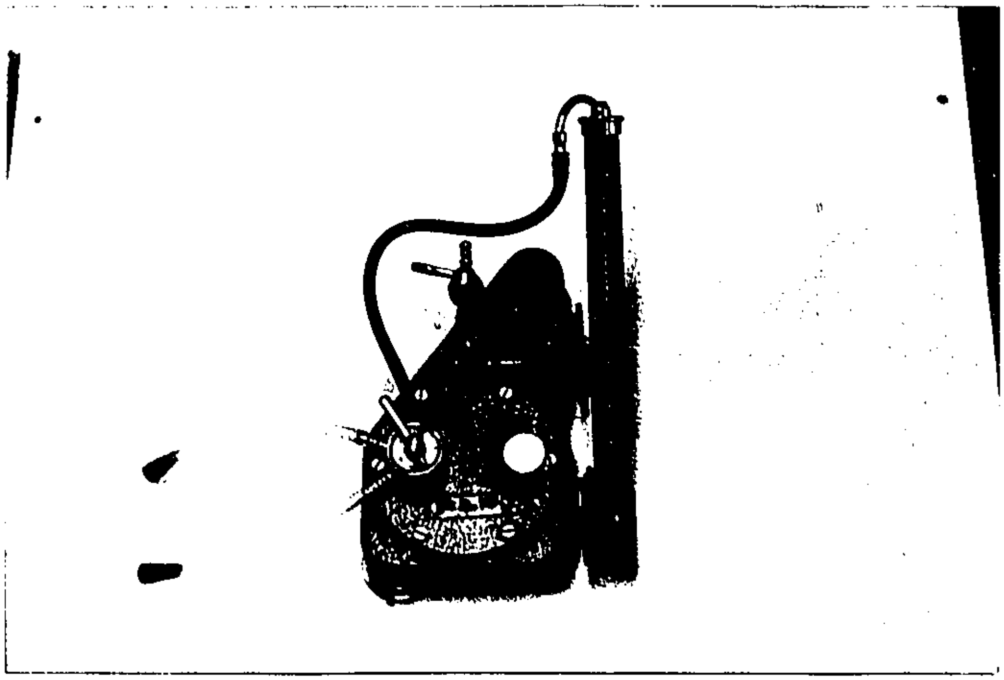

(a) Micro-Manometer

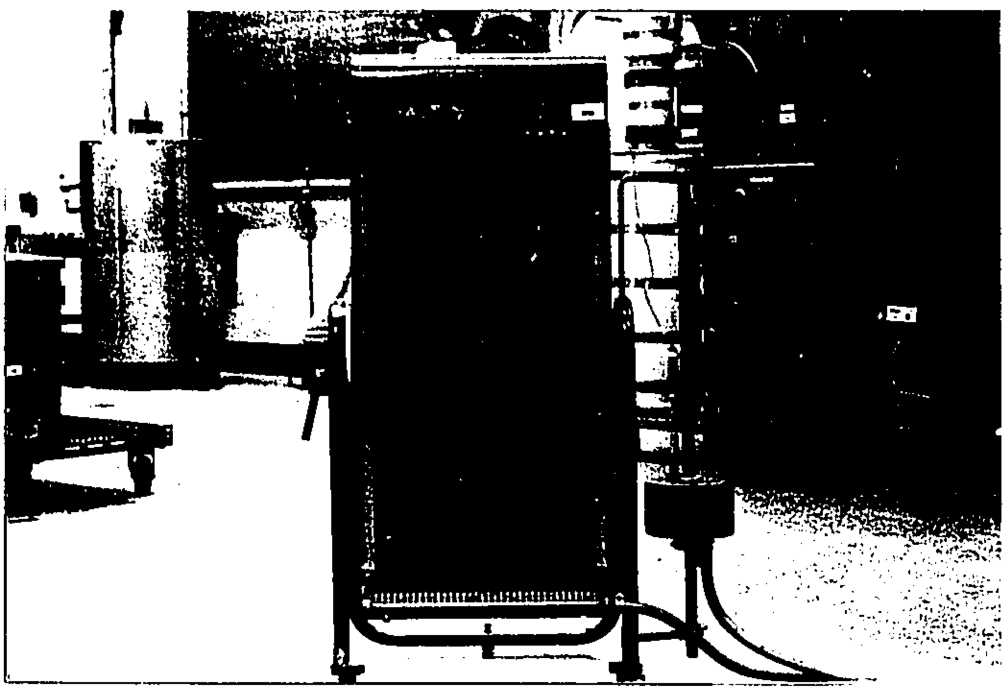

(b) Long-Slended Manometer

Figure 4.19 Manometers

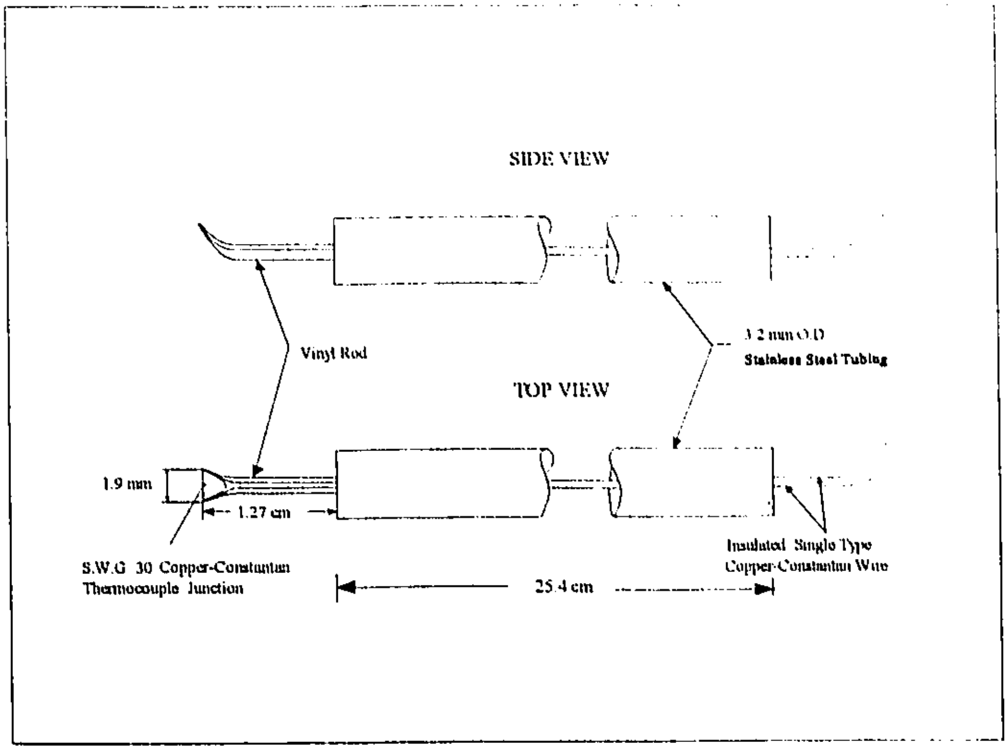

(a) Details

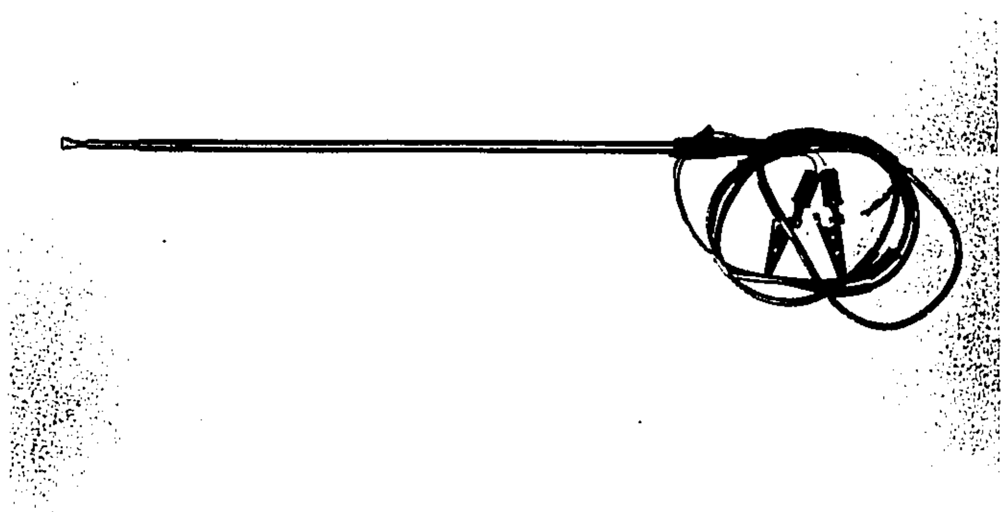

(b)

Figure 4.20 Thermocouple Probe

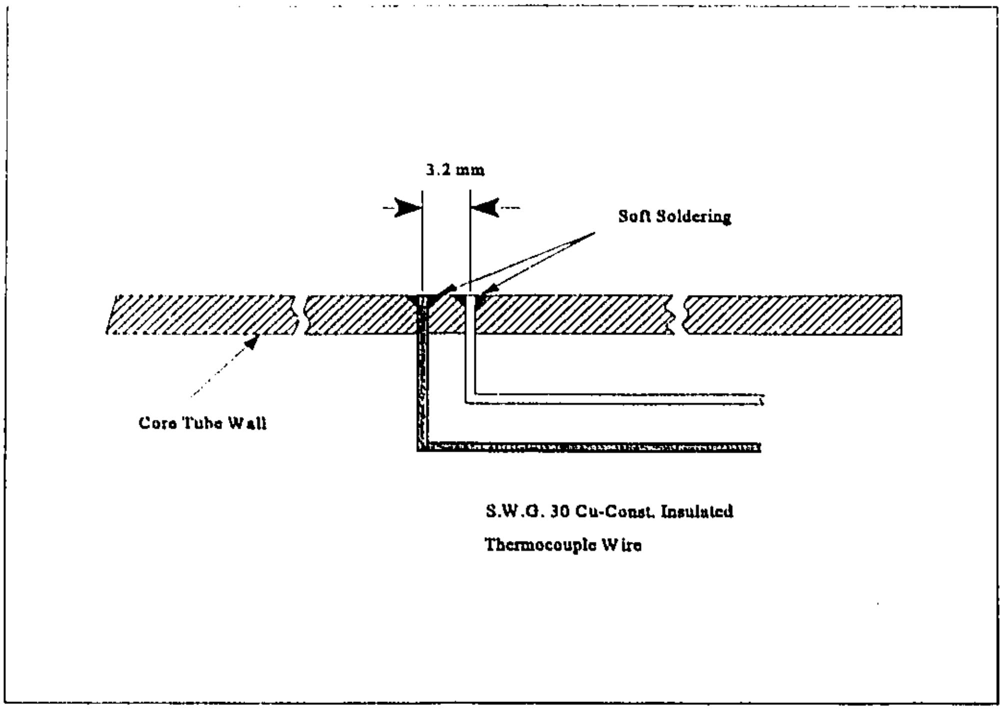

(a) Details

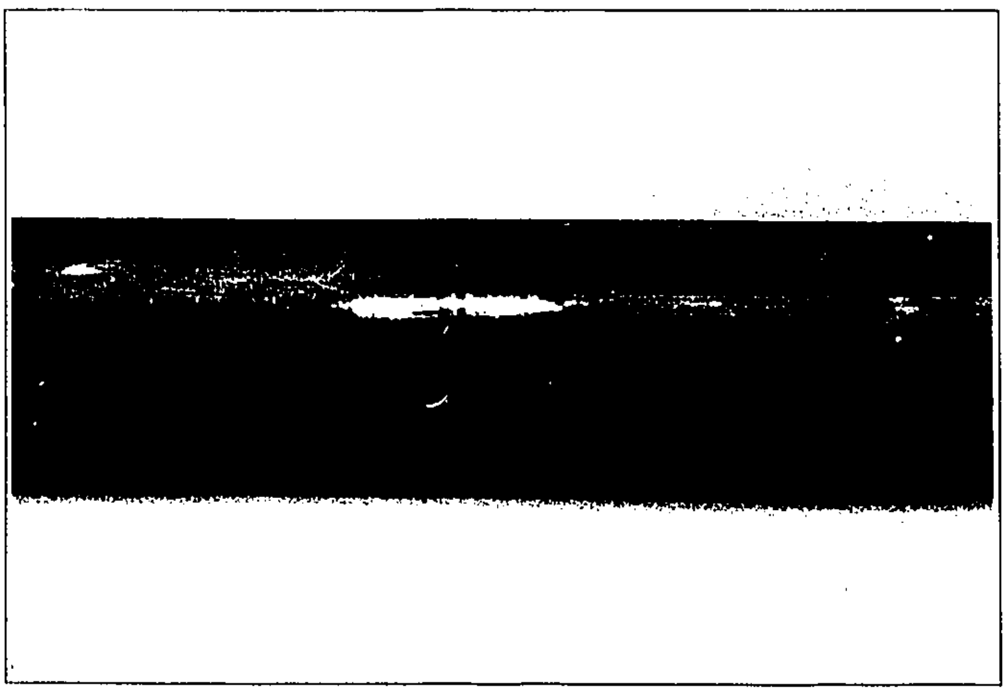

(b)

Figure 4.21 Split Junction of Inner Core Wall Thermocouples

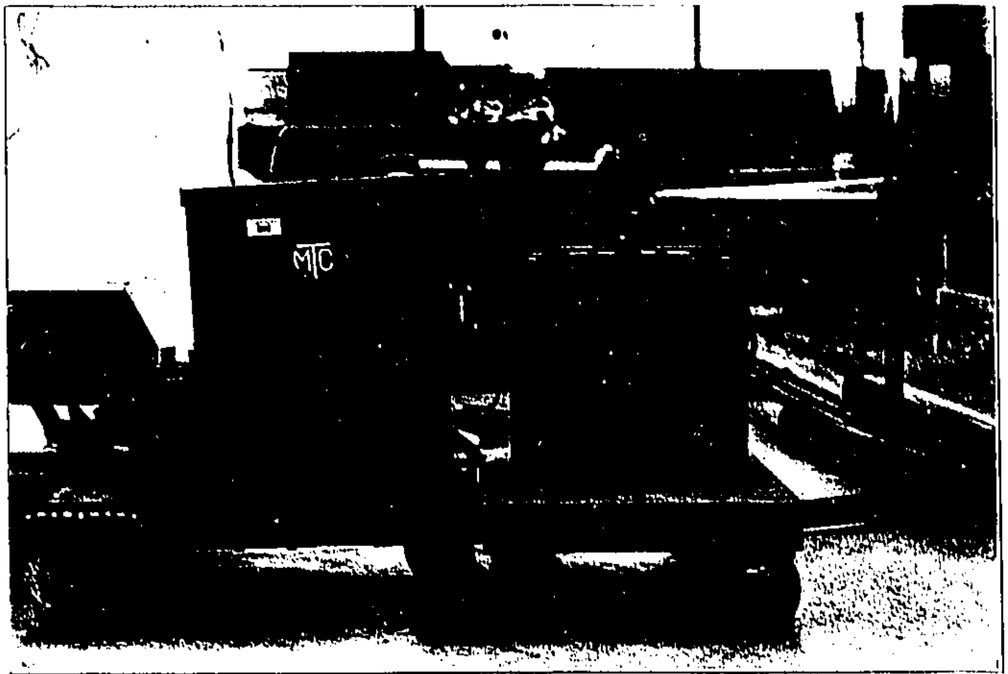

Figure 4.22 Step-down and Current Transformers

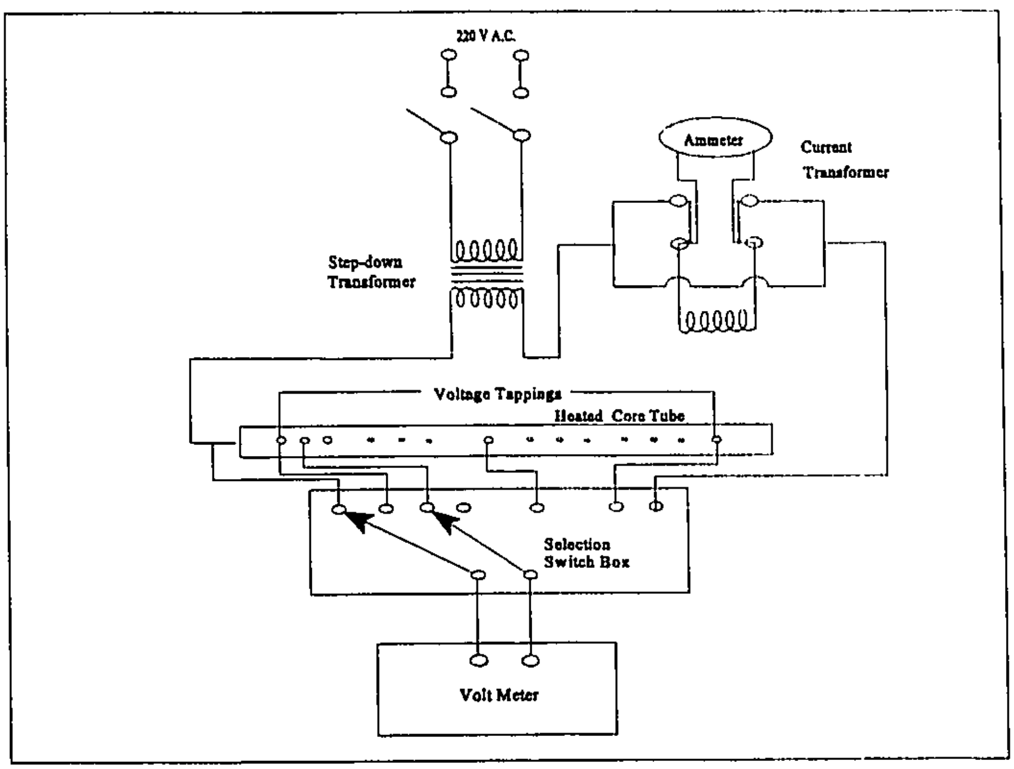

Figure 4.23 Power Supply and Instrumentation Circuit

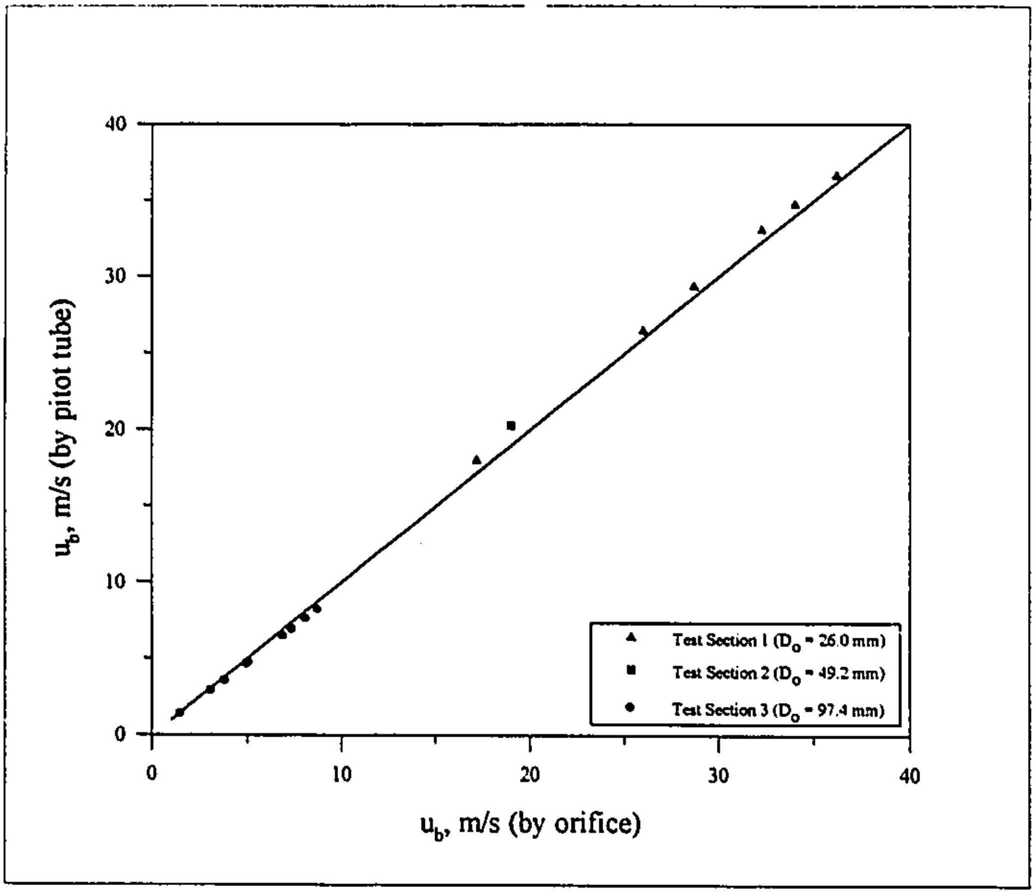

Figure 4.24 Calibration Curve of Orifice

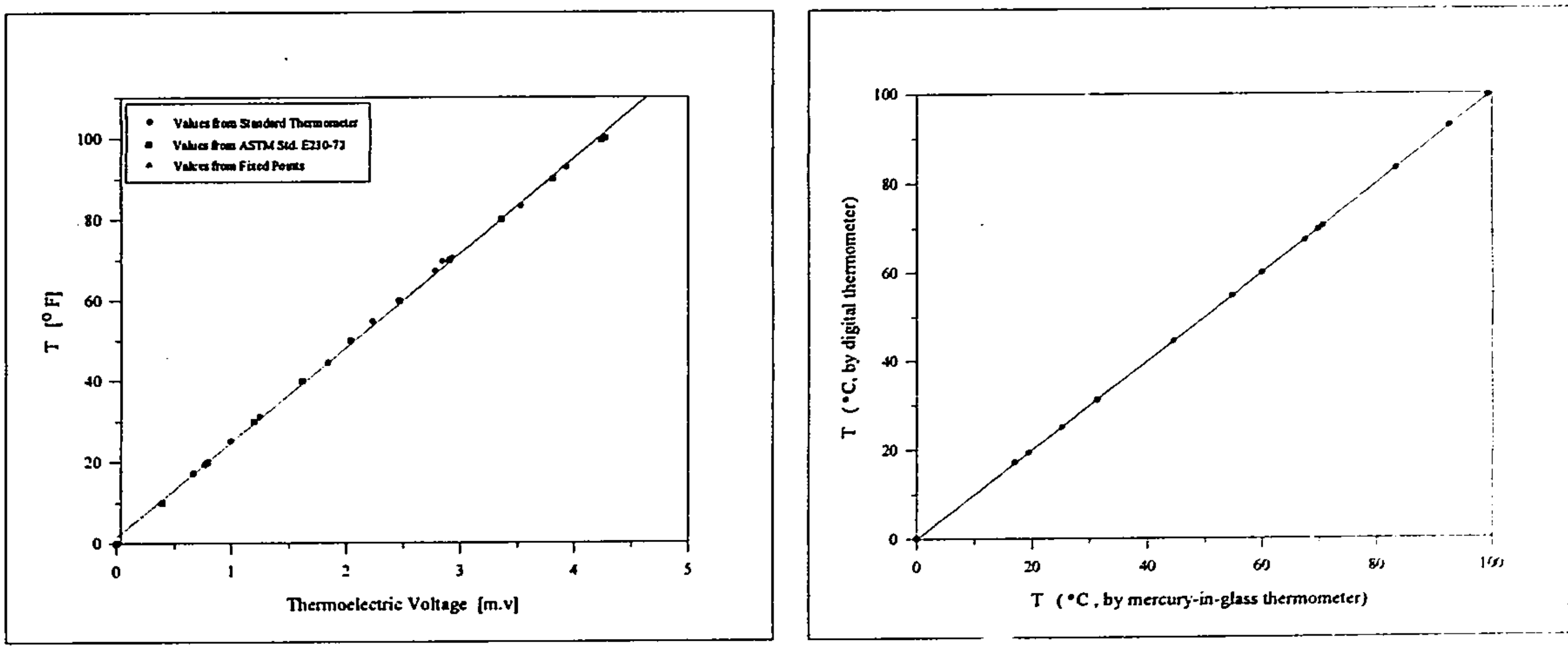

(a)

(b)

Figure 4.25 Calibration Curve of Thermocouples

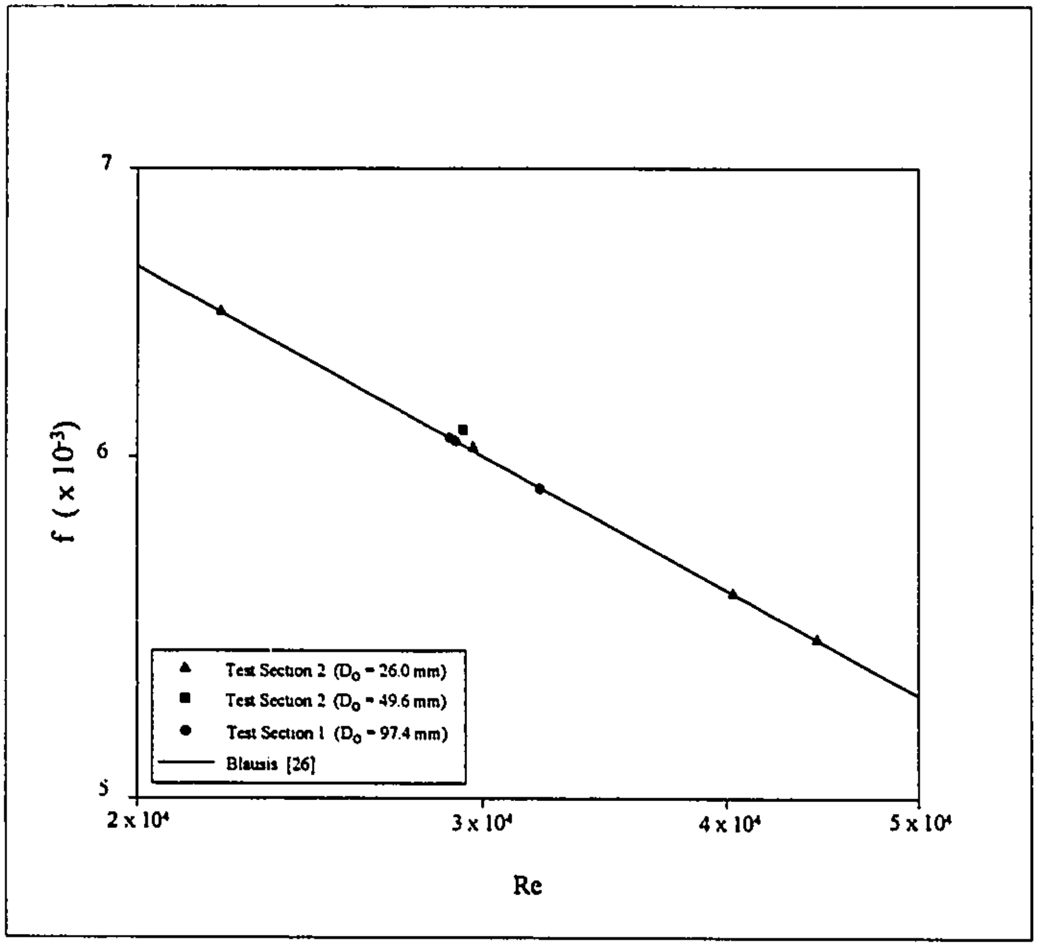

Figure 4.26 Friction Coefficient, Pipe Flow (without Inner Core Tube)

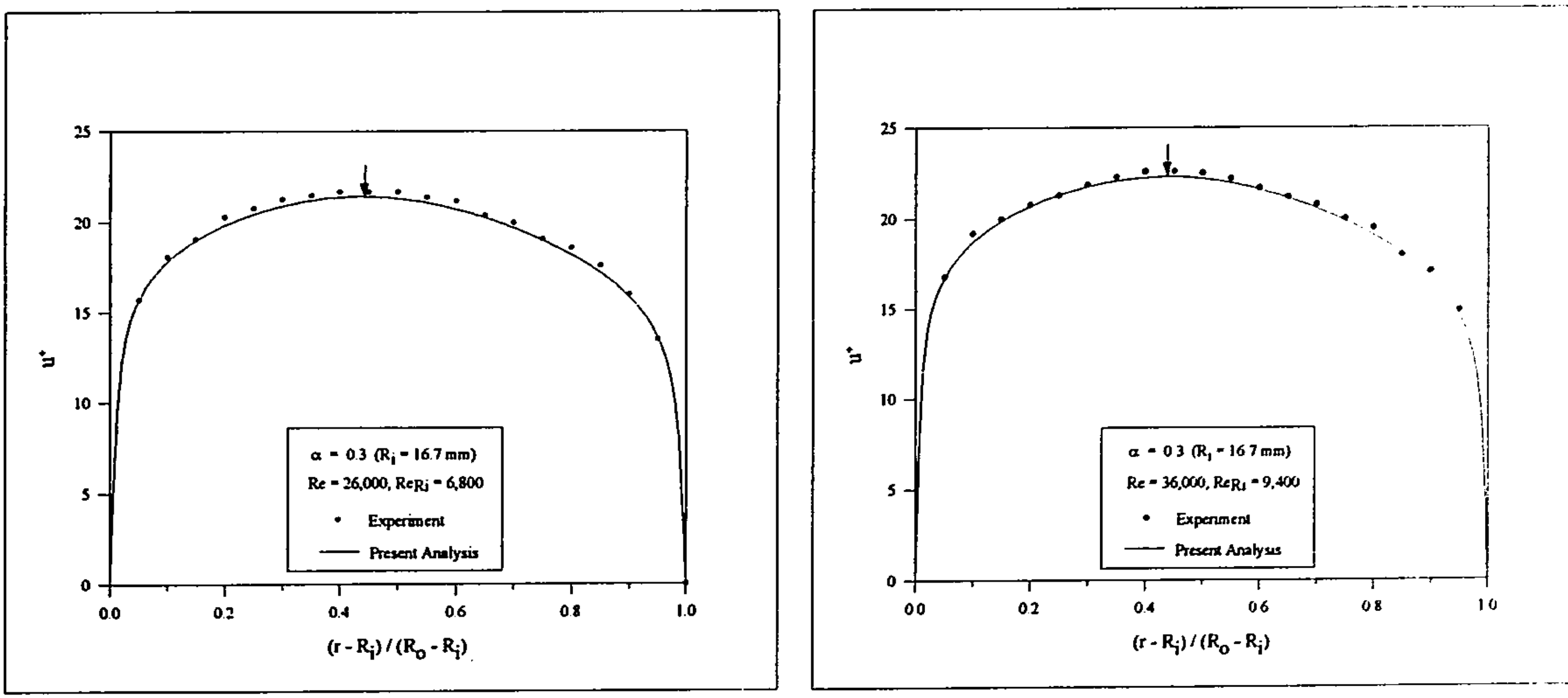

(a) Re = 26,000

(b) Re = 36,000

Figure 4.27 Comparison between Theoretical and Experimental Velocity Distribution, Fully Developed, $\alpha = 0.3$ ($R_i = 16.7$mm).
(continued)

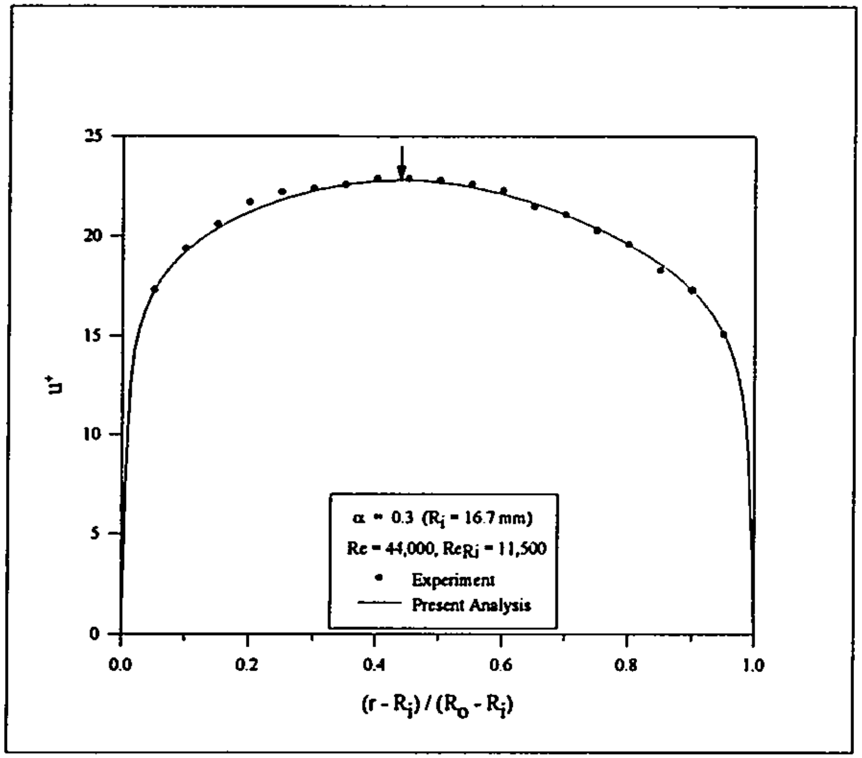

(c) Re = 48,000

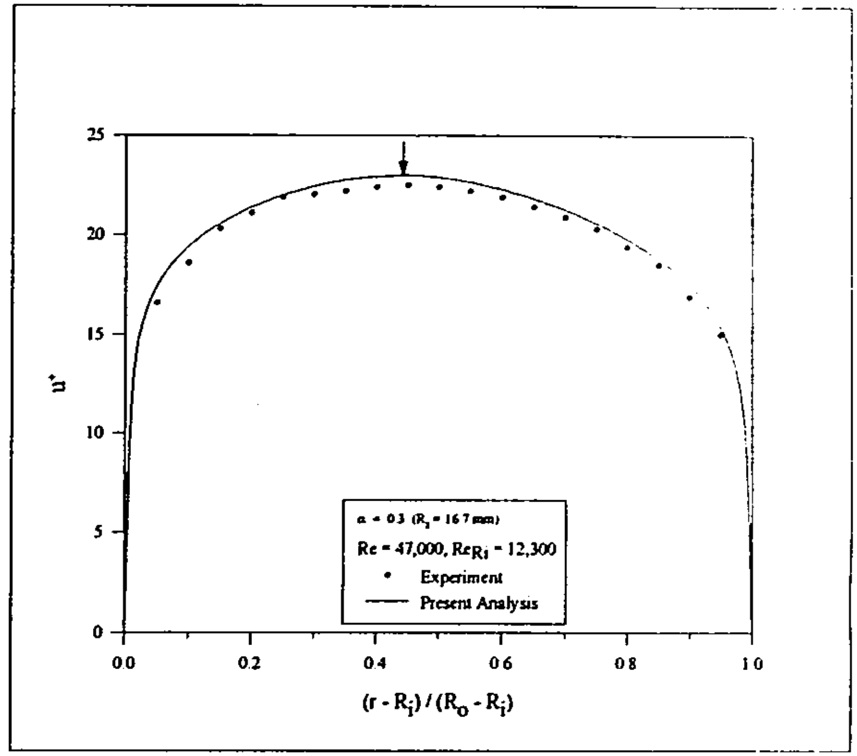

(d) Re = 52,000

Figure 4.27 Comparison between Theoretical and Experimental Velocity Distribution, Fully Developed, $\alpha = 0.3$ (R_i = 16.7mm).

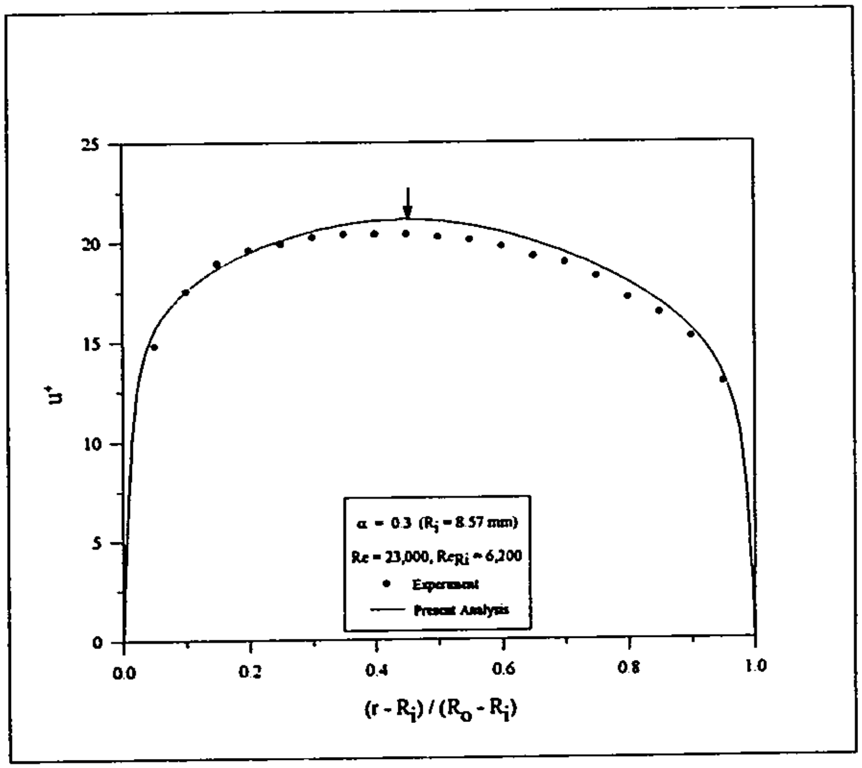

(a) Re = 23,000

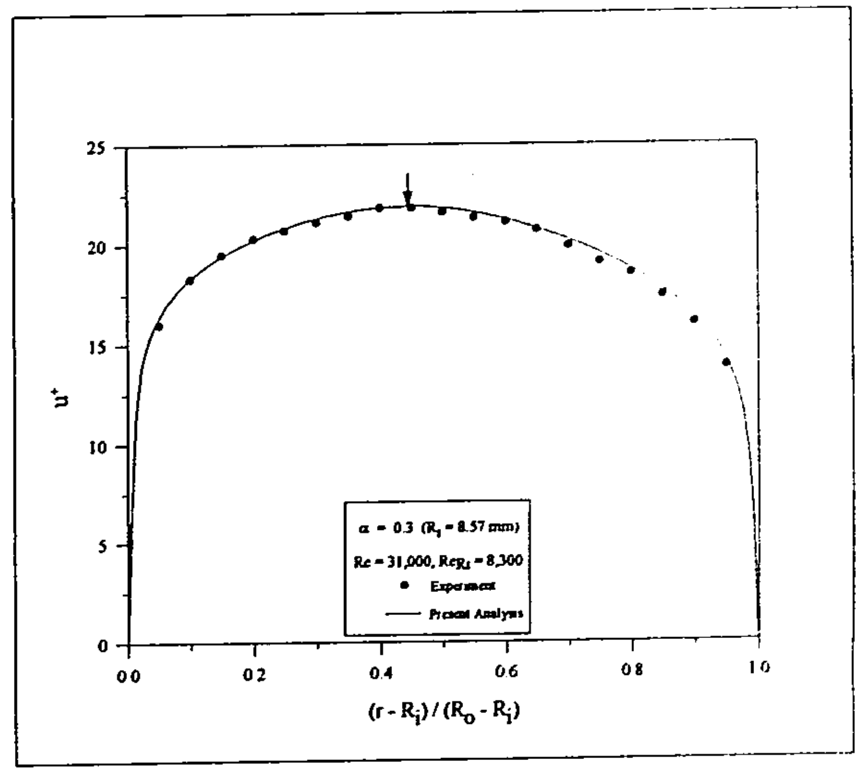

(b) Re = 31,000

Figure 4.28 Comparison between Theoretical and Experimental Velocity Distribution, Fully Developed, $\alpha = 0.3$ ($R_i = 8.57$mm). (continued)

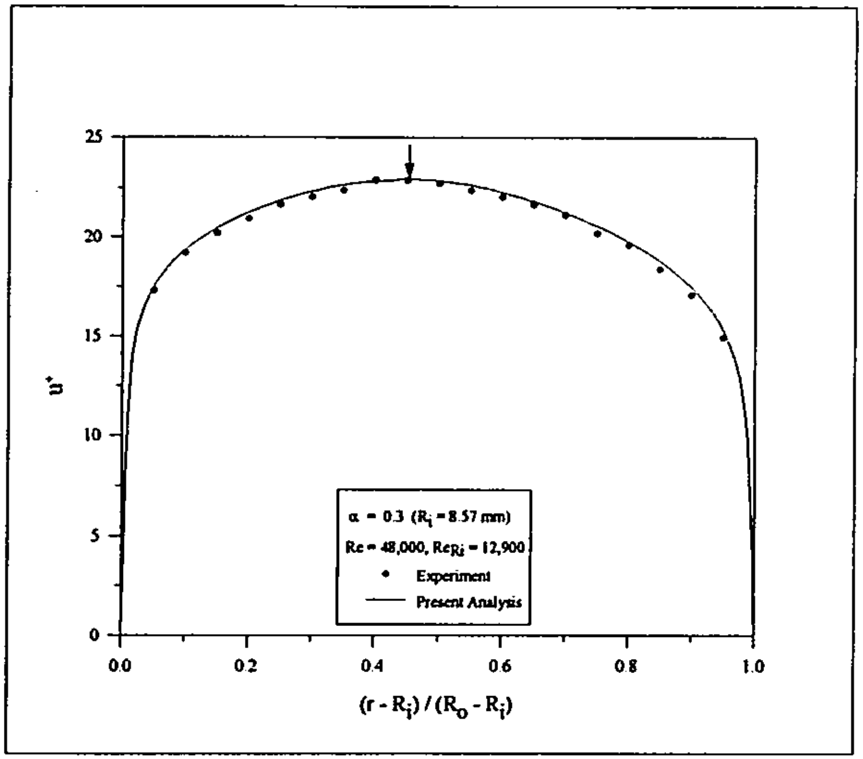

(c) Re = 48,000

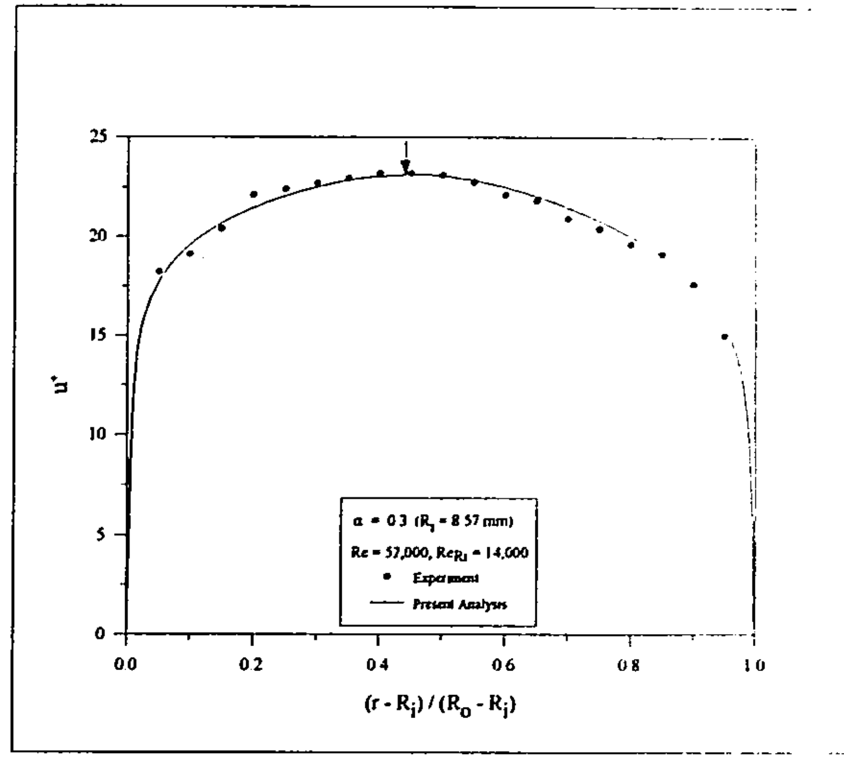

(d) Re = 52,000

Figure 4.28 Comparison between Theoretical and Experimental Velocity Distribution, Fully Developed, $\alpha = 0.3$ ($R_i = 8.57$mm).

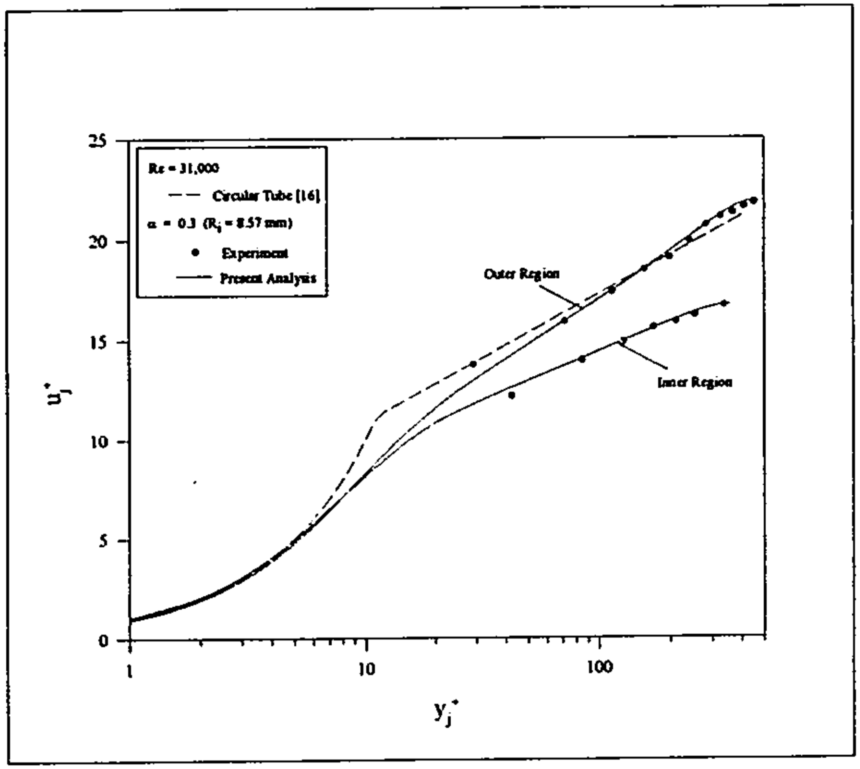

(a) Re = 31,000

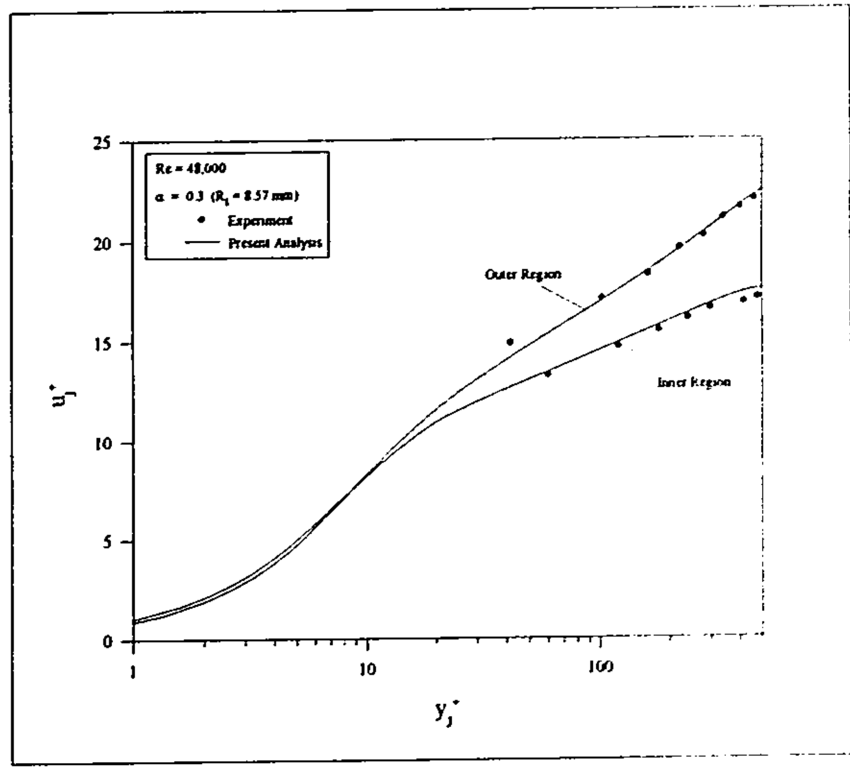

(b) Re = 48,000

Figure 4.29 Comparison of Experimental Results with Theoretical Velocity Distribution, Fully Developed, $\alpha = 0.3$ ($R_i = 8.57$mm).

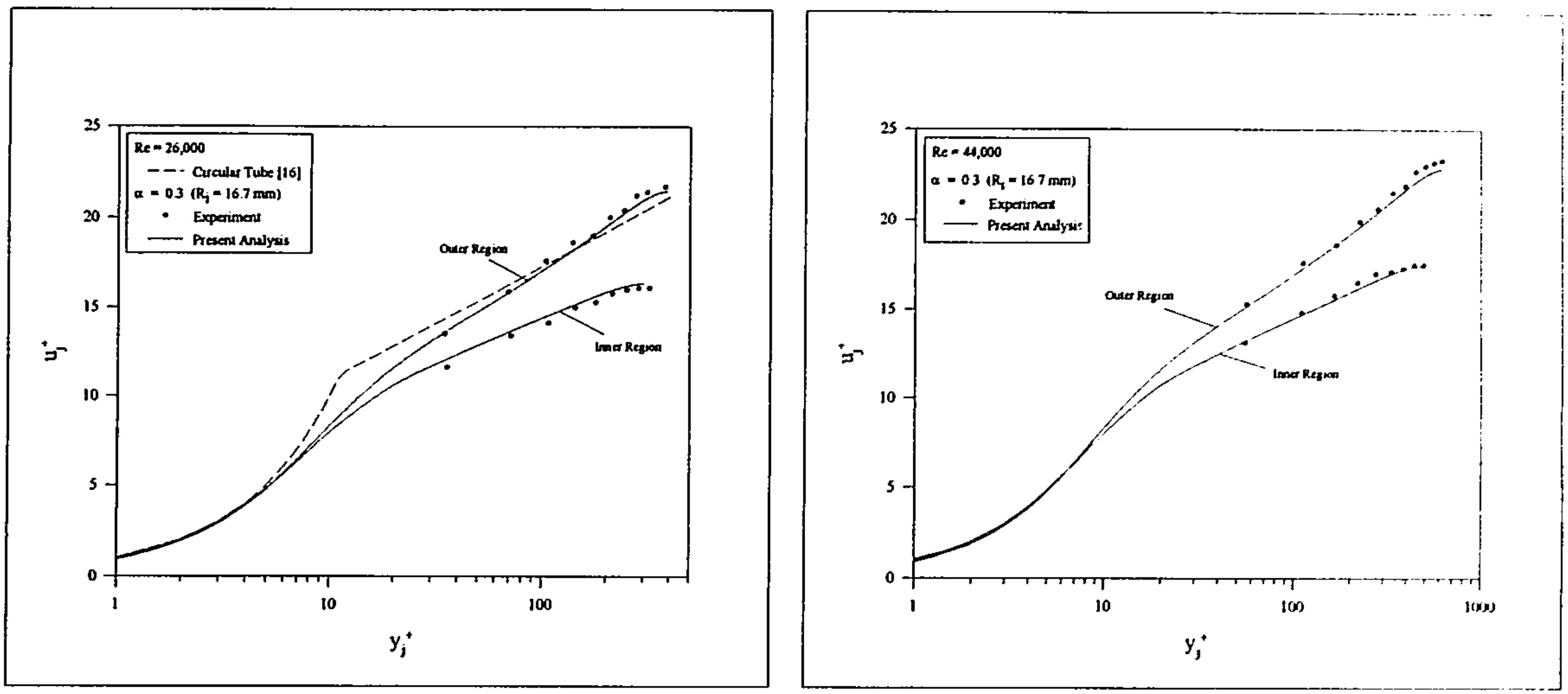

(a) Re = 26,000

(b) Re = 44,000

Figure 4.30 Comparison of Experimental Results with Theoretical Velocity Distribution, Fully Developed, $\alpha = 0.3$ ($R_i = 16.7$ mm).

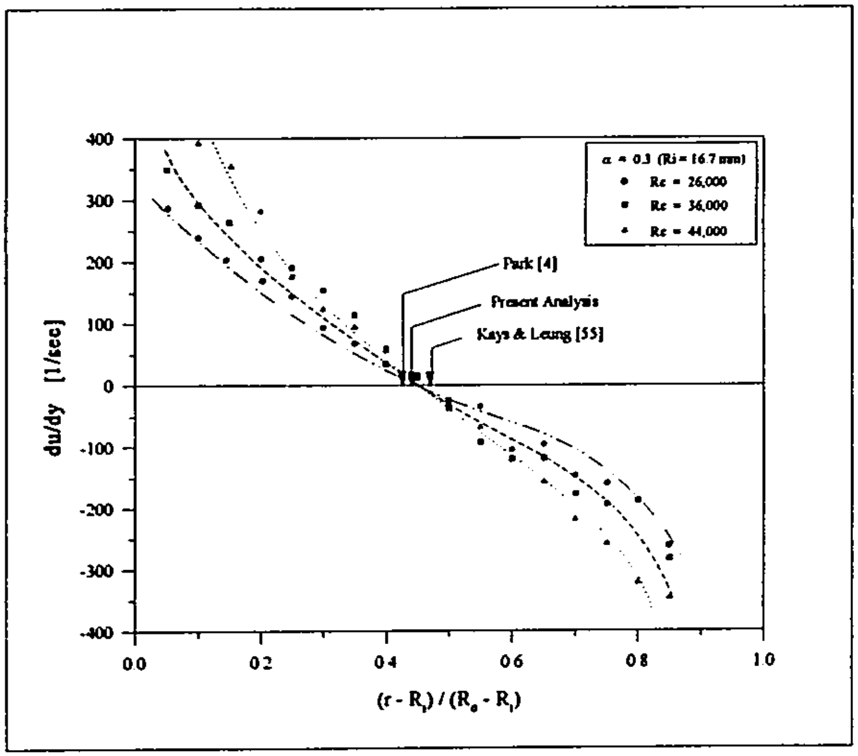

(a) $\alpha = 0.3$ ($R_i = 16.7$ mm)

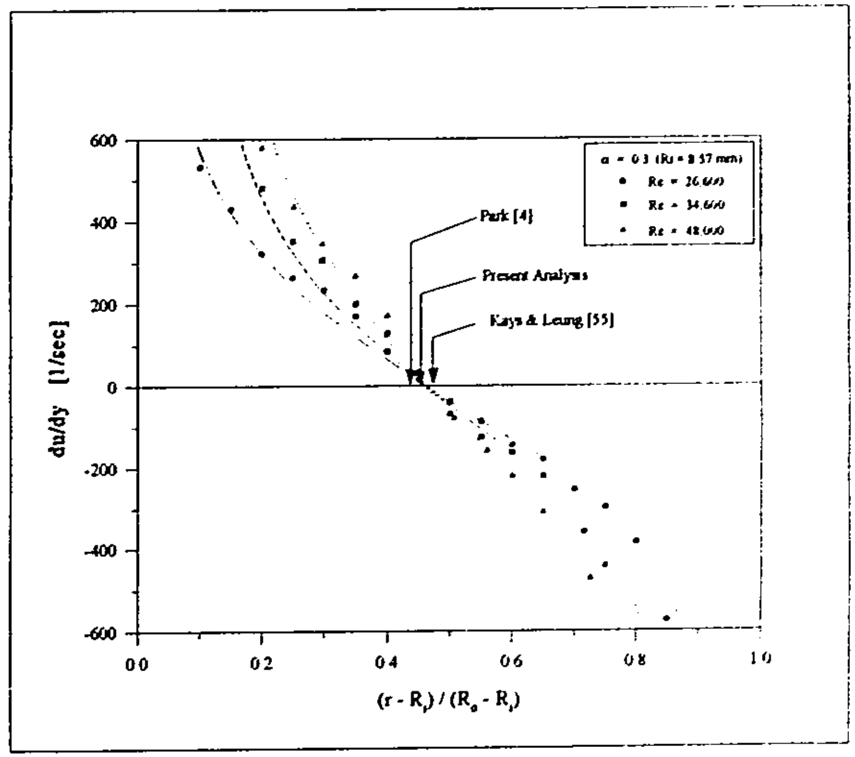

(b) $\alpha = 0.3$ ($R_i = 8.57$ mm)

Figure 4.31 Velocity Gradient in Region of Maximum Velocity

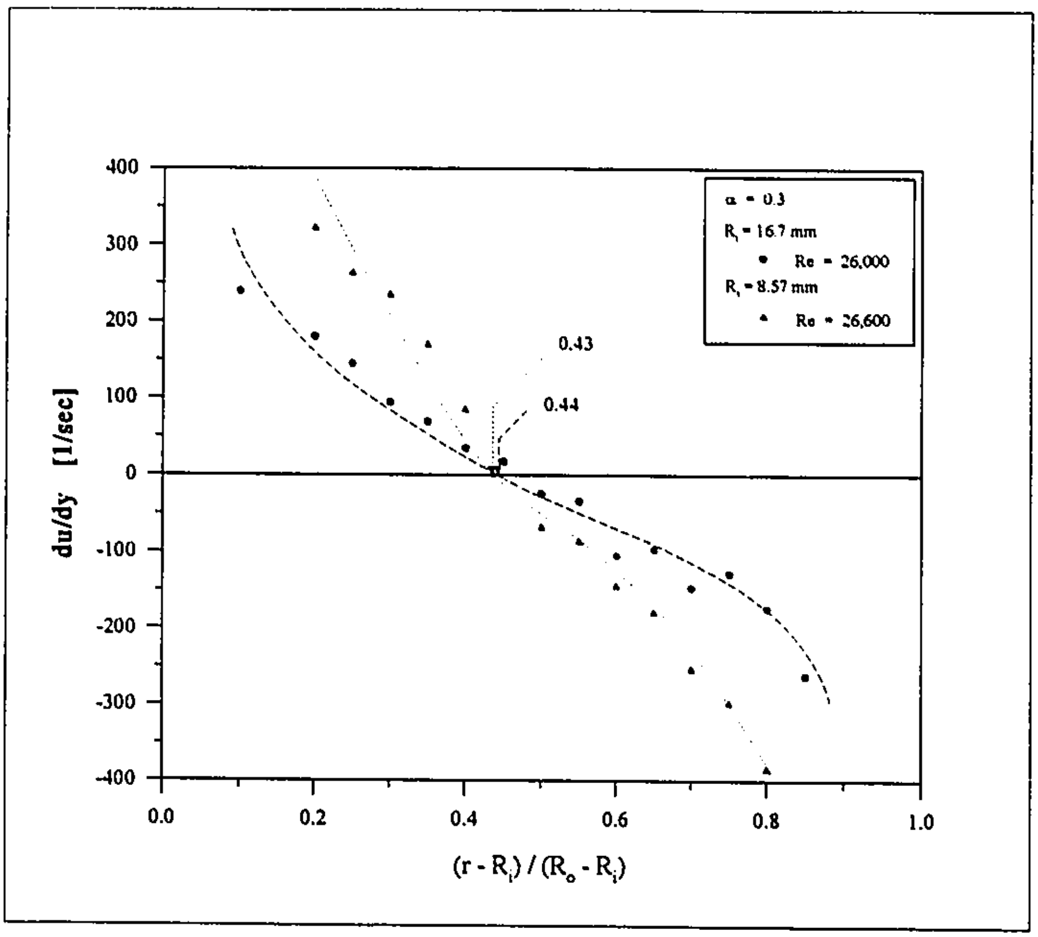

Figure 4.32 The Effect of Transverse Convex Surface Curvature, R_i, on Radius of Maximum Velocity, $\alpha = 0.3$, Re = 26,000

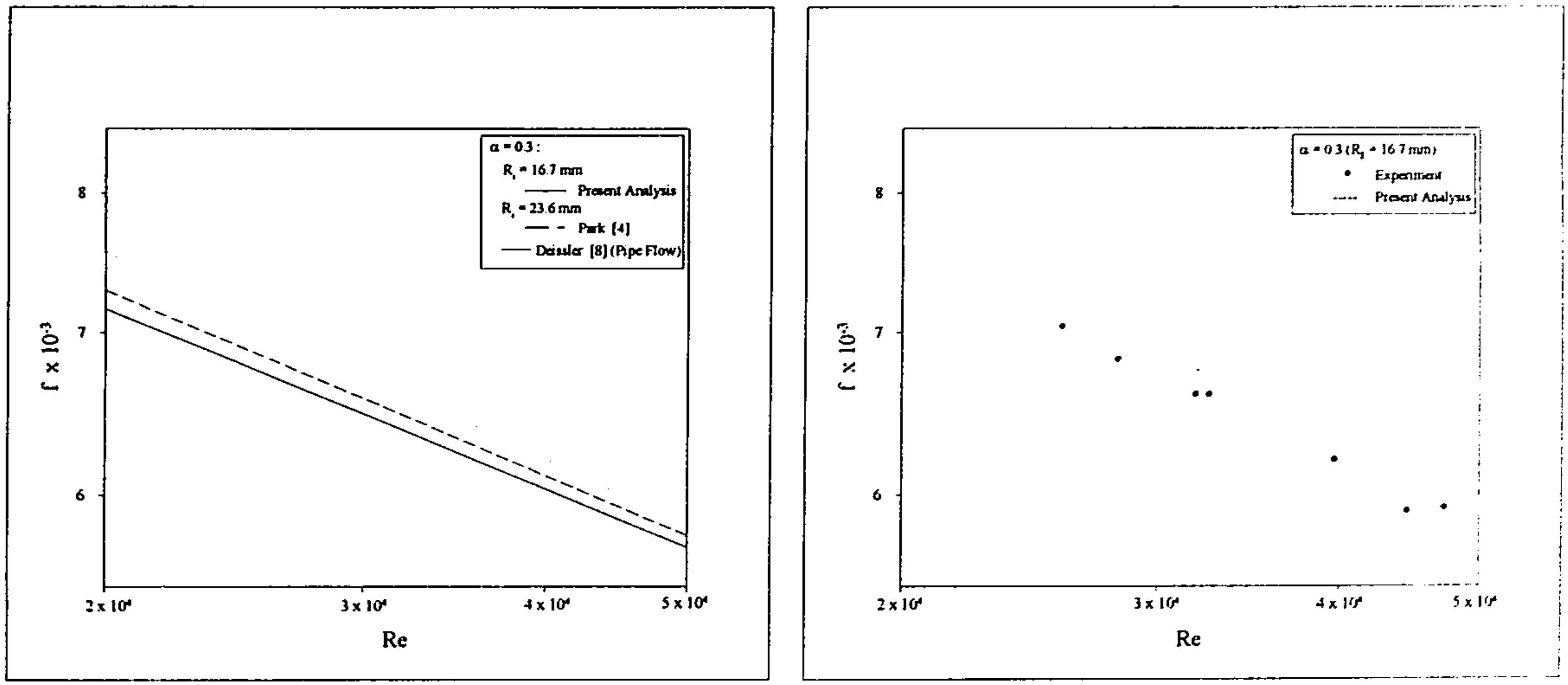

(a) Theory

(b) Experiment

Figure 4.33 Comparison between Theoretical and Experimental Friction Coefficient, Fully Developed, $\alpha = 0.3$ (R_i =16.7 mm)

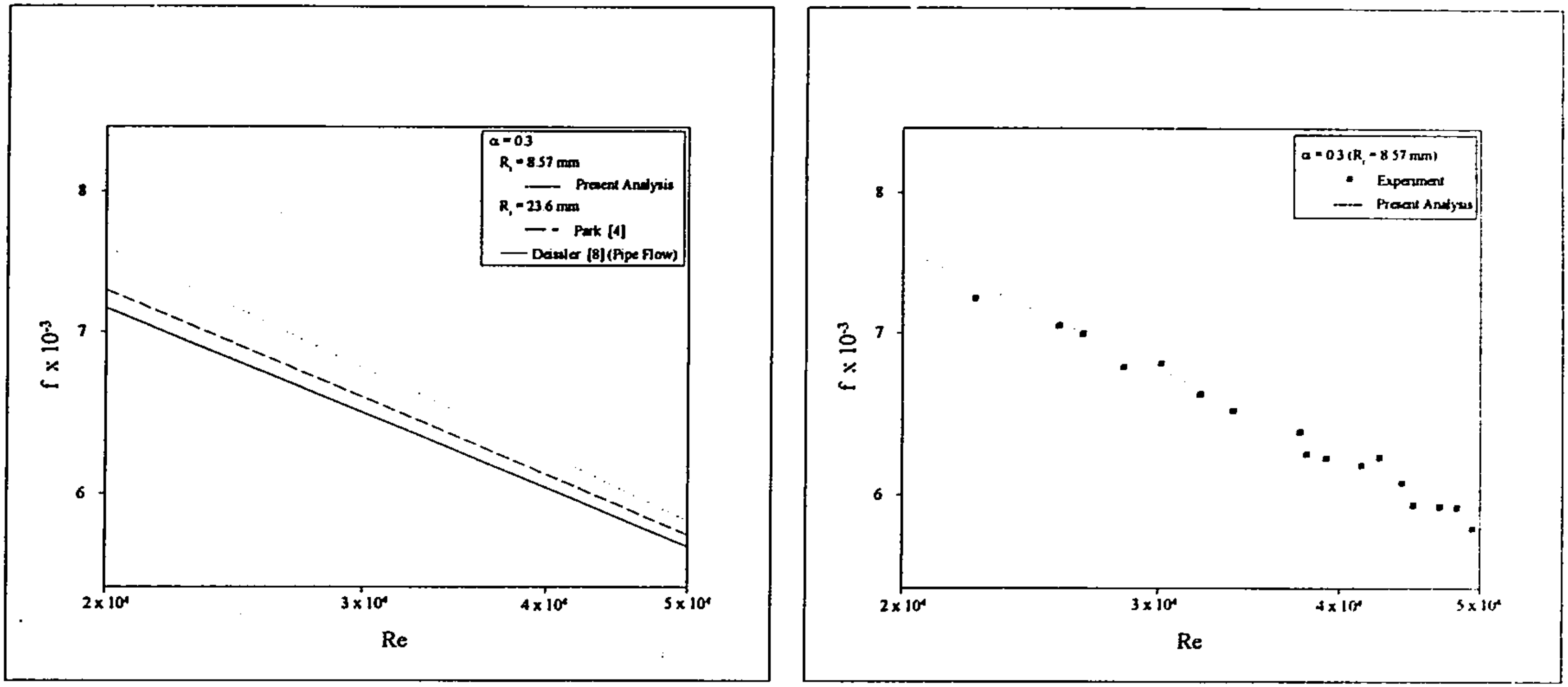

(a) Theory

(b) Experiment

Figure 4.34 Comparison between Theoretical and Experimental Friction Coefficient, Fully Developed, $\alpha = 0.3$ ($R_i = 8.57$ mm)

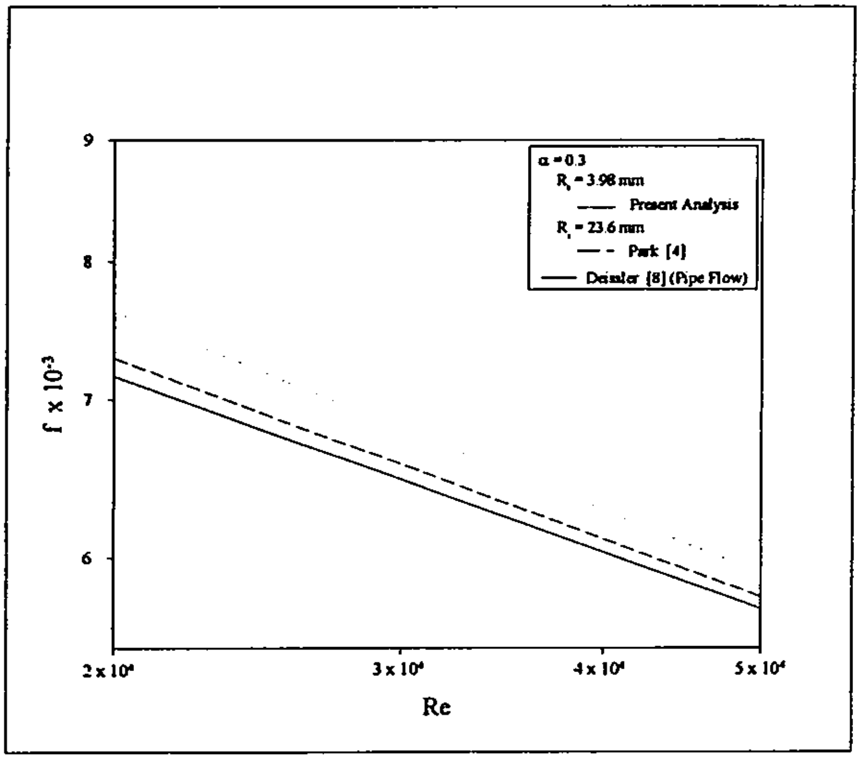

(a) Theory

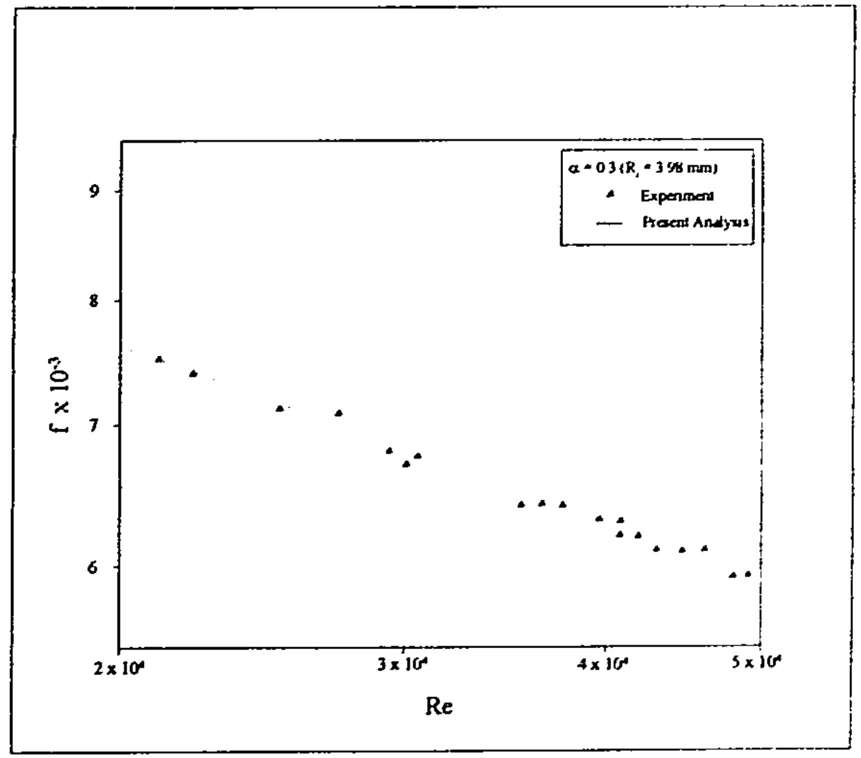

(b) Experiment

Figure 4.35 Comparison between Theoretical and Experimental Friction Coefficient, Fully Developed, $\alpha = 0.3$ ($R_i = 3.98$ mm)

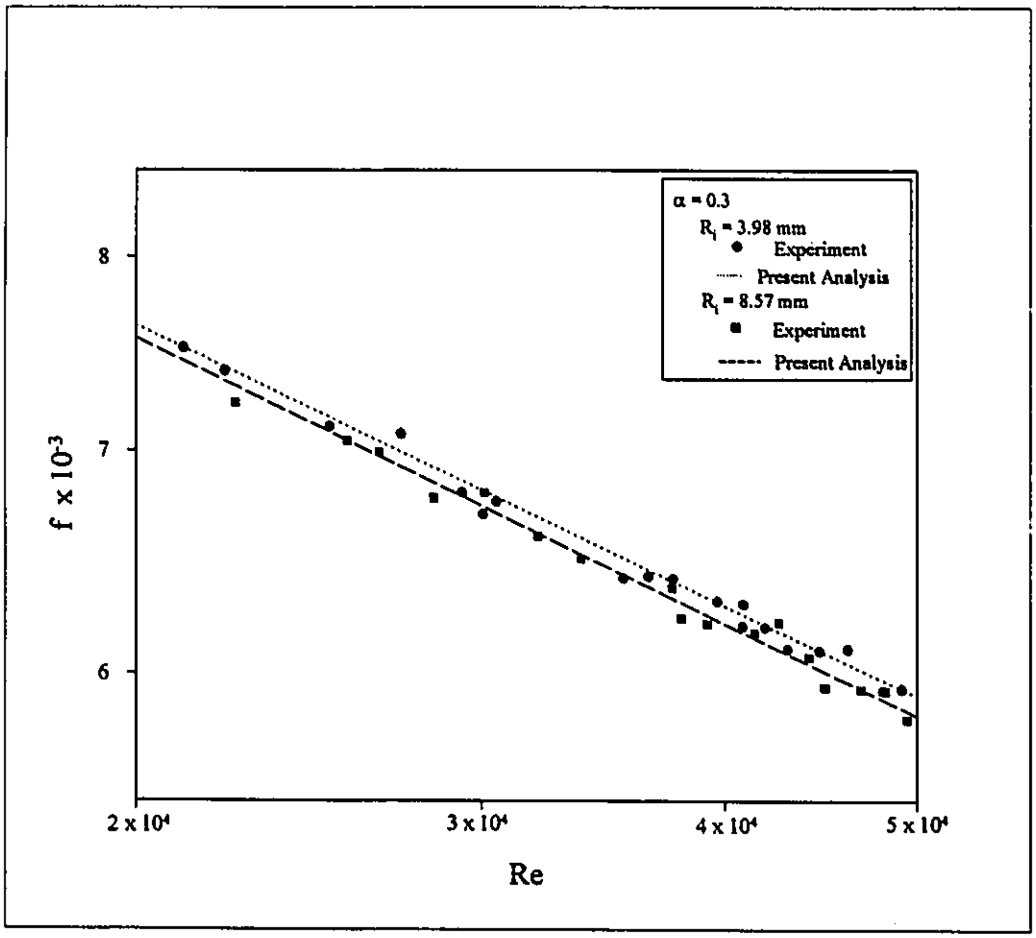

Figure 4.36 Effect of Transverse Convex Curvature on Friction Coefficient, Fully Developed Turbulent Flow

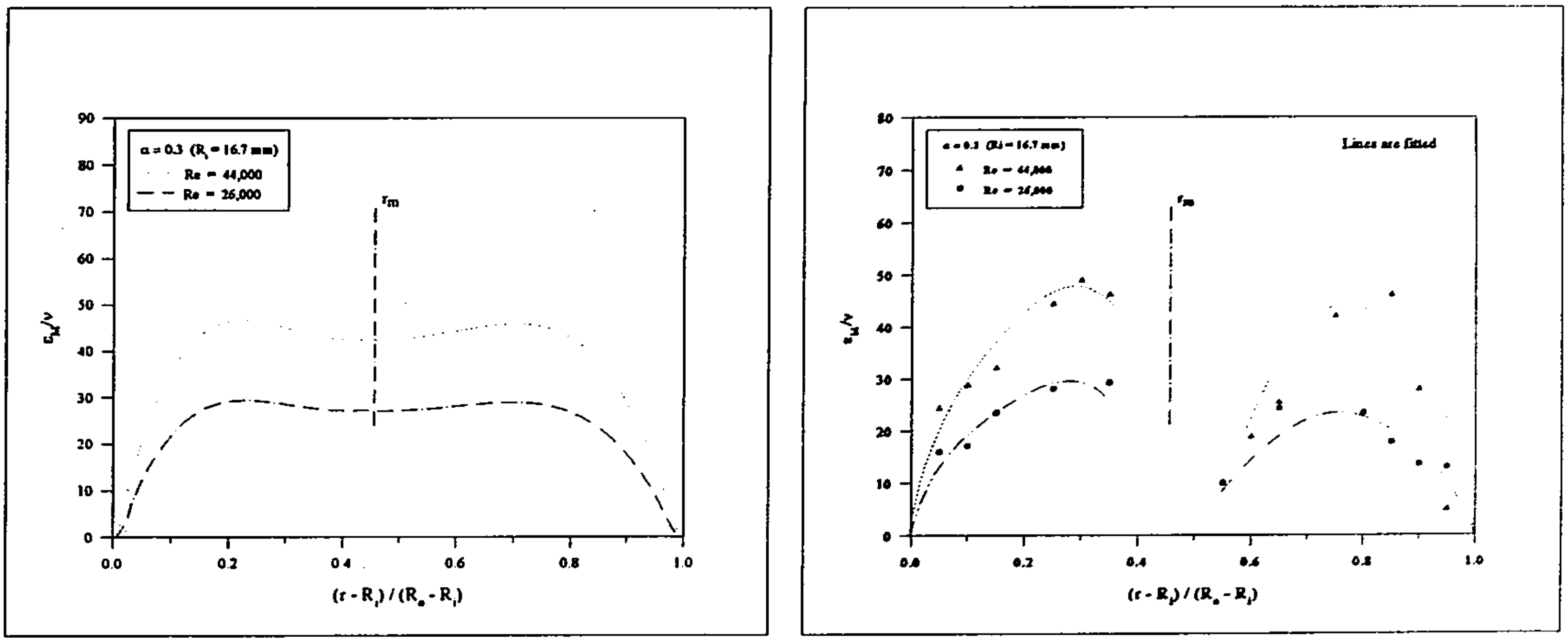

(a) Theory

(b) Experiment

Figure 4.37 Comparison between Theoretical and Experimental Eddy Diffusivity for Momentum, Fully Developed Turbulent Flow, $\alpha = 0.3$ ($R_i = 16.7$ mm)

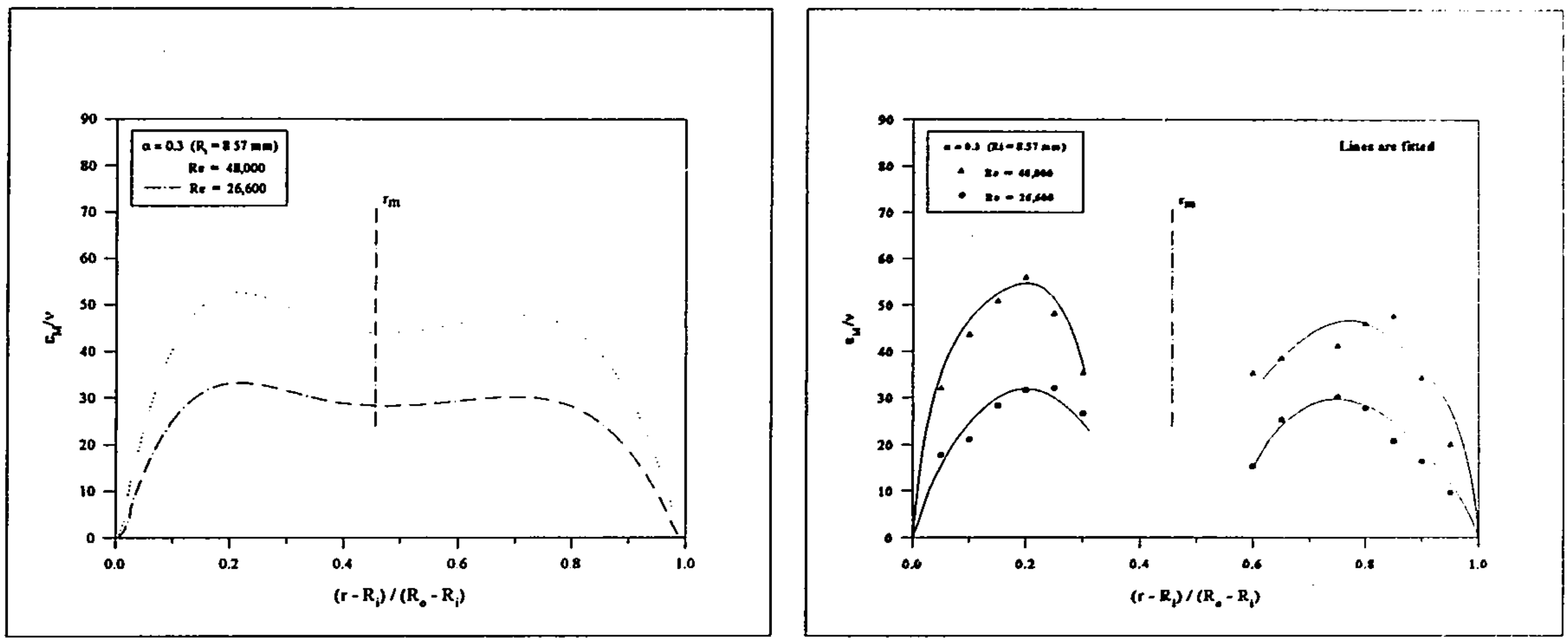

(a) Theory

(b) Experiment

Figure 4.38 Comparison between Theoretical and Experimental Eddy Diffusivity for Momentum, Fully Developed Turbulent Flow, $\alpha = 0.3$ ($R_i = 8.57$ mm)

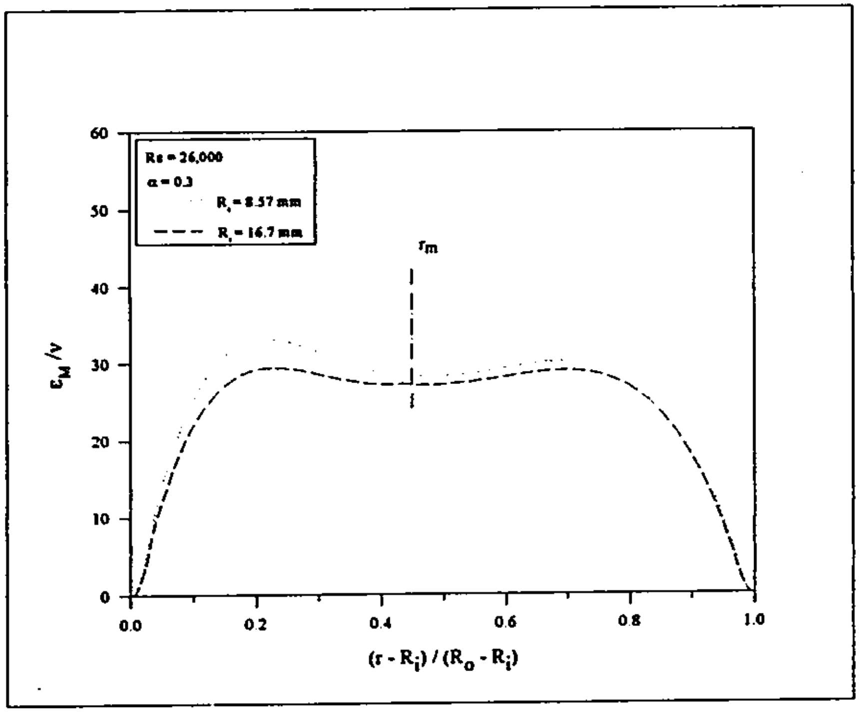

(a) Theory

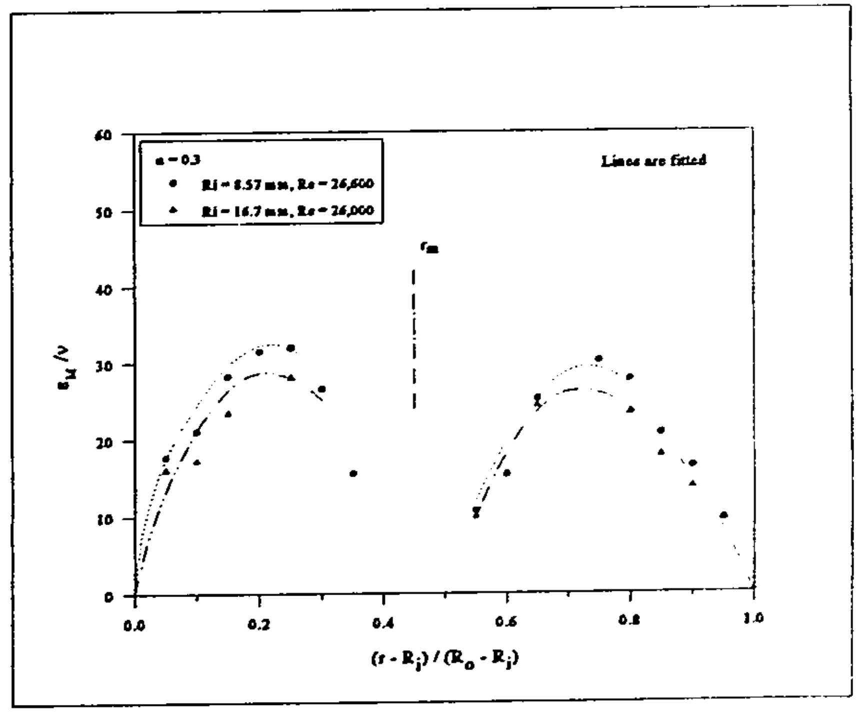

(b) Experiment

Figure 4.39 Effect of Transverse Convex Curvature on Eddy Diffusivity for Momentum, Fully Developed Turbulent Flow, Re = 26,000

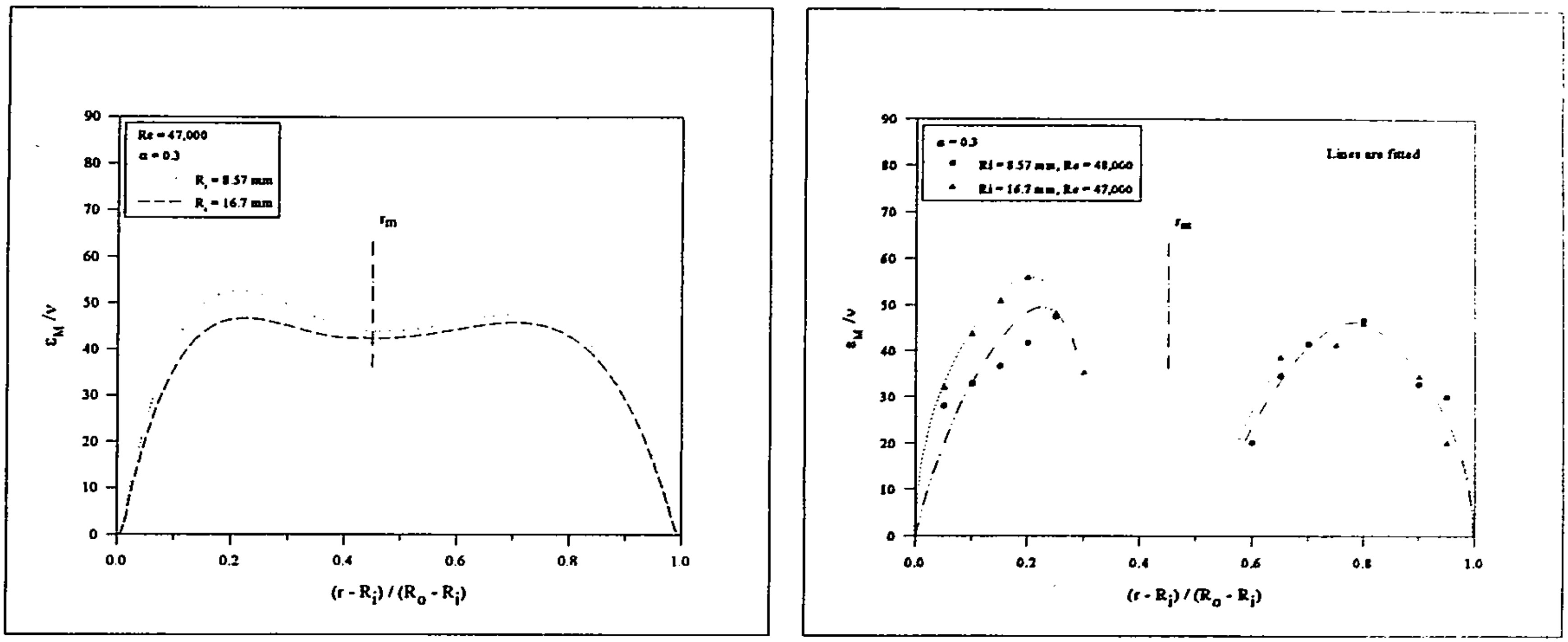

(a) Theory

(b) Experiment

Figure 4.40 Effect of Transverse Convex Curvature on Eddy Diffusivity for Momentum, Fully Developed Turbulent Flow, Re = 47,000

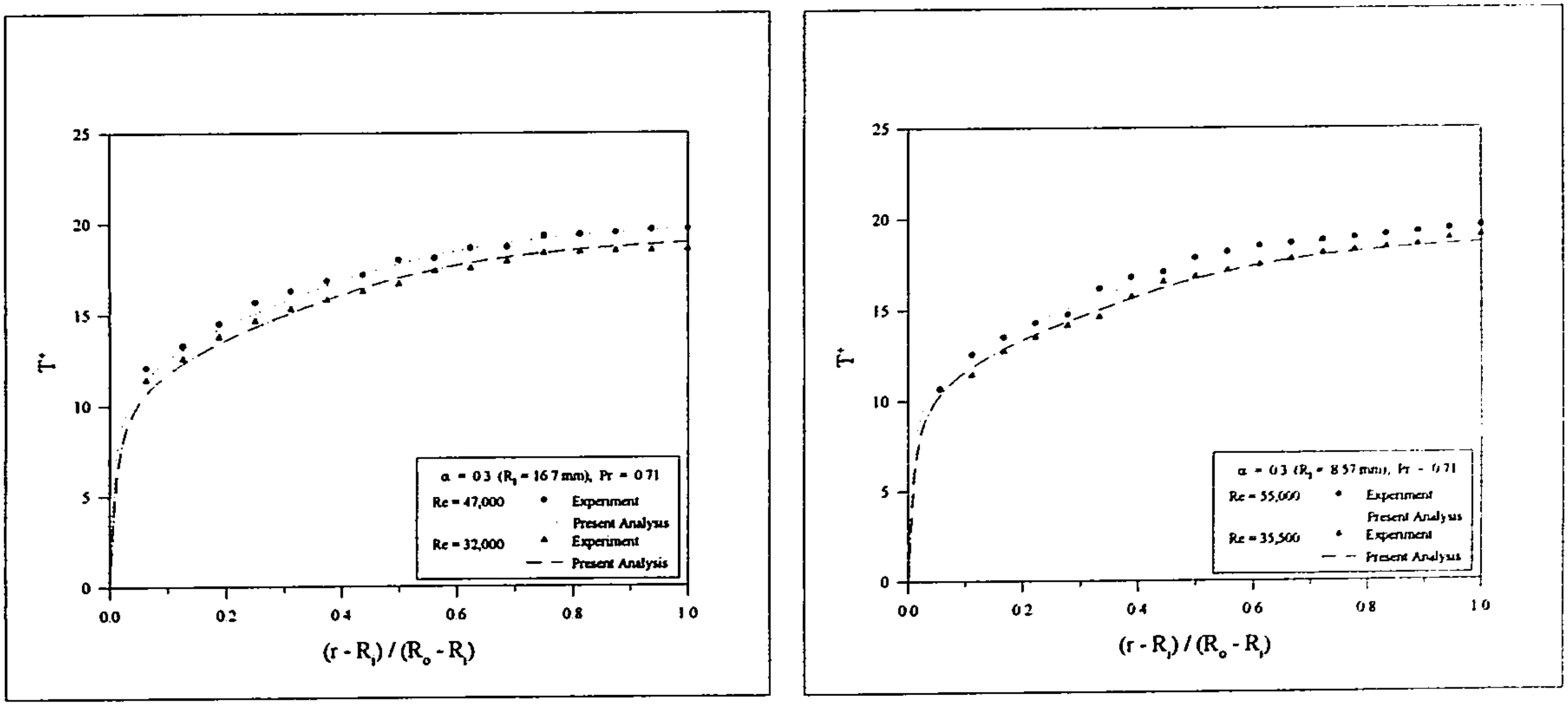

(a) $\alpha = 0.3$ ($R_i = 16.7$ mm)

(b) $\alpha = 0.3$ ($R_i = 8.57$ mm)

Figure 4.41 Comparison between Theoretical and Experimental Temperature Distribution, Inner Core Wall Heated, Outer Tube Wall Insulated, Fully Developed Turbulent Flow

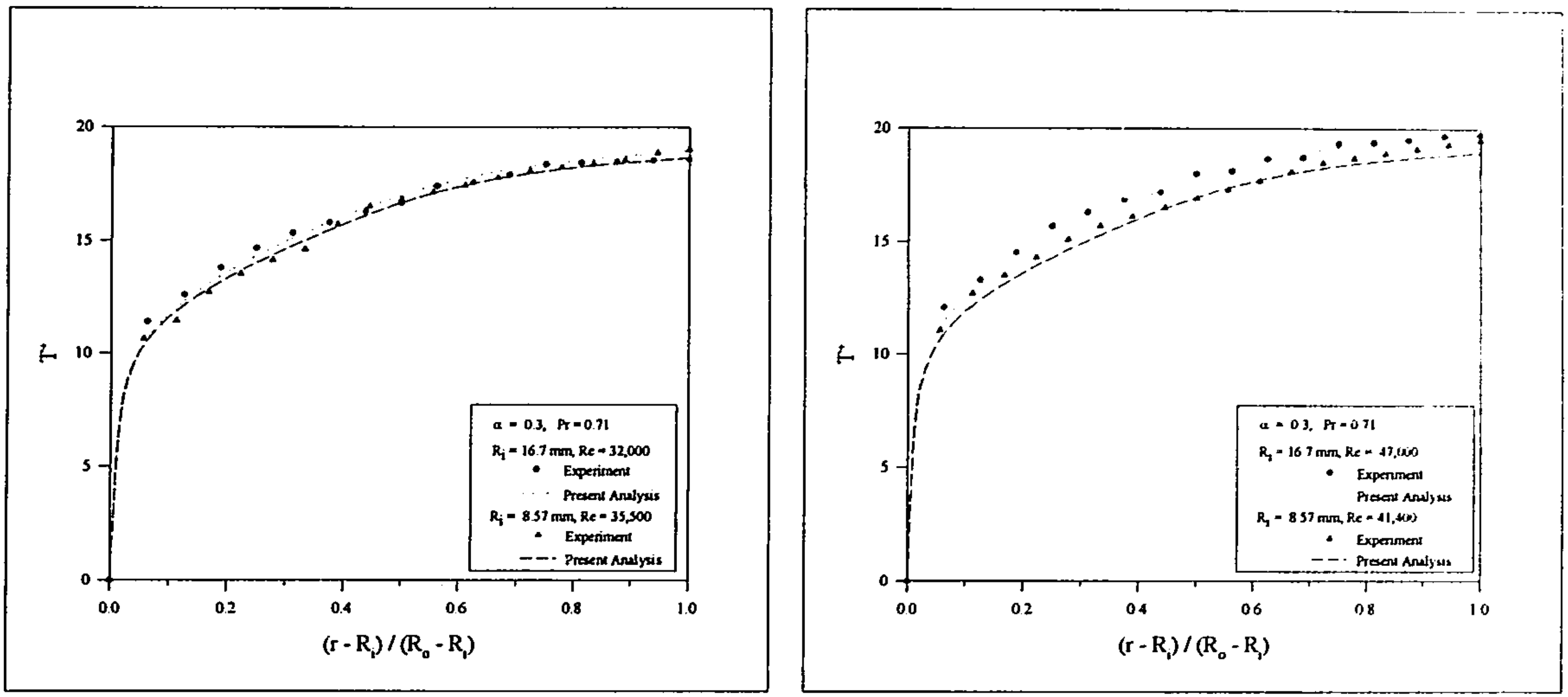

(a) Re = 32,000

(b) Re = 47,000

Figure 4.42 Effect of Transverse Convex Curvature on Temperature Distribution, Inner Core Wall Heated, Outer Tube Wall Insulated, Fully Developed Turbulent Flow

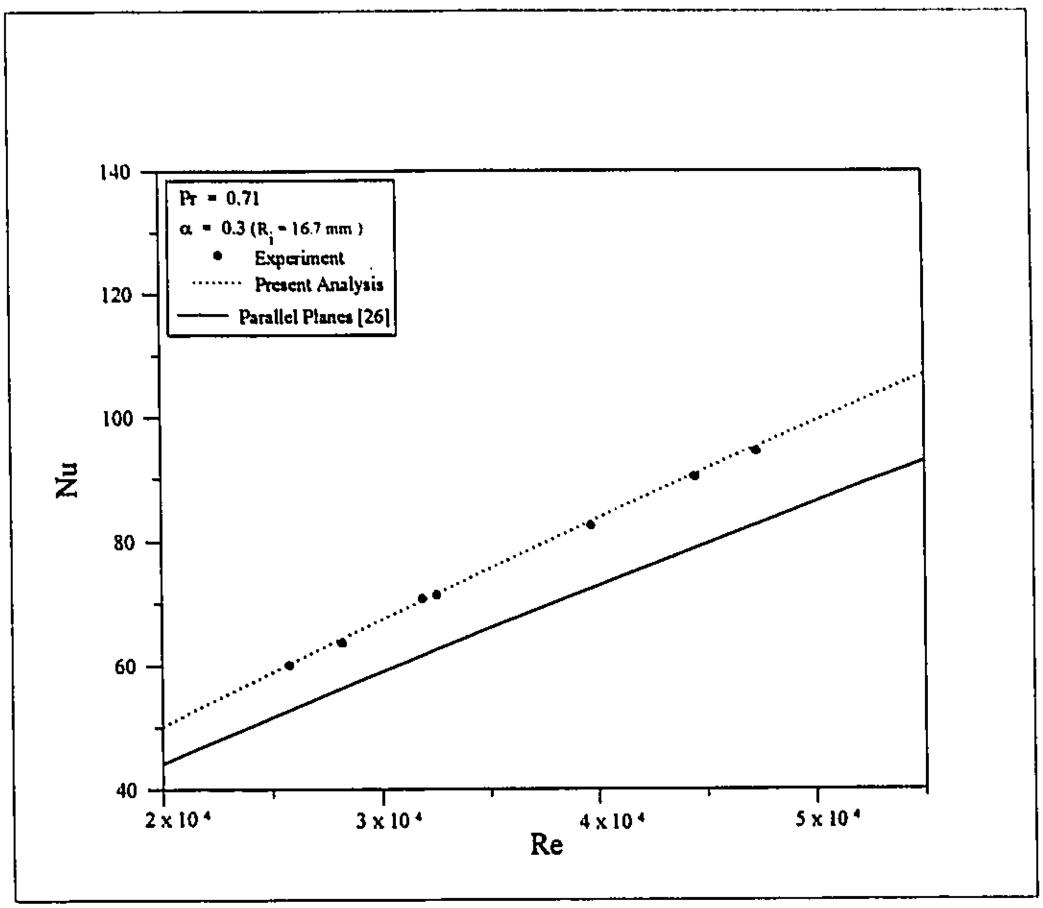

Figure 4.43 Comparison between Theoretical and Experimental Nusselt Number, Inner Core Wall Heated, Outer Tube Wall Insulated, Fully Developed Turbulent Flow, $\alpha = 0.3$ (R_i =16.7 mm)

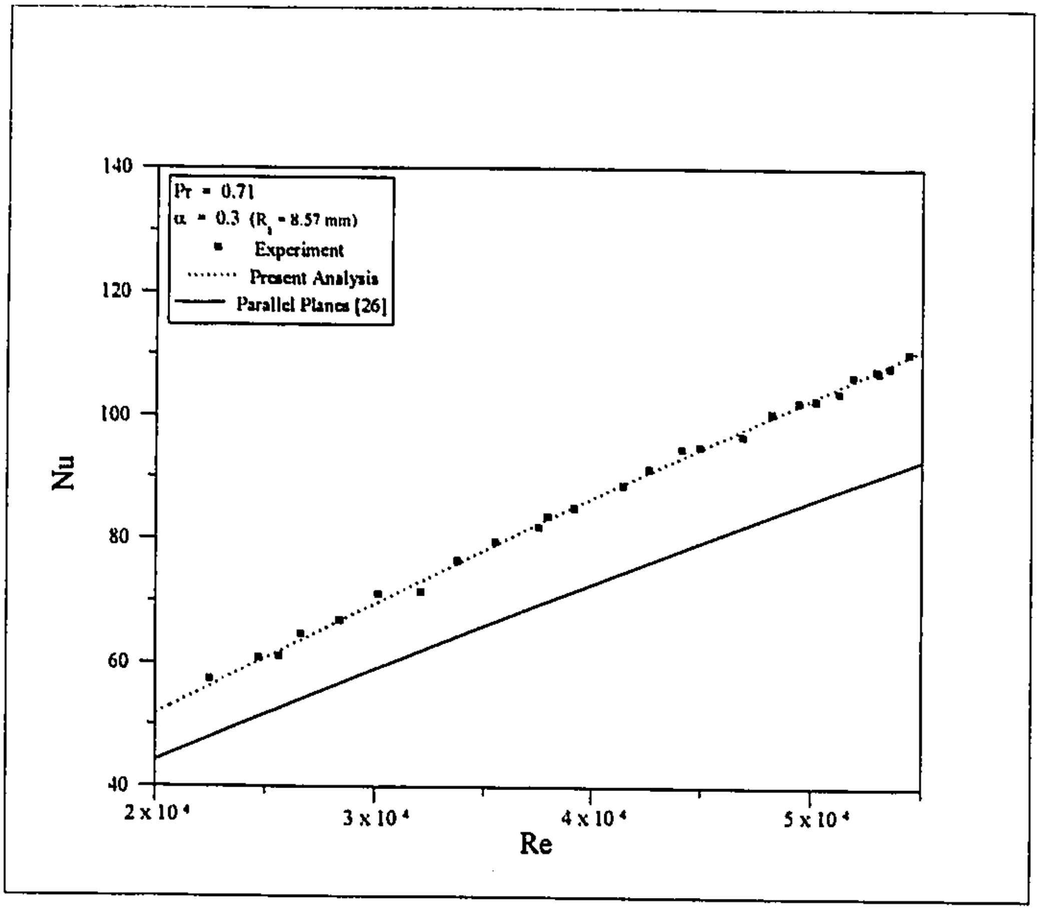

Figure 4.44 Comparison between Theoretical and Experimental Nusselt Number, Inner Core Wall Heated, Outer Tube Wall Insulated, Fully Developed Turbulent Flow, $\alpha = 0.3$ ($R_i = 8.57$ mm)

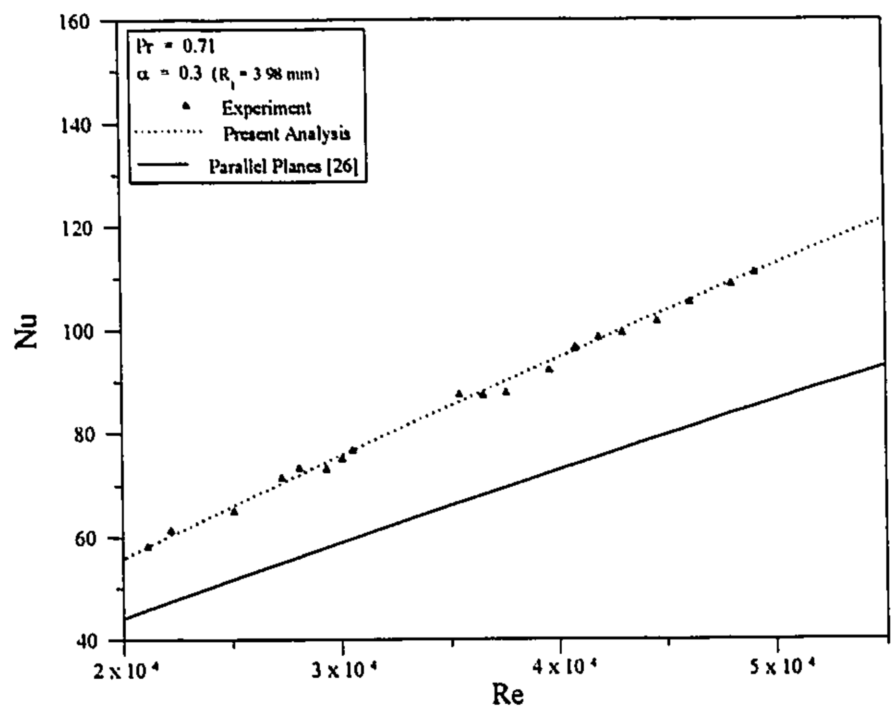

Figure 4.45 Comparison between Theoretical and Experimental Nusselt Number, Inner Core Wall Heated, Outer Tube Wall Insulated, Fully Developed Turbulent Flow, $\alpha = 0.3$ ($R_i = 3.98$ mm)

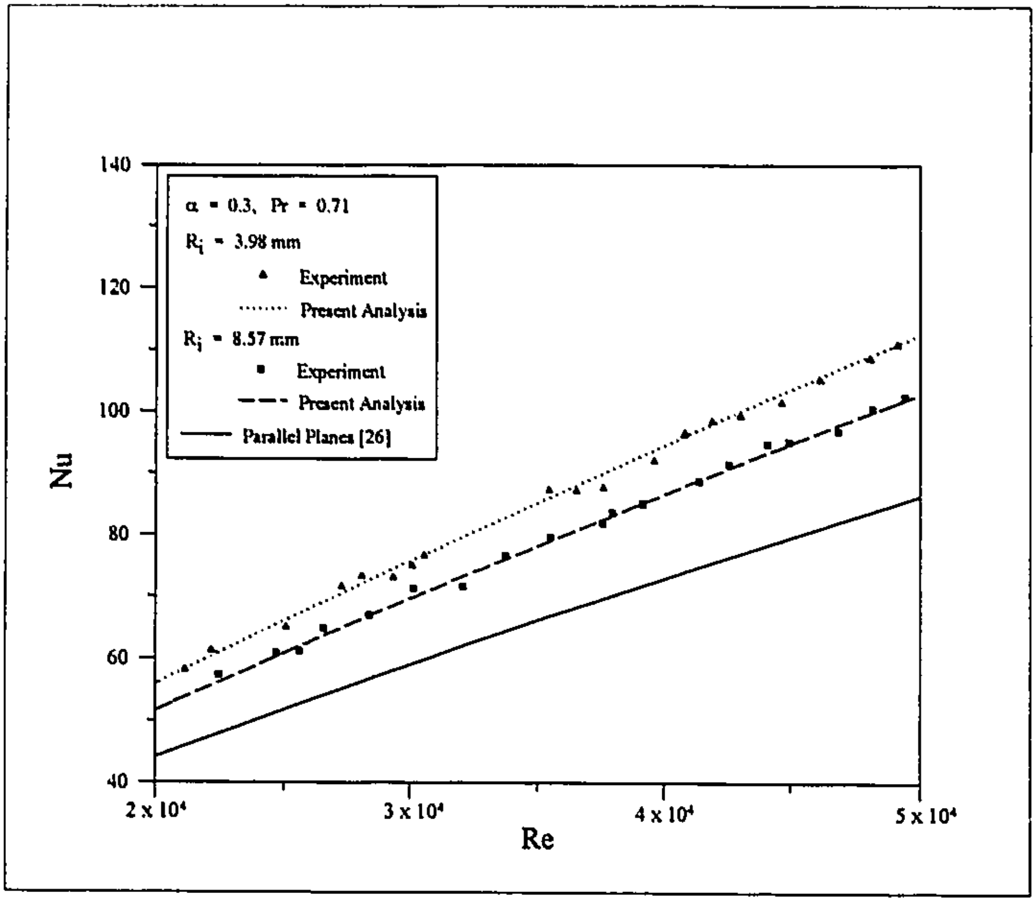

Figure 4.46 Effect of Transverse Convex Curvature on Nusselt Number, Inner Core Wall Heated, Outer Tube Wall Insulated, Fully Developed Turbulent Flow

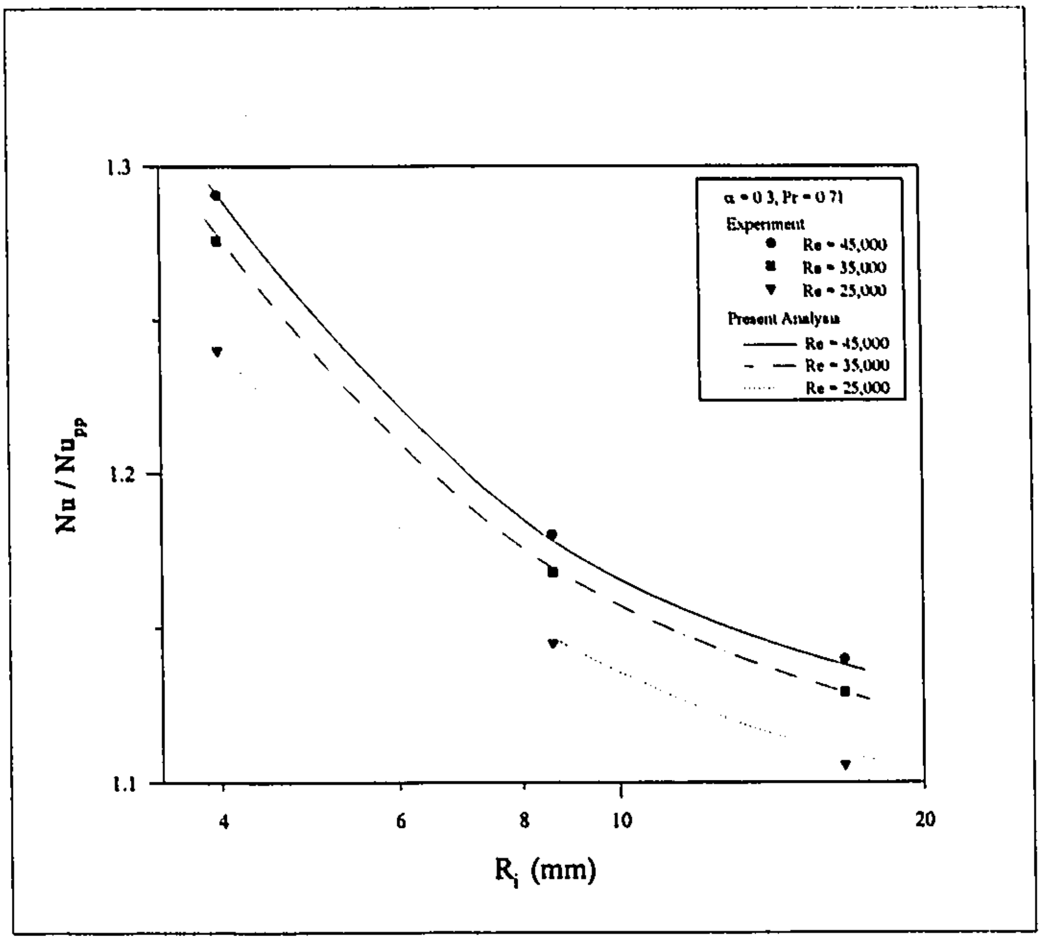

Figure 4.47 Effect of Transverse Convex Curvature and Reynolds Number on Nusselt Number, Inner Core Wall Heated, Outer Tube Wall Insulated, Fully Developed Turbulent Flow